Development of localised process parameter control for repeatability in metal additive manufacturing

Luke Patrick Dowling

SUBMITTED IN FULFILMENT OF THE REQUIREMENTS FOR THE DEGREE OF DOCTOR OF PHILOSOPHY AT UNIVERSITY OF DUBLIN, TRINITY COLLEGE DUBLIN, IRELAND,
FEBRUARY 2021.

Supervisor: Dr Daniel Trimble

The work presented in this thesis was conducted at the Department of Mechanical and Manufacturing Engineering, University of Dublin, Trinity College Dublin, Ireland.

Declaration

I declare that this thesis has not been submitted as an exercise for a degree at this or any other university and it is entirely my own work.

I agree to deposit this thesis in the University's open access institutional repository or allow the library to do so on my behalf, subject to Irish Copyright Legislation and Trinity College Library conditions of use and acknowledgement.

Luke Dowling

Department of Mechanical and Manufacturing Engineering

Trinity College Dublin, February 2021.

Summary

Due to the many advantages associated with metal additive manufacturing (AM) processes, research into these technologies has grown significantly over recent years. However, repeatability and reproducibility are critical issues in AM when compared to traditional manufacturing processes.

The overall aim of this project was to comprehensively investigate the sources of this repeatability issue and to develop a means of improving the process repeatability. This was achieved by a thorough literature review with an in-depth focus on the configuration present in the ProX DMP 200.

The causes and impact of repeatability were reviewed at three stages of the AM process: pre-process, para-process and post-process. It was found that the most impactful effect for repeatability is non-uniform energy density in the build area. This was predominantly due to errors associated with the F-Theta lens, plume absorption and the effect of angle of incidence on the powder bed.

A new energy density equation was developed to account for the spatially varying energy density in selective laser melting. This equation was used as a basis for location-dependent control of process parameters. These adapted parameters were tested using samples made of cobalt chrome alloy and 316L stainless steel.

The adapted parameters reduced the range of variation in local mechanical property values by up to 40%, representing a statistically significant reduction in the systematic variation between the centre and edge of the machine's working envelope.

Acknowledgements

Thanks to my parents, Jacqueline Sweeney and Joseph Dowling, and my sister, Chris Dowling for all the support throughout the PhD process and all the previous years of study.

Dr Daniel Trimble for the opportunity to undertake this PhD, who provided guidance, support and technical expertise throughout the PhD without which it would not have been possible to complete.

Dr John Kennedy for financial support and engaging problems through the AERIALIST project. The project allowed me to begin my PhD and I am particularly grateful for the guidance in the initial stages of my research.

Dr Larisa Florea for financial support and guidance during the final two years of the PhD as a part of her research group. Joining the group allowed me to broaden my research horizons and collaborate beyond pure engineering.

My thanks also to Lara Flanagan, Harry Shipley, Alex Conway, Colm Delaney, David Heaphy, Daniel Tobin, Jennifer Quirke, Carly Donoghue, Nicolas Blott and Niamh Kearney for all of their help, great and small, provided over the course of my PhD studies.

Table of Contents

Nomenclature

.STL	File format for CAD software created by 3D Systems
3D	Three Dimensional
3DP	Inkjet 3D Printer
AM	Additive Manufacturing
CAD	Computer-Aided Design
CoCr	Cobalt Chrome
CI	Confidence Interval
DLP	Direct light Processing
EBM	Electron Beam Melting
ED	Energy Density
EDM	Electrical Discharge Machining
FDM	Fused Deposition Modelling
FEF	Freeze-form Extrusion Fabrication
LMD	Laser Metal Deposition
LOM	Laminated Object Manufacturing
MJM	Multi-Jet Modelling
MPa	Megapascal
PBF	Powder Bed Fusion
RFP	Rapid Freezing Prototyping
SKU	Stock Keeping Unit
SLA	Stereolithography
SLM	Selective Laser Melting
SLS	Selective Laser Sintering
Ti64	Titanium 6% Aluminium 4% Vanadium alloy
UTS	Ultimate Tensile Strength

Chapter 1: Introduction

1.1 Introduction to Repeatability

An important factor taken for granted in the modern manufacturing world is the impact of standardised parts. Prior to the early 19th century, parts or components were generally bespoke to application and not mass-produced [1]. Standardised parts allowed for interchangeability and the mechanisation for mass manufacture of subassembly parts such as bolts. Standardisation requires that the parts be within a defined specification and tolerance; with tolerance being a measure of precision, and repeatability being another measure of precision. Tolerances determine the acceptable limits of variation in a measurement, whereas repeatability determines the variation itself.

Repeatability is defined in ASTM E117 as “precision under the conditions where independent test results are obtained with the same method on identical test items in the same laboratory by the same operator using the same equipment within short intervals of time”. Reproducibility is similar, however, requires that the test can be carried out in different laboratories, with different operators, and using different equipment [2].

There is a consensus among experts and stakeholders in the aerospace, healthcare, and automotive fields that the repeatability of metallic AM parts, are not sufficient to meet their stringent consistency requirements [3]. The most important of these industry requirements is Overall Equipment Effectiveness (OEE), which needs to be greater than 70% and to also have scrap rates of less than 1000 parts per million. These requirements are compared to existing world-class automotive production which has an OEE of 85%. However, current AM production is significantly below this target with an OEE measured at approximately 30% [4].

OEE is calculated as availability multiplied by quality, multiplied by performance [5]. In the AM context, the culmination of these variables results in a sub-par OEE, for several reasons:

- The availability is hampered by the intensive set up required for each print and the often-needed interventions during a print, such as filter changes.
- The quality is limited by the imperfections inherent in the process and the significant repeatability concerns.
- The performance of the machine is harder to quantify due to its machine-specific nature, however, the general cycle for producing AM parts does contain a multitude of steps and delays which can reduce performance.
- As each of the components of OEE are combined multiplicatively, the weaknesses are magnified to give an OEE that is far from what would be expected in traditional manufacturing contexts.

Weller et al. [6] further demonstrated the impact of lack of AM reproducibility, in a comprehensive economic review on how AM is used in industry, and limitations on its use. The greatest barrier to a manufacturer's investment in AM systems was the limited reproducibility of parts resulting in a greater number of part rejects, which is a critical factor when calculating the quality term for OEE. The gains of AM cost reductions are lost economically if more rework is required in the production cycle. As additive parts are usually unable to be reworked or conditioned to conform to standards, they must be completely scrapped in the event that they are out of specification.

It is clear that a repeatability barrier exists in achieving high OEE in AM, and thus has the effect of hampering the adoption of AM as a mainstream manufacturing alternative. Hence, a major drive to improve the repeatability of additively manufactured parts is much needed.

1.2 Introduction to Additive Manufacturing

Additive manufacturing was invented as a functional rapid prototyping system. The concept for 3D printing was first described by David E. H. Jones in his article series published by new scientist in 1974 [7]. The first functional AM materials were developed by Hideo Kodama et al [8] in 1981. The first metal additive manufacturing technology was selective laser melting, which was developed in 1995 at the Fraunhofer Institute in Aachen and patented by Meiners et al in Germany [9].

The technologies used in AM has developed significantly over the years. Both historically and currently, the AM process can be described by a simplified number of steps:

- The part to be manufactured is designed in a CAD software package.
- The final CAD design is imported into a preparation software to orientate and add supports to the part to enable printing without excess overhangs or unsupported surfaces.
- The part and supports designs are imported into a slicing software that extracts the two-dimensional cross-section of the design layer-by-layer. Each layer, when added back together, forms the three dimensional part to be created. These software operations can all be in the same software package but more commonly they are different programs that can read a common file type such as .stl.
- The sliced layers are created sequentially from the base by a variety of techniques leaving the final part.

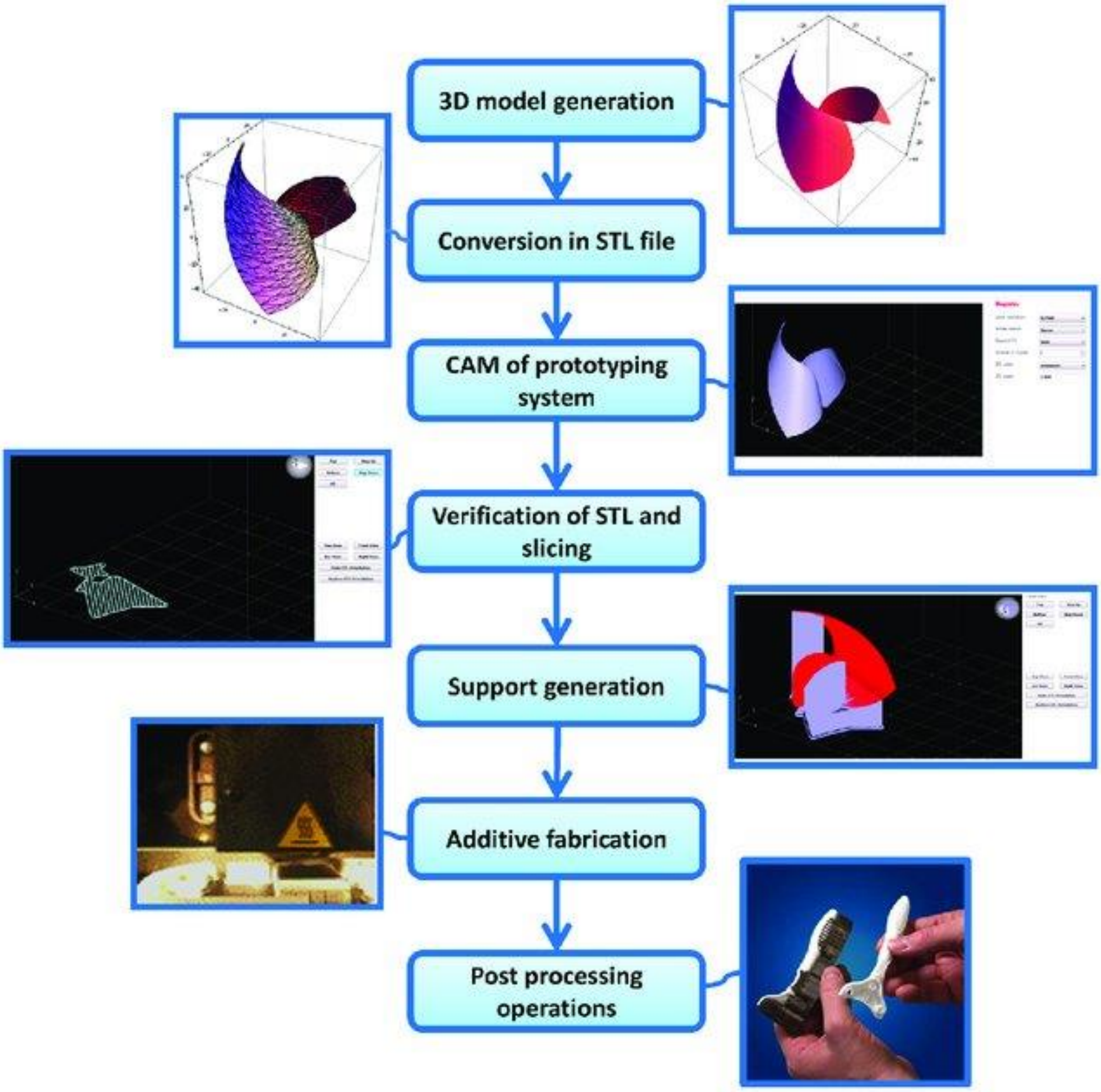

Figure 1: Additive manufacturing process [10]

While initially conceptualised as a rapid prototyping mechanism, currently, AM is a growing field in both applied research and industrial application. The recent Wohlers report on the AM industry showed an 80% growth in metal additive manufacture, while the AM industry as a whole grew by 21% [11]. The field of AM comprises a wide number of technologies as seen in Table 1 adapted from Prakash et al. [12]

Technology	**Material Preparation**	**Layer creation Technique**	**Phase Change**	**Typical Materials**
SLA	Liquid Resin in a vat	Laser Scanning	Photopolymerization	UV curable resin
DLP	Liquid Resin in a vat	Masked Flash Lamp	Photopolymerization	UV curable resin
MJM	Liquid polymer in jet	Ink-Jet printing	Photopolymerization	UV curable plastic
RFP	Liquid droplet in a nozzle	Droplet deposition	Solidification by freezing	Water
FDM	Filament in nozzle	Continuous extrusion	Solidification by cooling	Thermoplastics
Robot Casting	Paste in nozzle	Continuous extrusion	N/A	Ceramic paste
FEF	Paste in nozzle	Continuous extrusion	Solidification by freezing	Ceramic paste
SLS	Powder in bed	Laser Scanning	Partial Melting	Thermoplastics, Metal
SLM	Powder in bed	Laser Scanning	Full Melting	Metal
EBM	Powder in bed	Electro beam scanning	Full Melting	Metal
LMD	Powder in nozzle	Powder and Laser injection	Full Melting	Metal
3DP	Powder in bed	Droplet deposition	N/A	Polymer, Metal, other powders
LOM	Laser cutting	Binding of sheets with adhesives	N/A	Paper, Plastic Metal

Table 1: AM techniques

A common factor in all these technologies is a phase change of material followed by the binding of materials together. This allows for free-flowing materials such as liquids or powders to be used as the initial feedstock in the process. The non-bonded material can then easily be separated from the solid material to leave the complete solid parts.

For each of these various AM techniques, there is a large number of commercially available AM machines. Table 2 contains a brief breakdown of some key metal additive printing machines currently available in the markett, including specifications of the resolution, minimum feature size and the total build volume that can be availed to produce parts.

Technology	**Machine**	**Resolution**	**Minimum wall feature**	**Build volume**	**Material**
SLM	Realiser SLM50	100 µm	0.2mm	300 x 300 x 300 mm	Metal
SLM	ProXDMP320	30 µm	100 µm	275 x 275 x 420 mm	Metal
SLM	SLM280	75 µm	150 µm	280 x 280 x 365 mm	Metal
SLM	RenAM 500S	20 µm	100 µm	250 x 250 x 350 mm	Metal
SLM	EOS M400	100 µm	100 µm	400 x 400 x 400 mm	Metal
LMD	rpm-innovations	0.125 mm	1.5 mm	1500 x 1500 x 2100 mm	Metal
EBM	Arcam Q10plus	140 µm	200 µm	200 x 200 x 180 mm	Metal

Table 2: AM machines and capabilities

The notable commonality of all machines outlined above, is a constrained build volume which limits fabrication to small functional parts. When focussing on the metal AM, the most common technology form is powder bed fusion, which can be separated into selective laser sintering (SLS), selective laser melting (SLM) and electron beam melting (EBM). The advances in laser technology and the improved part quality available from an almost identical process has led to a reduction of the usage of SLS as a manufacturing system. This has driven the research previously carried out into SLS being refocused to SLM research. The increase in the volume of publications for research into the field has been accelerating over the past few years. This is illustrated in Figure 2, which shows the number of papers published with the keywords SLM or EBM found on the search engine on Scopus.

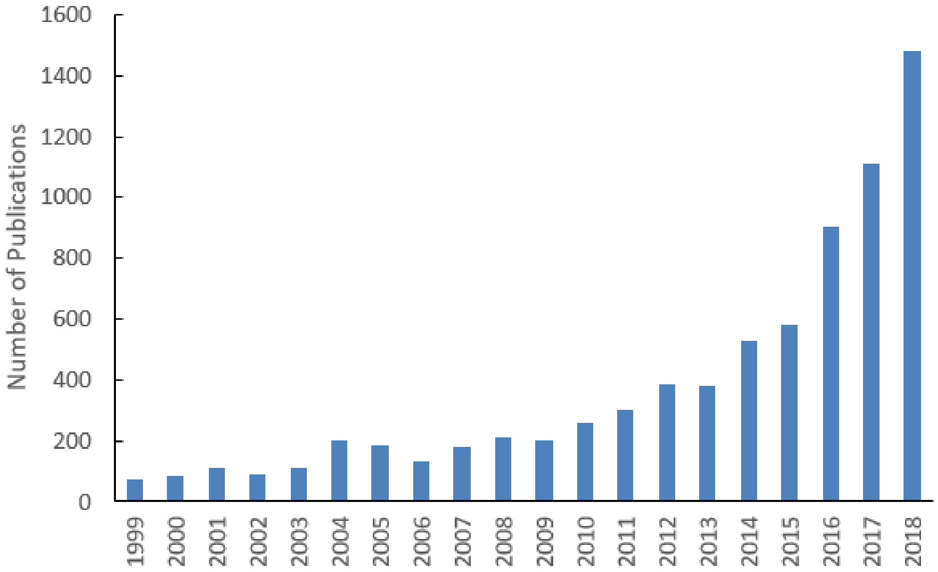

Figure 2: Number of publications with keywords SLM or EBM (Scopus, 2019)

The AM production of parts by powder bed fusion follows a repeating cycle for the creation of the sliced layers. The cycle is in the form of alternating between powder bed layering and laser beam scanning.

Firstly, the build platform is dropped by the slicing distance to provide space for the layer to be formed while maintaining a constant distance between the build surface and the energy source. The powder is fed into the build area from the feedstock and a powder layer created by evenly spreading this powder across the build area. The spreading can be accomplished by a range of methods including scrappers or rollers passing over the area. This even layer of powder is then defined as the powder bed.

The scanning step occurs when the energy source passes over the cross-section defined by the slicing software in a pattern to completely scan the area. The energy is directed by the use of scanning galvo-mirrors in SLM and through magnetic coils in EBM. The energy interacts with the powder causing it to be heated rapidly and melted to form a liquid, known as the melt pool, which solidifies and cools down to form fused metal. The now solidified material matches the cross-section of the part at that layer. The cycle is repeated and by the joining of the layers, the part is created.

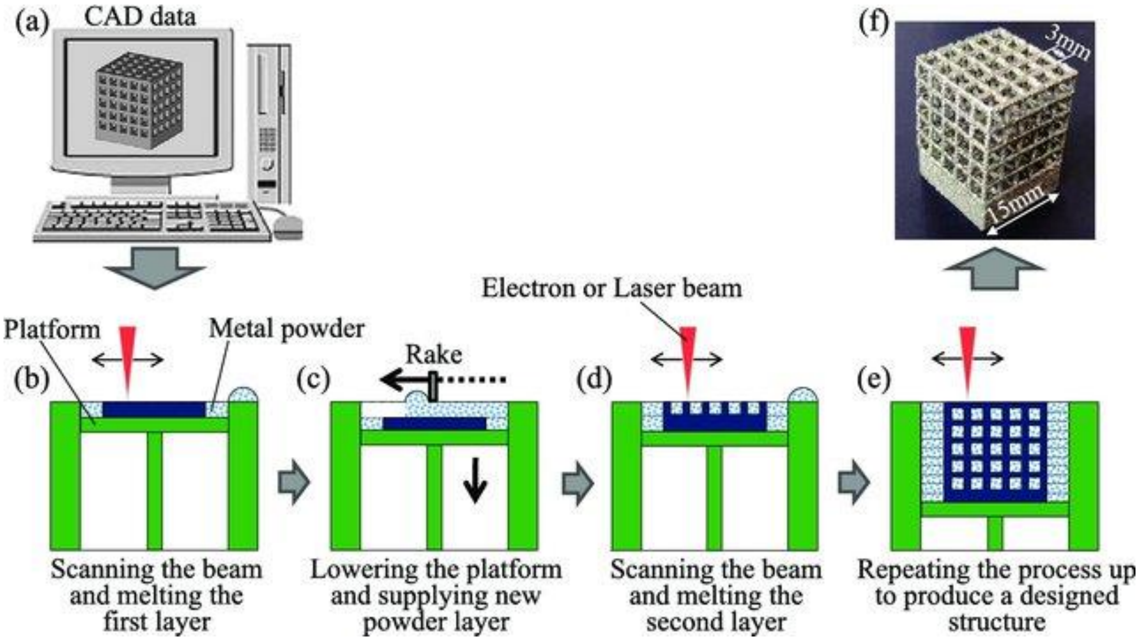

Figure 3: Idealised PBF process [10]

An idealised PBF machine is shown in Figure 3. The process is fully contained in a chamber to isolate the powder from the atmosphere and provide energy containment. An additional common feature of PBF machines is a third piston for the collection of excess powder in the process for future recycling and reuse.

1.3 Advantages of Additive Manufacturing

AM has several advantages over traditional manufacturing methods. These advantages drive the uptake in the technology as a manufacturing system over the traditional machining or metal forming manufacturing systems.

AM can produce complex parts [13] that were previously not feasible to produce [14, 15] from a technological standpoint, such as controlled and graded lattice structures. These structures were historically not able to be produced for many reasons such as critical internal features that cannot be accessed with a tool, or fine lattice structures that cannot be cast due to the small feature size preventing the liquid metal from flowing sufficiently into the mould.

The ability of AM processes to create complex internal geometries and variant internal structures can be seen in the paper by Cathchpole-Smith et al. [16] as shown in Figure 4. A sample was manufactured using the University of Nottingham logo to demonstrate how varying the lattice volume fraction results in a distinct thermal profile. Heat sinks or thermal insulation layers can be developed that are optimised for thermal conductivity whilst retaining the advantages in weight reduction that lattice structures provide to an overall design.

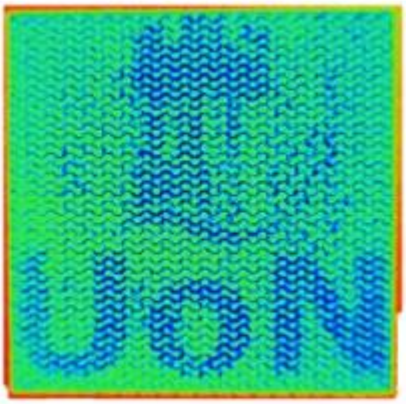

Figure 4: University of Nottingham logo in TPMS lattice

AM is also capable of creating complex geometries that were previously attained by having a series of connected parts. This allows for a reduction in the number of joints necessary in an assembly. This can be particularly important in cases that operate in high temperatures or pressures where joints can be a source of leakage or potential failure. An exemplar of this is in the General Electric LEAP engine where the number of parts present in the nozzle assembly was reduced from 25 individual pieces brazed together to 5 parts [17].

Figure 5: GE Leap engine nozzle

The ability of AM methods to facilitate the creation of these complex parts is one of the most commonly considered advantages, as it is easier to appreciate a new capability compared to an incremental improvement; but it is not the only advantage.

The economic drivers for the growth of AM usage in the industry are strong, particularly considering the impact that complexity or customisation has on traditional manufacturing. Figure 6 taken from Pinkerton [18] illustrates the relationship between additive and traditional methods. The figure shows that for complex, low-volume parts, AM has a strong cost advantage over traditional methods.

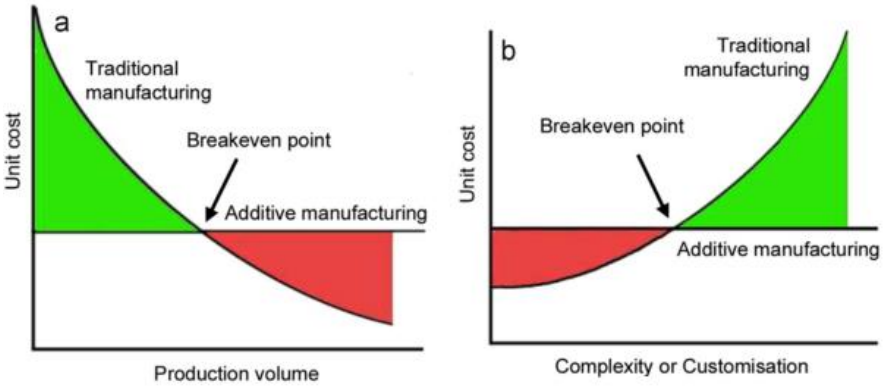

Figure 6: Breakeven Point analysis of additive manufacturing

The cost of a part produced by AM does not have the same complexity concerns as traditional methods. In traditional manufacturing processes such as casting and forging, each SKU requires dedicated infrastructure such as moulds and dies. The fixed cost of creating a mould or specific tooling can be substantial in order to meet the tight tolerances or for complex moulding. This creates an exponential increase in cost as the complexity of the part to be produced increases. However, the cost of this cast or tooling is spread over the entirety of the production volume. This doesn’t occur in AM, eliminating a certain level of economies due to scale in the process. This has the effect of the unit cost of an AM part being completely decoupled from complexity and number of parts. This creates a market niche for AM in low-volume and high complexity parts, where it presents an option for a cheaper per unit cost compared to traditional manufacturing process.

The advent of net-shape AM, in which the part is produced to its final shape without significant further machining has also given an important advantage to AM over traditional methods in relation to the amount of wasted material used in the process. By definition, subtractive methods require more material than the final part contains. The removed material from an initial workpiece is hard to recover in a traditional case as it is frequently mixed with lubricant or other cooling fluids during the manufacturing process. The valuable material needs to be fully separated and removed from the waste stream which can be a costly or energy-intensive process. The difficulty in recovering the removed material and the lack of financial payback leads to it being disposed of as waste. This waste is not present in additive methods as any non-bound material remains in its initial useable form ready for use in future processes. The ability to not require excess material leads to material cost savings. The savings in the material costs found by using AM technologies over traditional manufacturing can be substantial when considering the high-end materials used in AM such as Ti64 and CoCr which cost €400/kg and €200/kg respectively in 2019.

AM machines also provide substantial flexibility for production, the entire process is carried out by computer-controlled lasers without physical tooling or moulds. This allows rapid changes between SKUs to adjust production to consumer needs without tool change downtime, which is traditionally associated with changing the manufacturing profile. The ability to use the same feedstock for all parts also allows a reduction in the storage of materials of varying thicknesses and dimensions to fit various part designs. The ability to rapidly transition between designs allows for a more readily replenished supply of parts and reduce the level of stock required to be held on hand for consistent supply within the overall supply chain.

The AM process can be used to produce parts from materials that are difficult to work or machine using traditional methods such as Cobalt Chrome, Inconel and Titanium alloys. These materials have exceptional wear, abrasion and corrosion resistance [19]. These desirable properties, however, lead to excessive tool wear and time usage under traditional milling or alternative machining methods. The AM process mitigates the mechanical properties of bulk solid material by working with the material in a liquid state. By eliminating or reducing the tool usage on the material, the cost of replacing the tools as they wear down is also reduced.

An indirect advantage provided by AM is its unique suitability to facilitate forms of genitive design and topology optimisation. Both of which produce parts to meet desired conditions or constraints with the minimum amount of material. A frequent effect of minimising the material is a complex strut or lattice structure. A prime example of this is from Orme et al. [20] The paper describes work done for Surrey Satellite Technology LTD (SSTL) Technology Demonstrator Space Mission that is currently functioning in orbit (case studies 1 and 2), and a system of five components for the SpaceIL’s lunar launch vehicle. Figure 7 shows the results of this optimisation which allowed significant reductions in the mass of the parts. The bracket was reduced from 425g to 89g for the un-optimised heritage part, a structural insert had a 40% reduction in weight and the landing legs a reduction from 4.0Kg to 3.0Kg.

Figure 7: Topology optimised parts

The paper had the following conclusion; “The authors are hard-pressed to envision the design of the bracket pictured without the tools implemented in this work, and furthermore, even if the design were conceived, it would be extremely difficult (if even possible) and costly to manufacture with traditional subtractive methods". This demonstrates the ability of additive manufacturing to facilitate topology optimisation which is a major advantage over traditional manufacturing methods.

1.4 Disadvantages of Additive Manufacturing

AM manufacturing has not been fully adopted to replace traditional metal forming methods or subtractive methods of manufacturing. While AM has significant advantages, it also has limitations and drawbacks that can prevent the move from traditional manufacturing to AM.

The material deposition rates of AM are significantly lower than the equivalent material removal rates found in traditional manufacturing methods. The record for the fastest milling rate currently stands at 16,400 cm^3/min in aluminium [21], the fastest deposition rate for metal AM currently stands at 200 cm^3/min [22]. Even though the subtractive method may need to remove more material to get a final part, the near two order magnitude speed difference enables faster part production. This results in a significantly longer cycle time for AM parts compared to traditional methods. This limitation impedes AM applications competing at this mass manufacturing level.

The process of AM can be inherently hazardous. The materials used to feed the process, be it monomer or metallic powder, can be irritants or carcinogenic, necessitating sufficient physical separation and PPE for the operator. The metallic powders provide both an inhalation risk for the user as they are small and light enough to be suspended in the air. As with any fine powder, an additional risk is created in that the powder in AM has the ability to create an explosive atmosphere. This necessitates an inert atmosphere or vacuum to be applied to the process at all points. The SLM process can also generate pyrophoric black soot as a by-product of the fusion process. This by-product will ignite when in contact with air increasing the risks caused by the fine powder and also needs to be eliminated from the process and safely disposed of.

AM usually necessitates a high initial investment. The machines require high-intensity lasers and the connected cooling apparatus along with a sealed operational area that is not needed in the traditional methods such as casting or forging. These stringent requirements increase the initial cost. While in operation the machines also have high energy requirements to power the laser system and frequently need a constant supply of inert gas or high vacuum to operate safely leading to not insignificant running costs.

These high initial costs can be compounded by the difficulty in changing material being used in a specific machine. To prevent the risk of forming alloys or amalgamations, all of one material has to be fully removed and common components cleaned between materials. This process is time consuming a limits the flexibility of the AM process. In serial production this disadvantage is mitigated by having an AM machine per material which is costly. Whereas for research or small scale manufacturing the prohibitive cost of additional equipment necessitates machine downtime, reducing its OEE and incurring time costs.

As seen in Table 2, there exist considerable size constraints in the application of AM to an industrial setting based on the available production machines. The constraint is in the form of a small build volume. Parts obviously must fit wholly in the build volume which limits applications, but also this constrained build volume cannot be fully utilised as the parts being build have orientation constraints that lead to loss of build plate utilisation. These size constraints limit the number of parts that can be produced on a single build plate, giving rise to even longer per part production cycle times. The build volume challenge also limits the advantage of reducing the number of parts, joined parts are larger and get constrained by the build volume. Any part that cannot be wholly fitted inside the build volume must be made in an assembly form, while the traditional means of manufacturing more readily can scale to larger machines to produce parts of any useful size.

As shall be addressed later in this thesis, several imperfections can be present in an additively manufactured (AM) part such as a rough surface finish or porosity, both internal and in the form of surface defects. The process can be prone to failure due to thermal warping or uplift in manufacturing. These issues can cause the complete part to fail and due to the batch production nature of AM, a single part failure can lead to an entire build failure. This effect can lead to a lower part yield compared to a traditional manufacturing system. The additional limitation present is the inability to rework AM parts or to easily convert these failed parts back to the finely graded powder that is required by the process. This leads to out of spec parts being completely discarded as waste.

AM’s unique capabilities have led to its adoption in various industries and fields. Although the adoption of the technology for mainstream production has been stymied by the disadvantages already discussed, many companies have found that the advantages outweigh the restrictions, a selection of which are shown in Table 3

Company	Application	Reference
Carboni e Metalli	Motorcycle parts	https://www.carboniemetalli.com/the-lunar-project
DePuy Synthes	Medical Implants	https://3dprintingindustry.com/news/depuy-synthes-expands-3d-printed-titanium-implant-portfolio-162269/
Stryker	Medical Implants	https://www.stryker.com/builttofuse/media/assets/TRITA-BR-2%20Tritanium%20Manufacturing%20Overview%20FINAL.pdf
GE	Aerospace	https://www.ge.com/additive/stories/qa-ge-additive-pittsburgh-achieves-as9100d-iso-90012015-certification
Safran Electrical & Power	Aerospace	https://www.betaty.pe/case-studies/safran-electrical-power/
Betatype	Automotive parts	https://www.betaty.pe/case-studies/automotive-headlights/

Table 3: Examples of Commercial Additive Manufacturing Usage

This adoption by both large and small companies shows that the advantages of AM have been judged to outweigh its corresponding disadvantages. By mitigating the disadvantages, the adoption of AM will continue to increase.

1.5 Research objective

Repeatability is a major issue in the uptake and usage of additive manufacturing, however, despite a significant volume of research focusing on the capabilities of AM, there is a lack of research focused on its repeatability and reproducibility. The overall research objective is to improve the repeatability of the SLM process

To achieve this objective, there is a series of research questions that need to be answered.

1. **Is there a repeatability issue in AM, and how does this compare with traditional manufacturing methods?**
   Repeatability and reproducibility have been identified in this thesis as a concern for the adoption of additive manufacturing to mainstream manufacturing. However, the actual level of repeatability has not been clearly defined, merely stating that the current level is insufficient. The first objective is to define the level of variation currently present in the process as compared to traditional manufacturing methods.
2. **What are the potential sources of variation causing the repeatability issue?**

   The next question is to identify the sources of variation in the process, that are the root cause of the repeatability concern. The sources of variation need to be quantified to allow for prioritisation and mitigation of the largest sources of error.

3. **Can the errors or sources of variation be mitigated?**
   A means of addressing the sources of variation and mitigate their effect on the overall performance of the additive manufacturing process will be developed. This will be in the form of modified process parameters to account for the variations.
4. **Can improved repeatability be achieved in the process?**
   The modified process parameters will be used in the realistic setting of part manufacturing. The manufactured parts will be tested against the unmodified process produced parts.

1.6 Thesis Outline

Chapter two of the thesis will be a literature review. The literature is assessed to determine the levels of repeatability present in the published works, reproducibility will also be accessed by comparing studies with similar parameter sets. The AM process is separated into pre-process, para-process and post-process stages and a critical review of the causes of variation at these stages is conducted. This chapter will address research questions one and two

Chapter three will cover the development of a modified energy density equation. This chapter will contain an in-depth analysis of how targeted major sources of error vary across the build plate. The new equation will account for these variations contributing to allow for the variation to be mitigated. This will address research question two and provide the basis to answer research question three.

Chapter four outlines the experimental methodology that will be used for creating experimental parts to be evaluated for the repeatability experiments in both geometric and mechanical properties. The chapter includes details on the control system present in the machine to be used for all the manufacturing processes. This chapter will also clearly lay out the statistical tests, against which the data produced will be assessed.

Chapter five will address the geometric properties of AM parts. These properties will be analysed first as geometric effects could impact the mechanical properties. This chapter will address research question one and aspects of research questions three and four.

Chapter six will assess the mechanical properties of AM parts. The chapter will include an in-depth analysis of parts in the multiple materials produced using the suppliers' recommended settings and parts produced using new settings informed by the modified energy density equation. This chapter will focus on answering research questions three and four.

Chapter seven shall be the conclusions of the thesis and include commentary on future work that could be carried out to advance this line of research further.

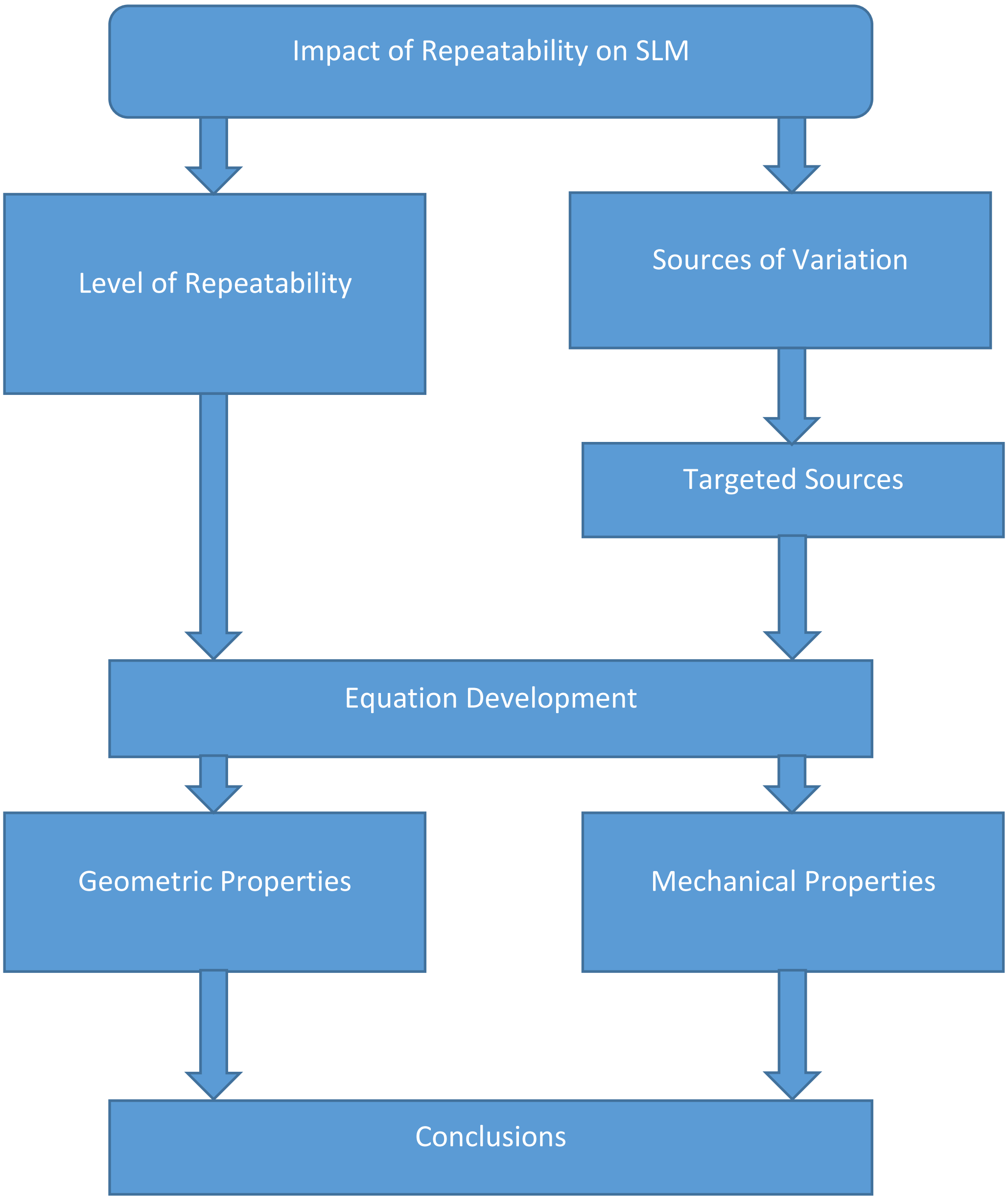
Impact of Repeatability on SLM
Level of Repeatability
Sources of Variation
Targeted Sources
Equation Development
Geometric Properties
Mechanical Properties
Conclusions

Chapter 2: Literature Review

In this chapter, the literature is reviewed for evidence that can support the existence of a repeatability issue in the SLM process. The chapter will review the various processes and effects within AM that could be influencing the repeatability currently present, demonstrating that the issue is extant and not merely a perceived failing in AM.

This literature review chapter is based on a review paper that was published in the journal of materials and design under the title “A review of critical repeatability and reproducibility issues in powder bed fusion” (DOI: 10.1016/j.matdes.2019.108346).

2.1 Evidence of a Repeatability issue in the process

To date, a significant volume of research has focused on the capabilities of AM, but there is a lack of research focused on its repeatability and reproducibility. The limited number of studies focused on repeatability in metal AM to date are more concerned with geometric accuracy and defect generation rather than the repeatability of the part properties. For example, Franchitti et al. [23] examined the effect of different parameters (orientation, build location, build height) on the dimensional accuracy of Ti6Al4V rectangular parts fabricated using EBM. Dimensional accuracy was determined by measuring the sample thickness. The authors reported that the most significant factors affecting accuracy was the sample orientation and build location. Grasso and Colosimo [24] published a review of the current state-of-the-art in-situ monitoring methods available to reduce process defects in powder bed fusion processes such as EBM and SLM.

Despite the lack of literature available specifically focused on repeatability in AM, the research that does exist is very informative for this thesis. Commonly, the results of experimentation are presented including their standard deviations, demonstrating the statistical significance of these results to draw strong conclusions. The standard deviation can be taken as an indicator of repeatability in a single data point. Reproducibility information can also be derived from comparing studies using identical machines between different research groups or in the form of inter-laboratory tests [25].

The most important and commonly investigated mechanical properties are the ultimate tensile strength (UTS) and elongation of the produced samples [26]. The materials with the most focus in powder bed fusion research are cobalt-chrome (CoCr) and titanium alloy (Ti64), with the published data from a large selection of this research shown in **Error! Reference source not found.**A & B.

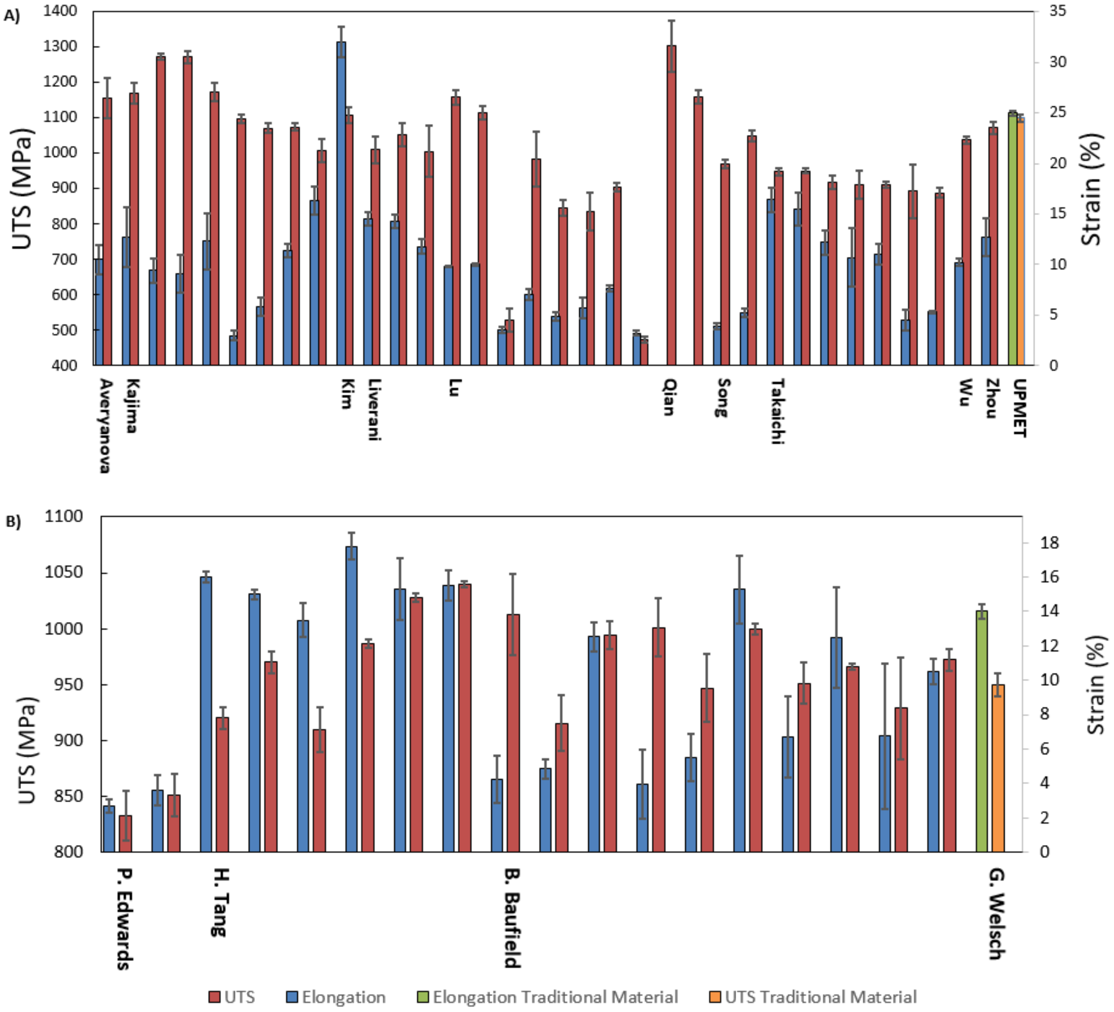

Figure 8: UTS and Elongation of CoCr (A) [27–36] *and Ti64 (B)* [37–40]

It can clearly be seen that there is a large variation of both the mean UTS and elongation at break for each data set. This level of variation is to be expected as each data set represents different operating parameters. However, the error bars shown in the figures represent the standard deviation on each data set, which can be used as a measure of the process repeatability. For example, Takaichi et al. [27] fabricated Co-29Cr samples for mechanical testing using SLM over a range of different energy densities (300 to 800 J/mm^3). The authors recorded standard deviations of up to 75

MPa for UTS and up to 2.9% for elongation which is significantly larger than that which is found in wrought parts made of the same material (shown in a different colour in the figures). The increase in standard deviations and the wide range in the values recorded for the AM produced parts when compared to the traditionally produced equivalents, demonstrates that a repeatability issue is present.

The literature also can be examined for reproducibility information by comparing studies. The energy density or specific energy input is commonly used as a defining variable in laser-based AM [41–43]. Figure 9 summarises the UTS results from different studies carried out at the same energy density in cobalt chrome and demonstrates they have divergent mean values and standard deviations. To compare the values, a two-tailed t-test is undertaken using the values from the papers surveyed by Lu et al., Liverani et al. and Qian et al. [30, 31, 33]. The two-tailed P-value from the tests equals 0.0014 for the 100 J/mm^3 case and the two-tailed P-value is less than 0.0001 for the 115 J/mm^3 case. By conventional criteria, a P-value of less than 0.05 is considered statistically significant [44]. The P-values from these tests are an order of magnitude less than this critical P-value and shows that there is a significant difference between the means of mechanical properties for a common energy input. This result can be used to show a lack of reproducibility present in the AM process.

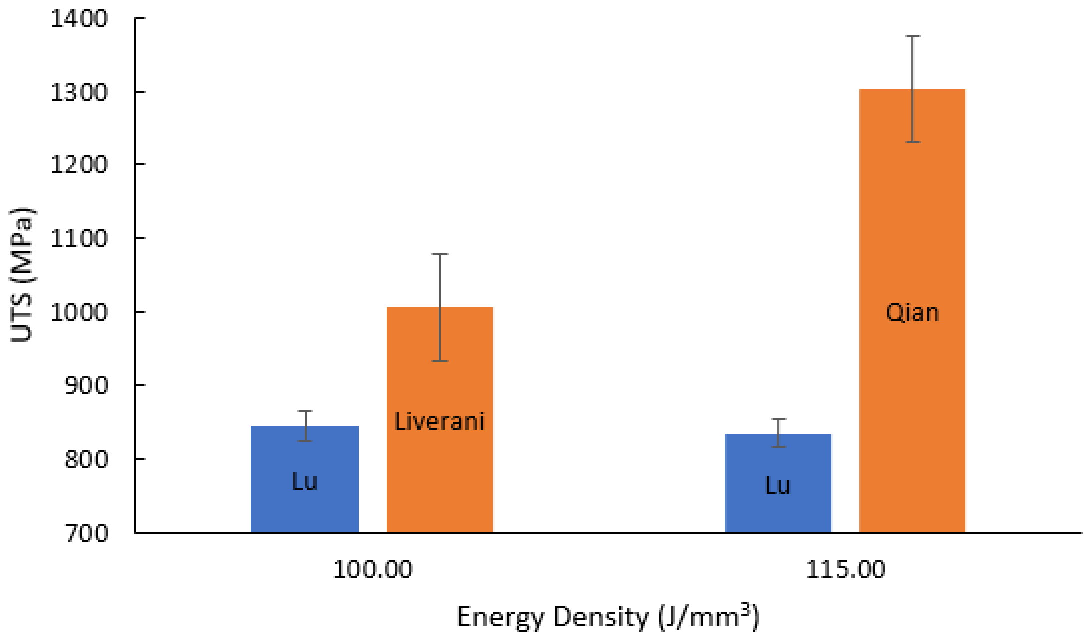

Figure 9: Reproducibility comparison at two energy densities [30, 31, 33]

In order to compare the level of repeatability across a range of materials and manufacturing processes, both additive and traditional in nature, this thesis uses the coefficient of variation as a comparison metric. The coefficient of variation is the ratio of the standard deviation to the mean for a population or sample [2].

$$CV = \frac{\sigma}{\mu}$$

In the case of UTS, AM produced materials have a slightly higher coefficient of variation than the traditionally produced counterparts shown in Figure 10A. When considering elongation, the variation in the AM materials is an order of magnitude larger than that of traditionally manufactured materials, as seen in Figure 10B.

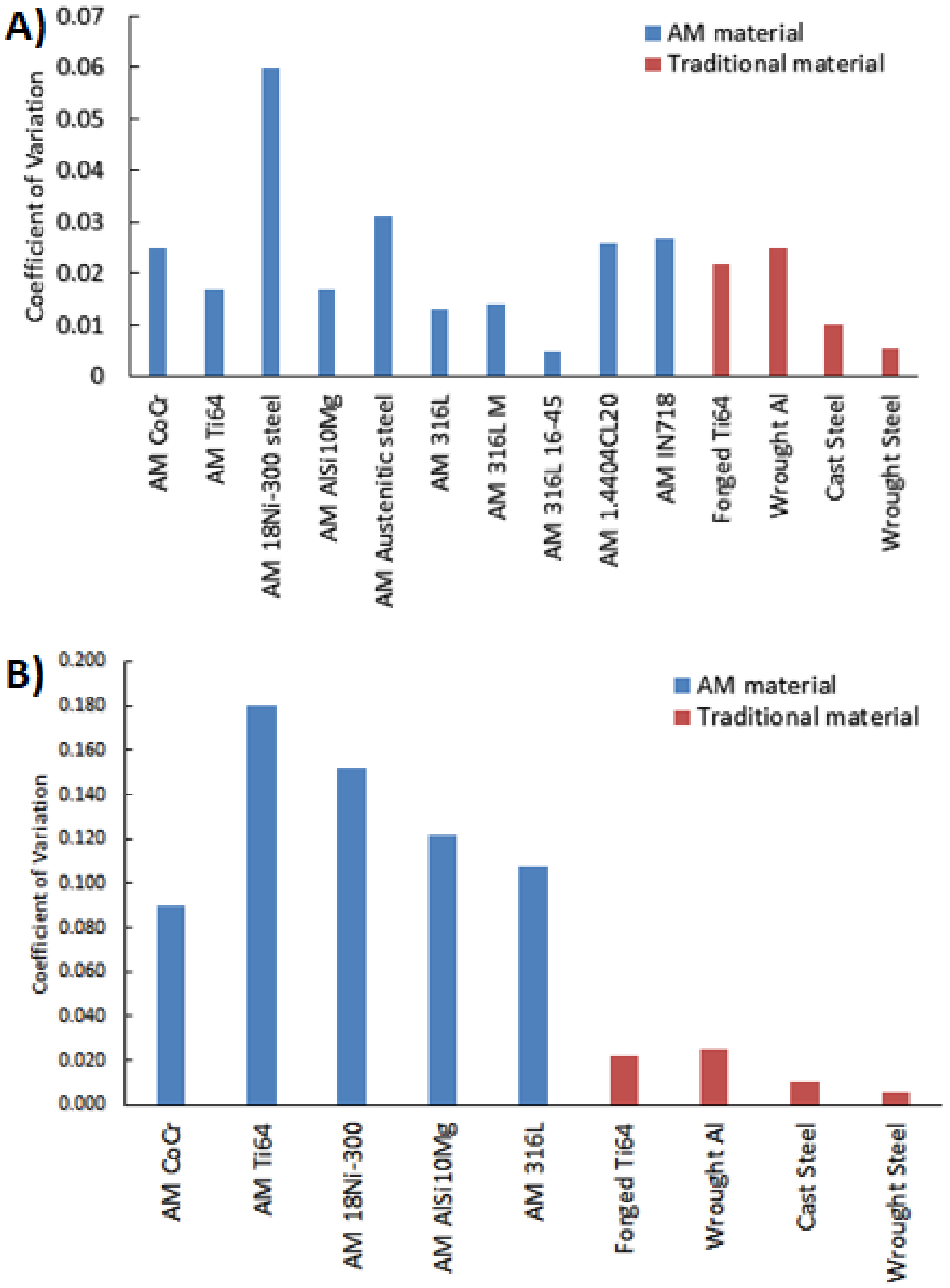

Figure 10: Coefficient of Variation of UTS (A) and Elongation (B) for AM materials [2–14,16–21] and traditionally produced materials [51–53]

The survey of the available literature showed that the coefficient of variation was found to be higher in AM (UTS of 0.05, Elongation of 0.13) compared to traditional manufacturing methods (UTS of 0.016, Elongation of 0.016). This trend is consistent across different materials, machines and/or process parameters, thus clearly demonstrating that repeatability is a systematic issue across powder bed fusion-based AM.

During studies into the PBF, over 157 process parameters are present that can impact part quality [54, 55]. These process parameters can frequently be grouped into single factors. For example, the scan strategy contains information on scan length, hatch spacing, scan speed, the order of scanning and hatch rotation [56]. These factors can be further characterised as pre-process, para-process and post-process factors as shown in Figure 11.

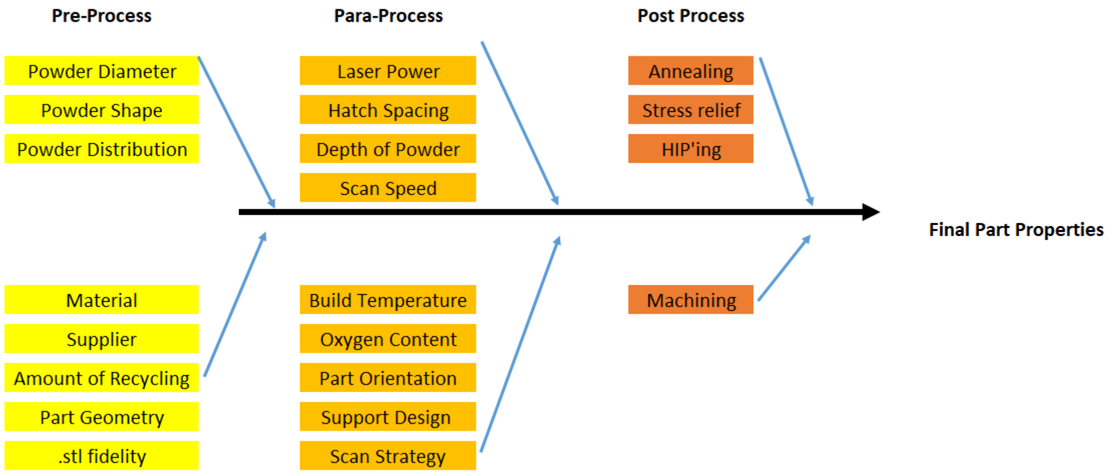

Figure 11: Fishbone diagram of the AM process

The pre-process includes all factors which contribute to the final properties before the AM process occurs. The para-process encapsulates the actual AM critical process of laser to material interaction. The post-process is any additional activity that is undertaken once the part has left the AM process. All the factors have an impact on final part properties but not necessarily to the same magnitude. The goal of the literature survey is to identify the effects which have the greatest impact and the greatest ability to be tuned for improved repeatability

2.2 Pre-Process Effects

The initial stage of the pre-processing of a part is the generation of a .STL file. These files are currently the standard input for all 3D printer slicer software and consist of a triangle-based mesh capturing the 3D geometry of a given design. The fidelity of this mesh to the designed CAD can have a significant impact on the AM part repeatability and accuracy. The discreet nature of the mesh causes issues in approximating curved surfaces such as cylindrical struts which adds in a geometric error [57]. This is further limited by the memory constraints of the computer system used to generate the mesh

[58]. Fine details such as curves require more numerous and smaller triangular unit cells. The memory constraints make this an unavoidable error between the design and the produced parts.

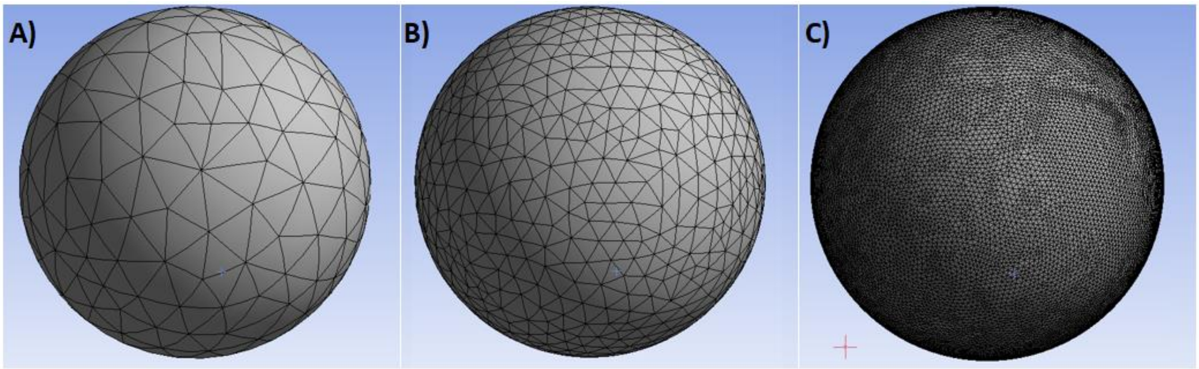

Figure 12: 10mm sphere meshed for .stl with features of A) 1mm B) 0.5mm C) 0.1mm

This exponential increase in memory usage can be easily illustrated when examining a nominal sphere of 10mm diameter meshed with increasing levels of precision as seen in Figure 12, where a 10mm sphere has been meshed at 1mm, 0.5mm and 0.1mm precision levels. The memory required to store these meshes as .stl files is shown in Table 4. This effect is magnified when more complicated or intersecting geometries are used, which already require significant memory. This memory restriction can lead to reduced part accuracy.

	A)	**B)**	**C)**
Mesh Unit	1 mm	0.5 mm	0.1 mm
Memory usage	75 KB	277 KB	6453 KB

Table 4: Memory Usage

The second issue inherent to all AM technologies is geometric accuracy defects, such as the staircase effect as seen in Figure 13 [59]. This effect leaves a saw tooth effect, resulting from both hatch spacing and layer thickness. This saw tooth effect causes significantly increased roughness on angled surfaces. This results in a different characteristic to those surfaces that are perpendicular or parallel to the build direction.

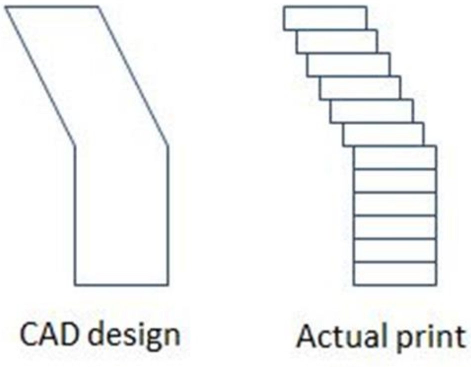

Figure 13: Staircase Effect

Another important component of the pre-process is the generation of support structures for the part. These structures connect the build plate to the part and provide structural support during the printing process, anchoring the part in place to prevent deflection from the stresses generated by the large thermal gradients. This is particularly important for arched or overhanging structures which require cantilevers that may be significantly weaker than the final structure and unable to support their weight until completion [60].

The optimisation of support placement begins with the orientation of the part [61]. This optimisation must balance the various factors of the process such as the volume of support to be added, the total height of part and the generation of entrapping surfaces. Balancing the level of importance given to each of these factors gives rise to a series of potentially “optimal” solutions to the part orientation. These optimum solutions are only geometry dependant, with a lack of inherent understanding of the properties of the part being created.

There currently exists no means to optimise orientation for the most repeatable results. The selection of which optimal solution to use and the weighting to assign to each of the individual factors is a user-defined or specified process. This can lead to a reproducibility issues as different users can define different optimums leading to varying orientations and corresponding variation of mechanical properties.

These varying orientations are only a single step in the selection of support. The types of support available are also myriad, for any given surface options of support type include; Block, Line, Point, Web, Contour, as well as combinations and hybridisations of all these types [62]. Beyond the type of support, each has further parameter selection such as the thickness of the lines or dimensions of the cones. This gives a near-infinite range of possible support structures for any given surface, many of which are equally suitable for adequately supporting the surface. The infinite support options that a user can choose from facilitates circumstances where parts can be produced with differing properties, leading to reproducibility concerns.

Material absorption is a critical factor in AM. Reflectivity and its corresponding inverse quantity of absorption are important when considering the laser interaction with the material powder. . The absorption spectrum of the material defines how much of the laser energy is absorbed and converted to heat which is required for melt pool formation. The absorption spectrum for a series of common AM materials is shown in Figure 14.

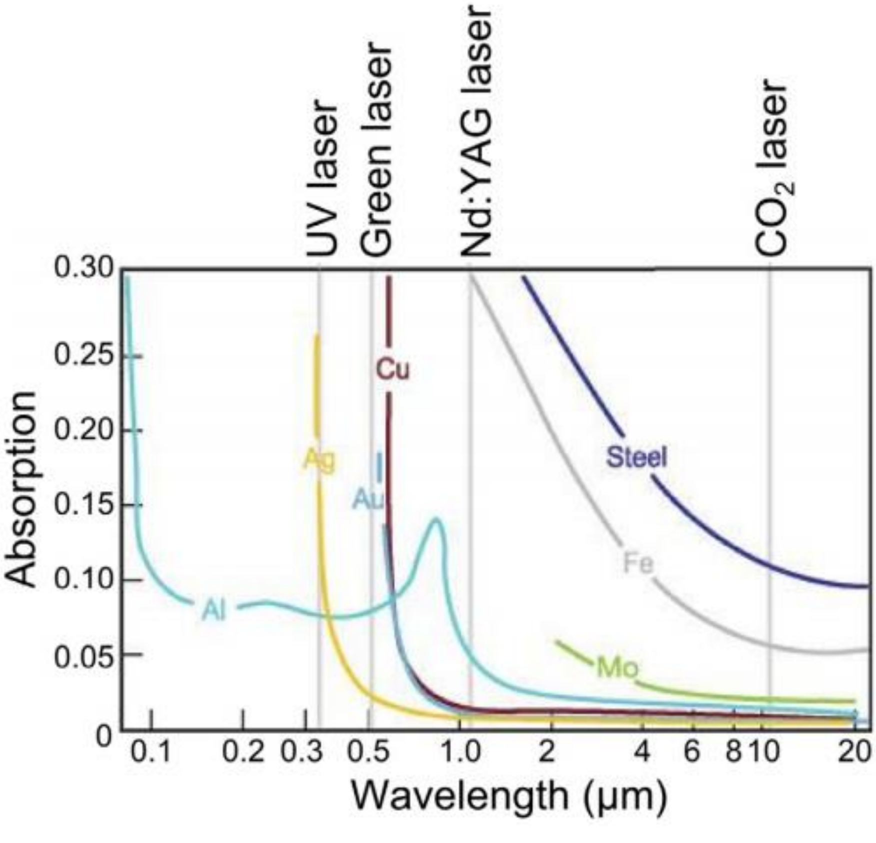

Figure 14: Absorption for common AM materials against wavelength (adapted from [63]*)*

The wavelength of a laser is non-variable due to the fundamental relationship it has to the gain medium present in the laser pump. The photons generated by the laser are produced with a wavelength matching the energy difference in the electron ground and excited state [64]. This fundamental factor of the process prevents variable wavelength from being a potential source of error in a machine.

The reflectivity of a material can also have a temperature dependence, as seen in Figure 15. This is due to the fundamental mechanism of laser absorption in metals being predominantly absorbed by free electrons in an “electron gas” [64]. For most metals as temperature increases, these free electrons are more likely to interact with the metal structure rather than re-radiate the incident laser. This creates a fall in reflectivity, which correspondingly increases the absorption of the metal. This change in absorption with temperature needs to be considered in the AM process as the metal goes through a wide temperature range in the process from room temperature to its melt or vaporisation temperature.

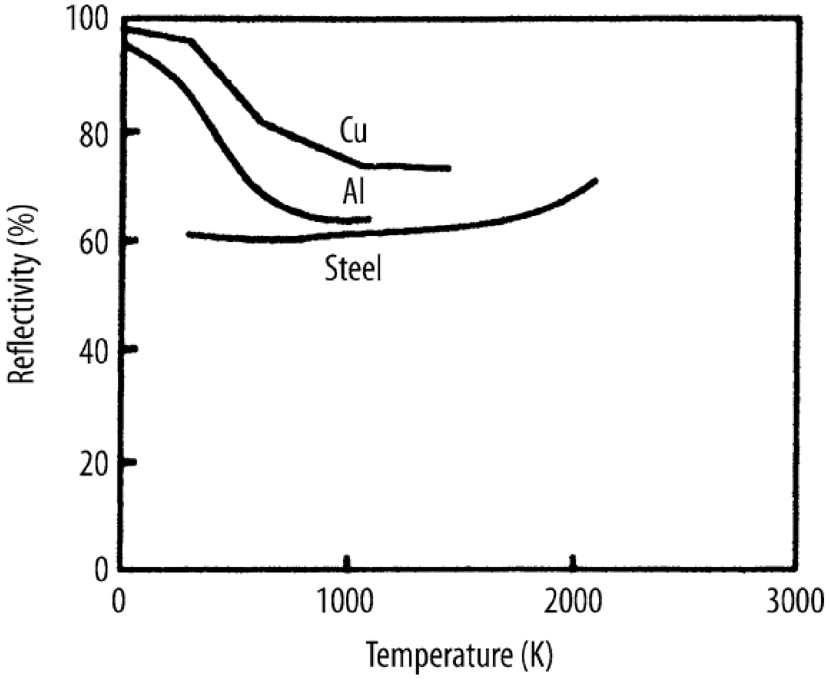

Figure 15: Reflectivity against temperature for common materials taken from [65]

The absorption of the powder bed is largely determined by the normal flat-surfaced absorptivity according to Boley et al. [66]. Their predictive model gives a reasonable approximation of the absorptivity of the powder from flat surface absorptivity.

However, Boley et al. did calculate and measure a variation in absorptivity based on the particle size distribution of the powder between a uniform hexagonally packed powder, a bimodal distribution and a Gaussian distribution of powder particle size. The calculations were done for a wide variety of materials, the most important of which for AM purposes are stainless steel and titanium and are tabulated in Table 5.

Material	λ (µm)	A (Flat)	A (Hexagonal)	A (Gaussian)	A (Bimodal)
SS	1	0.34	0.60	0.58	0.63
Ti	1	0.39	0.64	0.62	0.66
Ti	0.45	0.45	0.69	0.67	0.71

Table 5: Material Absorptivities

There is a clear change in absorptivity in these materials as the powder distribution varies. This is a potential source of repeatability loses due to variations in powder supplier or the progression of the powder recycling modifying the distribution from one typing to another.

The next principle pre-process parameter that affects repeatability, is the morphology of the powder being used. Powder morphology covers the particle size distribution and the shape characteristics of the individual particles, such as sphericity and uniformity. The powder morphology is a critical factor in determining the optical penetration depth [67, 68], thermal conductivity and packing density of the powder bed.

Optical penetration depth indicates the depth that the energy will penetrate the powder, which is intrinsically linked to the formation of the melt pool [69]. Optical penetration depth is defined as the depth at which the intensity of the radiation inside the material falls to 1/*e* of the original value, which is approximately 36.7% of the initial value. A graphical representation of the optical penetration depth in powder is shown in Figure 16, adapted from Zeng et al. [70]. The graph shows a 1 mm square section of the powder bed. The intensity of the laser is reduced by reflections and absorption of the powder particles. At 0.6 mm from the surface level on the graph, only one of the trace beams continues propagating through the material resulting in a drop below the 1/*e* energy level. A variation in penetration depth can cause a corresponding variation in the melt pool depth. If the melt pool depth becomes greater than the layer height, this can add melting-solidification cycles to underlying formed layers. The melt pool depth being less than the layer height will lead to poor interlayer bonding and delamination between the layers. This variation leads to quality issues such as porosity defects and thus affects the mechanical properties. This was shown in the study by Gong et al. [71] which characterised the melt pool in Ti64 as a means for process parameter selection.

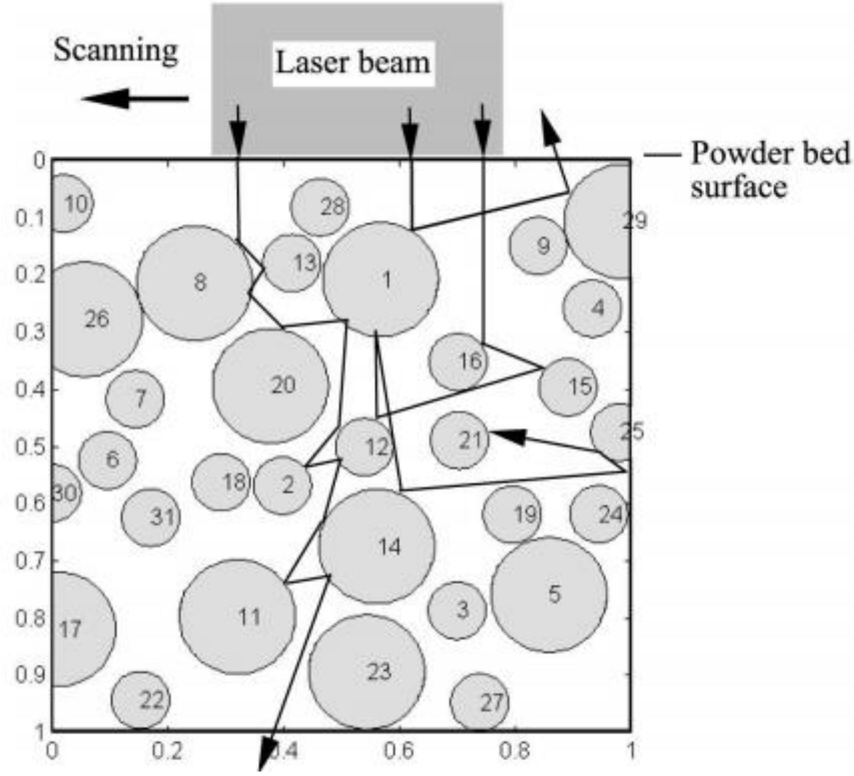

Figure 16: Optical penetration depth adapted from Zeng et al. [70]

The thermal conductivity of the powder bed determines the size and cross-section of the melt pool generated. The size and shape of the melt pool have been shown to affect the mechanical properties of a completed part due to the formation of pores and rough surfaces. This has been demonstrated by several authors in both simulations of the melt pool and experimental measurements [72–74]. Varying powder morphology can affect the conductivity by changing the level of connection between particles and changing the gaps between the particles. The thermal conductivity may also be changed due to the varying composition of the powder, particularly in the case of titanium-based matrix composites [75]. The melting point of the ceramics is significantly higher than those of the metal component of the matrix

[76], potentially leading to a variation in melt pool dependant on ceramic concentration both in a build and between builds as the material is processed.

The packing density of the powder bed can directly affect the optical penetration [77] and thermal conductivity [78], as already discussed. Separate from these effects, low packing density can cause voids in the powder bed. This can lead to an unstable melt flow as the voids respond differently to the laser heating than the powder particles. This unstable melt flow has been shown to be a factor in the formation of defects [74]. The study by Abd-Elghany and Bourell [79] characterised the packing density of 304L stainless steel powder at various layer thicknesses and the effect this had on the material properties, the results of which are shown in Figure 17. The conclusion from the study states that there is a strong positive correlation between a more densely packed powder bed and the creation of a higher part ultimate tensile strength.

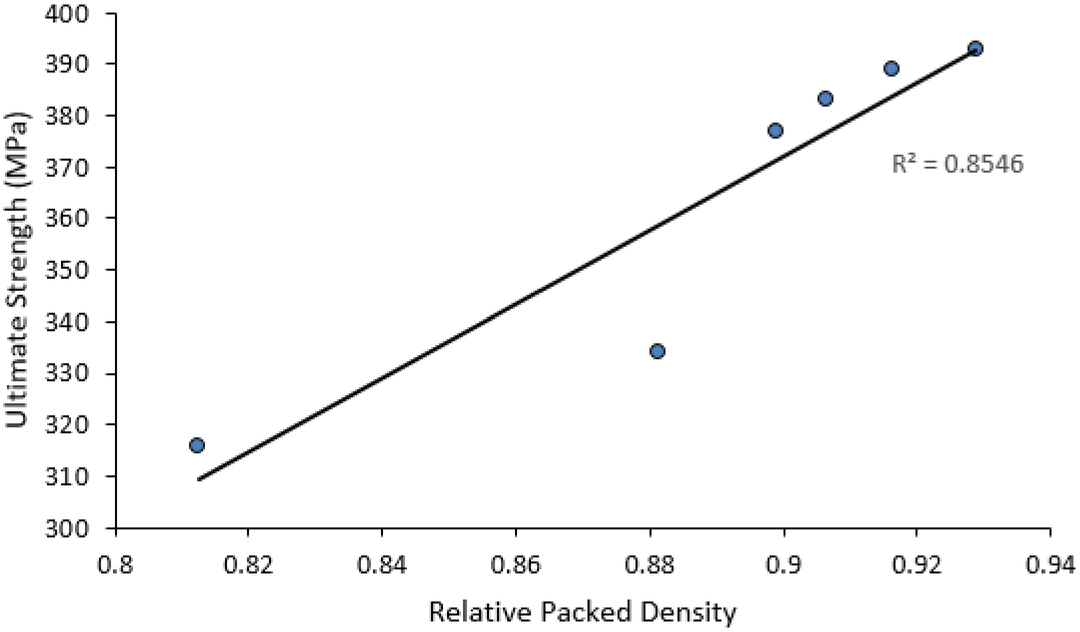

Figure 17: Packed Density against Ultimate Strength adapted from [79]

The packing density of a powder is also related to its flowability [80], which is a complex phenomenon. The factors that are important in its characterisation are the shape of the particles and the powder size distribution. A powder comprised of spherical particles has a higher flowability than one composed of particles with an angular shape, due to the reduced particle interlocking and the free rotation of the powder [81, 82].

The size distribution is an important factor in determining the size of voids. Small satellite particles connected to large particles can impact the packing density by reducing flowability due to increased mechanical interlocking [83]. Conversely, satellite particles are also being able to fill the voids present between packed large particles. Figure 18 has combined data for different powder size distributions in cobalt chrome taken from a series of studies [27, 30, 31, 33, 35]. The figure shows a significant difference in UTS with powder variation between the 22 µm case and the larger particle sizes. The more interesting for repeatability purposes is the difference in uncertainty moving from a standard deviation of 24 MPa to 44 MPa to 59 MPa as the powder size increased. The larger particles appear to result in stronger parts, however the repeatability of these parts is reduced. This cross publication conclusion reinforces the findings of Simchi [84] who investigated a wide range of iron powder sizes and found that fine powder agglomerates can have increased reflectivity, reducing absorbed energy.

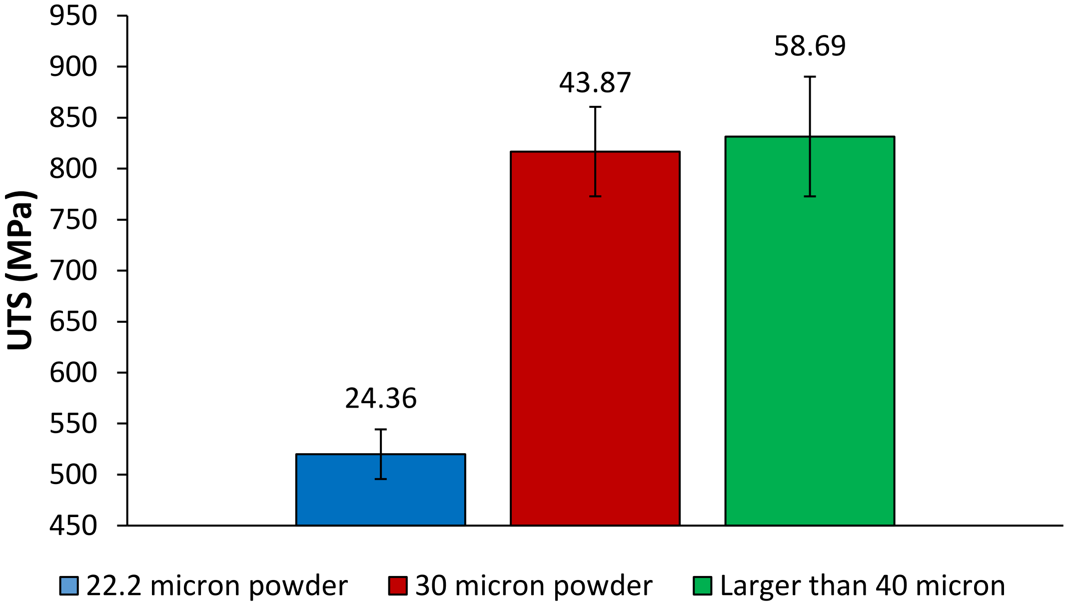

Figure 18: Powder size and UTS data taken from studies [27, 30, 31, 33, 35]

The particle size distribution of the powder used in AM follows a statistical distribution both within a single container [85] and across batches of produced powder [86]. This can be seen in Figure 19, taken from the study of Inconel (IN738LC) powder batches by Engeli et al. [87]. It is common practice for multiple batches of powder to be used in a single build, and the inherent variability in the powder supplied leads to variations in powder conditions.

This is both an in-build and build-to-build concern for repeatability. The in-build repeatability is of concern due to the layering mechanism creating a stratified set of properties, due to the progression through batches of powder [49]. Coupling these stratified properties with a variation in powder properties due to powder feedstock gives rise to a potentially greater variation in physical properties. Kulkarni et al. [88] found that "a very small change in the particle size distribution, span, or the wall friction properties can influence the flowability", which has already been noted to impact packing density. The sensitive nature of flowability can impact part properties which contribute to a build-to-build variation.

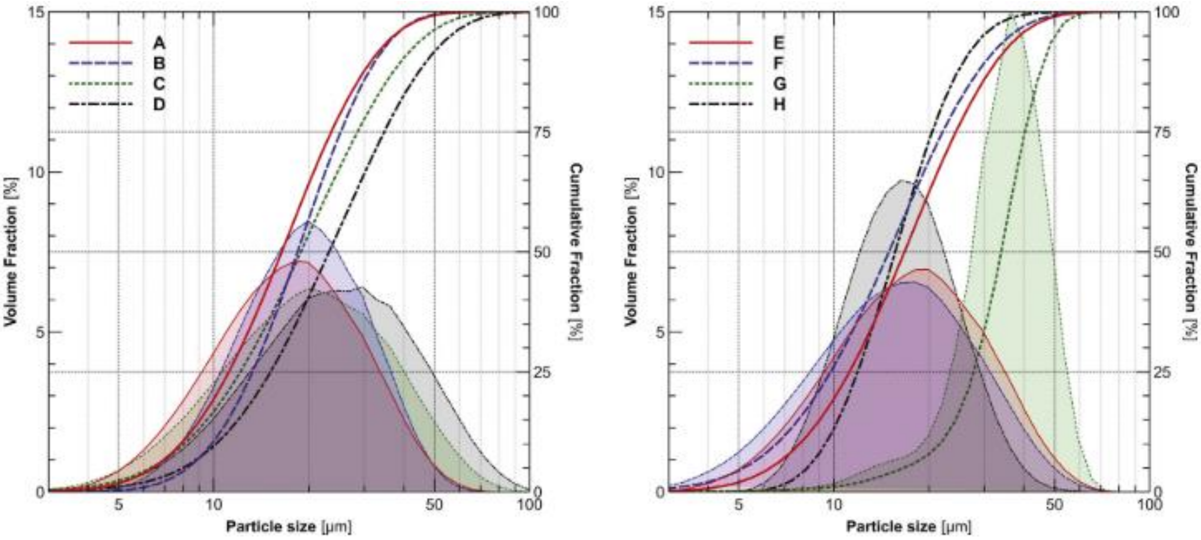

Figure 19: Powder size distribution of multiple batches of powder, taken from [87]

Herbert [89] proposed a mechanism for describing the spreading of powder in a layer. This theoretical mechanism stated that the size distribution can vary with location within a powder layer, as size segregation can occur during spreading. This theory was reinforced by the work of Slotwinski et al. [90] who conducted a study on the powder properties in an individual layer of a print in additive manufacturing. Their findings showed that larger particles are preferentially transported across the build plate, leading to a graded distribution of particle sizes across the build plate. It is therefore possible that this variable powder size within a layer, could lead to changed properties across a build.

Research into the effects of using different powder sources and grades provides direct empirical evidence of the powder variation affecting the final properties [48]. An example is shown in Figure 20, adapted from Gu et al. [91]. The study investigated both the shape and size distribution of the Ti6Al4V powder. The process parameters were held consistent across the powders: Trial A processed all the powders following the settings recommended by Raymor, one of the suppliers, whereas Trial B processed all powders using optimal parameters based on modelling of melt pool overlap. The different powders showed significant changes in the standard deviation values of the yield strength and UTS between the different suppliers in both trial cases. This reinforces the repeatability concern as any change in powder supplier or grade of powder can have a dramatic difference in the material properties produced by the process.

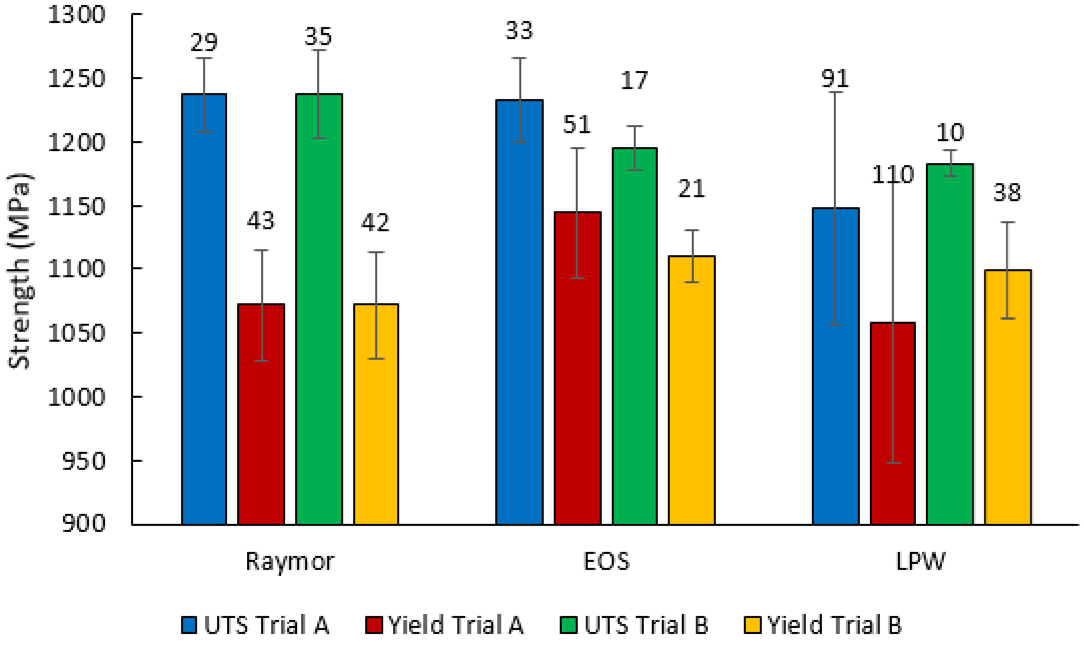

Figure 20: Ti64 powder variation effect on properties, adapted from [91]

A variation of powder morphology can also be created as a function of the process. The nature of the SLM process gives rise to ejected material which can settle on the powder bed ahead of the laser scan. This material ejection is in the form of small particle size material, which is seen as sparks or splatter [73]. The addition of small particles to the powder bed from this splatter can skew the particle size distribution from normal and can give an uneven surface between layers leading to porosity development [74].

The powder is commonly recycled from build to build as most of the powder forming the bed is not fused. Even under maximum build plate usage conditions, less than 20% of the volume is melted [92]. The process requires material to be supplied to create the powder bed beyond what is melted to form the parts. The unused powder is recycled and reintroduced into the process. However, its properties may have deviated from the virgin material due to this recycling [86]; most commonly in size distribution but also in becoming less spherical [38, 90, 93]. A clear example of this is shown in the study by Tang et al. [38], in which a series of tests on reused Ti64 powder processed by EBM were conducted, the results can be seen in Figure 21.

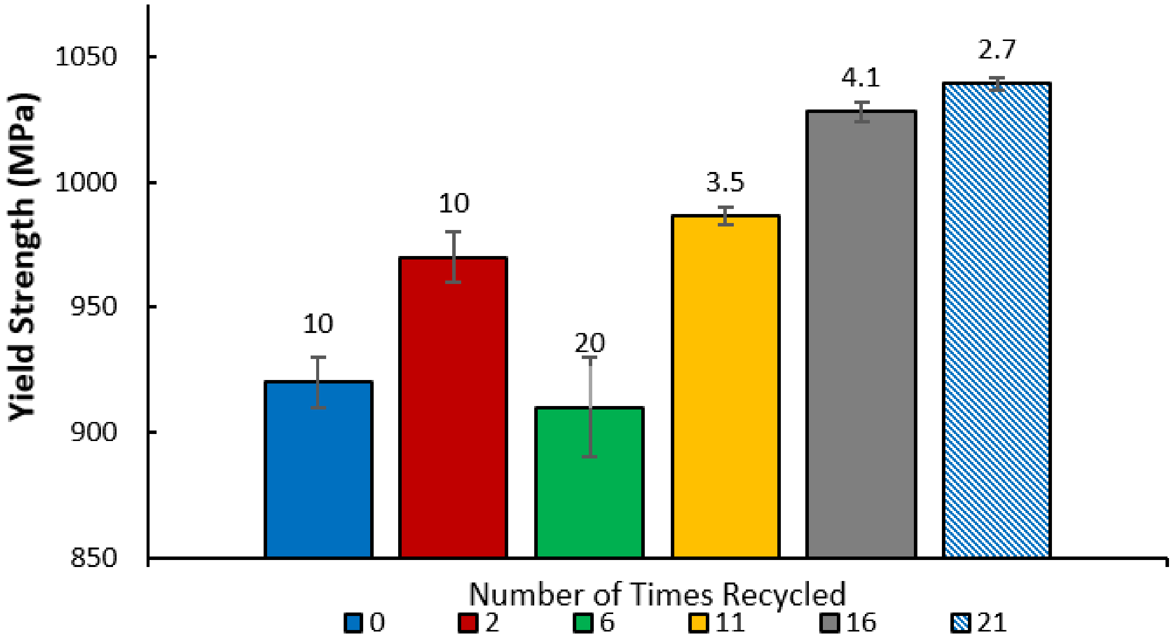

Figure 21: Ultimate Tensile Strength against the level of recycling (adapted from [38]*)*

The measured changes seen by Tang et al. [38], could be deemed beneficial to a produced set of parts and beneficial to the process in general due to improved mechanical properties. The study also showed a reduced variation within an individual build. The authors of the study concluded, “Reused powder showed no measurable undesired influence”. However, any influence desirable or not, changes repeatability, specifically in a build-to-build case. The parts produced by the same machine using the same parameters have a significant variation in mechanical properties which correlates to the number of times the powder has been recycled, which by definition reduces the repeatability of the process.

The pre-process powder properties can be affected by a number of factors including supplier, the specific batch from a supplier and the re-usage cycle of the powder. The powder properties have been shown to directly impact the mechanical properties of produced parts and also indirectly impact the part quality due to defect generation.

Methods to improve the repeatability due to the powder effects include controlling the feedstock and monitoring the produced powder bed for inhomogeneity. For example, accurately characterising the powder in order to use the correct processing parameters for the specific feedstock rather than for a generic feedstock. Decost et al. [94] developed a system to classify both representative and atypical powders. This was achieved by using computer vision and machine learning. A significant advantage of their approach is that it is autonomous, objective and repeatable. The ability to classify the full powder morphology being used could significantly improve reproducibility as the variation in feedstock would be reduced. Alternative means to control the powder morphology such as ball milling prior to production has also been investigated by Attar et al. [95]. This research indicates possible improvements to the repeatability of the process, but was limited in its scope and did not provide a strong conclusion compared to no ball milling. This area of research is generally underdeveloped and further focused study is required.

Examining the produced powder bed for variations is an alternative means by which repeatability could be improved. Methods of this in-situ analysis have been developed and proposed by Foster et al [96] and Zhang et al. [97]. Both studies suggest the use of camera systems to image the powder bed before and after scanning a layer. This will allow the potential development of closed-loop process control. The ability to recognise variations in the powder bed enables remedial action to be taken, such as recoating or dynamically modifying the processing parameters to fit the powder bed generated, and not an idealised general powder bed. This could improve the repeatability of parts in a single build by accounting for any powder variations.

2.3 Para-Process Effects

The crux of the process considered in the overall powder bed fusion process is the laser interaction with the powder bed. The interaction of the laser and the powder is a complex phenomenon due to multiple phase changes that the powder undergoes and variable absorbance based on the temperature of the material. These interactions happen on short timescales due to the focused nature of a laser spot on microscopic spatial scales with rapidly moving scan rates. Operating at these small interaction windows means even minor perturbations can have a significant effect on the process.

The energy density or specific energy input is used as a primary comparison variable in laser-based AM [41–43] to encapsulate all the laser characteristics in a single variable. The energy density is used to generate relationships with relative density [29, 98, 99] which is further connected to strength and elongation [100]. Energy Density is commonly formulated as

$$\psi = \frac{P}{v * h * d} \tag{1}$$

where ψ is the energy density (J/mm^3), P is laser Power (W), v is the scan speed (mm/s), h is the scan spacing (mm) and d is the depth of powder (mm) [101]. An alternative means of calculating energy density has also been used in some studies to explicitly include the time interaction of the laser.

$$\psi = P_d * t_i \tag{2}$$

$$P_d = \frac{4P}{\pi D_b^2} \tag{3}$$

$$t_i = \frac{D_b}{v} \tag{4}$$

$$\psi = \frac{4P}{\pi D_b v} \tag{5}$$

The additional terms are the power density P_d, the beam diameter D_b, and the interaction time t_i [102]. The two energy density calculations differ in their formulation, with equation *(1)* having a relation to the setpoints for the depth of powder and hatch spacing. Whereas equation (5) relies on the measured value in the beam diameter and postulates that the depth of powder and the hatch spacing are a derivative of this energy density rather than a determined set point. The existence of two different formulations for energy density can lead to variation in the literature, as depending on the formula used, the properties for a given energy density can vary widely.

As a corollary, the same mechanical properties can also be attributed to varying energy densities. This occurs due to the reporting of just the energy density instead of the actual process parameters used in studies. This leads to reduced reproducibility in the field as a whole, as insufficient information is transmitted to allow for a rigorous reproduction of results.

Neither equation is inherently superior to the other, which has led to both being prevalent in the literature. The desire to keep energy density consistent while changing process parameters dictates which equation to use in each instance. In cases of modifying power or scan speed, both are applicable. However, the lack of all pertinent variables of hatch spacing and depth of powder prevents them from being used for ED control in all possible variations that may be desired.

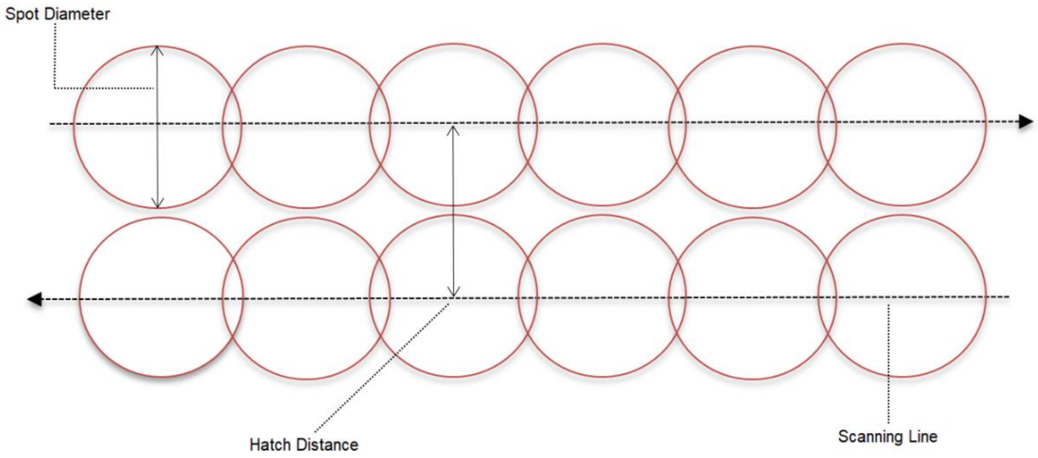

Figure 22: Graphical view of energy density variables

The scan spacing and beam diameter, while not directly synonymous, are related variables. To accurately control the level of re-melting, the scan spacing and thus beam diameter must be considered to define the overlap of the scan passes. Re-melting can have a significant effect on the final microstructure [103] and by extension, mechanical properties in both a positive and negative way. For example, studies by Van Den Avyle et al. [104] and Yahata et al. [105] demonstrated that re-melting was found to reduce defects in Inconel and deoxidify titanium respectively, thus improving their properties. However, if excess re-melting occurs, the microstructure can become undesirable as shown by Charles [106] wherein a banded microstructure was discovered to form in Ti64 due to the reheating cycle, not the original quench. This banded microstructure has been shown by Wang et al. [107] to introduce anisotropy to the mechanical properties. This anisotropy directly affects the mechanical properties of the samples relative to other samples without this banded microstructure. Anisotropy in the mechanical properties can cause reduced repeatability, as any change in the orientation of individual parts modifies the properties.

Zhu et al. [99] and Han et al. [108] investigated the relationship between energy density and part density. Their results showed a non-linear but consistent relationship across both studies shown in Figure 23. The studies show a range of energy densities that give a good relative density of the produced part. Both studies showed evidence of density improving with increased energy input or energy density until hitting a maximum at 60 J/mm^3 for Zhu et al. in CoCr, and 138 J/mm^3 for Han et al. in Ti64. However, a sharp drop in relative density occured when the energy input dropped below this level,.This is likely due to a transition from a laser melting regime to a laser sintering regime caused by incomplete melting of powder particles, resulting in a poor bond with entrained porosity developed. The exact threshold for this drop is material and process specific. Deviating from this optimum plateau over a section of the manufacturing envelope could lead to a reduction in part quality and build process repeatability. A similar density drop occurs when the energy density goes beyond the optimum plateau as the powder is vaporised rather than melted creating a void which develops into porosity.

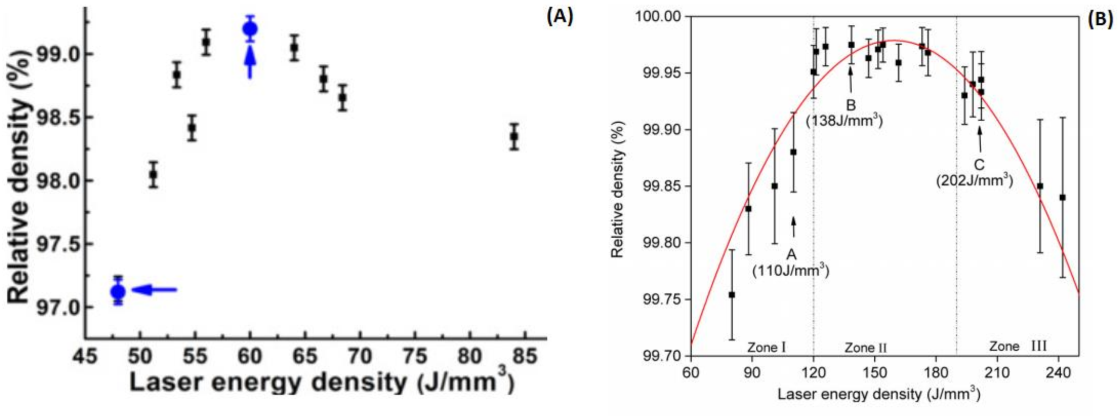

Figure 23: Energy density to relative density curve adapted from (A) Zhu et al.[99] *and (B) Han et al* [108]

The connection of mechanical properties such as elongation and tensile strength to relative density is well documented. In the study by Verlee et al [100], a range of densities from 81% to 98% were investigated. The study showed a direct relationship between higher relative density resulting in higher UTS and Elongation. This connection between mechanical properties and relative density and thus energy density, allows us to state a plateau of mechanical properties must also exist with a sharp drop in performance when deviating from the plateau. The potential for the energy density to vary across the build envelope makes this fact a critical concern for repeatability within an individual build.

The beams used in modern lasers use diffraction-limited optics to provide a tight focus [109]. The laser source used in AM is not a perfect system, with inherent power fluctuations particularly at higher power levels used in the manufacturing process [110], as shown in Figure 24. The fluctuation of power can lead to repeatability issues as inconsistent melt pool effects such as excess vaporisation could occur from the transient higher energy levels.

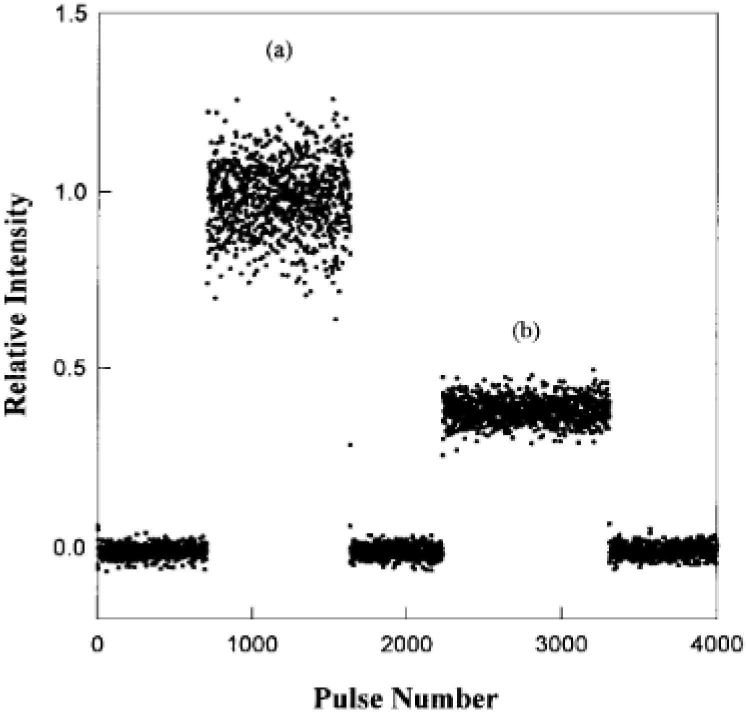

Figure 24: Relative intensity of laser pulses [110]

The fluctuations of energy reaching the build plate are further increased by transmission variations due to plume development and accumulation of process by-products in the process chamber [111]. The fluctuations can impact part quality, raising a repeatability concern as the energy reaching the build plate may not remain constant during the entire process.

The by-products produced from the process are usually found in the plume and specifically in the condensate cloud produced by the vaporisation of the powder material. This cloud is comprised of nanoparticles from material that has cooled and condensed out of the vapour state. The particles remain in suspension due to their light nature and take time to settle on the surfaces of the process chamber. This condensate is produced consistently in the process and allows a film of settled condensate to build up. This film is on all surfaces and in some cases without sufficient filtration, can build up on the transparent window through which the laser beam is directed. This can lead to the laser beam becoming obscured by what is in effect an additional thickness of the powder material prior to reaching the build platform. This film could also act to increase the level of thermal aberration experienced at this window, turning it into an additional lens resulting in a further variation in the laser focussing on the build platform. As this film develops over time, its effect will be spatially gradient over the build which could lead to a repeatability concern, particularly in the case of layers of nested parts.

The fluctuations in power can also lead to a change in the spot size or track width of the beam. This can be seen clearly in Figure 25, adapted from Kusuma et al. [112] which shows the percentage standard deviations of measured track widths at different laser powers. Both the standard deviation of the track width measurements and the spread of the data are observed to increase with laser power. This shows that in a single machine with higher laser powers, the output is less consistent than at a lower power operation setting.

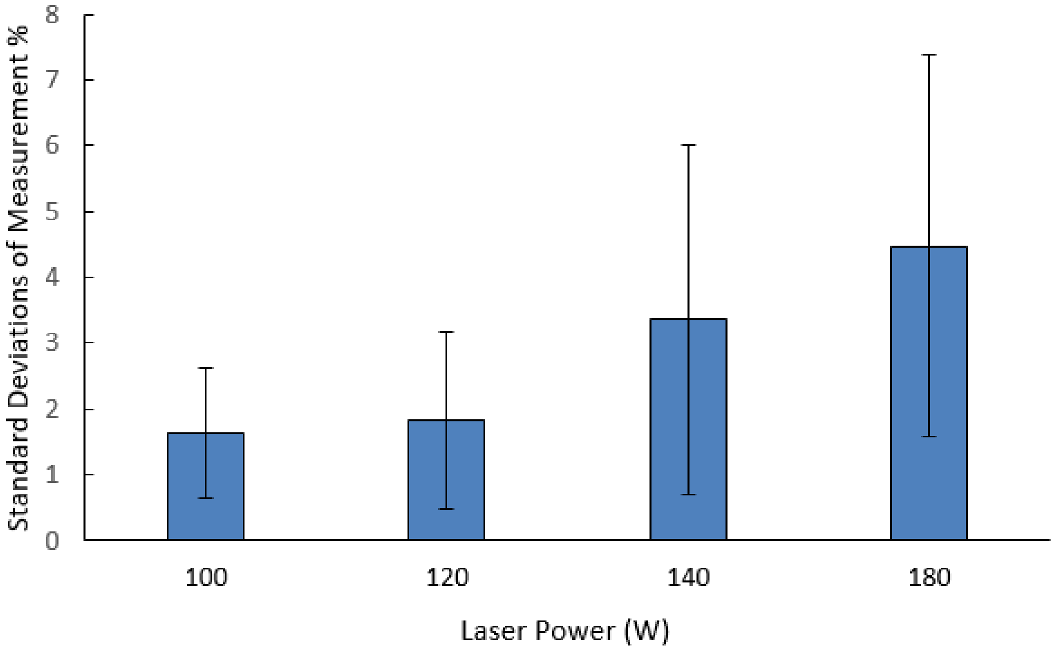

Figure 25: Percentage standard deviations of track widths at different powers, adapted from Kusmana et al. [112]

The spot size of a laser can be calculated in a number of different ways including full-width half-maximum (FWHM), D4σ method and $1/e^2$ method. The derivation of these methods is based on the intensity profile of the beam and are inherently independent of power variation. These calculations for spot size do not intrinsically have a power relationship, however, while useful the scientific spot size of the beam does not provide the most useful measurement of the beam diameter. In AM, the effective laser spot size is a more useful measurement, where the effective spot size is defined as the area receiving the minimum irradiance required to melt the powder.

Thus if the power is increased with all other parameters kept constant, an identical Gaussian profile upshifted on the irradiance axis is generated as seen in Figure 26. This leads to a greater section of the beam contributing to the melting process, increasing this effective spot size [113].

The effect of laser spot size on the resultant microstructure of an AM part was studied by McLouth et al. [114], whose study was carried out on Inconel 718 parts produced by SLM. The spot size of the laser was modified by changing the manufacturing focal offset without modifying any other processing parameters. They concluded that an offset focus or larger spot size gave rise to “coarser microstructure and stronger crystallographic and morphological textures in both the as-built and fully heat-treated conditions”. These microstructure changes would introduce changes in the mechanical properties and could potentially add a repeatability concern due to the stochastic nature of power fluctuations in the laser system.

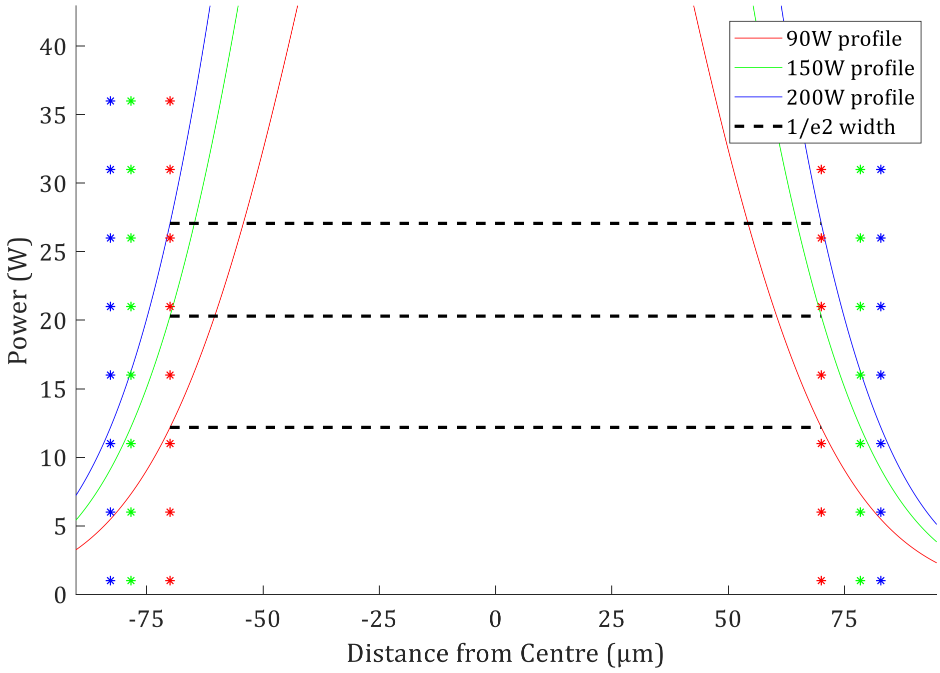

Figure 26: Laser spot size with respect to power

The increase in the spot size of the laser has two critical effects. It leads to a reduction in energy density as the power is spread over a wider area and the overlap between adjacent laser passes is increased. The increase in overlap causes the greatest potential effect. The overlap change causes the area of remelting to be increased changing the distribution between remelted and non-remelted resultant microstructures. There is also a change in total power to which the powder is exposed. This is graphically represented in Figure 27, as the overlap increases the normalised power over the area between passes rises.

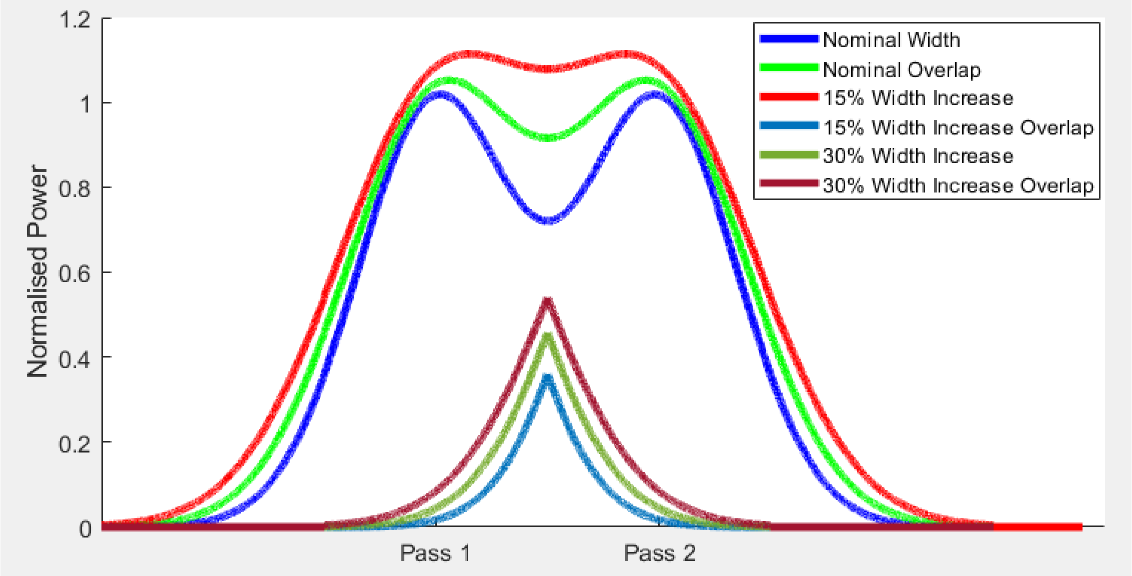

Figure 27: Overlap of Adjacent Laser Passes

The beams used in modern lasers use diffraction-limited optics to provide a tight focus [109]. However, this tight focus only exists in a narrow region of the beam. The beam width varies along the beam propagation path following the equations (6) and (7), wherein z is the distance from the focus, w_0 is the waist radius (the narrowest part of the beam), λ is the laser wavelength and n is the index of refraction.

$$w(z) = w_0 \sqrt{1 + \left(\frac{z}{z_R}\right)^2} \tag{6}$$

$$z_R = \frac{\pi w_0^2 n}{\lambda} \tag{7}$$

The focus plane of the laser propagation system should be positioned to lie along the plane of the active layer in the build. However, the beam may become out of focus at certain points in the build due to immovable or transient optical effects such as thermal warping of the lens. The focus plane could also deviate from the active layer in the build due to inaccuracies in the positioning of the build piston or the levelling of the build plate. Following equation (6) this will lead to an out of focus beam, resulting in a greater beam diameter. This out of focus nature can also lead to the cross-sectional shape of the beam becoming more elliptical as it moves out of focus [115]. The beam diameter can also be increased when the beam becomes elliptical as its angle of incidence on the plate is changed [116], as will be discussed in detail in section 3.1.3 Angled Incidence. It has been shown that the shape of the beam, specifically studied by Roehling et al. [117], can have a direct impact on the mechanical properties of a produced part. The experimental results found by Roehling et al. were supported by a series of simulations of the process using the ALE3D software package. The results show clear evidence of a scan directional dependence created by an elliptical spot not present in a circular spot. This dependence leads to narrower melt tracks and higher peak temperatures in the melt pool as seen in Figure 28. These narrower tracks could change the conditions present in adjacent scans and the higher temperatures can introduce melt pool variability and excess particle ejection or vaporisation. The effects of this concept are described in the work by Qiu et al. [74], wherein the role of melt flow is extensively addressed in both modelling and experimentally concerning Ti64. They found that unstable melt flow gives rise to porosity defects and increased surface roughness.

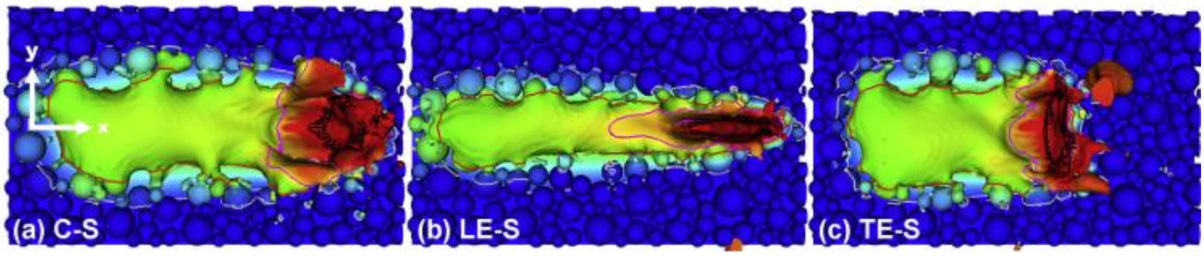

Figure 28: Beam shape effect on the melt pool [117]

The effect of the change in melt pool formation is shown in the cross-sectional view in Figure 29. The longitudinal elliptical beams lead to greater ejected material and the development of internal porosity. The scan vector used in AM is commonly rotated between layers [118, 119]. This leads to a variation between longitudinal and transverse elliptical passes through a part, which can lead to variable porosity and mechanical properties in each layer. In extreme cases, the differences between each layer could also lead to the development of delamination in the build.

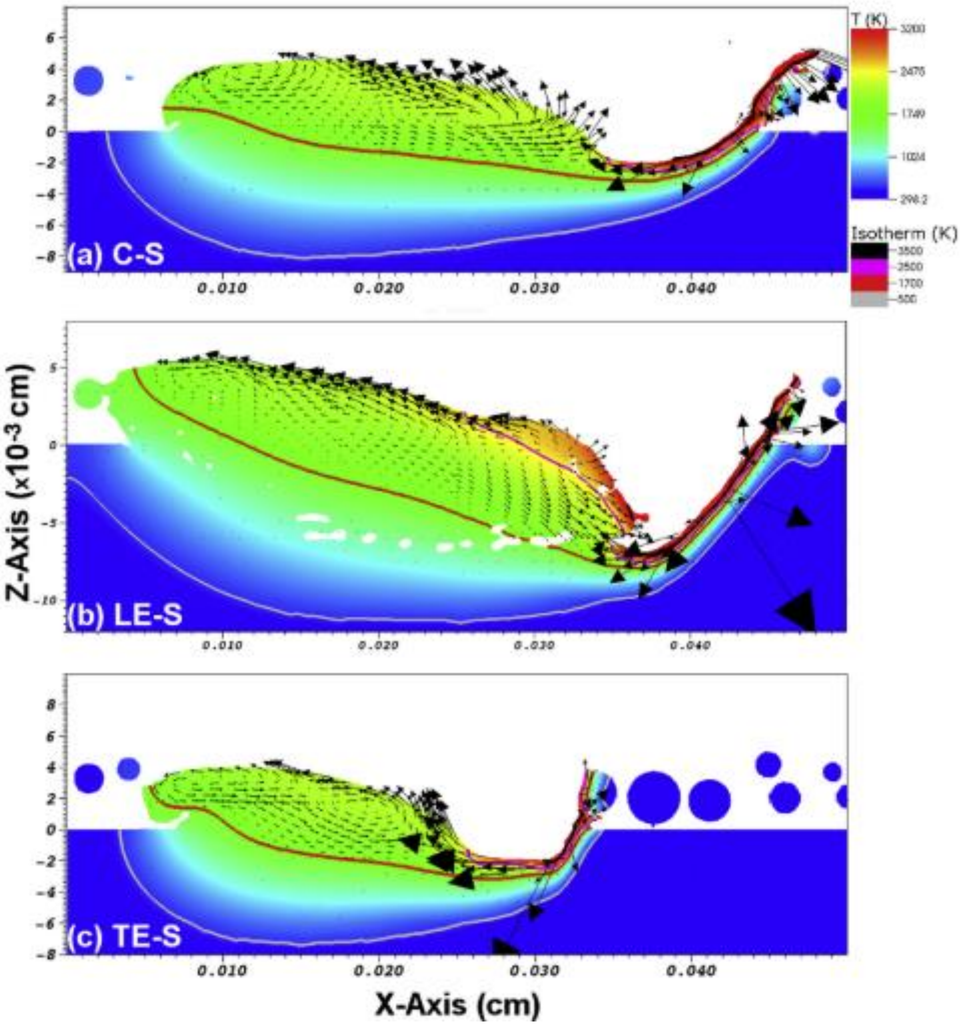

Figure 29: Melt track formation [117]

As both the size and shape of the laser spot is location dependant, the energy density must also be location dependant due to the energy being spread over a varying spot area. This will lead to both the physical and geometric properties of the part becoming build plate location dependent. This dependency gives rise to a significant repeatability challenge as each part will have a different location on the build.

The laser parameters used for producing parts are usually found empirically, and thus can be unreliable when applied in locations and systems other than their formulation system. The empirical values are found for a specific system and cannot be taken to be ideal for all possible systems used in AM. The level of power required for the process is commonly considered in ranges. The process is an optimisation problem with a vast number of potential control points. The optimisation is also based on a specifically targeted characteristic. For example, designing for a particular microstructure or density can require very different parameters sets for the same material [29, 120]. This has been shown clearly in the study by Gu et al. [121], where the influence of energy density on porosity and microstructure was evaluated in 17-4PH stainless steel. They showed that different parameter sets such as changes in scan speed, gave rise to varying physical properties. However, the properties do not reach maximums at the same location, as seen in Figure 30. The selection of process parameters to get the desired property can be a repeatability issue without the understanding of interconnectedness present in the properties. For example, one cannot assume that a part would exhibit the same microstructure when the parameters are modified to produce a denser part. It is also noticeable that the standard deviations present at each setting vary across the parameter sets. Selecting the process parameters with the best resulting part properties can give rise to repeatability issues as the spread in the part properties is not constant while changing process parameters.

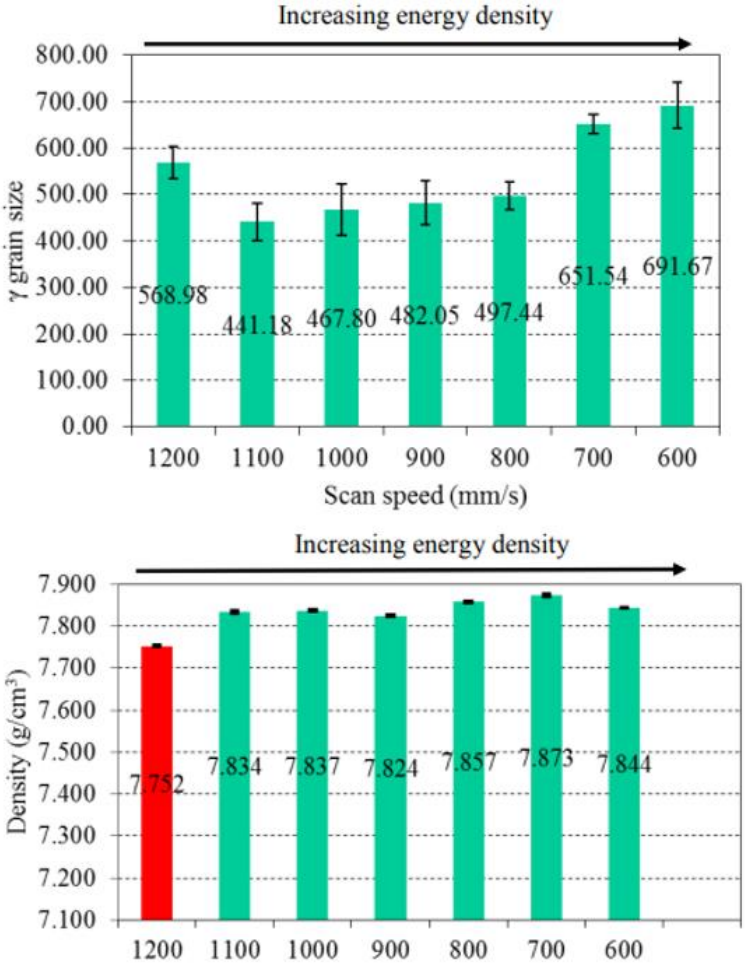

Figure 30: Density and Grain size against scan speed, adapted from [121]

The effect that scanning strategy has on the resulting part has also been studied by Demir and Previtali [122]. The study showed the impact that the scanning strategy can have on the part quality. Variations in scan strategy were shown to impact the magnitude of the residual stresses, surface roughness and geometric accuracy of the produced parts. It was noted in the study that the remelting scan strategies also increased the dimensional errors of the parts produced [122], this will result in a reduction in the geometric repeatability. The scan strategy can also affect repeatability, as shown in Figure 31. The strategies investigated were based on secondary passes over the workpiece. The second pass options were as follows: no second pass, full-strength second pass, reduced strength second pass, focally offset pass. It was found that not only is the density changing as the scan pattern changes, but also the magnitude of the errors changes, with the final polishing strategy having the spread of results halved compared to the no second pass condition [122]. The effect of correcting the scan strategy for a single variable can cause unintended quality reductions elsewhere. This illustrates one of the key challenges of AM repeatability, in that the optimum settings for one property are not optimum for all properties.

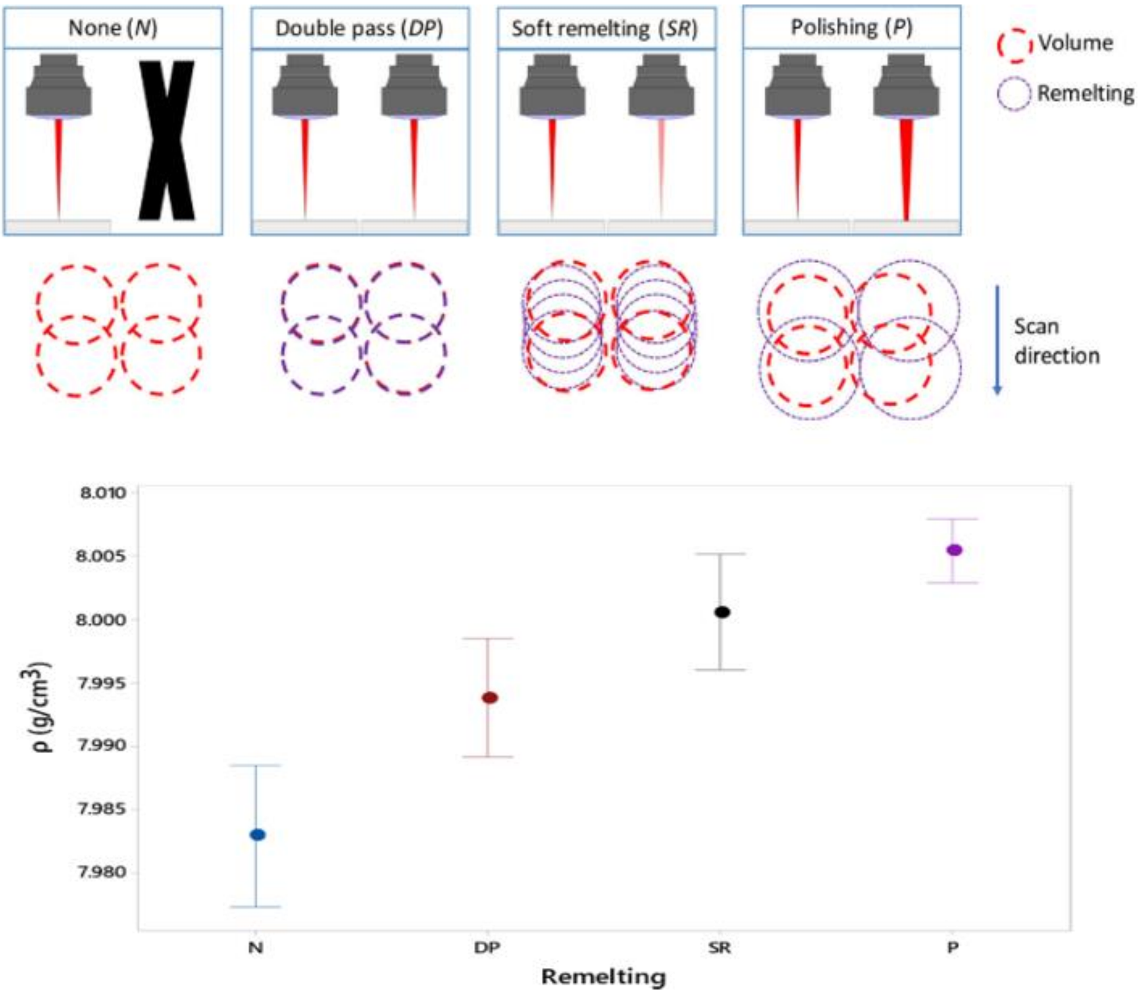

Figure 31: Effect of scan strategy on density, adapted from [122]

The effect of scan strategy was further investigated by Ali et al. [118], who found that the standard scan strategy used in the production of Ti6Al4V parts produced the lowest residual stresses as shown in Figure 32. The spread of the residual stresses, however, was greater for the standard strategy than the 2x2 case. In selecting the lowest residual stress for the standard, a less repeatable strategy resulted.

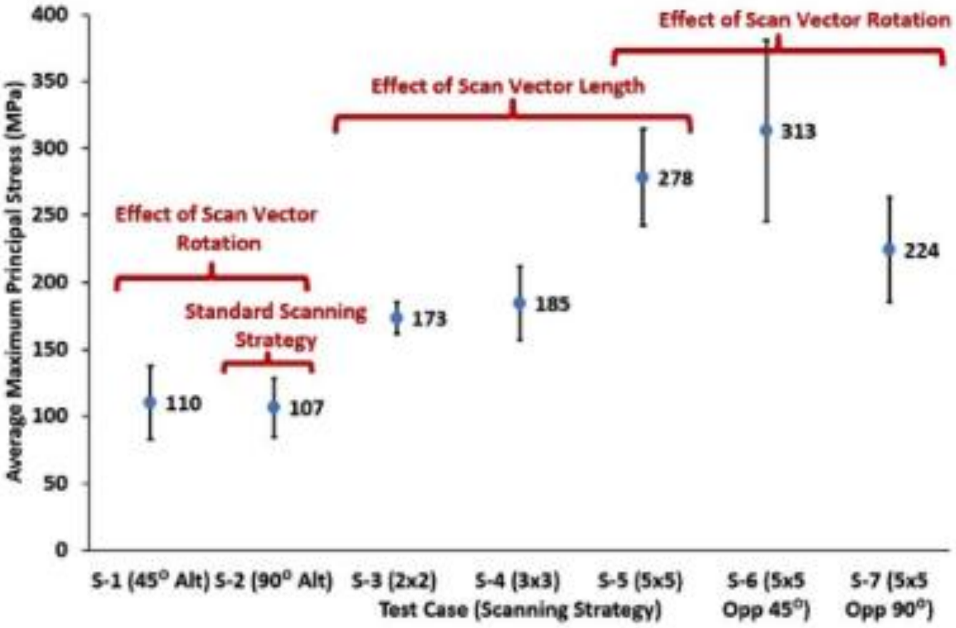

Figure 32: Principal stresses for different scan strategies [118]

The common theme across the studies into the laser characteristics used in AM, is that selecting parameters that give the best physical properties are not necessarily the optimum parameters for repeatability. The systemic selection for material properties over repeatability could be a major contributing factor in the lack of repeatability in AM in general. The lack of explicit information about how certain physical properties were optimised and how the process parameters were selected by these optimisations give rise to a number of claimed optimum process parameters for the same physical property. This lack of information can lead to the selection of suboptimal parameter sets when repeatability is the desired outcome.

Some research has focused on investigating the in-situ monitoring of the powder bed fusion process. For example, the National Institute of Standards and Technology (NIST) is developing a focused testbed for enhanced process control [123]. This testbed allows in-situ continuous feedback control to be developed to improve repeatability. The research by Aminzadeh [124] demonstrated the ability to detect defects as they are forming using a visual camera for quality inspection focusing on porosity occurrence. Work by Demir et al. [125] monitored the process using co-axial measurements with the processing laser. The monitoring consisted of using a visible light camera to monitor the stability of the melt pool and a near-infrared camera to monitor thermal effects. The ability to detect defects forming during the process would allow the targeted use of corrective scan strategies such as the polishing-type remelting pass used by Demir et al. [122] to reduce or remove these defects, thus improving both part quality and repeatability.

2.4 Post-Process effects

After AM parts are created, it is frequently required that they are further processed to modify their properties. This is done in a traditional manufacturing context as well. However, uncertainty is created around the properties of AM parts as the level of post-processing can give rise to different properties. The post-processing of AM parts could hide issues inherent in the process as they are removed post-processing, masking the underlying inconsistencies. The most common post-processing carried out is machining to give a better surface finish and to remove supports. Other post-processing includes heat treating to provide stress relief or anneal the parts and hot isostatic pressing to reduce the porosity in the parts.

The surface of an AM part is frequently rough. The surface roughness values for as-built additively manufactured parts [126] is an order of magnitude greater than the surface roughness found in parts made by casting [127] or wrought [128] materials. This roughness is due to the layered nature of the parts' construction creating a stair-stepping effect that is heavily dependent on part orientation [129] as noted in section 2.2 Pre-Process Effects. The use of supports on overhanging surfaces also gives rise to localised roughness peaks where the support remains [130]. AM parts are commonly machined to reduce the surface roughness found from these effects, as the rough surface impacts the fatigue of additive parts. Without machining, they exhibit a decreased fatigue life [131].

The process of powder bed fusion gives rise to residual stresses in the part. The stress is created by the large thermal gradients created in the laser scan, as the laser passes over an area the powder rapidly heats to melting and then back to solidification [132]. The large gradients lead to localised expansion and contraction within the constrained metal creating stress within the metal part. The residual stresses cause deformation and cracks during post-process machining and heat treatment, as the stress is no longer constrained [133].

Stress relief reduces the residual stresses left in the part from manufacturing and can have a significant impact on the mechanical properties, surface quality and microstructure of a produced part. This can also lead to a change in the repeatability of the measurements. This can be observed in tighter standard deviations from more consistent part post-processing or a greater spread due to additional processes with their own inherent errors creating a larger deviation. Figure 33 shows the effect of post-processing and build orientation of titanium parts produced using SLM from a study conducted by Wauthle et al. [134]. It can be seen that post-processing improved the consistency of the maximum strength values but increased the spread in the elongation comparisons. The trend in standard deviation is clear with a reduced deviation found in the UTS case as the level of post-processing increased with heat treating and then further hot isostatic pressing (HIP) treatment. However, this trend is not consistent. For example, in considering elongation, it is evident that the heat-treated parts have a tighter distribution but the HIP samples have a wider spread compared to even the as-built samples. The post-processing gave rise to improved mechanical properties but at the cost of more variation between samples in some cases.

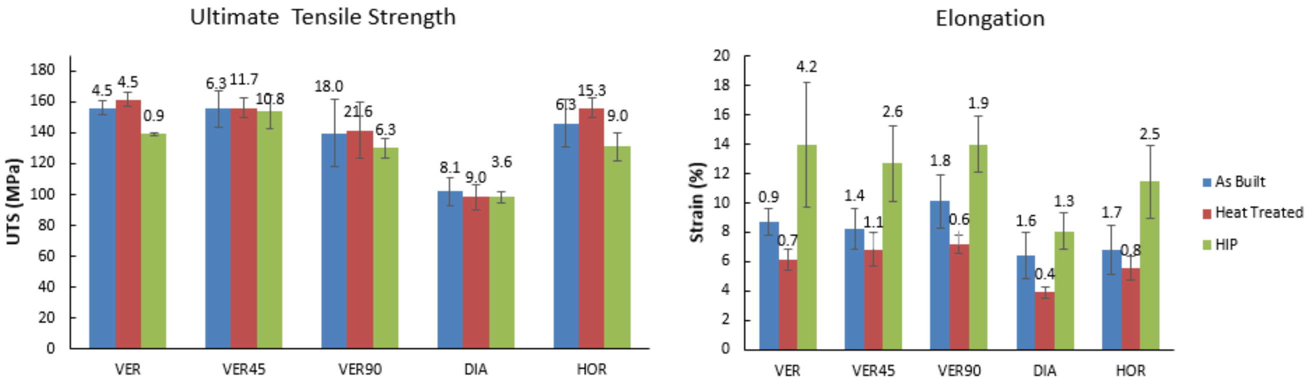

Figure 33: Effect of post-process and orientation on UTS and elongation of Ti64 SLM parts, adapted from Wauthle et al. [134]

An example of how post-processing can affect the variability in mechanical properties can be seen in Figure 34 which shows the UTS and elongation for SLM Ti64 parts that have undergone different heat treatment cycles. Data is adapted from the study by

Vrancken et al. [135]. It can be seen that after heat treating, in general, the elongation improves and the UTS decreases as to be expected from a stress relieved material. The more important factor from a repeatability point of view is the spread of results.

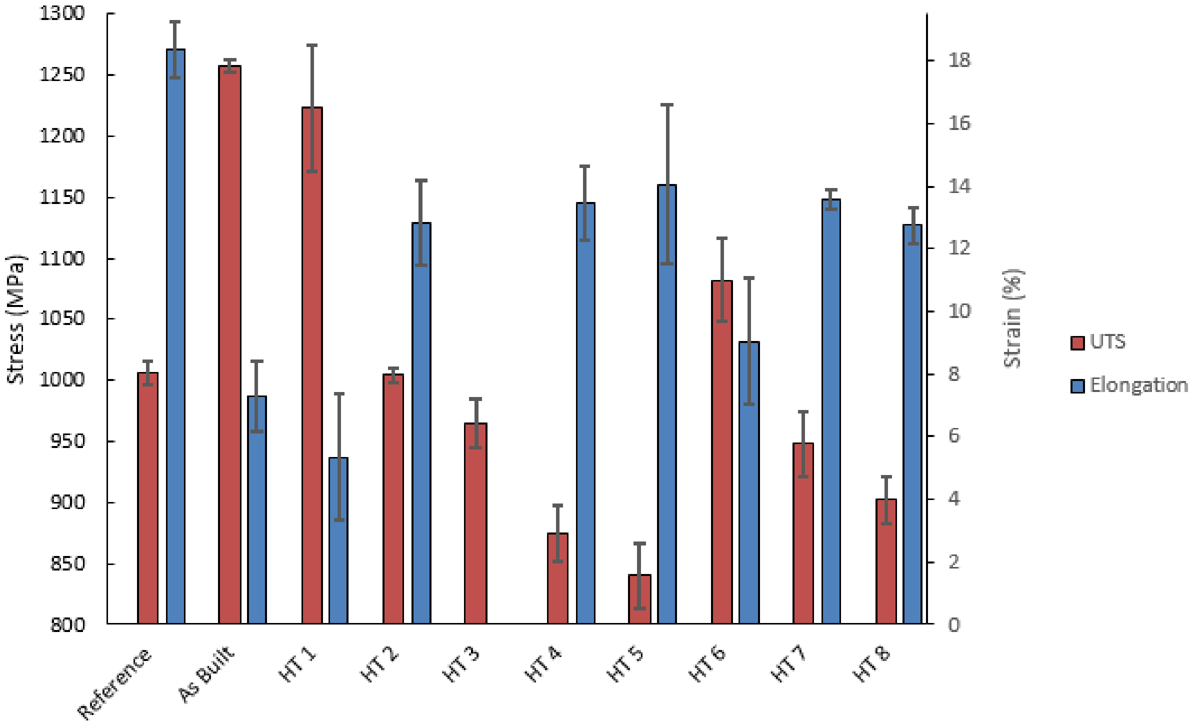

Figure 34: Effect of different heat treatments of SLM Ti64 parts, adapted from Vrancken et al. [135]

The standard deviations are extracted out to allow closer examination in Figure 35. In all UTS cases, the standard deviation of the results is larger when samples underwent heat treatment compared to as-built samples. A similar trend can be seen for elongation in most cases. The act of post-processing the parts, while improving the physical properties for certain applications, has a detrimental impact upon repeatability.

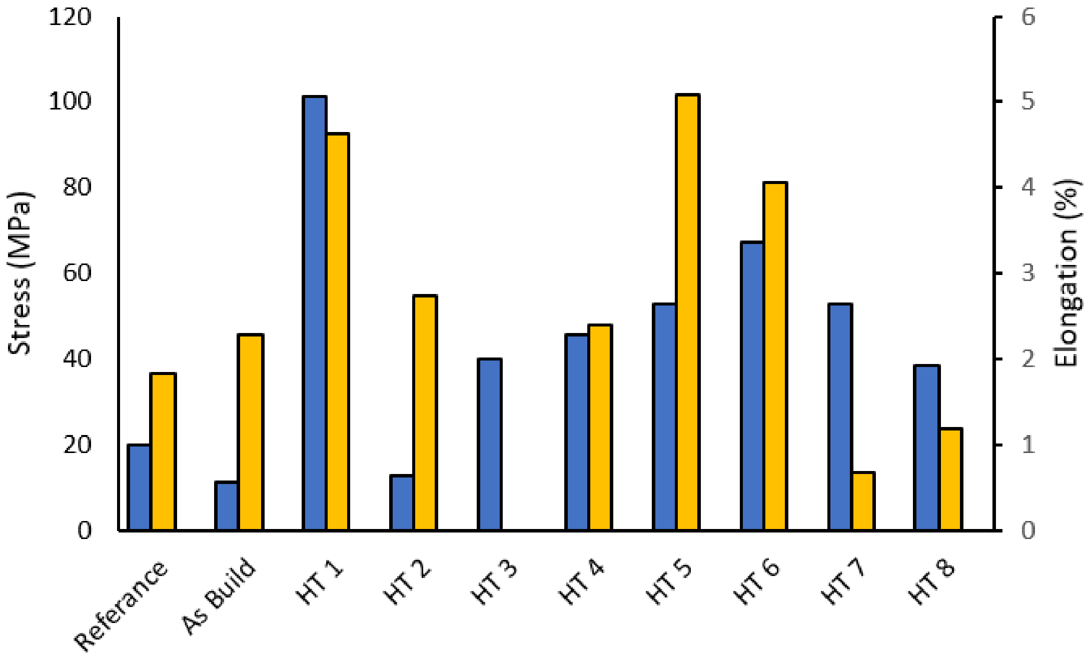

Figure 35: Standard deviations of different heat treatments of SLM Ti64 parts, adapted from Vrancken et al. [135]

The post-processing of a part is undertaken to change the mechanical properties significantly. The selection of the correct post-processing to apply to as-built microstructure is not a simple task in AM, as the starting microstructure can vary significantly in the as-built part based on process parameters [136]. When homogenous and consistent wrought material undergoes post-processing, the standard deviations of its mechanical properties remain consistent across the treatment. This can be seen in studies of varying heat treatments of wrought material such as those carried out by Leyens et al. [137] shown in Figure 36. It can be seen that all the treatments, while giving different property values had similar relative errors noted by the uniform error bars across the treatments. This is contrary to what was found in the AM cases, giving a clear contrast when applying post-processing the AM samples.

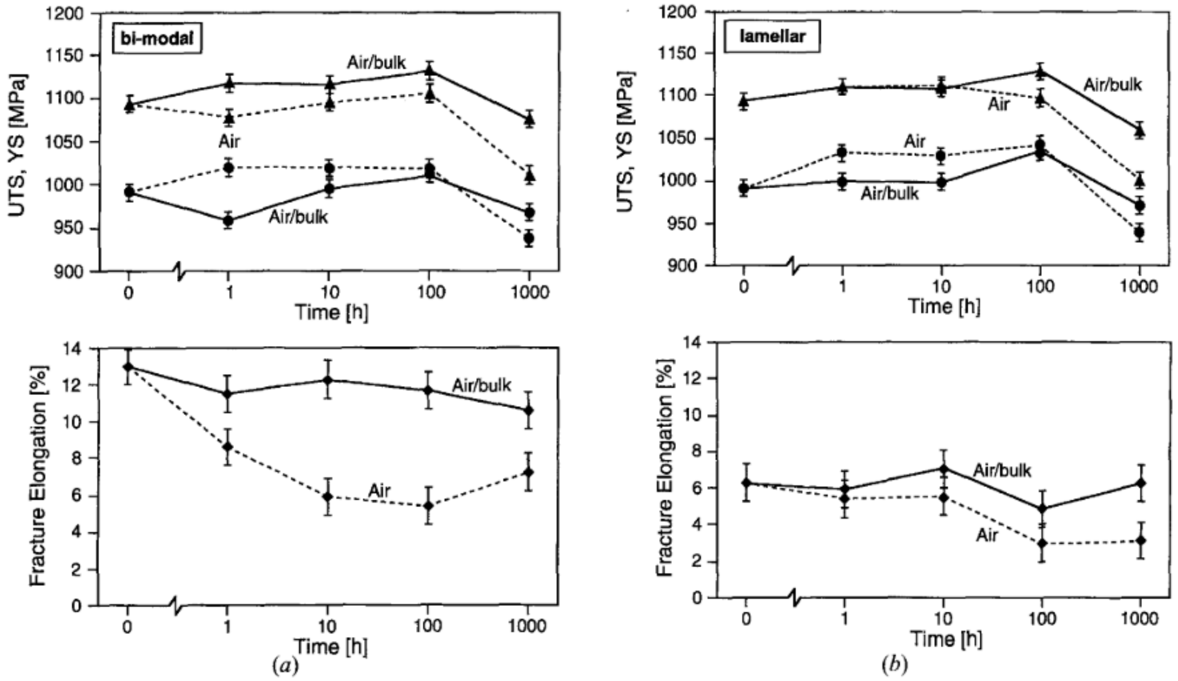

Figure 36: The effect on mechanical properties of Ti64 under different annealing times and different solution heat treatment temperatures of (a) 990 °C and (b) 1060 °C, taken from [137]

Vrancken et al. [135] summarise one of the issues found in post-processing AM parts as: "Application of standard heat treatments shows that these treatments do not lead to the usual or expected results, SLM produced parts need to be treated differently to bulk alloys". Specific desired properties need varying and targeted treatments, the incorrect application of post-processing leads to the creation of undesired microstructures. The unexpected and unusual results give rise to inconsistency which hampers repeatability. The improper application of bulk-determined heat treating can lead to an increased spread of results. This is further expanded due to the different effects the post-processing has on a given microstructure which may be batch-specific, leading to a build-to-build variation.

The means to improve the repeatability and reproducibility at the post-processing level are multifaceted, focussing on two key steps: the elimination of the need for the post-processing; and improvements of the consistency of the parts before post-processing.

The elimination of post-processing could be found by improving the surface roughness using techniques such as optimised support to reduce the support requirements with associated roughness [138, 139] and reducing the layer thicknesses to reduce the staircase effect found due to the layering system. This, however, will not eliminate the need for heat treatment as it is common to both traditional and non-traditional manufacturing techniques.

The improvement of post-processing input will be accomplished by improvements found in pre- and para-process techniques. The inconsistencies and variations that have been accruing in the process to this point are exaggerated by the post-processing. This in effect means that a more consistent input will be able to produce a more reliable output from the post-processing. From this evidence, it can be hypothesised that the crux of solving the post-processing repeatability concerns lies not in the process but in the pre and para-process repeatability.

Chapter 3: Development of Modified energy density equation

Having analysed the various factors that can impact the AM repeatability process, this chapter considers the factors that most impact quality of AM processing. It is intended that by considering these factors, a method to maximise AM processed part repeatability can created.

This chapter will detail the development of a modified energy density equation based on the commonly accepted formulation. The modified equation will account for the spatial variation that some of the sources of error induce in the process. The equation will be evaluated compared to the currently accepted energy density equation, to determine the level of energy change that could be expected within a build.

3.1 Sources of error targeted

The selected material can greatly impact the availability of variation in pre-process factors such as powder morphology. The material also dictates the type and availability of post-processing that can be carried out on the completed AM part. Furthermore, as discussed in 2.4 Post-Process effects, the variation of part properties coming into post-processing can affect its effectiveness. The post-processing would occur at a point potentially after repeatability has degraded from the desired level. Once the para-process was selected as the area of focus, several specific sub-areas were further analysed in-depth for their potential sources of error that could have detrimental effects as discussed in section 2.3 Para-Process Effects. The sub-areas were specifically accessed for any spatially related variation which would reduce repeatability between parts in a single build. The accessed areas with spatial variation were the F-theta distortion, plume absorption, angled incidence on the plate and powder reflection efficiency. This shall each be now be analysed in depth.

3.1.1 F-Theta Lens

The build plate and subsequent powder bed can be considered as nominally flat and level. This necessitates that the lenses used for focussing the processing laser beam for the manufacturing by SLM also need to have a flat scan field. Traditional spherical optics are incapable of producing this flat scan field, as a traditional flat field scanning lens has a relationship of F-tan(Theta) which introduces a non-linear deflection of the image based on the angle of the light passing through the lens. The F-Theta design linearises the spherical non-linearity within the operating angles of the lens before hitting the lens diffraction limit. A comparison of the lens systems is shown in Figure 37.

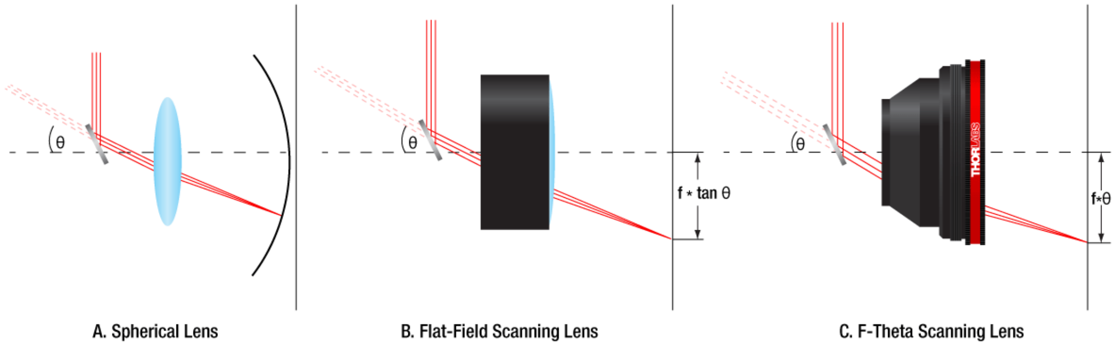

Figure 37: Optical lens comparison is taken from THORLABS

All optical lenses can be subject to imperfections and aberrations even within tight manufacturing tolerances. These can be either chromatic or monochromatic in nature. As the AM process uses inherently monochromatic laser light, only the monochromatic effects need to be considered, the predominant aberrations present in a lens include spherical aberration, coma and astigmatism [140].

Spherical aberration is when the light rays from the lens do not all meet up exactly in the same focus. This can take the form of positive aberration, in which the rays passing through the periphery of the lens are bent too much, leading to a spread of the focus in the direction of the lens and the inverse for negative aberration. This could lead to a wider focus spot of the laser, because instead of an incident point it is created by a combination of non-converging light rays.

Astigmatism occurs when the light propagates with a substantial angle against the optical axis. This causes the distance from the lens to the focal point to be somewhat different between principal axes. In the focal plane corresponding to each of those directions, a point is thus imaged to an elliptical region.

These variations are inherent to the lens and are usually corrected in lens design through the use of aspherical lenses. However, variations can still be present due to imperfections in the lens manufacturing process. Furthermore, as the lens is being used to focus a high powered laser, some degree of thermal aberration is induced [141]. This total distortion modifies the magnification of any image passing through the lens, in this application the laser spot size. This can take the form of either an increased magnification with distance from the optical centre (pincushion distortion), or a decrease (pincushion distortion) [141]. A graphical representation is shown in Figure 38.

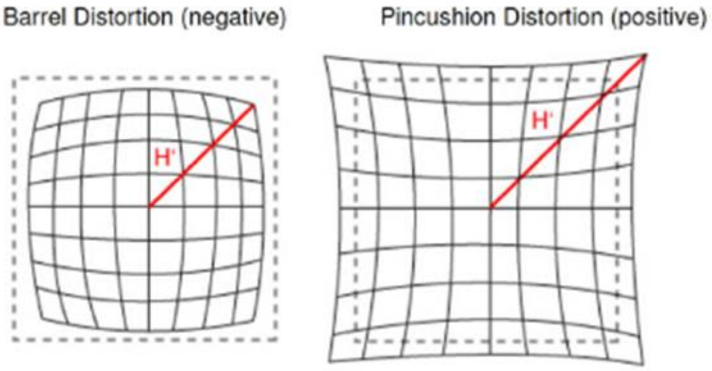

Figure 38: Barrel and Pincushion distortion

The level of distortion due to the various imperfections and aberrations is both calculable and measurable. The information about the distortion is provided by the manufacturer of the F-Theta lens in the form of a distortion map such as seen in Figure 39.

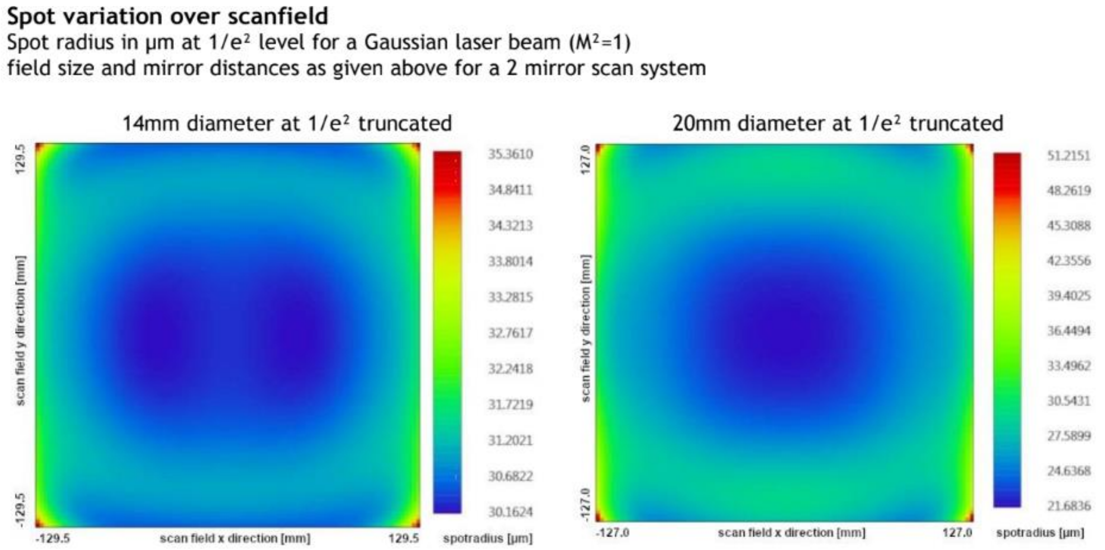

Figure 39: Image variation over the scan field of the F-Theta lens

The effect of this distortion is a varying spot size or beam diameter term in the energy density equation as the beam moves around the build volume. The magnitude can be seen to have a dependence on the initial beam diameter prior to reaching the lens. However, in all cases, the level of change can be on the order of several percent of the total energy easily transitioning from the optimum area of processing.

The F-Theta distortion of the focusing lens used in this study is specified by the manufacturer of the lens. It is given in the form of a distortion map as shown in Figure 40. The build plate locations are overlaid on this distortion map and the level of distortion can be read indirectly by using image processing of the distortion map. This exact distortion coefficient (δ) can be extracted using a MATLAB imaging process to examine the part location on the map and correspond it with the given scale. The value for the distortion coefficient can then be used to model the spot diameter at that location.

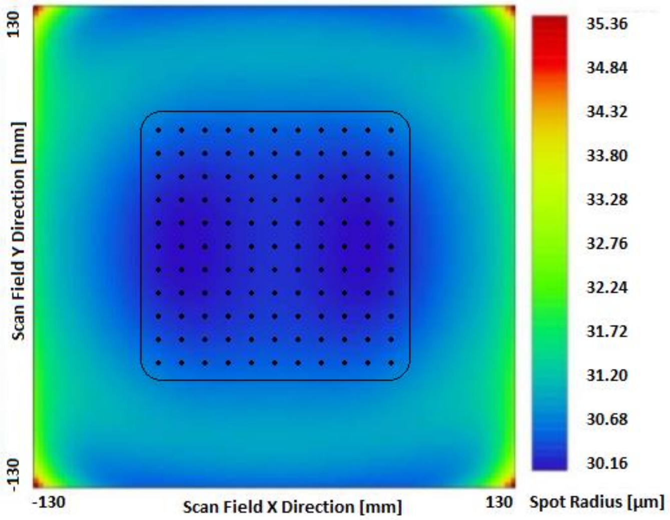

Figure 40: F-Theta distortion map with overlaid build plate and part locations

3.1.2 Plume absorption

An effect commonly neglected in determining the energy density is the disparity between the energy supplied and that which reaches the build plate. The laser beam has a non-zero propagation path length to reach the build. Along this propagation path, the beam energy is being dissipated, reducing the beam power. The dissipation through the chamber can be considered negligible except in the plume region directly above the build plate. In this region, the area is filled with particles ejected from the build surface and due to the vaporisation of powder. These particles give rise to both Mie and Rayleigh scattering due to the particle size continuum ranging from vapour condensate to ejected powder particles [142, 143]. The particles can also absorb some of the energy and cause occluding of the build plate [144]. The plume contains a gradient of these particles and the density of the plume reduces away from the incidence point as can be seen when observing in the AM process, an example of which is taken from Ye et al. and shown in Figure 41.

Figure 41: SLM plume and splatter [145]

The plume radiates from the laser incidence point on the powder in an expanding pattern of reducing concentration [146], leading to a variation in the attenuation conditions in the plume. Shcheglov et al. [146] studied the plume attenuation during laser welding using a 5kW laser. It was found that while the laser used in the SLM process is significantly weaker, the broad shape of the plume is comparable between the two processes. A key finding for the study was a map of the extinction coefficient varying in height and distance from the centre of the laser interaction as seen in Figure 42.

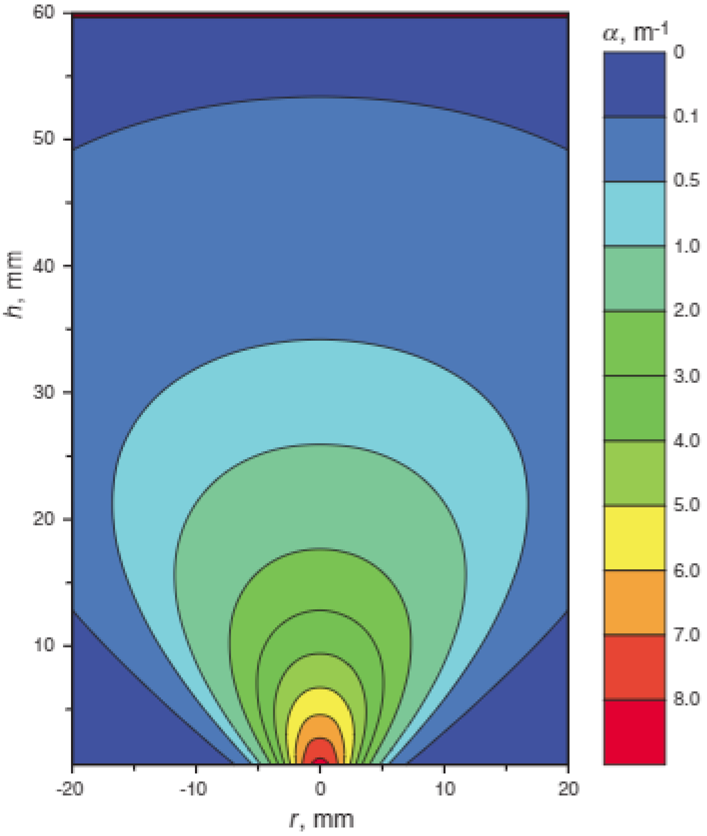

Figure 42: Modelled distribution of extinction coefficient from Shcheglov et al [146]

The extinction coefficient was calculated using the Rayleigh approximation depending on the theory of giving efficiencies for absorption and scattering.

$$Q_{abs} = N\frac{4\pi a}{\lambda} Im\left(\frac{m^2-1}{m^2+2}\right) \tag{8}$$

$$Q_{sca} = N\frac{8\pi^4 a^4}{3\lambda^4}\left|\frac{m^2-1}{m^2+2}\right|^2 \tag{9}$$

Where N is the number of particles, a is the particle diameter, λ is the radiation wavelength and m is the complex refractive index of a particle. The total attenuation of a beam can be calculated following the equation below from Greses et al. [147]

$$E_{attenuation} = P\left(1 - e^{-(\alpha_{sca}+\alpha_{abs})z}\right) \tag{10}$$

Where E is the energy loss factor, P is the power, α_{sca} is the scattering coefficient, α_{abs} is the absorption coefficient and z is the path length. The coefficients of scattering and absorption are related to the efficiencies by multiplying them by the respective cross-section of the particles. As the continuum of particles generated from the laser to powder interaction remains bounded in size by condensate and ejected powder particles. Any increases in the laser power lead to greater vaporisation which increases the recoil pressure and correspondingly increases the amount of ejected material, as described by Khairallah et al. [73]. Thus, the variation between the modelled extinction coefficient from Shcheglov and any laser has a pseudo-direct relationship to the laser power.

As the angle of incidence changes, this lengthens the track of the laser through the plume, provided the plume is not completely bypassed. The height of the plume can be varied by many factors including laser power and strategy. A study into a range of these strategies gave an average plume height of 5mm in an SLM process [148], giving the location of the upper boundary to the plume where the attenuation will be negligible. For an intensity comparable to the SLM process, Hansen et al. [149] calculated an absorption coefficient of 2.7m^{-1} and a scattering coefficient of 0.761 m^{-1} giving an overall extinction coefficient of α =3.46 m^{-1}. This gives a range for the central value of the plume attenuation. Now with scaling for both location and magnitude of the plume absorption a new map for specifically SLM can be created.

The height of the plume can be variable depending on several factors including laser power and scan strategy. A study into a range of these strategies gave an average plume height of 5mm in an SLM process [148]. This value can be used to compute the path length of the laser through this attenuating region to include as the z value in equation (10) for each location. This allows the plume absorption (E) to be calculated directly.

3.1.3 Angled Incidence

The laser beam impinges on the build plate at a variable angle based on the travel path from source to location. The centre of the build plate is directly under the centre of the final focussing lens giving a 90-degree angle of incidence. The remainder of the building envelope has an angle of incidence less than this 90-degree case. This angled incidence creates an elliptical projected area on the build volume from the circular beam. The spot size is elongated parallel to the displacement from the centre, creating the ellipse major axis. The minor axis remains equal to the diameter of the circle at the centre. This can be seen in Figure 43 where identical cylindrical beams create different size spots on a level surface.

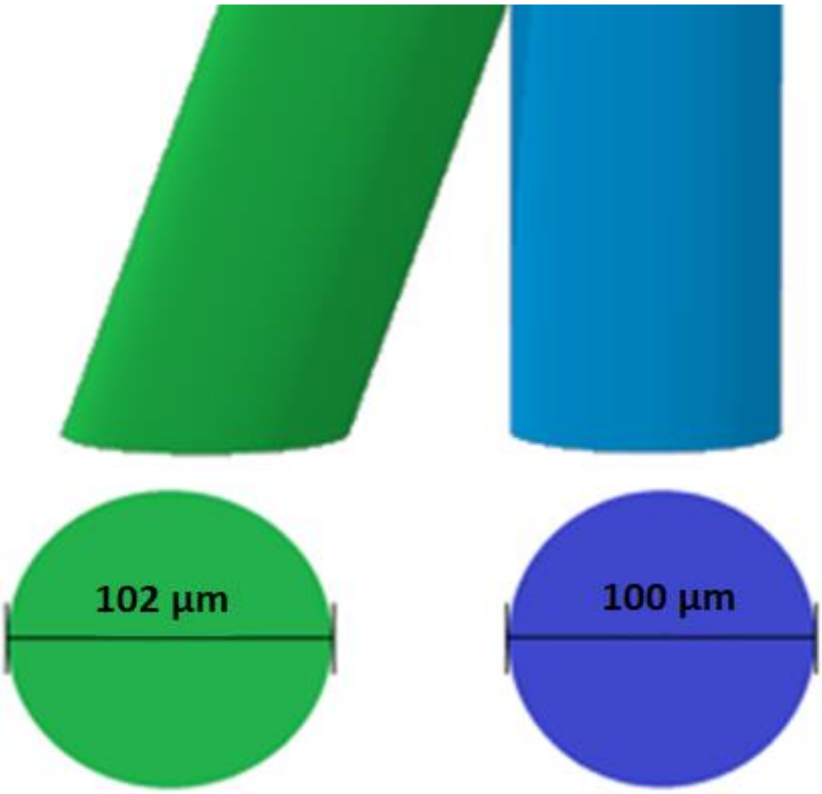

Figure 43: Angled incidence

The equation governing this change in area is as follows for a circular beam;

$$A_{ellipse} = \frac{\pi}{4} D_{minor} D_{major} \tag{11}$$

$$D_{major} = \sqrt{(D_{centre})^2 + (D_{centre} * \tan{(90 - \theta)})^2} \tag{12}$$

$$D_{minor} = D_{centre} \tag{13}$$

$A_{ellipse}$ is the area of the ellipse, D_{major} is the diameter along the major ellipse axis, D_{minor} is the diameter along the minor ellipse axis, D_{centre} is the diameter of the circular beam and θ is the angle of incidence of the beam on the build plate.

Non-circular initial beams become more complicated to calculate as we can no longer construct the ellipse such that the major axis lies is along the line between the centre point and the target point. This will give rise to a variation in both the major and minor axis lengths. The variation can be decomposed into the movement along that axis from the centre, creating a Cartesian axis system along the ellipse. The spot size will then follow the equations 14 and 15, below:

$$D_{major,target} = \sqrt{(D_{major,centre})^2 + \left(D_{major,centre} * \tan\left(90 - tan^{-1}\left(\frac{d}{a}\right)\right)\right)^2} \tag{14}$$

$$D_{minor,target} = \sqrt{(D_{minor,centre})^2 + \left(D_{minor,centre} * \tan\left(90 - tan^{-1}\left(\frac{d}{b}\right)\right)\right)^2} \tag{15}$$

d is the propagation distance, a is the deflection in direction of the major axis and b is the deflection in direction of the minor axis. It is possible to translate the machine Cartesian coordinates to the ellipse Cartesian coordinates by transforming to polar coordinates and adding a correction factor aligning the two Cartesian systems. This allows the angled incidence on the build plate to be accessed for any commonly found beam shape, while also allowing for the beam shape being modified due to other effects such as defocus.

The spot size at any point can be calculated using equations (11), (14) and (15). To calculate the spot at all locations, the major and minor axis at the centre need to be accurately measured. This was measured using an Ophir Photonics SP928 beam profiling camera at the centre of the build plate with results shown in Figure 44. The measurements were taken to give the eccentricity of the beam and its orientation relative to the build plate.

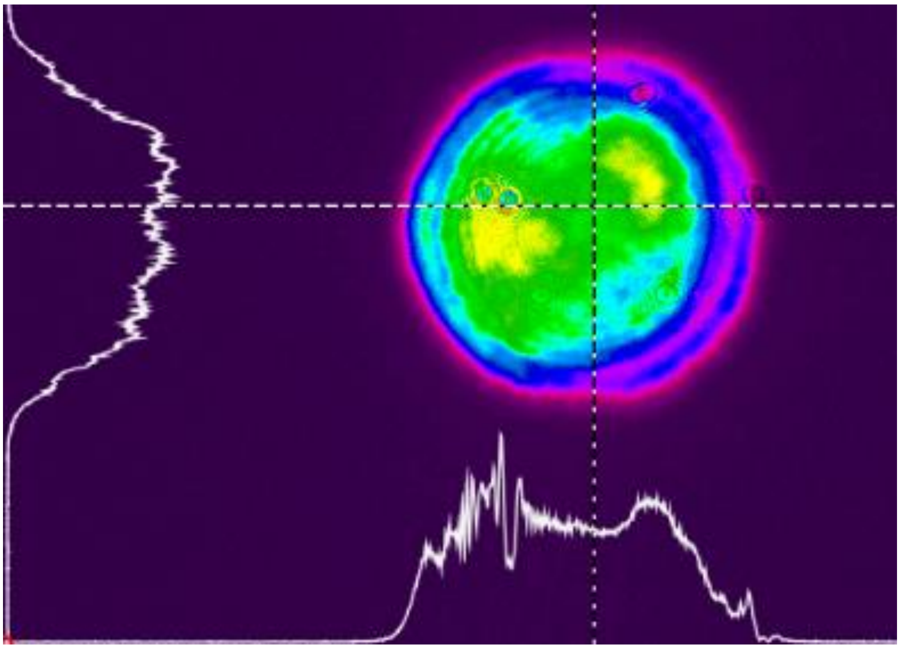

Figure 44: Beam profiler measurements at Centre

	Peak (counts)	D4σ X (µm)	D4σ Y (µm)	Area (µm^2)
Centre	3793	50.05	39.17	6168
Edge	3325	57.85	40.29	7322
Corner	3148	59.67	42.90	8042

Table 6: Beam Measurement Values

Additional measurements were taken with the beam profiler at other locations on the build area. These measurements show that the laser spot follows the theory developed for this angled incidence case. Key values are shown in Table 6. The measurements show that the area that the laser is acting upon increases with distance from the centre, and a corresponding decrease in peak energy was also measured. This peak energy is measured in the form of photon counts per pixel. This is a form of energy density, which supports the theory that has been developed that the energy density is not constant across the build.

The measured spot sizes are graphically shown in Figure 45, showing that initial centre beam is elliptical in nature. This initial elliptical beam creates a greater increase in major axis length than would be expected of a circular beam. The change also shows that the translation directly to the edge of the build plate also primarily acts upon the profile in that direction, as expected.

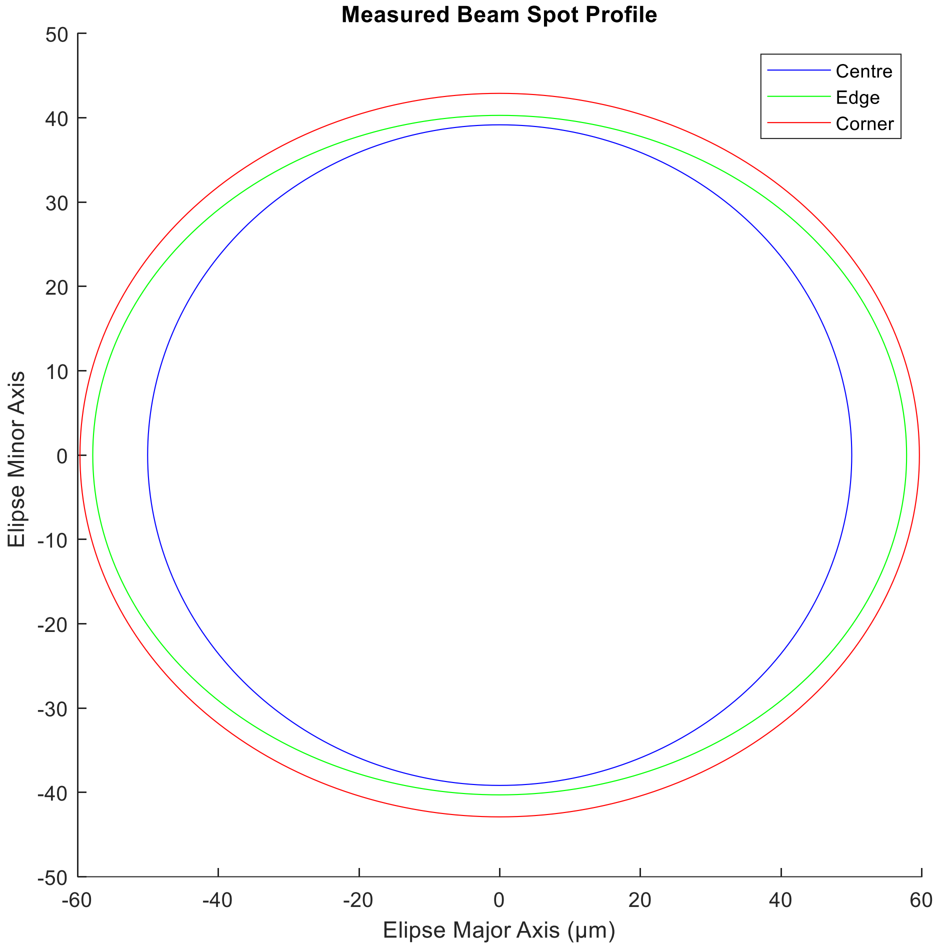

Figure 45: Beam Spot Profile

The measurements had to be taken at 10% of total laser power due to the fragile nature of the beam profilometer, and this was then converted to an equivalent spot size for the full power laser. This was done by multiplying the Gaussian power distribution uniformly across the beam, to reach the same total power available during processing. The equivalent spot size was in line with the previous measurements of the ProX DMP 200 carried out by Francis [150]. The spot size for the beam in the manufacturing configuration was assessed to be 120 µm. A comparison of the two spots is shown in Figure 46.

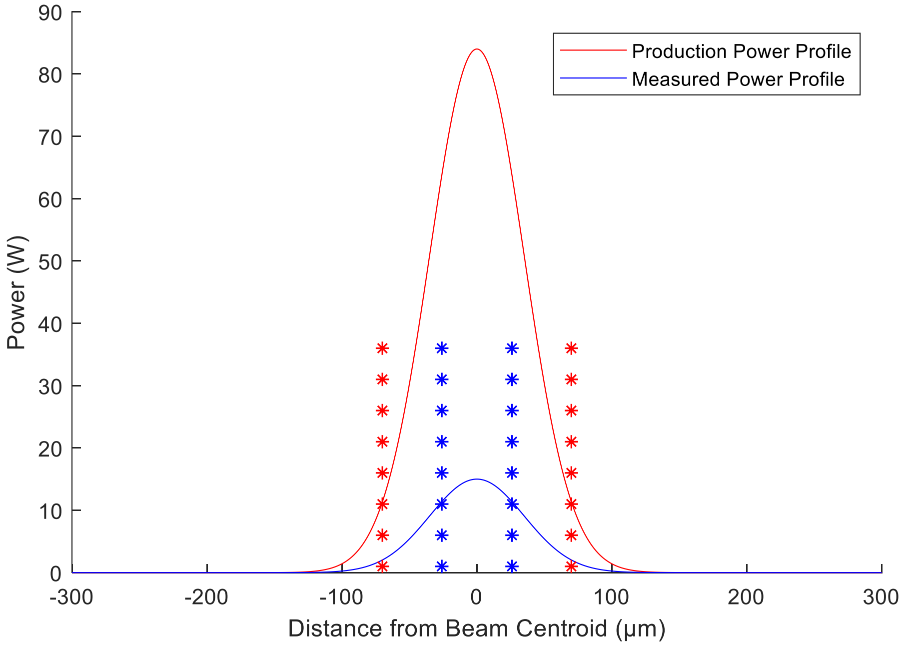

Figure 46: Spot size comparison

The measurements taken from the beam profiler show that the laser spot follows the theory developed for the angled incidence case. The measured values show the initial centre beam is elliptical in nature and its major axis does not lie along the machine coordinates directly. The rotation of the spot size relative to the machine coordinates is minor, but needs to be considered for the accurate calculation of the spot size at all locations of the build plate. This spot size will be used to calculate the diameter of an equivalent circular beam ($D_{b,m}$) at each location to mitigate the effect that alternating scan directions may otherwise have on the equation.

3.1.4 Powder Reflection Efficiency

The change in the angle of the beam impinging on the powder bed can impact the proportion of the beam energy that is directly reflected and absorbed by the powder bed.

This phenomenon occurs due to the change in the incidence of the beam on the individual powder particle. As the angle of incidence becomes lower, a smaller proportion of the beam can penetrate the depth of the powder bed. However, this generalisation does not always hold true in a local case. This can be due to the exact orientation of the powder meaning a lower beam angled beam can be reflected into the bed and be absorbed. The stochastic nature of the powder bed means that the reflection off the bed must also have a stochastic nature.

Reflection is the change in direction of a wavefront at an interface between two different media; in this case, the atmosphere and the metal powder particle. Reflection can be either specular or diffuse and are governed by the law of reflection and Lambert's cosine law respectively [151].

Law of Reflection

$$\theta_i = \theta_r \tag{16}$$

Lambert's Cosine Law

$$I_0 = \frac{I\cos(\theta)\, d\Omega\, dA}{d\Omega_0 \cos(\theta)\, dA_0} \tag{17}$$

Where θ is the angle measured from the normal (perpendicular to the surface), θ_i means the incidence angle, θ_r is the reflected angle, I is the radiance along the normal. $d\Omega$ is the solid angle subtended by the aperture from the viewpoint of the emitting element and dA is the area of the observing aperture, where the subscript 0 denotes the observer being at normal.

Both of these laws have a dependence on the angle of incidence of the beam onto the surface. While it can be stated, that in the global sense, the powder bed exhibits the properties of a diffuse reflector. When closely examining the powder reflection on a specific particle and ray level, the reflection is most accurately described by the law of reflection. This is due to the global powder bed having a rough surface, caused by the particles layered on it. Whereas when observing a specific powder particle, the surface is smooth particularly in the virgin spherical powder as can be seen in the SEM image taken from Fischer et al. [67]

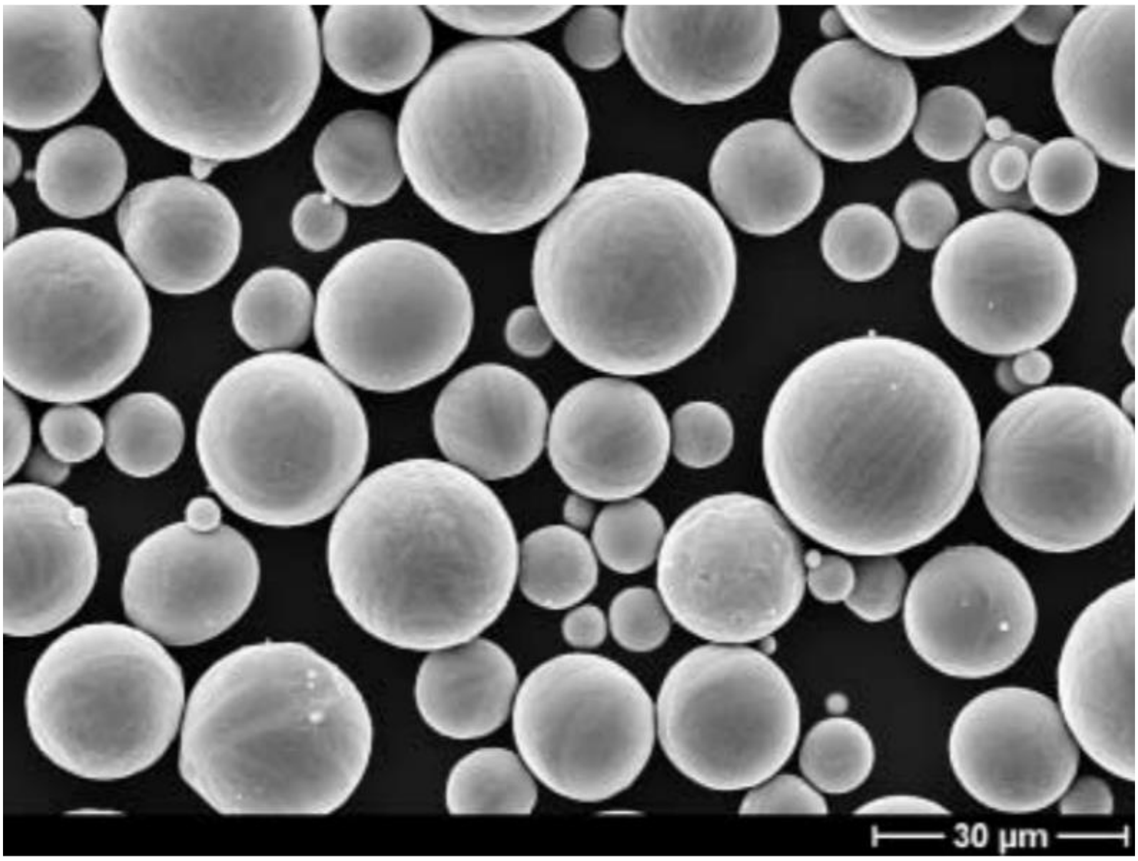

Figure 47: SEM image of virgin feedstock powder taken from Fischer et al. [67]

Irrespective of which reflection regime is observed for the powder bed, the reflectance will be angle dependant. The powder bed is not an impermeable reflective surface and will also have some proportion of energy transmittance into the powder bed bulk. The simplest consideration of transmittance is the proportion of the energy that is not reflected must be absorbed. As a relationship between reflectance and angle of incidence has been established, it must follow that a relationship exists connected the transmittance to the angle of incidence. The angled incidence has already been shown as being a source of variation in the process due to a changing area illuminated on the powder bed. This new transmittance relationship further increases the effect of angled incidence changing the apparent energy density across the build plate.

To determine the effect that the angle of beam propagation has on the absorption of the beam in the powder bed, a simulation of the reflection of a representative beam was created. Then the amount of energy reflected away from the powder bed at that angle was determined.

The reflection of the total beam can be modelled by separating the beam into individual segments. The segments can be computed individually to be able to get the full-beam reflection. The powder cross-section can be approximated as a circle. The normal that the beam is reflecting about is directly along the vector from the powder centre to the point of interaction between the powder and laser. The angle of incidence is measured by the angle between the laser propagation vector and the normal.

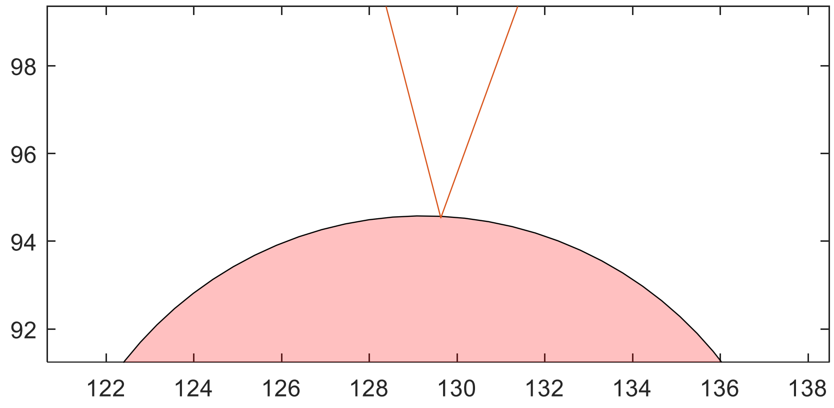

Figure 48: Beam segment reflecting off a powder particle

At each point of interaction, a proportion of the energy from the beam is absorbed. In cases where the beam is reflected away from the build plate, this would have the same absorptivity as a flat plate. In the powder case, however, a certain proportion of the reflections lead to further interactions with other powder particles. This leads to a greater proportion of energy being absorbed than would be expected from a flat plate of the same material. The level of these additional powder interactions is dependent on each reflection and as such also dependent on the initial incident vector of the laser.

There are myriad effects that could further change the absorption of the powder bed with angle. The AM process is inherently dynamic in nature, however a static approach will be used for this analysis. This is to minimise complexity that is beyond the scope of the overall thesis, and this is an obvious area for further research in the future. The static approach taken neglects the thermal effects, such as the temperature change of the particles, has on absorption. The deformation and displacement of the powder particles under the laser will also be omitted to maintain a static analysis.

The boundary conditions at the particle will be the flat plate absorption of the material for the wavelength of the AM system. This in effect will mean that at each laser interaction with the powder the reflected beam shall be weaker than the incident beam. The beam segments will be continue propagating until they have had 10 powder interactions, at which point the beam will be considered completely absorbed. The metric by which different angles will be considered is the proportion of energy that is reflected away from the powder bed relative to the worst performing angle.

This effect will be determined by the condition of the powder bed. Three cases have been analysed: uniform powder size in a close packing configuration; uniform size in a random packing configuration; and normally distributed random size in a random packing configuration. Each powder case is considered at the full angle from 65 degrees to 115 degrees, a range of ±25 degrees from normal incidence. This range was selected as it covers all angles expected in the manufacturing process, beyond the performance constraints of the F-Theta lens technology.

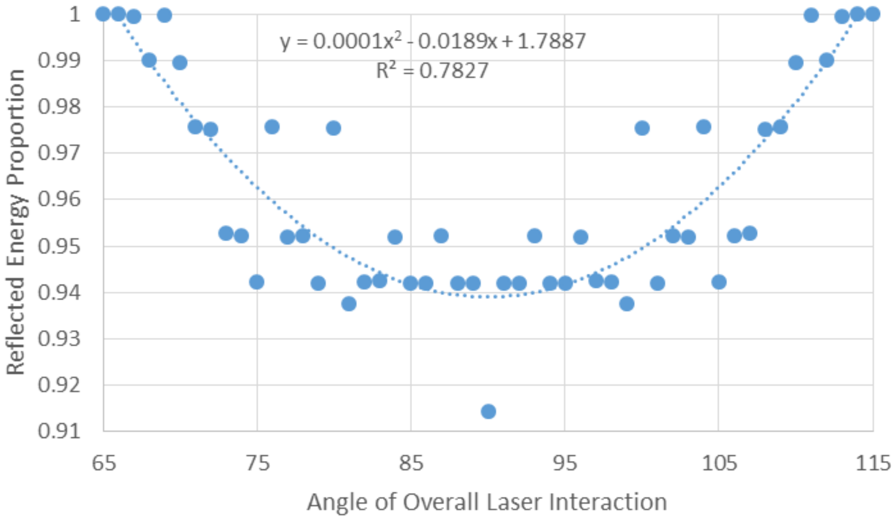

Figure 49: Uniform close-packed powder reflection fitted plot

The close-packed simulation gave a curved fit, and it is evident that there is a clear drop in reflected energy at the 90 degree or normal incidence. This simulation also had the greatest level of reflected energy, with the close-packed nature preventing pores or openings from being present. This, in turn, prevents keyhole absorption of the beam from penetrating deeper into the powder bed for further reflections and absorption. This led to this uniform packing system having 17% higher energy loss than the other simulations.

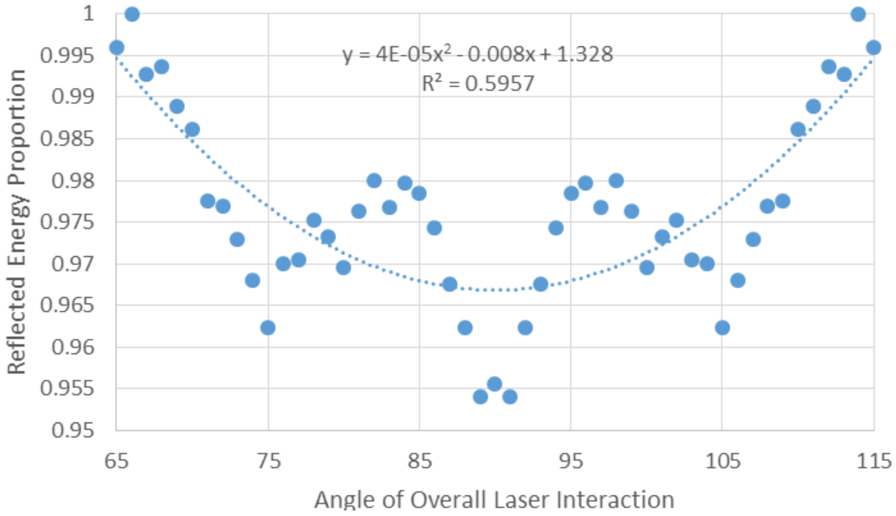

Figure 50: Uniform powder random packing fitted plot

The random packing of uniform particle sizes created a noisier plot. The drop in reflected energy is still evident in the normal incidence case. The level of reflected energy is also reduced in this case. This is due to the greater proportion of gaps in the powder bed, thus allowing the laser to penetrate deeper into the powder bed and greater absorbtion.

The normally distributed powder particles with random packing is the closest to the reality present in the powder bed. The powder bed was generated by constraining the system with a specified box acting as the powder constraint and then creating a series of pseudo-random particles matching the distribution of the real powder to fill the area. This area represents a cross-section of the powder bed with the top of the bounding box shown in Figure 51 being the powder bed surface. The constraint box was created to be deeper than a single layer to allow the freedom for all sized particles to be included. In cases constrained at an actual layer height of 30 µm, it was found that a heavily skewed distribution weighted to the small particles was generated. This was due to random placing of the powder meaning a small particle centrally placed eliminated the possibility of large particles fitting in the area. In the real physical development of the powder bed, large particles moved by the spreading mechanism would displace the small particles. However, in the random creation of virtual particles to fill the space, the new random particle was reduced in size to fit in the available gap. This changing size allowed for a packing density of particles in the simulation to more closely match the real packing density of the powder bed wherein smaller particles would filter into the gaps left by the larger particles. The generated powder cross-section was then treated to remove only a single 30-micron slice for the powder bed. This method of generating the powder bed for reflection also mimics the layering mechanism frequently present in AM systems such as in the ProX DMP 200 that is used for the generation of the physical test pieces. The final histogram distribution of the powder particle size distribution across all the simulated random powder beds is shown in Figure 52.

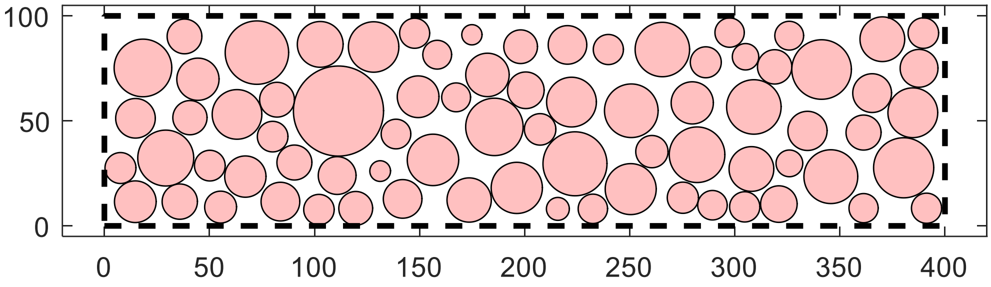

Figure 51: Randomly generated powder bed

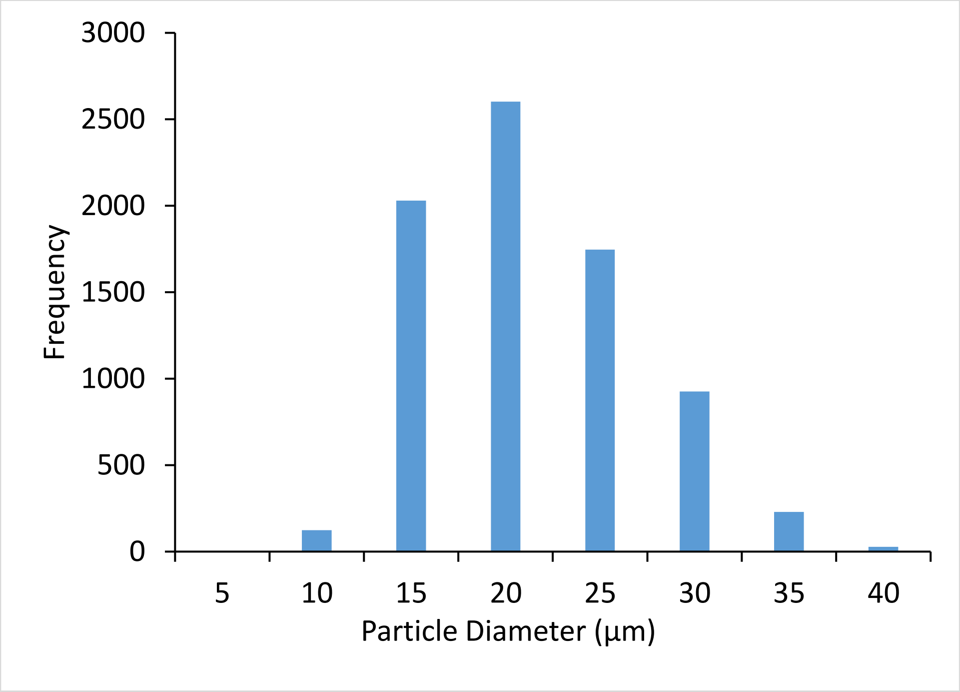

Figure 52: Simulated powder particle size distribution

The simulations were continued with new randomly distributed powder beds until the difference between energy absorbed at the normal and each angle converged. This gave rise to a symmetrical distribution meaning that only the magnitude of the angular difference, not its direction from normal, was critical. The plot of these differences is shown in Figure 53.

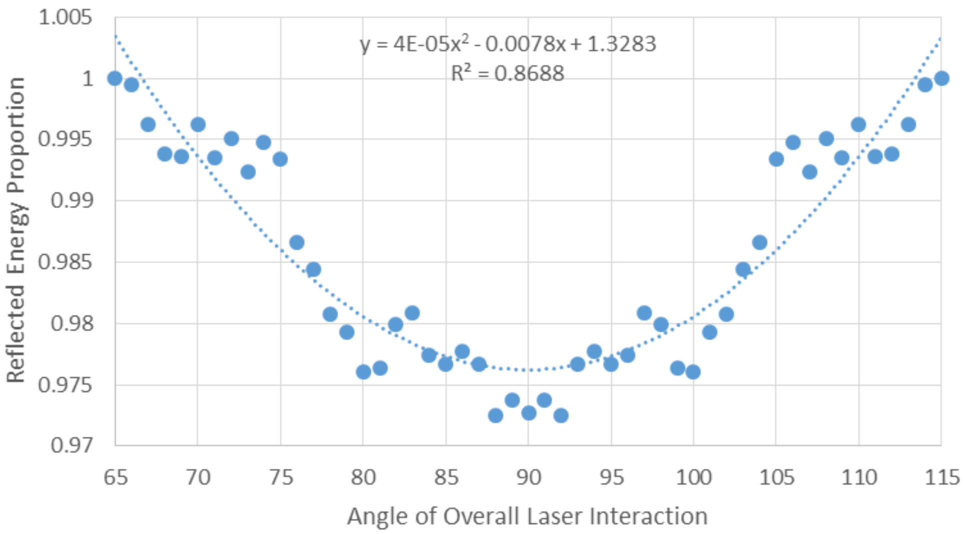

Figure 53: Normally distributed powder random packing fitted plot

This results in a difference in the energy that reaches the build area being absorbed between the centre and edge of the build area of 2.5%. This further magnifies the losses in energy already experienced by the beam propagating to the edge of the build.

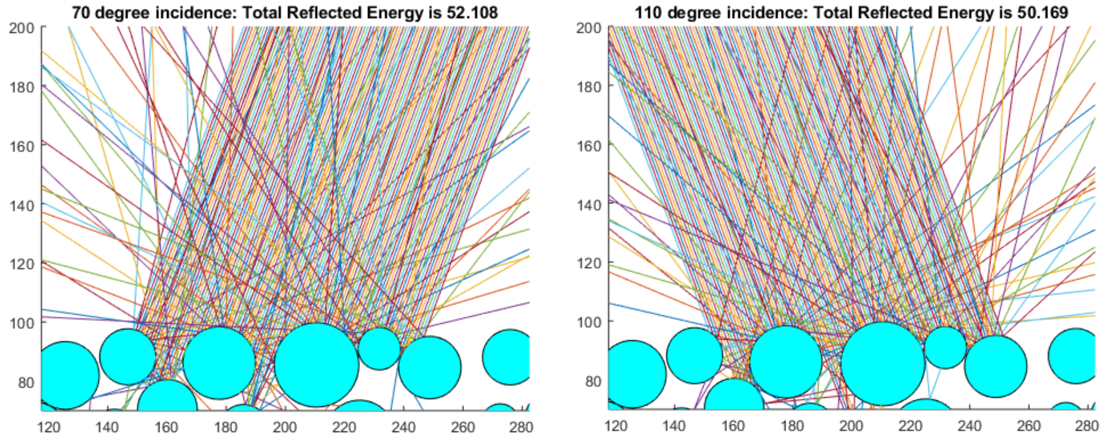

Figure 54: reflecting rays at 20 degrees from normal incidence

Figure 54 shows a pair of sample reflections off a single simulated powder bed at 20 degrees from normal. There is a marked difference in the total reflected energy between the two beams with the 70-degree case reflecting 4% more energy than the 110-degree case. This is mostly due to the effect of the internal reflections within the powder bed. In the 110-degree case, a more significant proportion of the beam can pass beyond the topmost surface of the powder bed and reflect on the 2nd layer of particles. This leads to those reflected rays needing to pass beyond the 1st layer of particles again to escape. This result demonstrates the keyhole absorption effect on a localised scale without the development of macro-pores that are traditionally the cause of keyhole absorption.

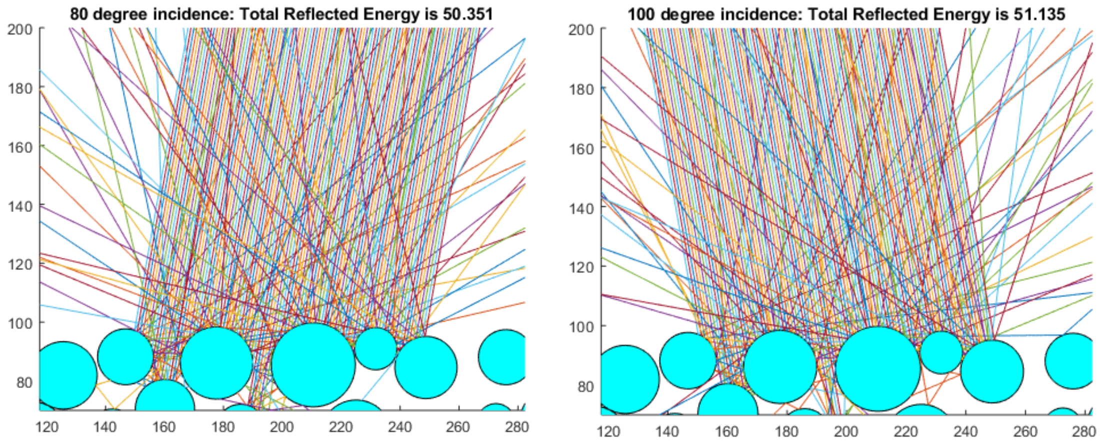

Figure 55: Reflecting rays at 10 degrees from normal incidence

Figure 55 shows the same powder bed but with laser incidence at 10 degrees from normal on both sides. A notable change from the 20-degree case is that in this arrangement, a greater total reflected energy is found on the opposite side of the normal. This is a clear example of the localised uncertainty with powder reflection. The theory would state that the effect should be symmetrical; only be affected by the angle of incidence; and that there would be no side that reflects more or less than any other rotation. This understanding, however, breaks down on a local specific slice. However, on a single scan pass, the laser does not operate on a single prismatic section of the powder bed. Each individual pass would cover an arbitrarily large number of individual powder cross-sections over its full track. This is what necessitates a convergence of a large number of random bed sections for the data on a representative bed to be generated.

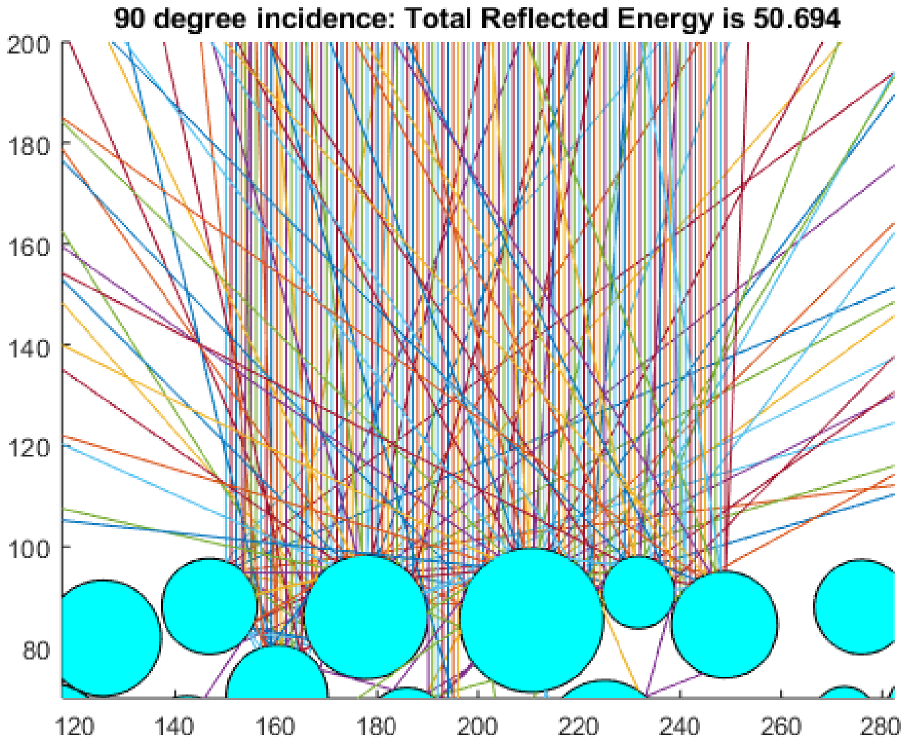

Figure 56: Reflecting rays at normal incidence

At normal incidence, the total reflected energy is lower than found at an angle as seen in Figure 56. This is due to the ease of the laser rays penetrating beyond the first layer of powder, noting that any gap between two powder particles can be entered. This was not the case in the angled rays, as the gap could be shadowed by the adjacent particles, thus preventing the ray capture.

3.2 Modified ED equation

The previous equation determining the Energy Density (ED) does not encapsulate the variation found in the actual process. A new modified ED equation based on equation (5) is proposed which takes account of sources of variation outlined previously as shown below.

$$\psi = \frac{4(P - E)\rho}{\pi\delta D_{b,m} v} \tag{18}$$

The sources of variation included are the distortion coefficient (δ), attenuation of the beam (E), powder bed reflectivity (ρ) and $D_{b,m}$ is the diameter of an equivalent circular beam at that location. This enables the ED to be calculated at any location and removes the scan direction dependence previously present in the t_i term of equation (5) which occurs in non-circular beams.

This equation, while improved over the non-modified version, still has a number of simplifications present. The first simplification taken is to assume that the build surface is perfectly uniform. As discussed previously, a real powder bed surface can have significant variation due to the inherent property of it comprising of packed powder particles. The nature of a packed powder gives a non-zero surface roughness, pits or voids in the surface and heterogeneous properties. These heterogeneous properties can also vary between powder deposited on virgin powder and that deposited on previously melted layers. These variations are complex, stochastic in nature and can dependant on the process history.

To account for the powder variations in the build plate, an active control mechanism is required. This necessitates the accurate characterisation of the powder bed during a layer and compensating dynamically. The active requirement would add an extra level of complexity to the model and require a calculation to be run during each layer. By simplifying the powder surface to a perfectly uniform representative bed, we neglect the local effects created by the rough powder bed at that location. These effects include the formation of an angular keyhole feature or other energy trapping effects. Most importantly, the simplification allows for the neglecting of process history in the build to give a more universal solution for all builds, not just the specific test case.

The second simplification is that the control of the system prior to entering the build volume is constant. This is to include the laser being steady-state with no variation in power, the scanning galvomirrors operating at the programmed speed independent of build location, and no other sources of variation across the build volume other than those specified in the equation. This is a major simplification of the process that we know to have other sources of variation as discussed in chapter 2.2 Pre-Process Effects. These factors include issues such as the accuracy of focusing of the beam, build-up of particles on the lens and inherent power fluctuations in the laser system. These variations, however, should be homogeneous across the build area and result in an effectively uniform migration of the expected energy density. This migration could move parts or all the process away from the optimised plateau of operation discussed previously.

The third assumption that must be made is that the macro geometry of the part is not important, and that each laser powder interaction is an independent event uninfluenced by previous or future scans. This simplification is required for the global application of the new system. If macro-geometry is to be considered then all possible geometric features would need to be considered for their effects which would be unwieldy at best and impossible at worse. The need for each interaction to be independent is a more practical consideration. The communication between powder particles by thermal transmission or remelting is beyond the scope of a generalised equation, be it the currently adopted ED equations or the new proposed equation.

The next stage in improving the process would be to evaluate this equation over the full build area. This is done by discretising the build area to allow for the calculation of the ED at each point. The build plate was separated into a grid with a mesh size of 1mm. This discretisation was chosen as it provides higher resolution ED maps than are required for the majority of parts. In addition, it is at the limit of the resolution available for the quantification of the F-Theta distortion from the manufacturers' specification. The new modified ED equation is to be calculated at each point on the mesh following the inputs of the sources of variation present in the process.

3.3 Evaluation of the ED equation over the build volume

The first step of the simulation evaluation is to run without any of the sources of variation included in the modified equation. At each subsequent step of the evaluation, an additional source of variation is changed from a constant to a variable based on distance. This allows for comparisons between the sources of variation to be made and ensure that each is independent of each other in the final result. Evaluating the modified equation where each of the sources of variation is constant gives rise to a flat energy density mesh as seen in Figure 57. The normalised ED mesh is completely flat with a value of 1 for all positions on the build platform. This is due to the base ED without any sources of variation not containing any information or dependency on distance from the centre of the build plate. In effect, this is the energy density map that would be expected from both the commonly used energy density equations (equations (1) and (2)). The complete lack of variation is contrary to what has previously been discussed but gives a baseline to make all future comparisons against.

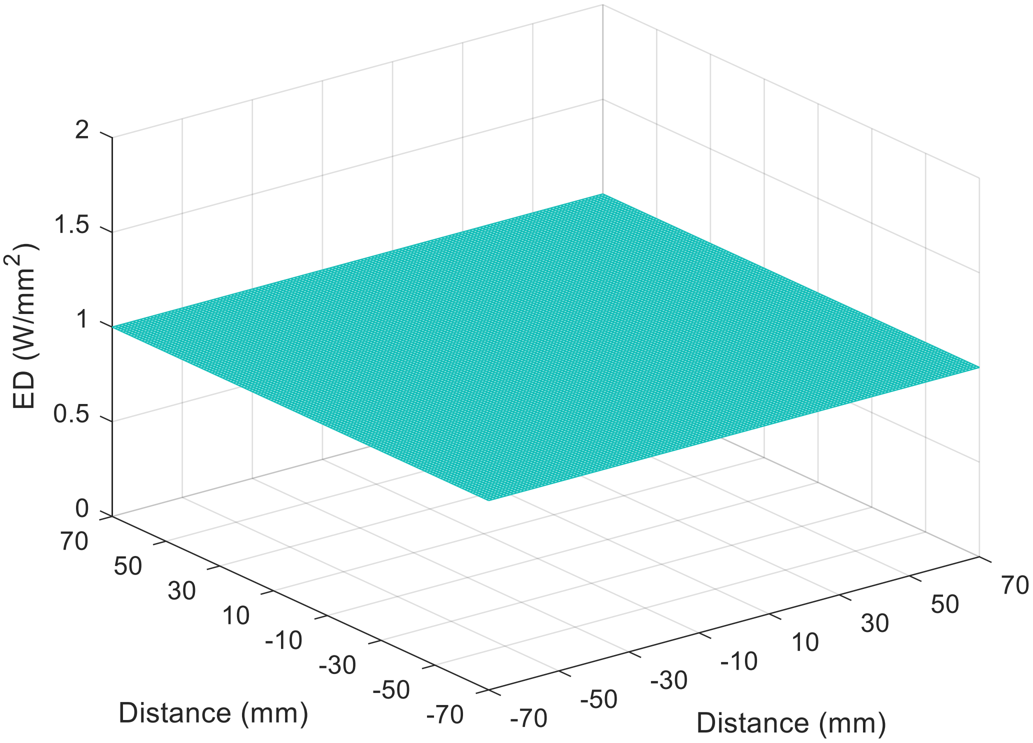

Figure 57: No sources of variation included

Next, the angled incidence values were set to be variable, with the evaluation of this input set creating the mesh seen in Figure 58. This evaluation of the equation now shows a varying ED depending on the location on the build plate. The relationship gives a smooth and domed ED mesh. The angular change of incidence and its direct trigonometric relationship to energy density leads to an accelerating decrease in ED at the edge and corners of the build area. Without any other sources of variation, the angled incidence produces a 2.5% difference in ED between the centre and corner of the build area. This change is minor due to the relatively long propagation distance compared to deflection from the centre. The maximum deflection angle from normal incidence is only 18°.

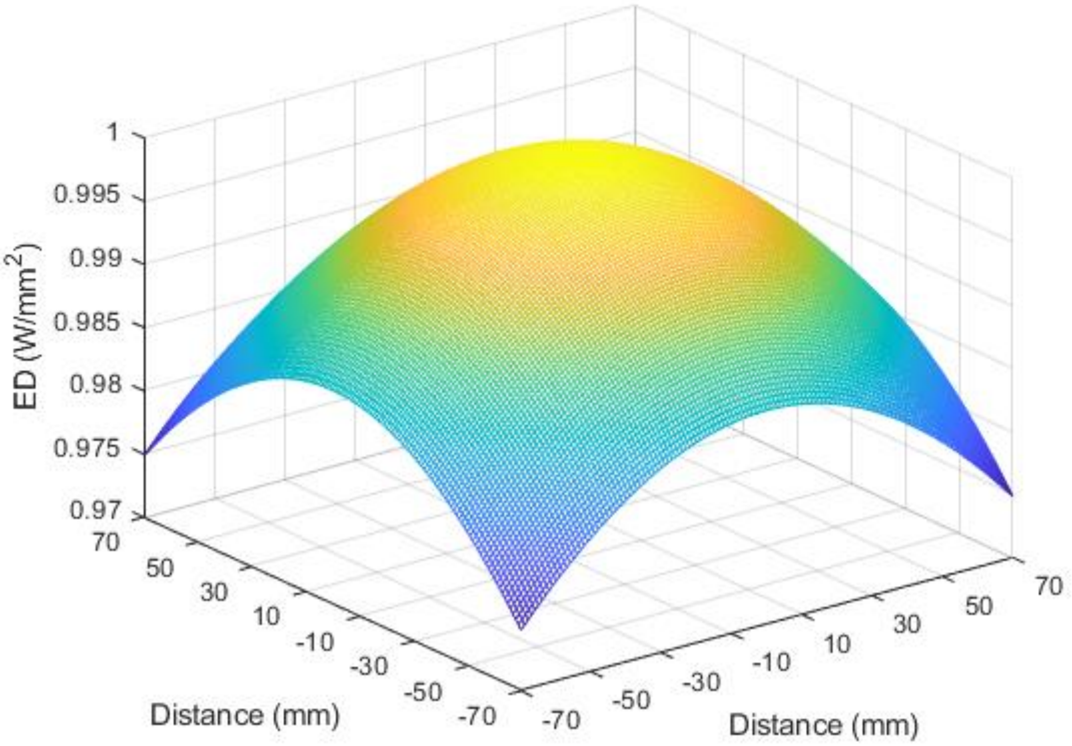

Figure 58: Angled incidence on build plate included

The mesh shown in Figure 59 has both the angled incidence and F-Theta distortion included. This mesh is no longer smooth, predominately due to the pixelated nature of the distortion plot provided by the F-Theta specification which was seen in Figure 39. The F-Theta distortion also acts by increasing the laser spot size, which directly compounds upon the dilation of the spot caused by the angled incidence. In this evaluation of the equation, the build plate is positioned in the centre of the F-Theta distortion plot in a predominantly stable area. In cases with a larger build plate or greater angle required to reach the corners, the distortion would provide a significantly greater reduction in ED at the corners. In the current machine configuration operating under the manufacturers' specifications, the predicted ED difference between the centre and edge is 5.2%. There is a non-negligible difference however between the x-direction and y-direction from the centre. At the current level, the difference is 0.4% at the edge of the build area, which at this stage is a tenth of the total difference from the centre.

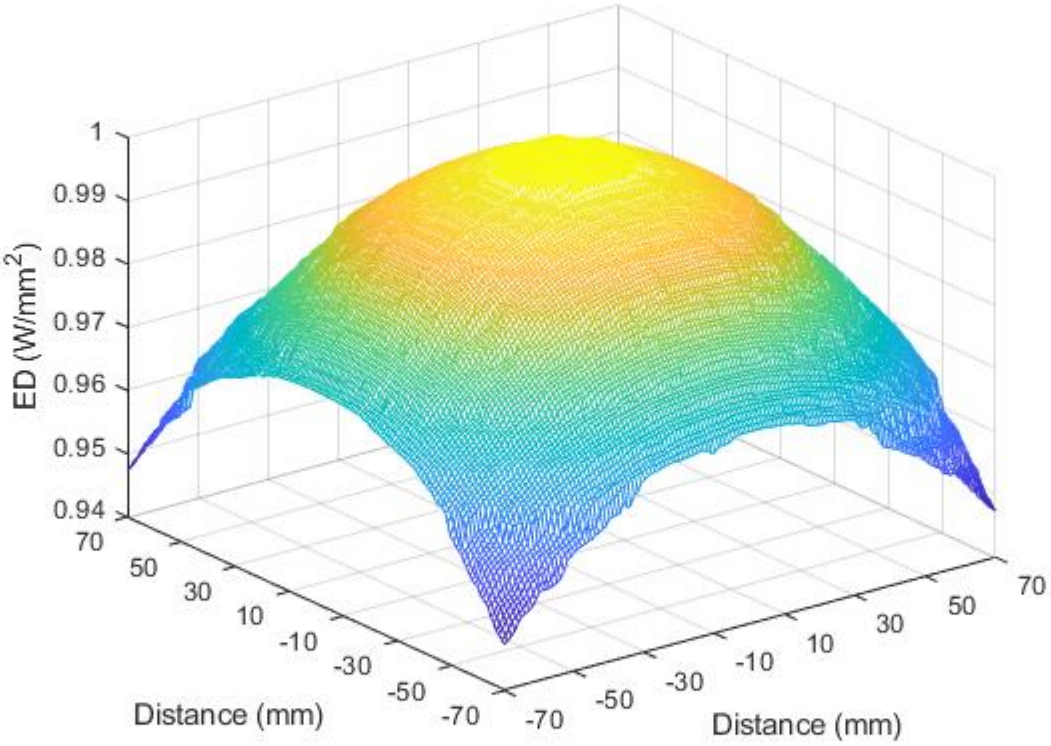

Figure 59: Angled incidence and F-Theta distortion included

The addition of plume absorption in Figure 60 dramatically changes the location of the ED mesh, and for the first time the ED at the centre is no longer normalised to 1. This is due to plume absorption being present at all locations in varying amounts. The angle the laser passes through the plume is not sufficient to bypass the plume at the edge of the build plate, which would lead to a rapid increase in ED, leaving again a difference of ED of 0.045 which translates into a 5.4% difference between centre and corner.

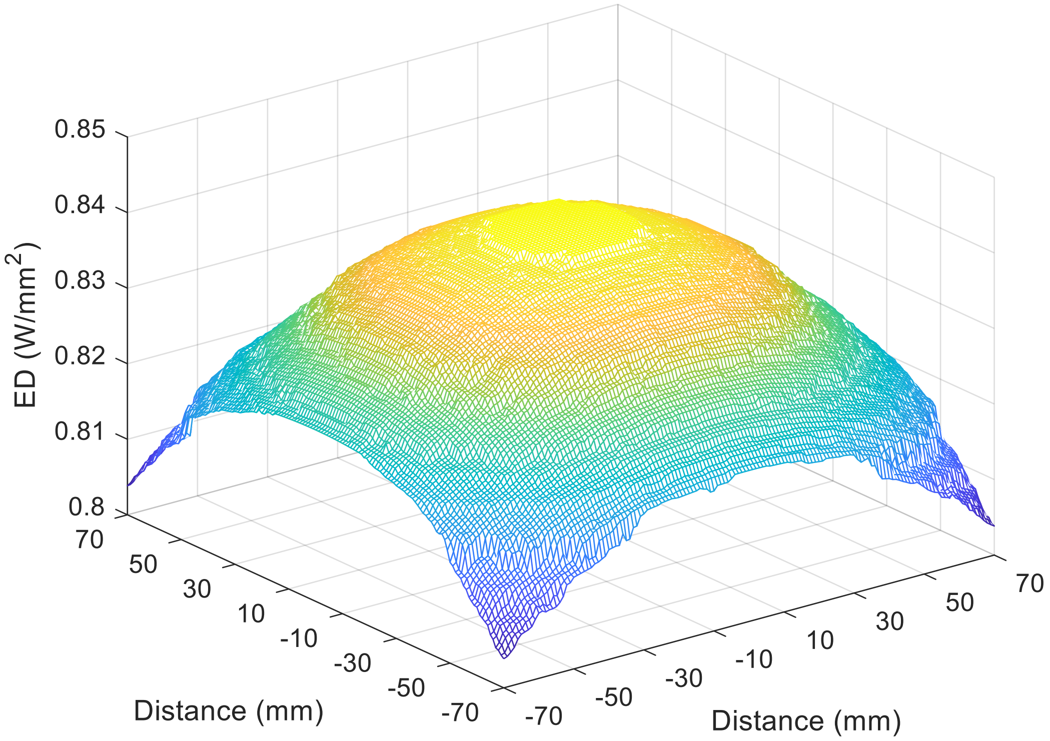

Figure 60: Angled incidence, F-Theta distortion and Plume absorption included

The further reduction in the energy being absorbed by the powder bed caused by the greater reflection efficiency at the greater incidence angles gives us the mesh shown in Figure 61. This final addition amplifies the magnitude of the ED drops from the centre to the corner to an absolute difference of 5.7% on the normalised scale. The more accurate comparison is a difference in actual energy reaching the powder bed of 6.8% between the centre and edge locations. This is a very significant drop and could easily lead to the energy density migrating below the optimal energy density for the production of good quality parts.

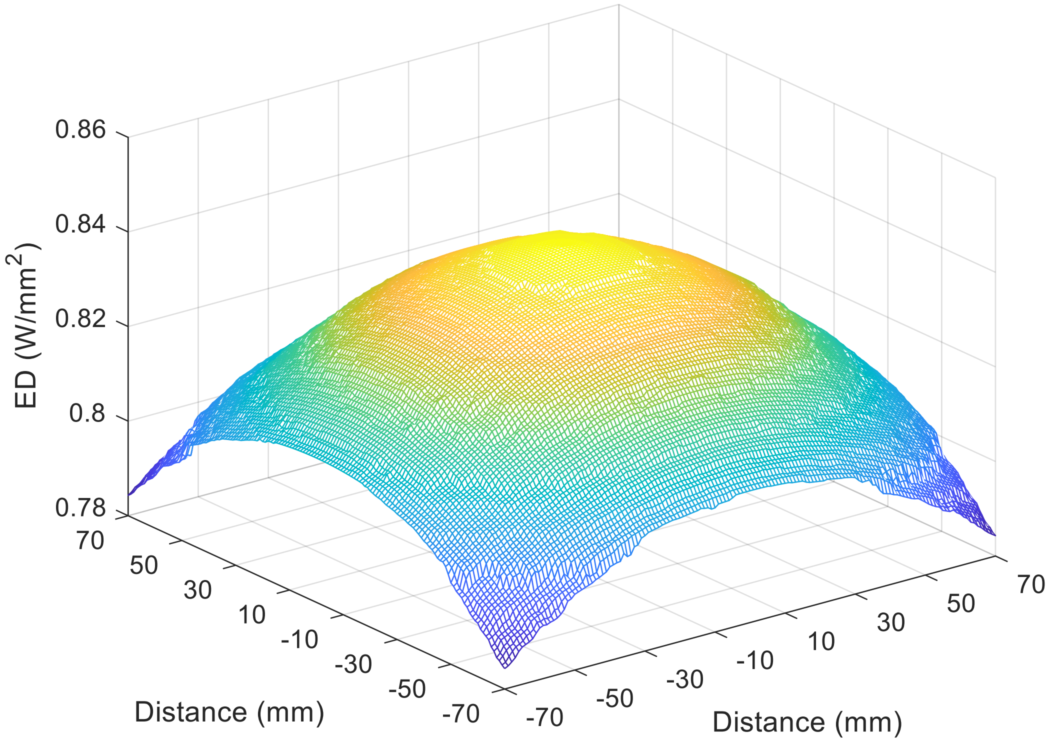

Figure 61: Angled incidence, F-Theta distortion, Plume absorption and powder reflection included

The four different cases and the baseline simulated are shown in Figure 62, and some key values from the simulations are shown in Table 7. These clearly show the large contrast between the newly proposed ED equation and the previously widely adopted ED equation. The large discrepancy between the two ED equations is easily enough to transition from the plateau of optimum processing to a suboptimal condition.

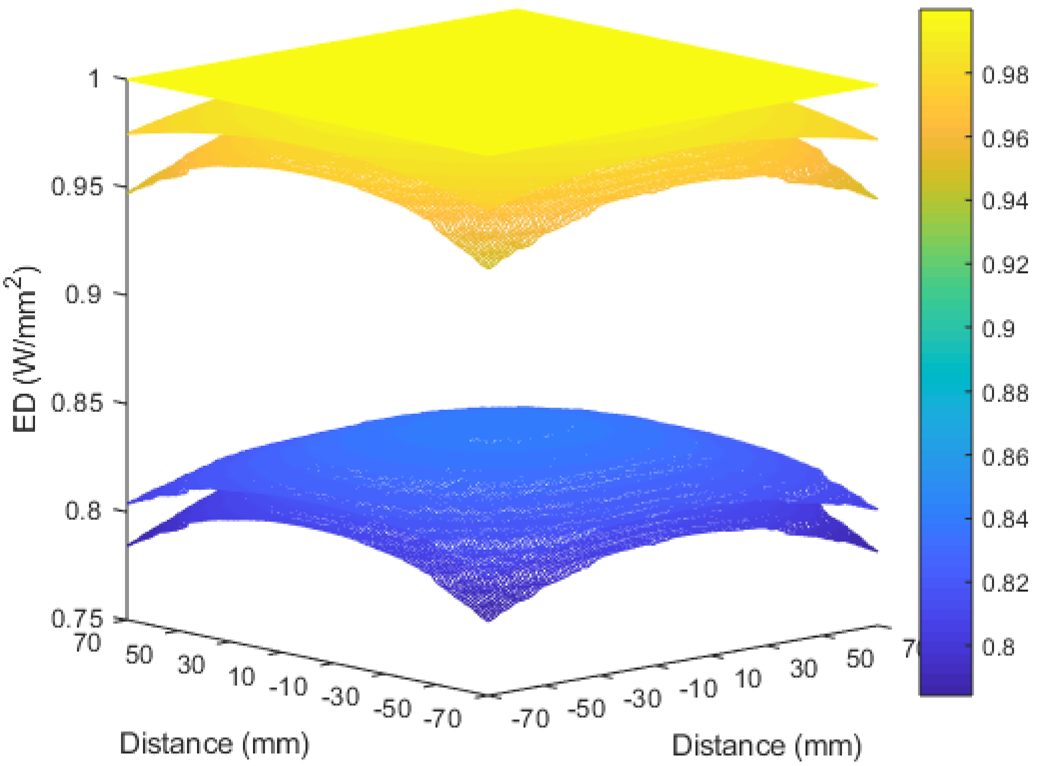

Figure 62: All meshes simultaneously

	Case (1)	**Case (2)**	**Case (3)**	**Case (4)**	**Case (5)**
Centre	1.0000	1.0000	1.0000	0.8411	0.8411
Edge	1.0000	0.9869	0.9663	0.8200	0.8079
Corner	1.0000	0.9748	0.9462	0.8038	0.7843

Table 7: Normalised ED for locations and cases

The spot size variation is also of direct interest due to its impact on the quantity of each scan that overlaps with previous scans. It also could be of interest when creating parts that are close in size to the spot size as the variation between the spot size at the centre and the spot size at the edges could directly impact the geometric repeatability. This is illustrated in Figure 63 where it can be seen that the spot is 11 µm larger at the furthest from the centre of the build area, representing an increase of 9%.

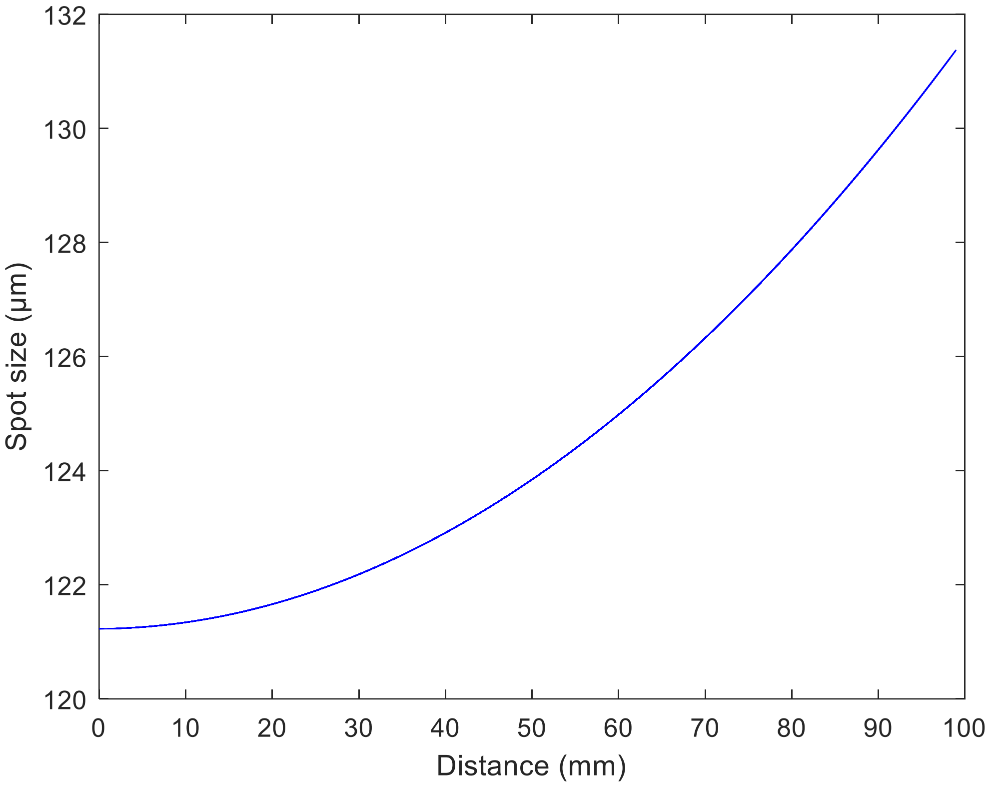

Figure 63: Laser spot size against distance from the centre

The simulation was repeated 6 times as a sensitivity analysis. This was done to determine if the order the variations are applied to the evaluating script affected the output. Theoretically, this would not be the case. The check eliminated the possibility of potential errors in the theory or coding that would introduce a dependency that was not obvious. The output of the evaluating script was found to be consistent with less than 0.01% variation, independent of the ordering that the sources of variation were applied.

The evaluating script was also run with variations of the fineness of the mesh from 0.1mm increments to 10mm increments, these are shown in Figure 64.

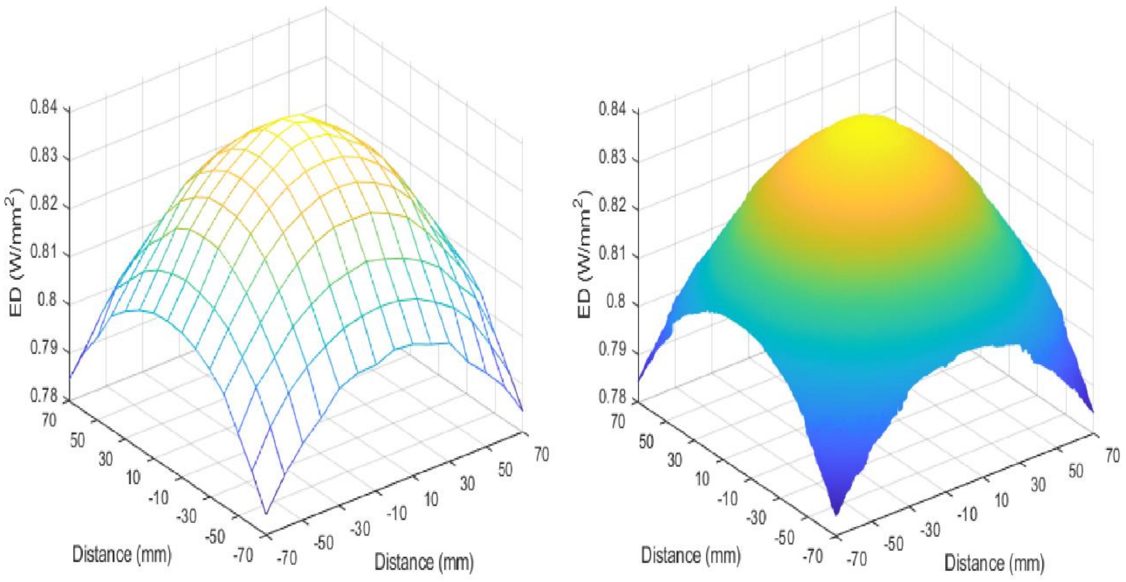

Figure 64: Mesh Fineness study

The larger-scale simulations resulted in an angular approximation of the domed characteristic feature apparent in the other simulation results. This angular approximation is wholly below the meshes of the finer resolution simulations leading to under evaluation of the theoretical ED at those interpolated points. In addition, interpolating loses a certain amount of the known variation found in the process caused non-linearly between these points. The finer mesh was found to not result in any improvement in the resolution of the ED map. Rather, it was found that at this level the dome became more sensitive to input step changes on the small scale. This is due to the discrete nature of the F-Theta distortion map limiting any simulation to its input resolution.

The overall results of the simulations, however, did not change with this difference in meshing. A consistent drop in energy density at the edges and corners compared to the central region was found in all mesh sizing.

The new ED equation is now validated against the theory and a useful understanding of the variation within the build envelope of a specific machine has been analysed. This evaluation is in effect a model of the ED present in the actual process.

Chapter 4: Experimental Methodology

The experimental method for the overall experiments is laid out in this chapter. This will include the specification of the sample geometries and the number of samples produced. The control system present in the tested machine configuration is laid out and the control parameter for any systematic changes is determined. A brief outline of the statistical methodology that will be used is also included in this chapter.

4.1 Geometric Samples

Many benchmarks have been proposed for quantifying the geometric accuracy of an AM system. These benchmarks are unsuitable for use in this case due to their size constraints, all the benchmarks found in the literature review were found to be for whole build plate comparisons. While the benchmarks found are comprehensive and cover a large range of geometric features to allow a thorough comparison of machines to be made, they are not sufficiently small to provide the localised information required for in build repeatability investigation. To provide this local information, a newly designed structure was created which met these size and location requirements, this structure is shown in Figure 65 and its engineering drawing is included in 9.2 Engineering Drawings.

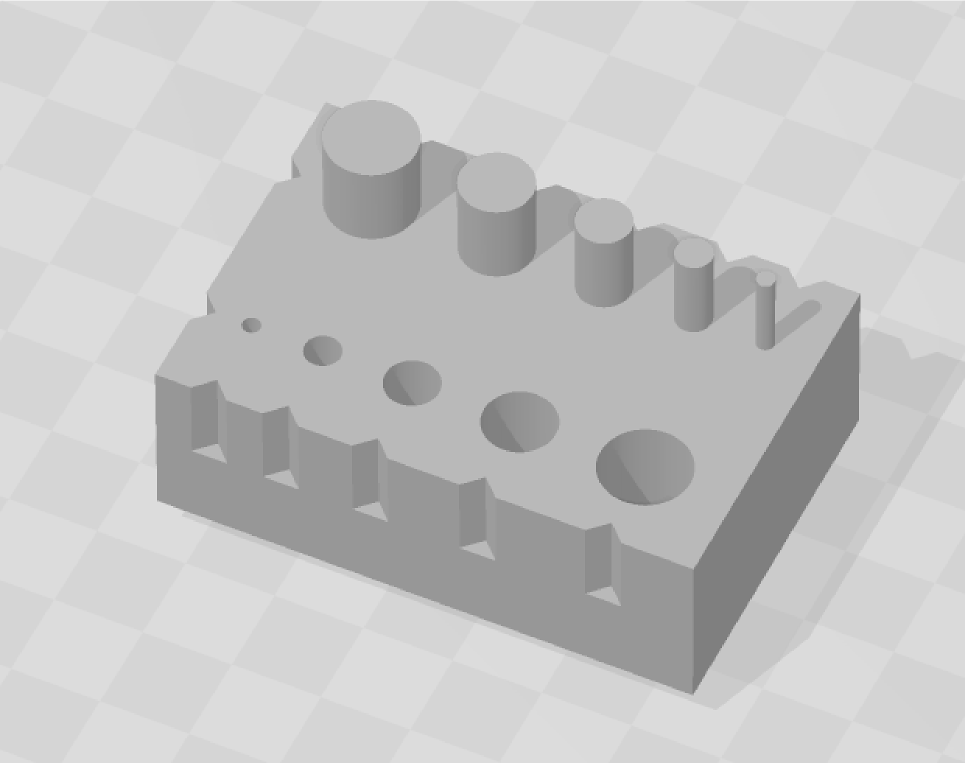

Figure 65: Geometric Benchmark Design

The sample has a total bounding volume of 6mm x 4mm x 4 mm. The key geometric features are 2 mm high pins that increase in diameter by 0.2mm increments from 0.2mm to 1mm. The holes are through-holes of corresponding sizes. Additional index indents are included along the perimeter of the sample to allow for tracking of features that are incomplete or failed. The small size of the sample allows for it to be produced in the same locations used for the mechanical properties, again giving full plate coverage and sufficient spacing to prevent interaction between individual samples.

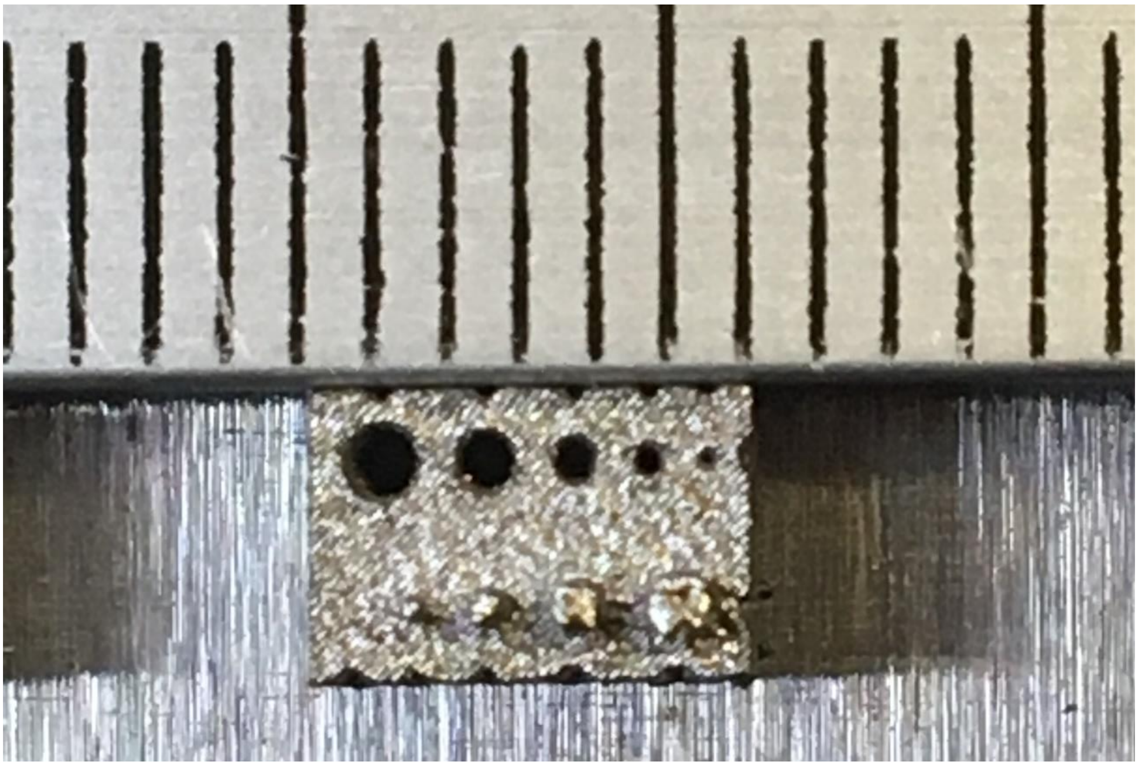

Figure 66: Geometric sample image

The samples were kept on the build plate without further processing to prevent any deformation of the geometric samples due to the removal process. The samples were imaged with a 12 Megapixel digital camera. The images included a graduated scale as seen in Figure 66. This scale allowed direct measurement by calibrating the pixel measurements with the included scale.

4.2 Mechanical Samples

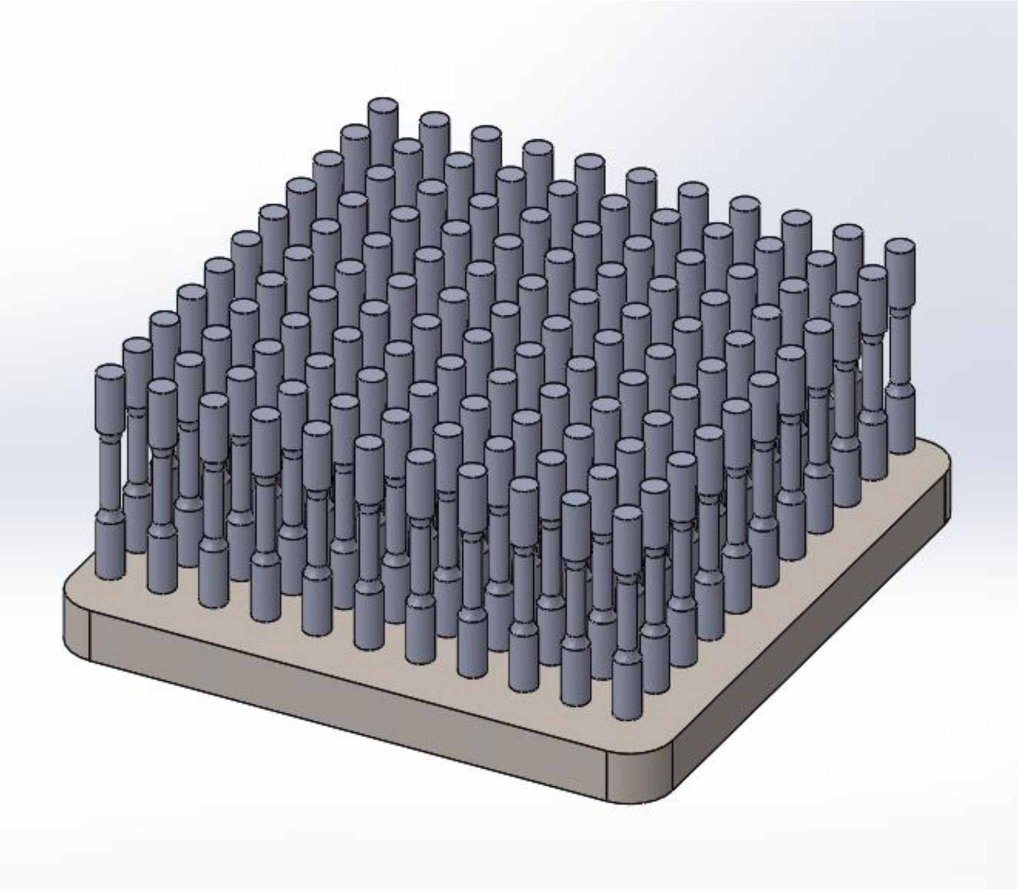

Figure 67: Mechanical samples layout

The samples created for mechanical properties testing match the standard outlined in ASTM E8 - Standard Test Methods for Tension Testing of Metallic Materials [152]. An experimental artefact was designed comprising 121 samples arranged in an 11x11 grid, giving full plate coverage with sufficient spacing to prevent any interaction between parts as shown in Figure 67. The specimens were given a 5mm spacing between each in both x and y directions. After printing, the samples were clearly labelled and then isolated from the build plate by wire EDM and left in the as-built condition without any heat treatment. For this first build, all samples were fabricated using the manufacturer’s specified parameter set. This consisted of a scan speed of 2500mm/s, laser power of 218 W, a layer thickness of 30 µm and hatch spacing of 40 µm. The samples were tested using an Instron 8801 following the ASTM E8 standards.

4.3 ProX System

4.3.1 Process Parameters

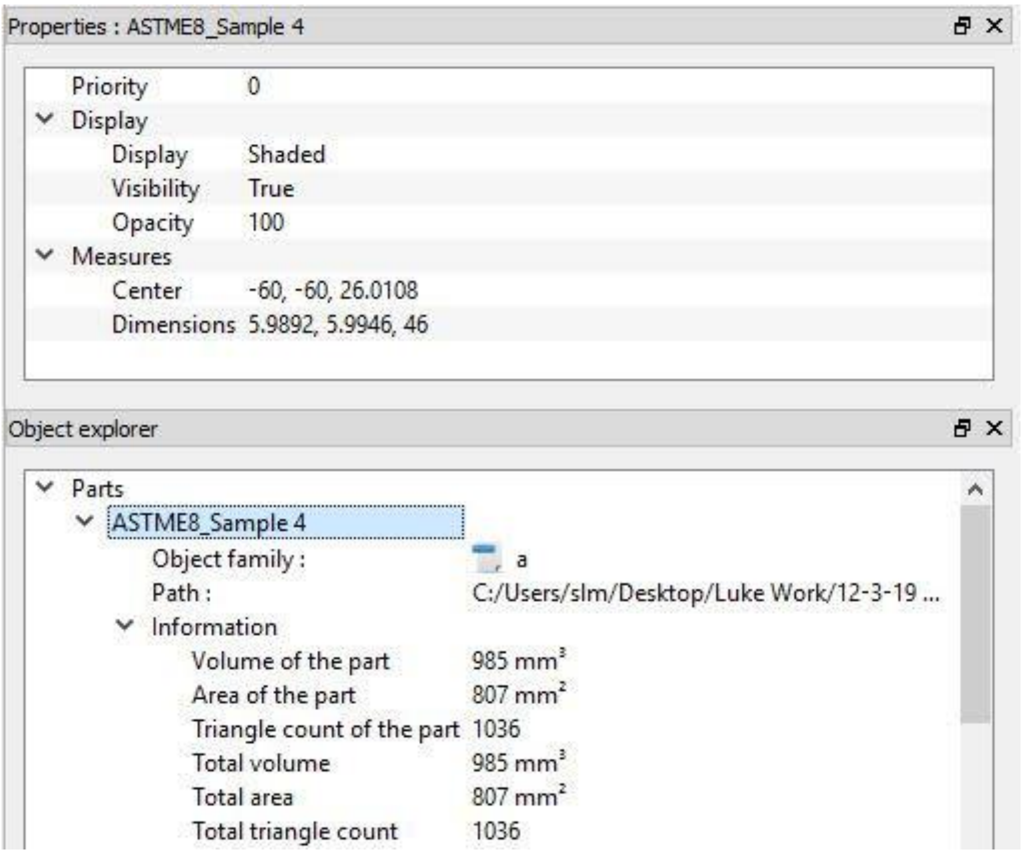

Properties : ASTME8_Sample 4

Priority	0
Display	
Display	Shaded
Visibility	True
Opacity	100
Measures	
Center	-60, -60, 26.0108
Dimensions	5.9892, 5.9946, 46

Object explorer

Parts	
ASTME8_Sample 4	
Object family :	a
Path :	C:/Users/slm/Desktop/Luke Work/12-3-19 ...
Information	
Volume of the part	985 mm^3
Area of the part	807 mm^2
Triangle count of the part	1036
Total volume	985 mm^3
Total area	807 mm^2
Total triangle count	1036

Figure 68: Part properties

The part properties for a print are readily available to review in the preparation software as can be seen in Figure 68, this includes the part location relative to the origin at the centre of the plate. The display settings are how the part is displayed by the preparation software (DMP ProX Manufacturing). These measures give the location of the part centre in the machine coordinates. The machine coordinates have an origin point at the centroid of the build plate with the z-component zeroed on the surface of the build plate. Total volume is the volume of melted powder that will be required to form the part. Total area refers to the parts surface area. Total triangle count is the number of triangles used by the .stl mesh to describe the part features. All totals include any additional support material that has been added to the part, such as a grid to raise the part off the build plate or to support overhangs to prevent sagging or poor surface quality.

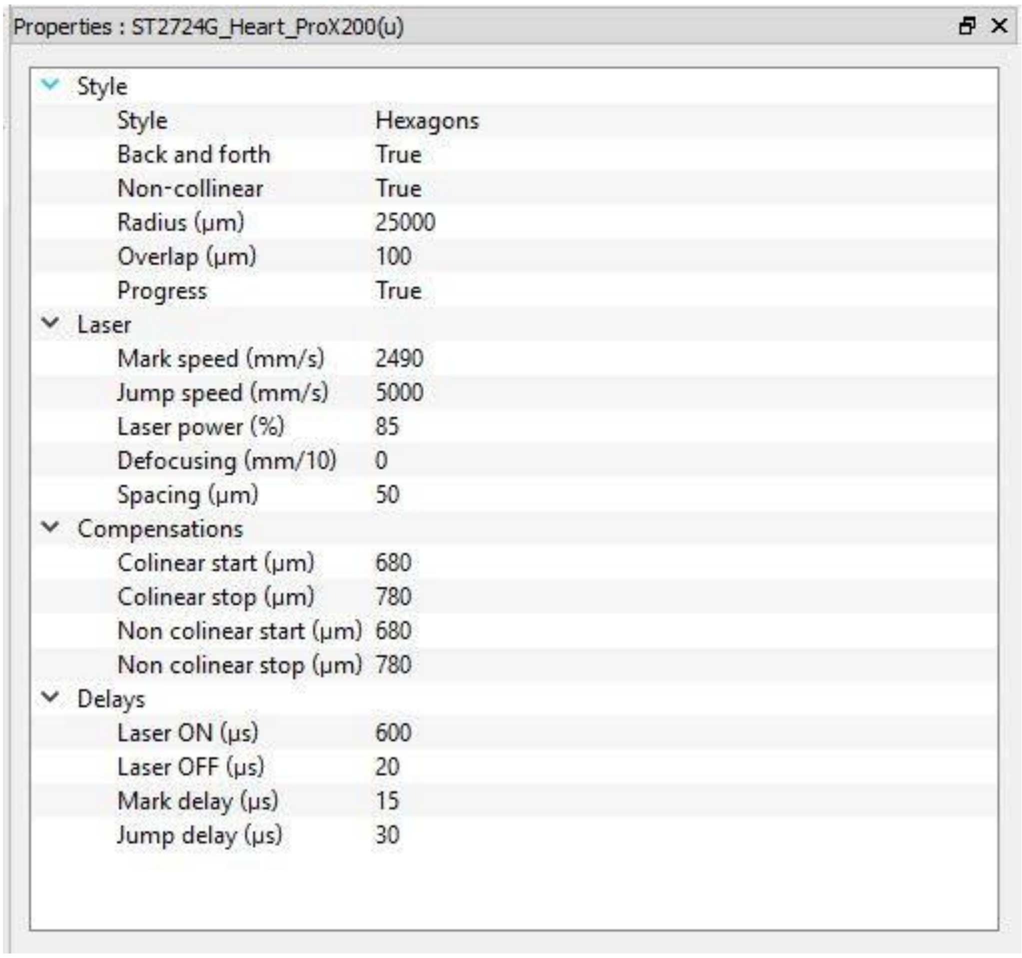

Properties : ST2724G_Heart_ProX200(u)

Style	
Style	Hexagons
Back and forth	True
Non-collinear	True
Radius (µm)	25000
Overlap (µm)	100
Progress	True
Laser	
Mark speed (mm/s)	2490
Jump speed (mm/s)	5000
Laser power (%)	85
Defocusing (mm/10)	0
Spacing (µm)	50
Compensations	
Colinear start (µm)	680
Colinear stop (µm)	780
Non colinear start (µm)	680
Non colinear stop (µm)	780
Delays	
Laser ON (µs)	600
Laser OFF (µs)	20
Mark delay (µs)	15
Jump delay (µs)	30

Figure 69: Laser settings

The laser settings are broken into scan style (or strategy) and laser parameters seen in Figure 69. The scan strategies include options of hexagons, contour, mesh and reinforced mesh. The hexagons strategy separate the scans passes which form a monolithic part into hexagons of a defined dimension. This is to limit the length of each individual scan. Adjacent hexagons overlap to prevent disconnects from being created internally to the part. Contour scan strategy creates scan paths parallel and inside the outer contour of the part. Mesh combines the contour of the outer surface with an internal mesh structure similar to the support while reinforced mesh has a similar strategy but with additional thicker internal supports to the part. All the parts created throughout this thesis followed the same hexagon scan strategy.

The laser parameters set points are also shown in Figure 69, importantly for scan speed (mark speed) and the laser power as a percentage of total available power (in the ProX case of 300W). Other parameters such as the laser defocus from the powder bed and the spacing between adjacent laser passes are also controlled in this panel. The laser parameters also include delays and compensations to ensure the start and end of the laser passes are provide the same effect on the bed over the full scan. These are required for the control transients present when starting and ending the control system.

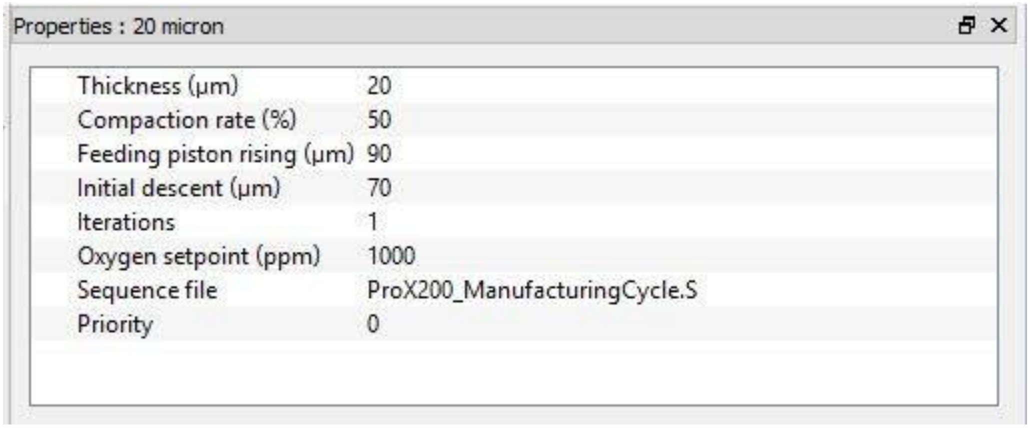
Properties : 20 micron

Thickness (μm)	20
Compaction rate (%)	50
Feeding piston rising (μm)	90
Initial descent (μm)	70
Iterations	1
Oxygen setpoint (ppm)	1000
Sequence file	ProX200_ManufacturingCycle.S
Priority	0

Figure 70: Layering settings

The layering settings determine the layering sequence between each layer of the build and are shown in Figure 70. Thickness determines the change in height between the layers. Compaction rate allows for the powder to be compacted by a roller to create a powder bed, it is in percentage additional volume added prior to compaction. Feeding piston raising is the level the feed piston is raised by to supply powder for the layer. The feed is usually 2.5 to 3 times the powder required for the pre-compaction layer. The excess is to prevent short feeding and to account for powder spread that does not lie on the build area. The initial descent is the amount the build piston moves down prior to raising to the correct layer level. The iterations are the number of times the roller/scrapper carriage cycles are done for each layer. The oxygen setpoint determines the O2 level that the build chamber is purged to below during operation to prevent the powder or part oxidising due to the high temperatures.

The powders used in all experiments were supplied by 3D technology and were directly from 3D Systems the vendor for the ProX DMP 200 machine used. The powder is produced by an atomisation process which gives a consistent size distribution and shape. The has particle size distribution of the powders are given as percentile and are tabulated in Table 8.

Percentile	Particle size
D10	5-10µm
D50	20-25µm
D90	35-40µm

Table 8: Particle size used

4.3.2 Choice of the Control variable

The potential sources of variation in AM have been laid out in

Chapter 2: Literature Review. The sources of variation are in the form of pre-process, para-process and post-process effects. The focus of this thesis is to produce a means to correct the lack of repeatability in the AM process. The area of the process that we can exert direct control over is the para-process and that is where our focus on control shall be concentrated.

As it was shown in 2.3 Para-Process Effects, an important factor in determining the mechanical properties of the part is the Energy Density (ED). The ED has now been demonstrated to vary across the build plate by the evaluation of the equation. The aim now is to create a modified set of process parameters using this equation to effectively flatten the ED against distance from the centre curve found to exist in the process.

Examining the two formulations for energy density, namely equation *(1)* and the new formulation of equation *(18)*, both reproduced below it gives a number of potential factors that can be modified to change the energy density.

$$\psi = \frac{P}{v * h * d} \qquad (1)$$

$$\psi = \frac{4(P - E)}{\pi \delta D_{b,m} v} \qquad (18)$$

Firstly, some factors cannot be directly modified or controlled. The distortion coefficient is dependent on the F-Theta lens used in the system; it is only modifiable by completely swapping out the lens with a new one. The addition of an improved lens could improve the ED spread, however, this is not possible with the currently available F-Theta lens technology.

The diameter of an equivalent circular beam at that location is dependent on the location on the build plate by definition. This diameter is dependent on the laser spot at the centre and propagation path. This obviously cannot be changed without a complete change of the upstream laser supply and focusing apparatus.

These terms are both the sources of error in the ED but also have fixed values, any means to change them would require a complete redesign and refit of the machine or changing the machine used. This need to swap machine, which will also likely have similar errors and the inherent nature of both these sources of error invokes the

Taguchi principle of “if you cannot remove the cause of the effect, then reduce the effect of the cause” [153]. By correcting the other parameters locally, the effect of the cause on the final properties may be mitigated.

Secondly, the issue present in the repeatability is contained on a single build. The depth of powder for each location in the build cannot be varied across a single layer, if a sufficiently controlled system was in place several layering operations could be carried out to create an effective powder depth change between each part. This method, however, would require the control to be sufficiently fine such that the difference between parts would be an integer number of layers in difference. This is not the case currently due to the nature of Powder Bed Fusion, the powder particles have a defined non-negligible size, and this creates a lower threshold for the layering system. Any layers that would be attempted to spread across the build that are smaller than the size of the smallest particle would have no powder deposition in the layer, this effect does not diminish until the layer size is sufficiently close to the size of the largest particles, which is where the machine currently operates. Alternative means of depositing the powder that does not require a spreader could allow for depth of powder variations, this too would lead to fundamental problems in a continued deviation from the level of the powder bed across the build. The difference in powder level between the central and edge sections of the build would increase with each layer until a point in which the angle of restitution of the powder was exceeded and no layer could be formed. The control for this variable is inherently constrained by the fundamental physics of the powder and powder layering process. Thus eliminating powder depth as a potential means for controlling the energy density across the build platform.

Hatch spacing was also eliminated as a potential control variable due to the effect it would have on remelting overlap, the modified values calculated would change the remelting regime sufficiently to give rise to porosity in the parts [154]. Modifying the hatch spacing would also open the possibility of reducing the geometric accuracy of the parts. The trade-off for potentially improving the mechanical properties consistency by modifying the hatch spacing, by certainly reducing the geometric accuracy is untenable for overall repeatability. This makes hatch spacing, while a possible control variable, has significant drawbacks making it less suitable as a variable to modify for improved consistency in a universal context.

Increasing the laser power would lead to a greater section of the beam contributing to the melting process, increasing the effective spot size [113], this would lead to an expanded melt pool. This as with hatch spacing would potentially introduce a geometric consistency concern. An expanded melt pool would also allow for a greater opportunity for satellite particles to join the melt pool. This increase in power would also potentially change the absorption characteristics of the plume adding a number of potentially nonlinear effects on the actual energy density from this modified power. The power is also functionally constrained due to the already high power output required for nominal energy density. The need to increase power at the edges to counteract the drop in power experienced would be problematic and in some cases would need to be increased beyond the capability of the installed laser power.

The final process parameter to consider is the scan speed. It is present in both formulations of the energy density, is easily controlled and modified. The level of discrete control is also high, the machine typically operates at a scan speed setpoint of 2500mm/s but can go to 5000mm/s, the control is on the level of adjustments in increments of 1mm/s.

Thus, both by the process of elimination and by its increased level of controllability the obvious choice of the control parameter is scan speed. The central section of the build plate produced the parts with the lowest standard deviations amongst groupings. It shall then be used as the optimum energy density. The other sections of the build will have reduced scan speeds to raise their energy density to match this optimum.

4.4 Statistical methodology

The measurements will be considered for trends in the individual samples. These trends can be in drops in performance related to distance from the centre, or any other apparent phenomena. The existence of trends other than distance from the centre will not necessarily discount the validity of the modified energy density equation but may be considered for future improvements.

Besides the trend from individual samples, which would account for the in-build repeatability, the global values will also be considered. The first key factor that will be determined for comparison to other builds or technologies will be the confidence interval for the mean value at both 95% and 90% significance values. This gives a firmly understood and quantifiable factor for the level of inaccuracy present in the process [44].

$$\bar{x} \mp \frac{z^{*}\sigma}{\sqrt{n}}$$

Where $\bar{x}$ is the mean of the sample, $z^{*}$is the critical value for the confidence level, σ is the standard deviation and n is the total number of samples. The confidence interval can also be considered for individual samples at a specific distance allowing us to define an area where the properties are not statistically different from the central values.

Repeatability is inherently a measurement of variance. As this research focuses on attempting to improve repeatability, an important metric is to determine if the difference in variance is statistically significant. The most appropriate test for this is the F-test [155]. The F hypothesis test is defined as follows:

$$H_0 : \sigma_1^2 = \sigma_1^2$$

$$H_a : \sigma_1^2 \neq \sigma_1^2$$

$$F = s_1^2 / s_2^2$$

Where s_1^2 and s_2^2 are the sample variances. The more this F ratio deviates from 1 the stronger the evidence for unequal population variances. The null hypothesis of equal variances is rejected once the F value is outside of the critical values of the F distribution.

The min-max range will also be considered, this value, while sensitive to outliers, gives a holistic understanding of the level of variation over the entire build plate.

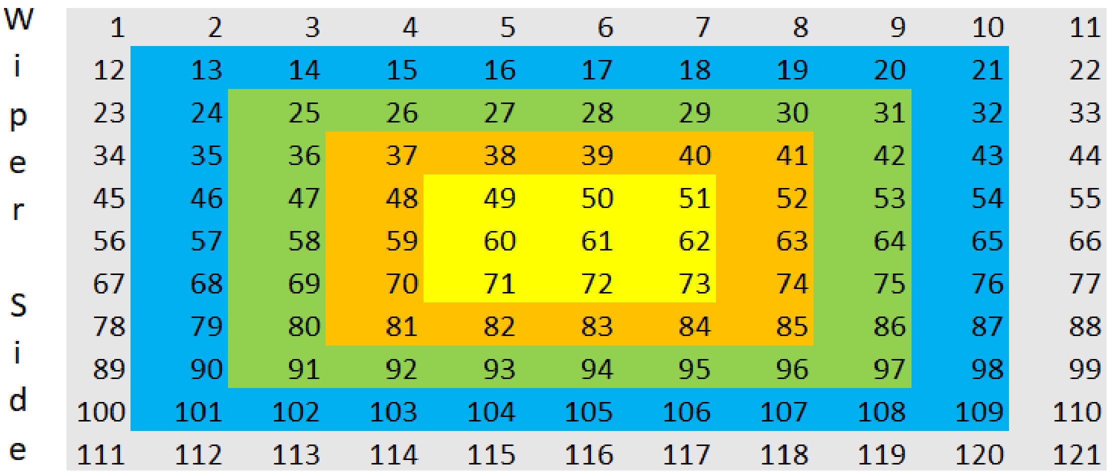

1	2	3	4	5	6	7	8	9	10	11
12	13	14	15	16	17	18	19	20	21	22
23	24	25	26	27	28	29	30	31	32	33
34	35	36	37	38	39	40	41	42	43	44
45	46	47	48	49	50	51	52	53	54	55
56	57	58	59	60	61	62	63	64	65	66
67	68	69	70	71	72	73	74	75	76	77
78	79	80	81	82	83	84	85	86	87	88
89	90	91	92	93	94	95	96	97	98	99
100	101	102	103	104	105	106	107	108	109	110
111	112	113	114	115	116	117	118	119	120	121

Figure 71: Labelling convention

The samples will follow a consistent labelling convention as laid out in Figure 71, this convention is that the sample on the top left when looking at the build plate from above is number one and then the labels iterate from left to right and then down. This exact tracking gives all the location information and can be used to access other trends across the various builds.

4.5 Microstructure

Representative samples from the central region, the edge of the build and the corner of the build were selected. These are then used to examine the microstructure present in the parts. The samples were first CT scanned, the results of which are examined in 6.6 Computer Tomography Results, these samples were sliced in an EDM machine to get a clean consistent cut. The slices were taken in gauge in both the transverse (green) and the longitudinal (blue) as in Figure 72.

Figure 72: Microstructure sample locations

The segments were hot mounted in conductive resin and then ground and polished to reach a mirror finish with no scratches. The grinding and polishing steps were through sandpaper of grades P600, P800, P1200, P2500 and P4000 for both materials. The CoCr samples were finally polished using a 1µm diamond suspension, this was sufficient to reach the desired finish. The 316L samples required further polishing with 0.2µm fumed silica suspension to reach the desired finish.

The samples were then electrolytically etched in a 10% nital solution at 10V for 5 minutes to reveal the microstructure.

4.6 CT Scanning

The samples were scanned in a Nikon xth22st at 128 kV and 250 µA giving an energy input of 32W. The sample was placed into a plastic cylindrical holder positioned adjacent to the x-ray source, this positioning gave a detection resolution of 16.75µm and thus a voxel resolution of 16.75µm^3. This means that when detecting defects or porosity, any cracks or pores smaller than this value will not be seen.

The individual slice files were reconstructed to give a 3D visualisation of the samples in Volume graphics VGStudio MAX 3.0. This visualisation required a beam hardening correction due to the low energy x-rays being absorbed at the part surface making it appear denser and correspondingly the internal core was made to appear less dense. After this standard correction process, a 3D image is generated as in Figure 73.

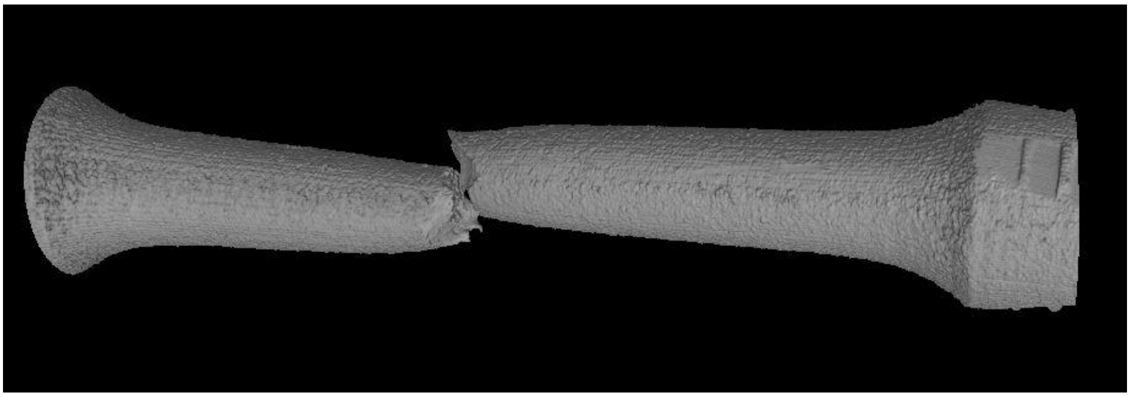

Figure 73: Tensile sample 3D visualisation

The region of interest was selected to avoid the fracture point, the surface of the samples where surface roughness and the beam hardening correction could lead to over-representing the porosity present. The grip sections were also to be avoided as they would have had compressive forces during tensile testing, these forces would close pores causing them to be no longer representative of the whole sample. This gave a cylindrical region in the core of the remaining gauge section of the sample.

The threshold for determining the porosity is found by examining individual slices of the reconstructing manually to find a pore. This pore is then used as the basis to search for all other pores automatically. The pore will have a lower voxel value than any other areas. This is due to fewer x-rays being absorbed by the entrained void than solid material. This value and range are checked against all the voxels present in the reconstruction.

This, of course, will be very sensitive to noise in the measurement or dead pixels on the detector screen. There are a number of other artefacts such as ring artefacts in the scan that will also be discovered. The software package eliminates the detected pores of size less than 8 voxels and has a probability minimum incorporated, these combined can reduce the number of false porosity detected by the dead pixels and scan artefacts. This makes the allows porosity to be measured accurately at the near-100% relative density that is present in the produced parts

Chapter 5: Geometric Properties

This chapter will assess the geometric repeatability found in the process. The literature does not suggest that a significant error is present, however, increased spot size is predicted by the modified energy density equation. This chapter will directly measure the geometric repeatability and any cause of repeatability concern for the geometric properties.

The hole features were analysed by importing all the images of the benchmark as seen in Figure 74 into MATLAB and checking for the reflected light intensity to drop indicating a hole being present. The areas that were detected to be a hole were then isolated giving a plot such as seen in Figure 75. The white areas are the areas that meet the detection threshold for a hole and the blue crosses indicate the centre of detected holes. As can be seen in the figure additional localised dark spots can occur due to the rough surface creating shadows. These dark spots, however, are smaller than the actual hole features and tend to be highly eccentric in nature and can be filtered out.

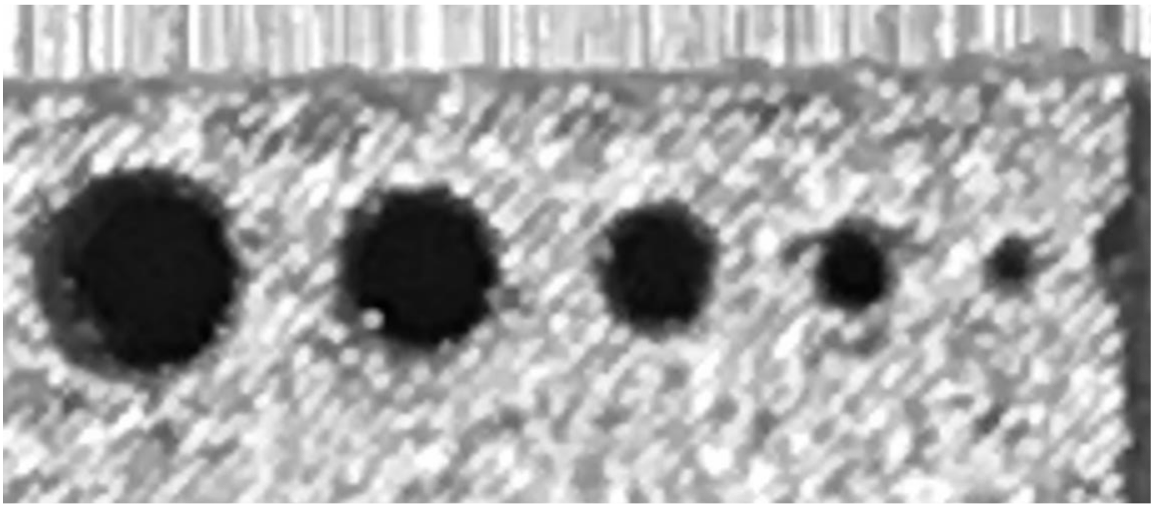

Figure 74: Hole Feature image

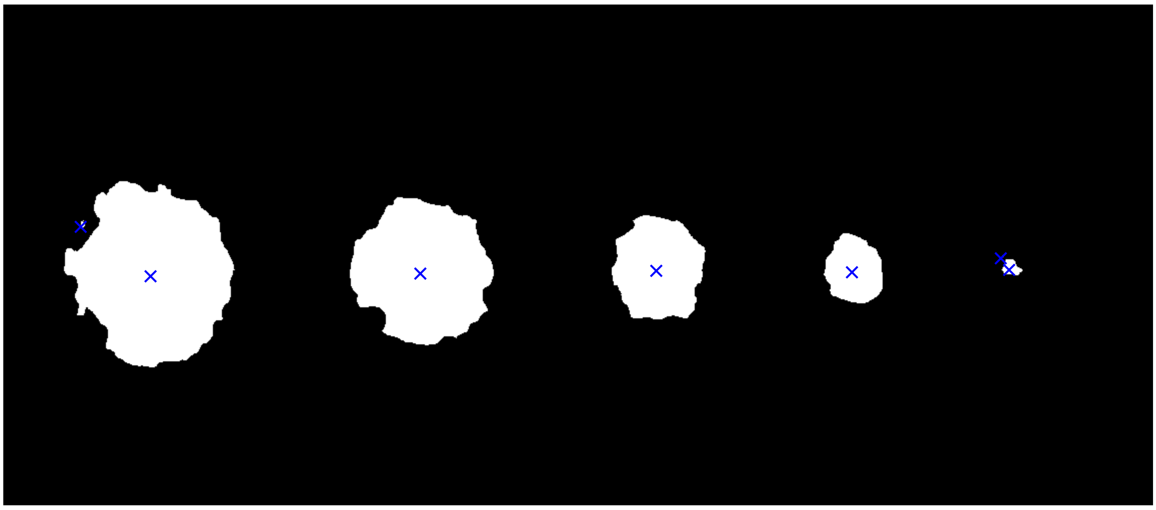

Figure 75: Hole feature thresholded

The measurements of the hole features can then be plotted against their position for analysis. The raw data for the nominally 1mm hole is shown in Figure 76 and the distance averaged values are shown in Figure 77.

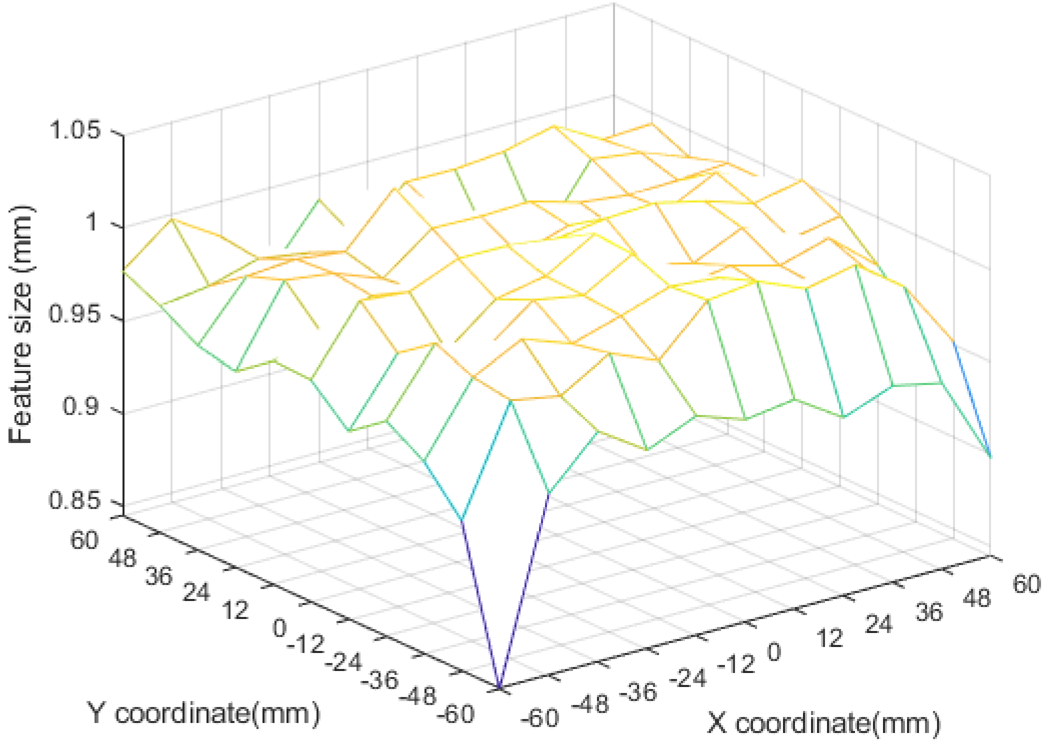

Figure 76: Hole feature raw data

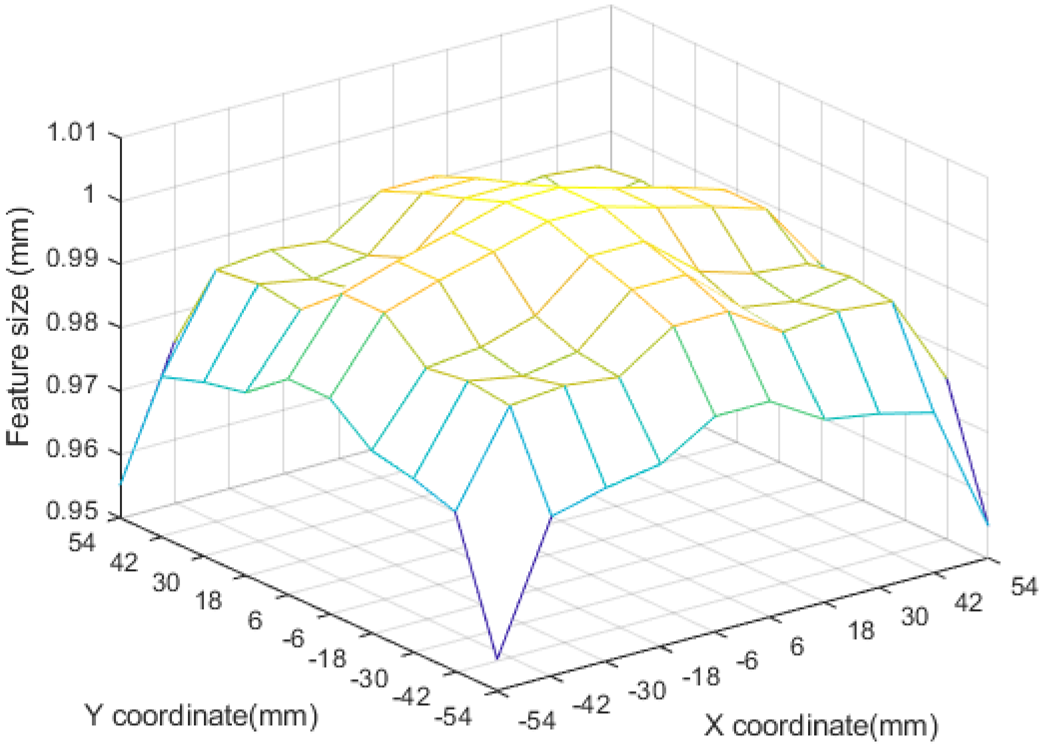

Figure 77: Hole feature distance averaged dimensions

Both these figures show the hole feature dimensions displaying the characteristic domed shape with the holes being larger in the central region and contracting in the edges of the build plate. The raw data is also the clearest example of the domed shape in raw data form, this discredits the hypothesis that the domed shape is an artefact of the averaging required to work with the noisy data present.

Nominal Value (mm)	**1**	**0.8**	**0.6**	**0.4**	**0.2**
Measured Average (mm)	0.983	0.785	0.583	0.390	0.210
Measured Standard Deviation (mm)	0.024	0.027	0.020	0.019	0.027
Measured Maximum (mm)	1.003	0.808	0.600	0.406	0.233
Measured Minimum (mm)	0.955	0.754	0.562	0.373	0.191
Measured Range (mm)	0.048	0.053	0.038	0.032	0.042

Table 9: hole feature geometric breakdown

The key results from the hole features are tabulated in Table 9. The measured range and standard deviation of each of the cases were very similar. This importantly demonstrates that the variation is independent of feature size, allowing the statement to be made that the variation is inherent to the process and not inherent to the part or feature. An unfortunate effect of this feature size independence is the elimination of the use of the coefficient of variation as a useful metric for comparing results. As depending on the nominal value considered for the hole features, a range of coefficient of variations from 0.024 at 1mm nominal to 0.128 at 0.2mm nominal.

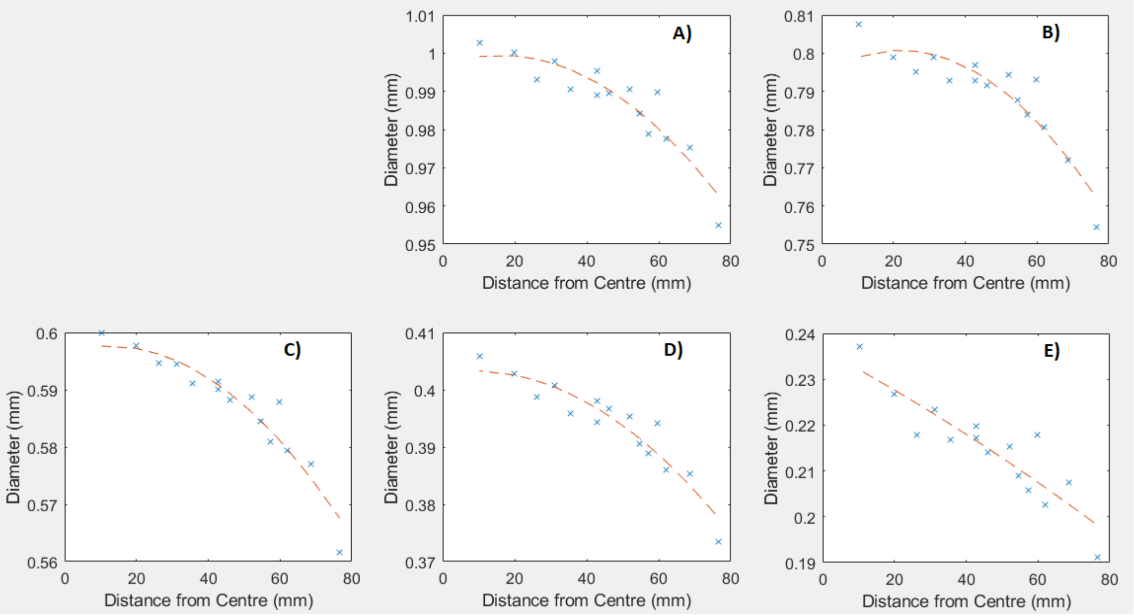

Figure 78: Fitted plots for pin features of nominal sizes A) 1mm B) 0.8mm C) 0.6mm D) 0.4mm E) 0.2mm

The fitted curve plots for all sizes can be seen in Figure 78. The fitted plots for the hole features show a similar change in feature size from the central region to the edge of the build plate. The curve also becomes less pronounced in the smaller features. Irrespective of the feature size examined, the holes were 30 microns smaller when comparing between the centre and the far from the centre. This is compounded when examining the tabulated fit data in Table 10. The independence of the difference with respect to feature size would indicate that the source of the error is common in all geometries, examining the pin features will confirm if this is true. The commonality would suggest that the error would be due to the fundamental interactions at the edge of the part, such as the expanded spot size predicted from the targeted sources of error.

Nominal Value (mm)	**1**	**0.8**	**0.6**	**0.4**	**0.2**
Fitted Maximum (mm)	0.999	0.799	0.598	0.403	0.229
Fitted Minimum (mm)	0.963	0.762	0.568	0.378	0.197
Difference (mm)	0.036	0.037	0.030	0.026	0.031

Table 10: Fitted Data for hole features

It was not possible to batch measure the pin case as was done for the hole features due to the similar reflectivity between the top of the pin and the remainder of the geometric benchmark.

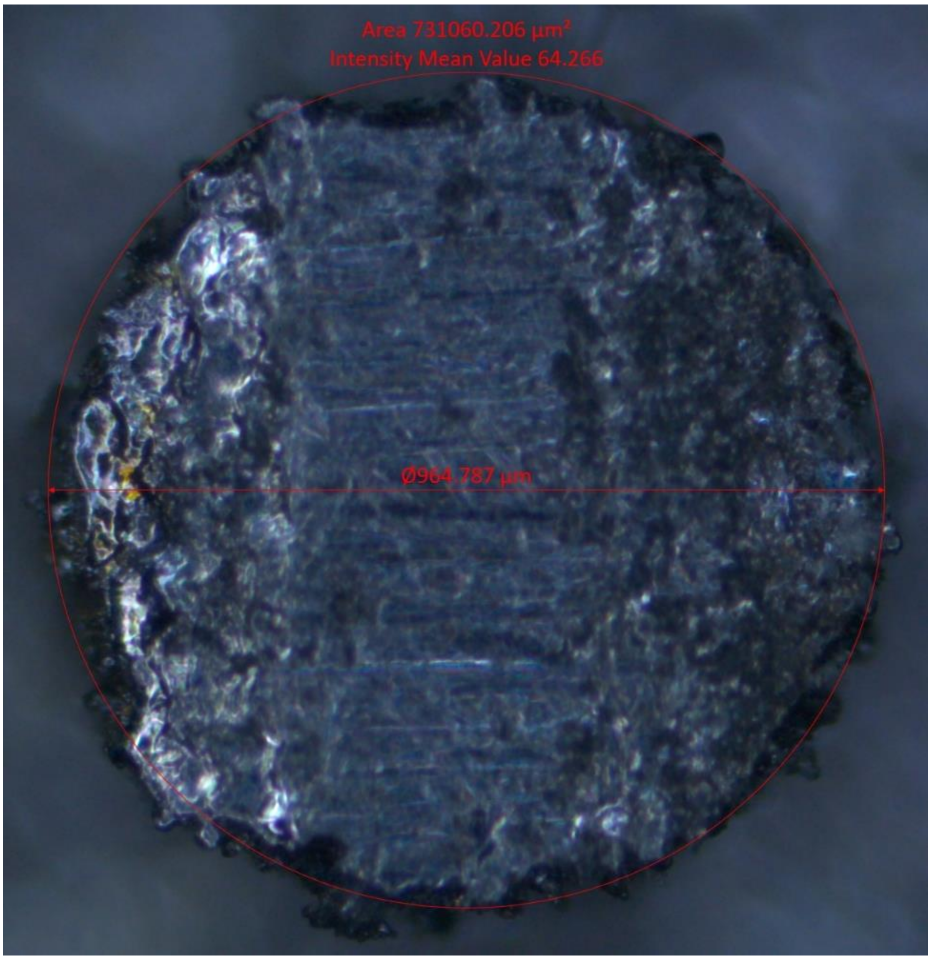

Figure 79: Geometric sample measurement

The pin features on the geometric samples were imaged under Leica S6E stereomicroscope at a 40x magnification and the circle of best fit was taken to determine the diameter of the nominally circular samples, as can be seen in Figure 79. This figure also shows the roughness present in the edges of the part due to partially bound powder particles on the surface. The 1mm pin is used as an exemplar of this form of geometric repeatability but the trends are consistent across the pins.

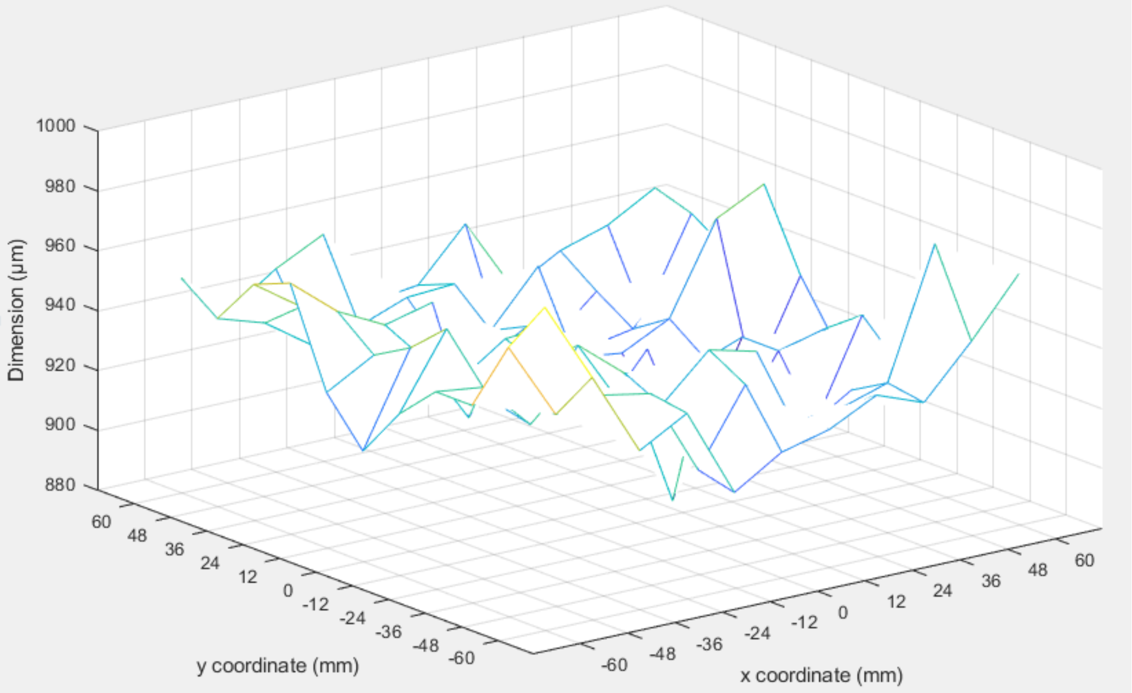

Figure 80: Base Case Raw Geometric Measurements

The data, while noisy in this unprocessed form, has some evidence of an inverted domed characteristic structure in the plotted properties. The raw results provide a very noisy plot shown in Figure 80, however global information such as the overall confidence interval and standard deviation of the total build can be calculated from this unprocessed data.

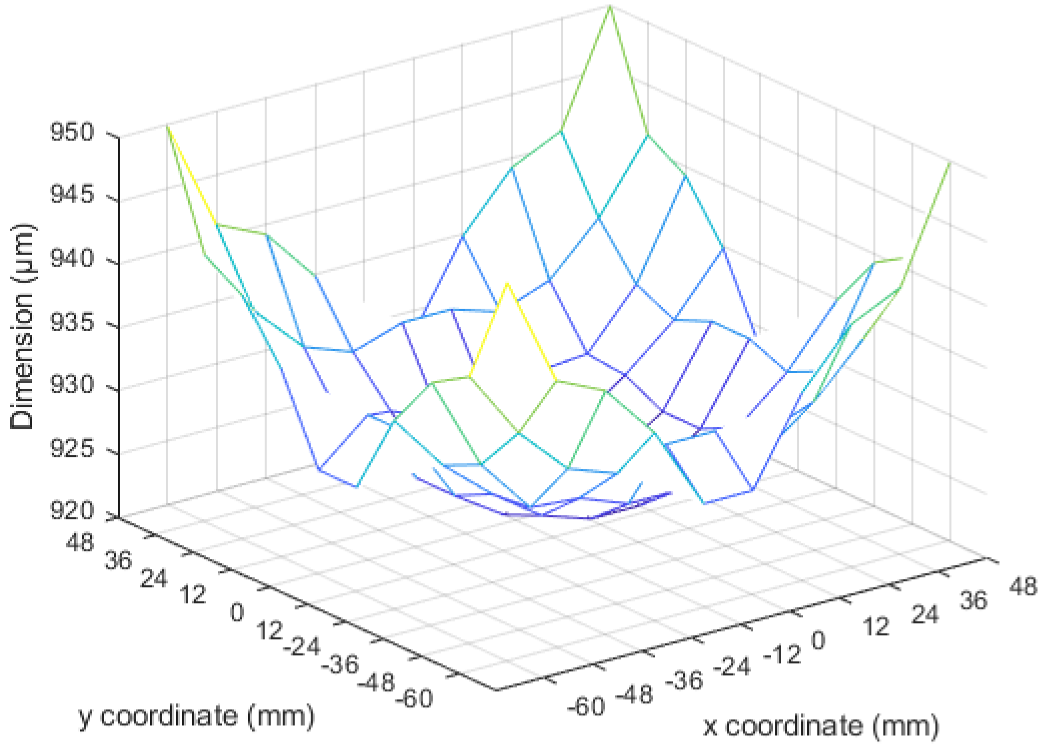

Figure 81: Base Case Distance Averaged Geometric Measurements

The samples were grouped based on distance from the centre of the build plate. The smoothed data very clearly shows the inverted dome that is predicted from the theory as seen in Figure 81, with the pins at the edge being larger than the pins present in the centre of the build area. There is a 30micron increase in pin size between the centre and the edge of the build area. This shows that the features encroach beyond the designed geometric boundaries.

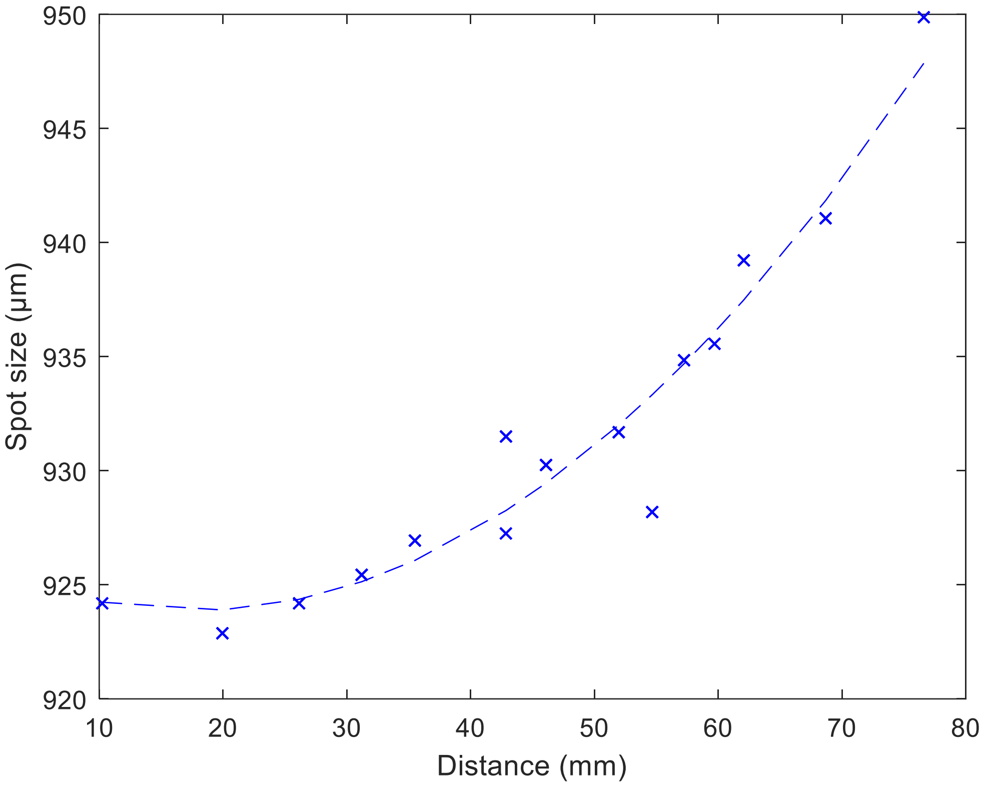

Figure 82: Base Case Geometric Measurements against distance from the Centre

The final averaged data shows a very clear increase in part size at the edges of the build plate, where the distance from the centre is greater. This increase in part dimension is in line with the theory developed on the increase of spot size in the evaluation of the modified equation, however, the magnitude of the variation is twice that calculated. This could be due to the geometric error causing the part to become larger on both sides of the part, whereas the prediction is only on one side of the part.

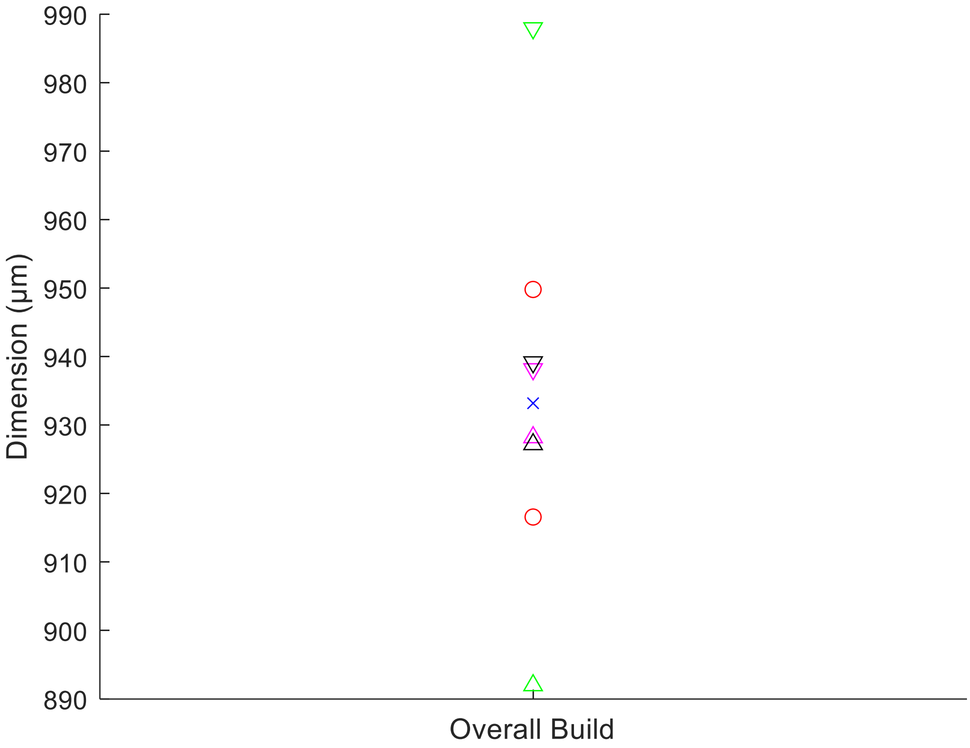

Figure 83: Base Case Geometric Measurements

The average value for the full data set was 0.933 mm with a standard deviation of 0.017 mm giving a coefficient of variation that was calculated to be 0.018. This is comparable to the coefficient of variation found for traditional manufacturing techniques.

A key issue in geometric repeatability of both sets of features is the joining of satellite particles to features an example for pins is shown in Figure 84 and a similar example for holes is shown in Figure 85. The addition of these satellite particles changes the effective diameter of the part by offsetting the circle of best fit for the part in pins and occluding a part of the hole in those features.

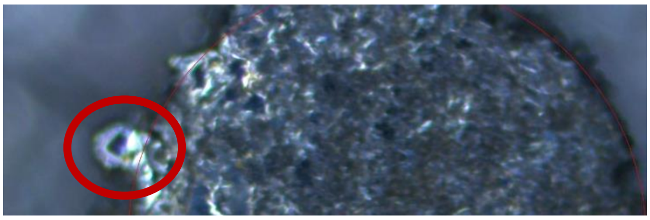

Figure 84: Satellite particle on pin feature

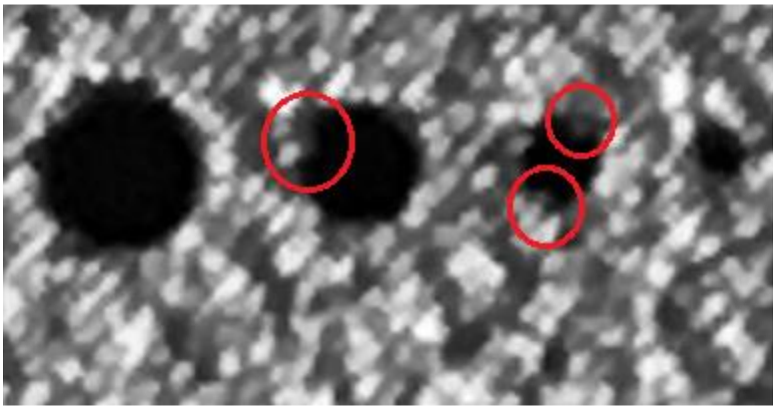

Figure 85: Satellite particle in hole feature

These satellite powder particles are formed by powder particles that were not sufficiently far into the laser track to be completely melted for the formation of the melt pool. In the bulk sections of a part, these partially bound particles would be remelted by adjacent laser passes removing them, however, on the part surface, there are no additional passes to melt these powder particles leaving them partially bound to the surface. This introduces a plausible explanation for the consistent variation from both the pin and hole features across the build.

The discrete nature of the laser scanning, specifically the discreet levels of hatch spacing and a scan being either occurring or not also introduces a minor variation in the inexactness of the scan vectors including compensations for the part. An example scan vector for a small pin feature is shown in Figure 86.

Figure 86: Scan vector of small feature

The scan vector discreteness gives a minimum limit of control for the parts of a hatch spacing which in the cases studied was a constant 30 µm. In the measured cases here the range in the parts from maximum to minimum was measured as being on the order of a single hatch spacing, and without fundamental reconfiguration of the machine and AM process this is at the physical limit of what is achievable in the current technology. The disagreement between the simulated and measured values can be seen from the geometric properties, this is shown in Figure 87.

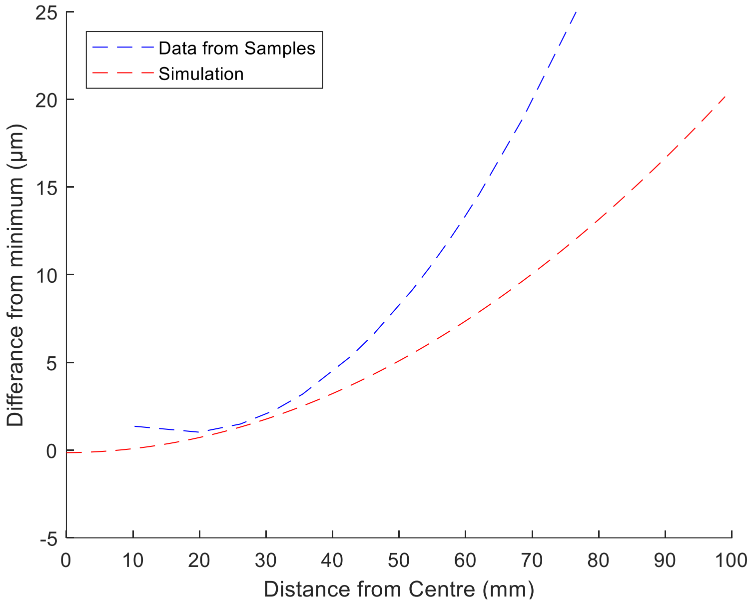

Figure 87: Geometric Difference from Maximum against the distance from the centre

The two data sets both trends to be larger at the edges than in the central region with an accelerating difference moving from the centre, however, the magnitude of the difference is under accounted for in the simulation. The difference from the minimum size in the simulation is twice the change in spot size for that point. This is due to a part requiring multiple adjacent scans and in effect will have the error appear on both edges of the part.

The existence of satellite particles contributes to the under-representation of the discrepancy between the centre and far from centre cases in the simulation. The larger circumference of the far from centre parts due is due to increases in the laser spot size. This increase in the circumference leaves a greater area for the satellite particles to potentially get attached to the part. These satellite particles when included in measuring the overall pin size, effectively increase the difference from the minimum at the centre. This causes a weak feedback-loop to increase in the geometric features differences, relative to the centre, beyond what a pure increase in beam diameter would be able to achieve.

The geometric properties have been shown to be comparable to those found for traditional methods. The root cause of the remaining geometric variation is due to an inherent property of powder bed fusion. This satellite particle issue and the discrete nature of the hatch raster to fill the geometric cross-section make further improvement in the geometric repeatability difficult to attain. This coupled with the acceptable level of repeatability already in the process shows that the geometric properties are not of major concern with the overall process repeatability.

The geometric accuracy for the machine is advertised as being ± 0.1-0.2% with ± 50 µm minimum, this concurs with the level found in the verification of geometric properties. The obvious means of correcting for the sizing error present in the parts is by using a scaling factor to correct the part dimensions by the error factor. However, due to the discrete nature of both the powder particles and the hatch spacing, under the current manufacturing parameters, it becomes exceptionally difficult to directly modify the scan pattern to remove this error. Any changes would potentially compromise the remelting overlap of the remaining parts. This limits the ability to improve the geometric repeatability of the AM parts as it is already at a good level of repeatability compared to the traditional manufacturing methods and it is currently already limited by fundamental aspects of the laser powder bed fusion process. There is potential to improve the geometric repeatability by the application of post-processing or having a fundamental shift in the powder composition used.

The limitation on improving the geometric repeatability during the process brings a tighter focus on the lack of repeatability in the AM parts mechanical properties. The repeatability of the mechanical properties is below that of the repeatability found in AM geometric properties. The more significant factor is that the mechanical properties are less repeatable than the equivalents produced by traditional methods. The need to address the lack of repeatability in the mechanical properties is thus the most pressing concern in the overall repeatability of AM produced parts.

Chapter 6: Mechanical Properties

This chapter will investigate the mechanical property repeatability in the AM process. The literature review demonstrated that the mechanical properties were less repeatable than would be found in traditional methods. This chapter will assess the mechanical properties in both CoCr and 316L. Representative samples will also undergo further study by SEM and CT scanning to provide a deeper understanding as to the root cause of the repeatability concern. This will also provide an explanation for an improvement that the modified equation would provide.

6.1 Tensile Testing Results of CoCr Builds

6.1.1 CoCr base parameter set

The new understanding of the sources of variation demonstrated that both the energy density and the beam spot size varied across the build plate. The first step in improving the AM process is confirming that the predicted variation is truly present in the process and is not an artefact of the evaluation process or merely based on the assumptions used to generate the new ED equation.

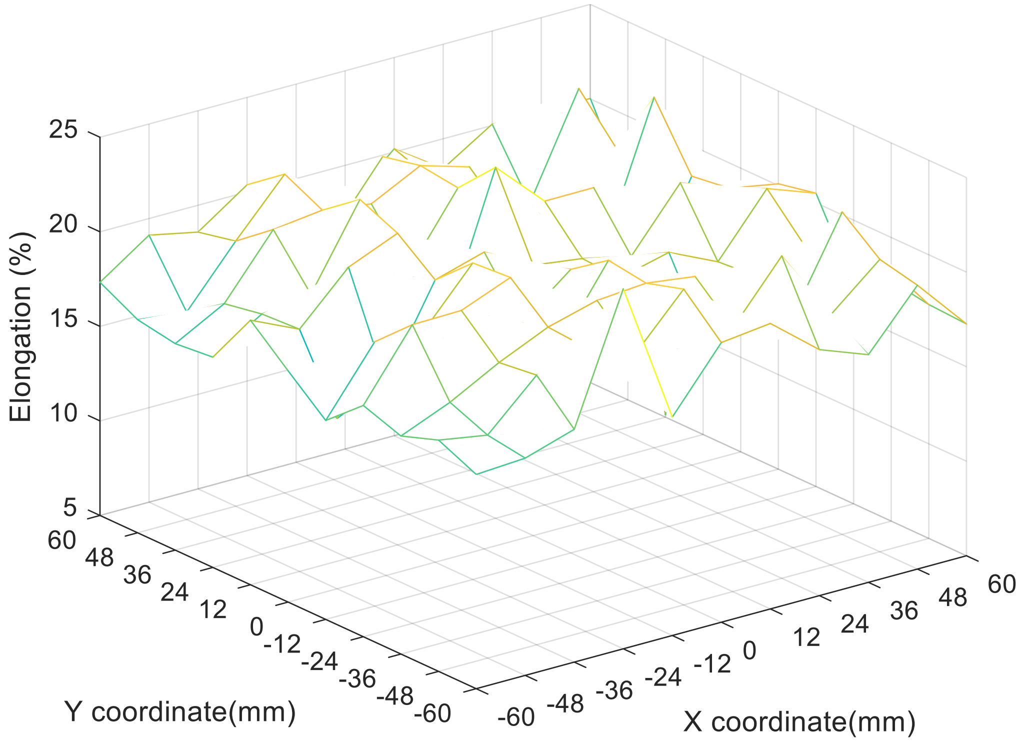

Figure 88: Base Case Raw Elongation

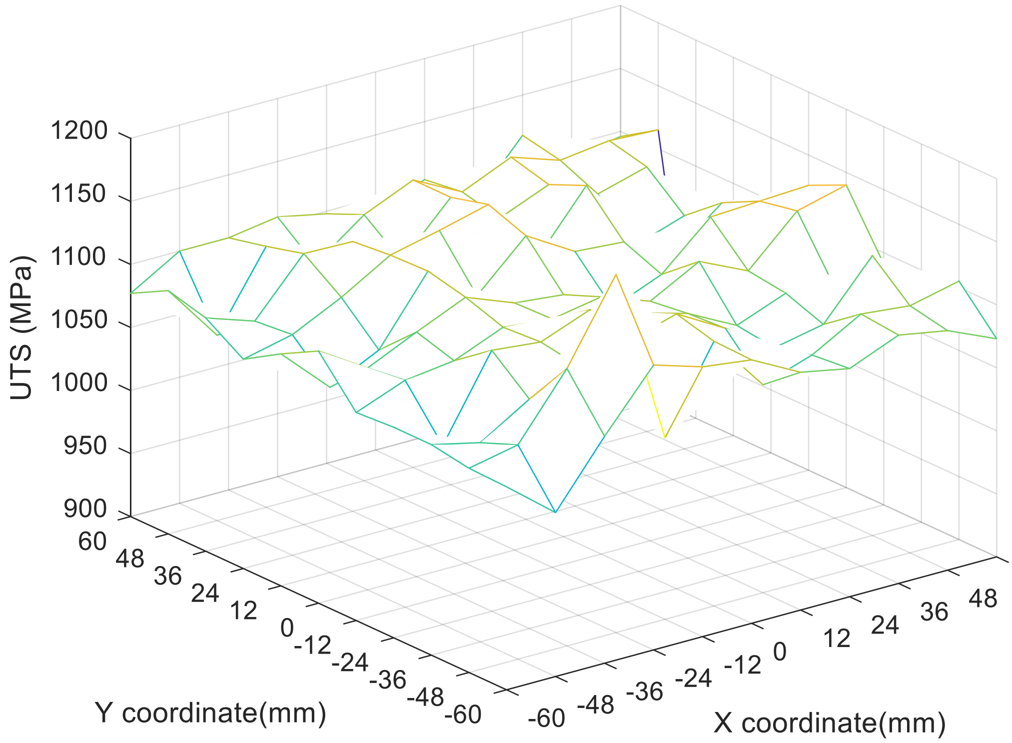

Figure 89: Base Case Raw UTS

The raw results are shown in Figure 88 and Figure 89, demonstrating the variability evident in the mechanical properties of a single build. The data, while noisy in this unprocessed form, has some evidence of a domed characteristic structure in the plotted mechanical properties, with a rise at the centre of the build and a drop at the edges. This would support the theory developed in the simulation. However, there exist clear potential outliers in the data both in unusually high (Sample 114) and low (Sample 33) mechanical properties. These samples were treated identically to all other samples but disrupt any trends present. These outliers show that there is uncertainty present in the process that can only be quantified with the large sample sizes that a full build provides.

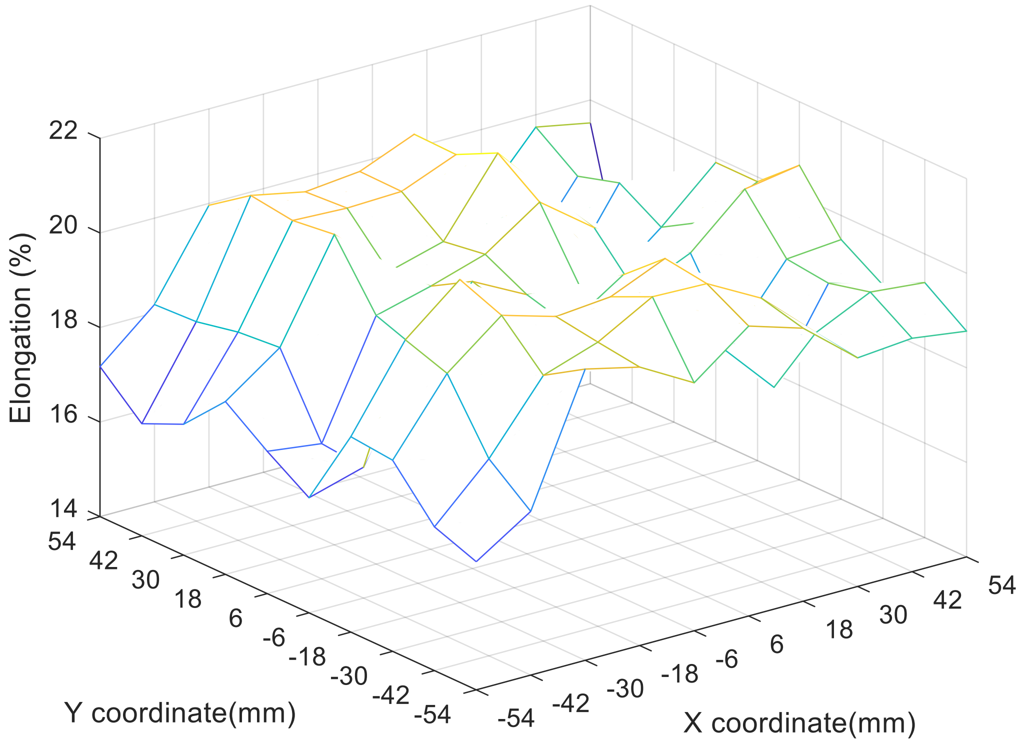

Figure 90: Base Case Averaged Elongation

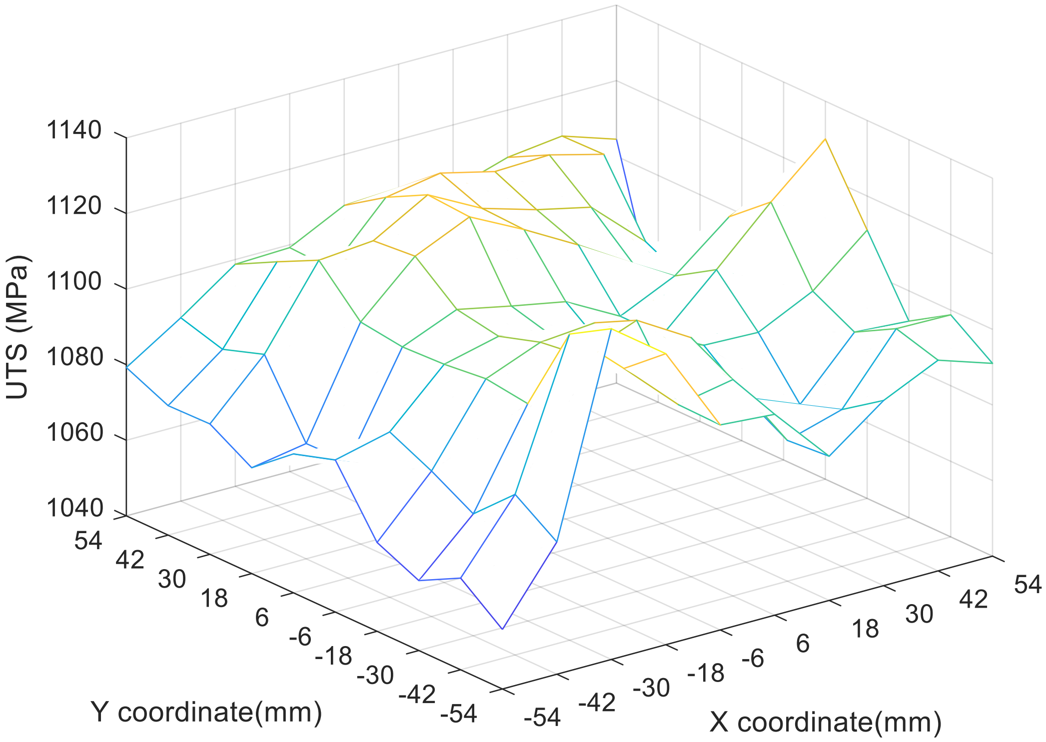

Figure 91: Base Case Averaged UTS

The results were grouped into sets of 4 adjacent samples to reduce the level of noise in the data, while maintaining the location groupings so that samples on the top left of the build were only with other top left samples. This gave rise to the result meshes that are shown in Figure 90 and Figure 91. This more clearly shows the domed shape that was expected, with some influence remaining from the random noise and outliers. This treatment of the results also suggests a variance in mechanical properties from the left to right of the build plate. This variance is not accounted for in the modified equation and suggests further sources of error present such as the effect that the spreading mechanism has on the powder bed creating heterogeneous powder properties. This would not be present in any equation based on their inherent simplifications.

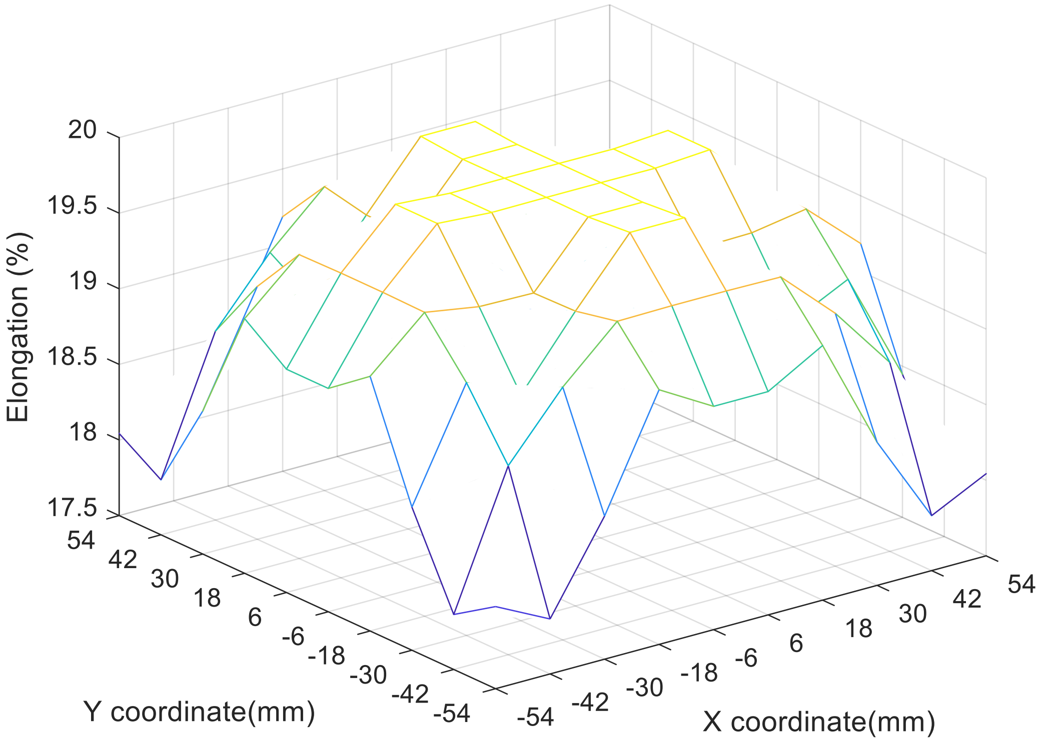

Figure 92: Base Case Distance Averaged Elongation

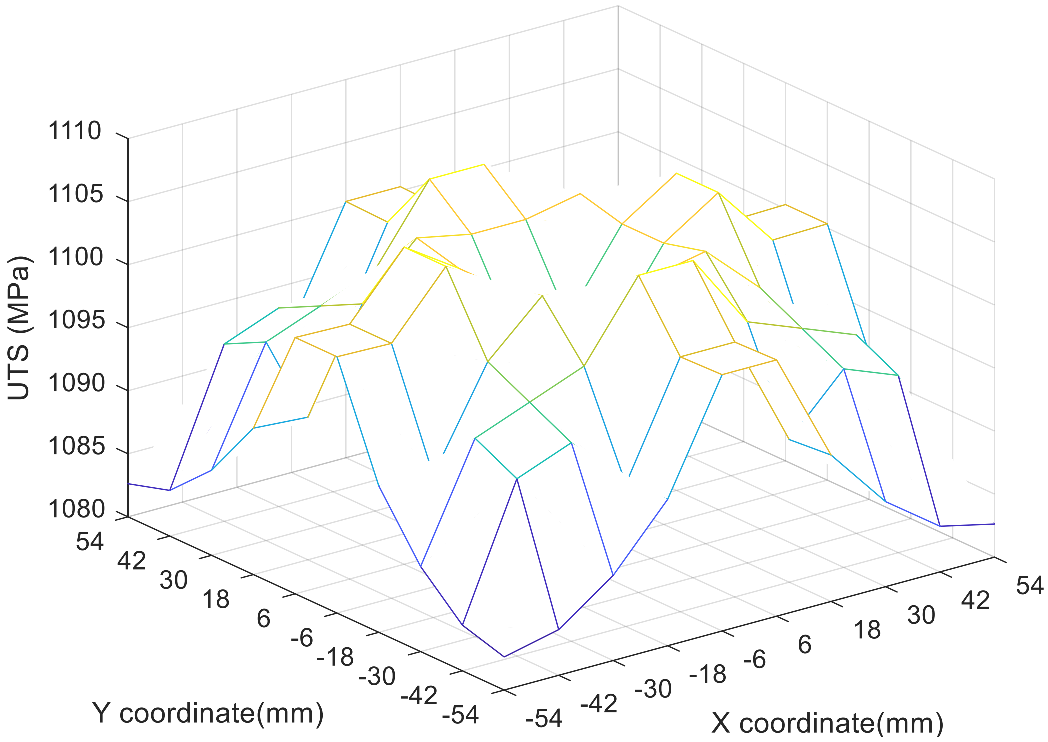

Figure 93: Base Case Distance Averaged UTS

The samples were grouped based on distance from the centre of the build plate, as can be seen in Figure 92 and Figure 93. This in effect introduced an eightfold symmetry around the centre. This grouping reduced the information available about specific points but had the benefit of diluting the noise in the data by using averaging. A side effect of this grouping was the elimination of the left-to-right or front-to-back variations that may be present. These left-right and top-bottom variations would need to be examined independently, but are beyond the scope of the current investigation. This interpretation of the results illustrates the dome shape that was found in the simulation of the energy density.

The predicted energy density and the final mechanical properties are shown in Figure 94. The domes do not line up precisely due to the non-linearity between energy density and final properties, but holistically show a striking resemblance between the two. This provides strong evidence that the new energy density equation does represent the process in the base case.

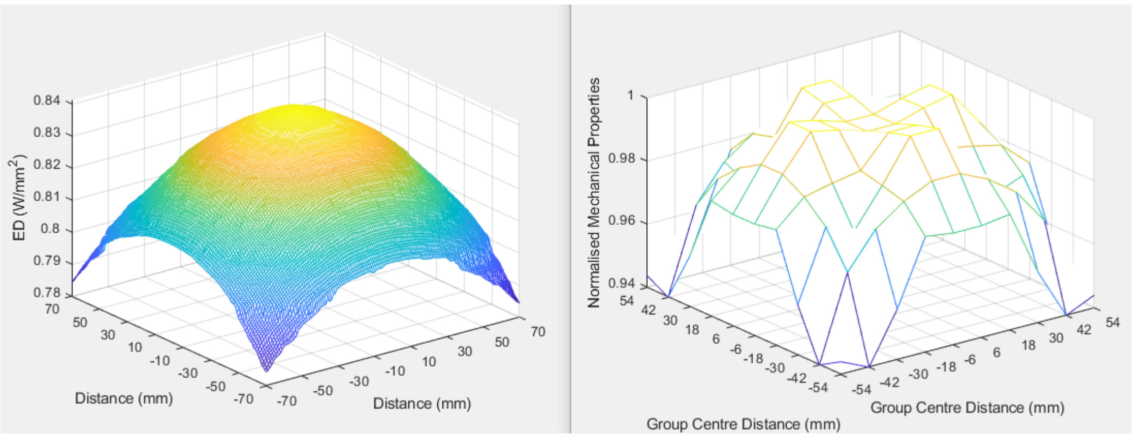

Figure 94: Comparison between mechanical properties and energy density predictions

The mesh plots can give a solid understanding of the data, but do not fully demonstrate the exact differences in the data over the full range. To simplify the data, each point is represented as an individual location with distance to the central point as its x-value and its mechanical property as the y-value. The corresponding plots for the 4 cases of data processing (raw, grouped averaging, eightfold symmetry and grouped eightfold symmetry) are shown in Figure 95.

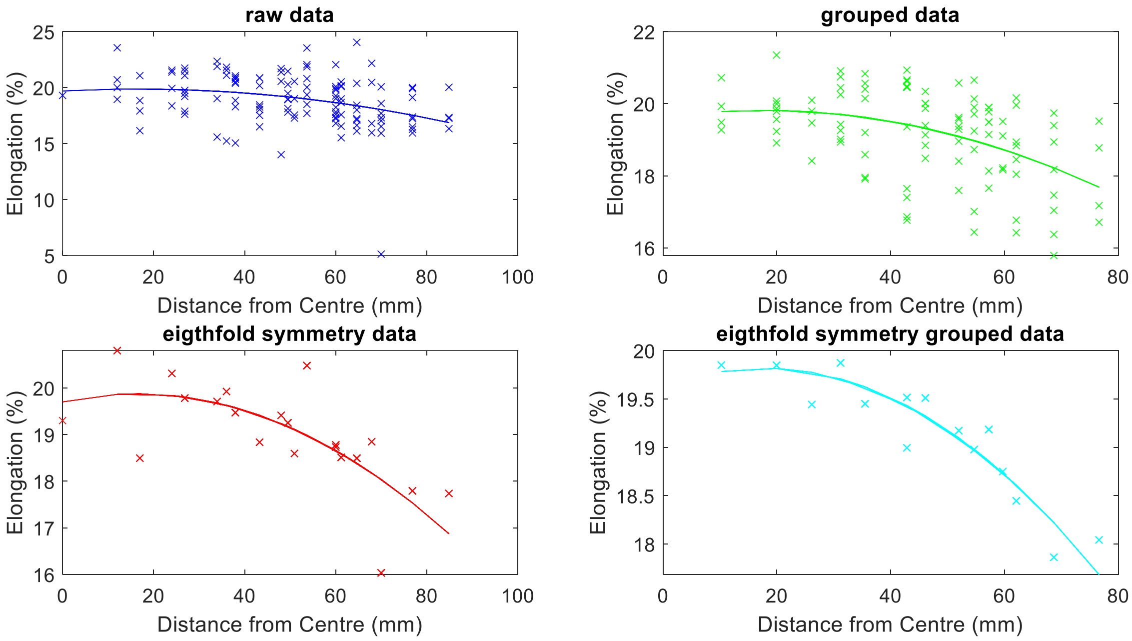

Figure 95: Types of data processing for distance from the centre analysis

The figures show that as the data is processed, the individual points become closer to the fitted trend of the data. The curve also appears more pronounced as the overall range of data is reduced. The data is now more focused on correcting the location-based variation, not the individual sample variation. This becomes more useful for repeatability improvement purposes. The more powerful correction for improving the overall build repeatability is in bringing the mean values of all locations closer, rather than having the individual location spreads being smaller. This is clearly demonstrated when examining the coefficient of determination for the fit, also known as the R^2 value. This is tabulated in Table 11, demonstrating how the fitted curves for the treated data more closely approximate the raw data.

Data Treatment	**Raw**	**Grouped**	**Symmetry**	**Grouped Symmetry**
R^2	0.1073	0.2106	0.5026	0.8713

Table 11: Coefficient of determination of data treatments

This improvement in the coefficient of determination is dramatic. This change is mostly due to the data treatment diminishing the effect of outliers and the noise, which are generated by the fundamental inconsistency of properties found from AM parts.

This treatment improves the trend line fit to the data; however, would not be useful if the trend line no longer had a relation to the underlying data. In effect, if the data processing causes the trend to exist, it would undermine the ability to make any useful predictions for the overall data. This was investigated and it was found that the trend lines generated by all stages of data processing were identical, as shown in Figure 96. This result allows the data to be processed from the full 121 samples to representative values at the 15 unique sample distances from the centre of the build plate to the edge. This allows for greater ease in parsing the data clearer presentation while still having fidelity to the full data set.

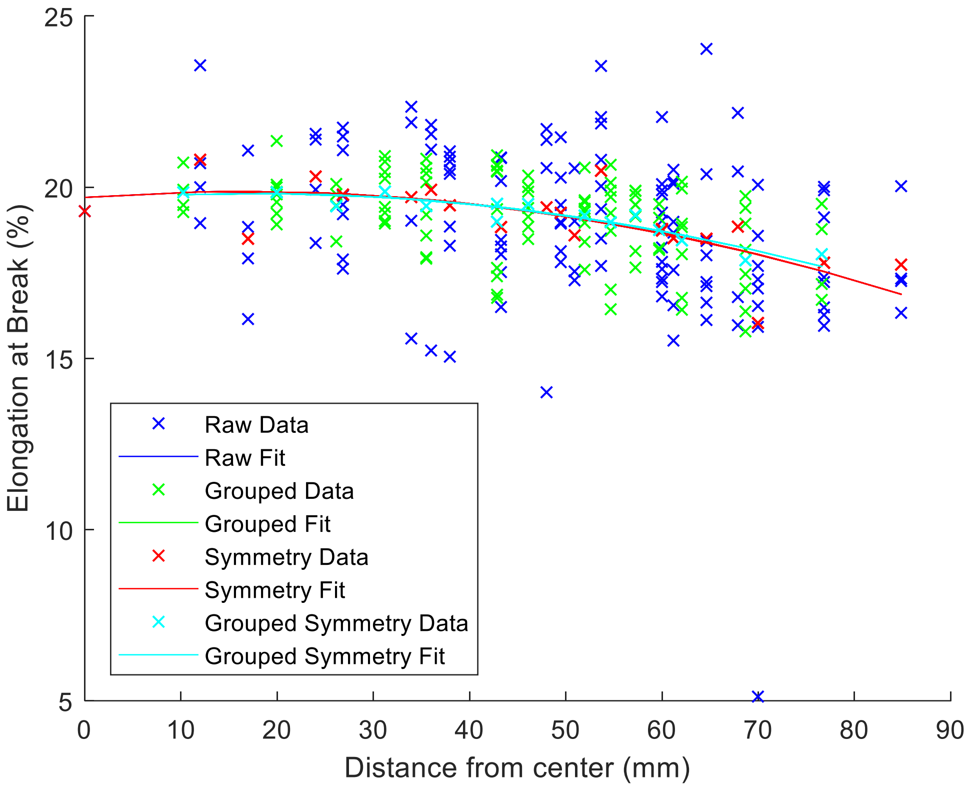

Figure 96: Data processing trends

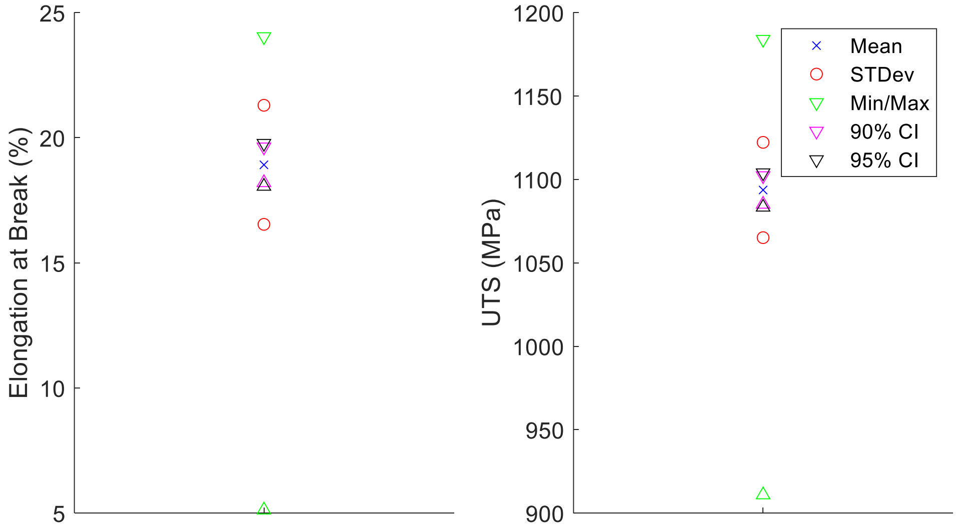

Figure 97: Base Case condensed data

Figure 97 shows the full plate data condensed into the average result, showing 90% confidence interval, 95% confidence interval, and standard deviations with the minimum and maximum values showing the full build range. From this data, it was calculated that the coefficient of variation for the mechanical properties was 0.026 for the UTS and 0.119 for elongation. These coefficient of variation values are directly comparable to those found in the literature as seen in section 2.1 Evidence of a Repeatability issue in the process . In this chapter, the literature is reviewed for evidence that can support the existence of a repeatability issue in the SLM process. The chapter will review the various processes and effects within AM that could be influencing the repeatability currently present, demonstrating that the issue is extant and not merely a perceived failing in AM.

This literature review chapter is based on a review paper that was published in the journal of materials and design under the title “A review of critical repeatability and reproducibility issues in powder bed fusion” (DOI: 10.1016/j.matdes.2019.108346).

2.1 Evidence of a Repeatability issue in the processThis gives further credence to the existence of a repeatability issue in AM and independently verifies that this repeatability concern is present in this manufacturing system.

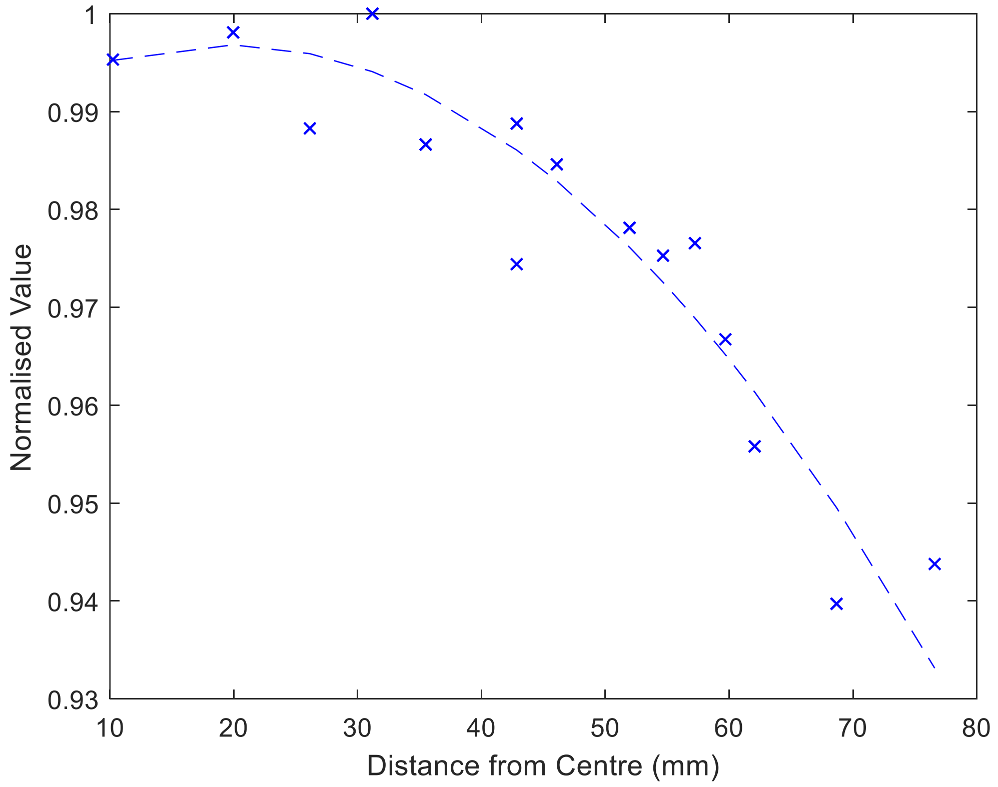

Figure 98: Normalised Mechanical Properties against distance from Centre

The results for both UTS and Elongation were normalised and combined to create Figure 98. This figure compares the normalised mechanical properties to the distance from the centre of the build plate. It can be seen that as the location of the part moves further from the centre, its properties degrade. This degradation in performance is a major contributing factor to the lack of repeatability in AM. There exists a drive to use the full area of the build plate when producing parts, leading to parts wholly being present in the degraded performance area of the build. In the case of monolithic parts that cover a large section of the build, this variation in properties could introduce an unpredicted local weakness, reducing the part's overall performance.

The broad trends from the verification of both the geometric and now the mechanical repeatability of part properties agree with the evaluation of the modified ED equation. The dome shape generated in the simulation was found to occur in all accessed cases Furthermore, the mechanical properties align with the prediction, despite the coupled non-linearity between ED and mechanical properties.

There existed additional trends in the data that were not predicted by the modified equation, the most prominent of these trends was a variation in the mechanical properties from the left to right of the build plate. This is likely due to effects related to either the deposition, transportation or compaction of the powder from the layering mechanism. This trend adds uncertainty to the results, however, it cannot be removed due to the configuration of the machine.

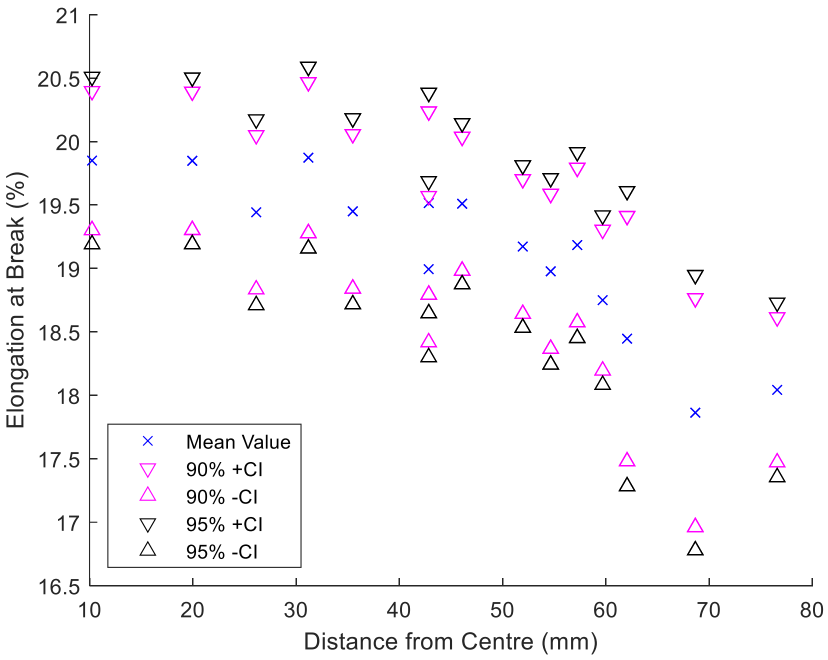

Figure 99: CoCr Base Case Elongation

The elongation plot shows a clear decrease in the mean value as the samples are taken further from the centre of the build plate. This is supported by the confidence intervals becoming completely divergent beyond the 68mm distance grouping. At this point, there exists no overlap at either the 90% or 95% confidence intervals. This means that it is statistically unlikely that the samples could have the same mean by pure random variation in the sampling.

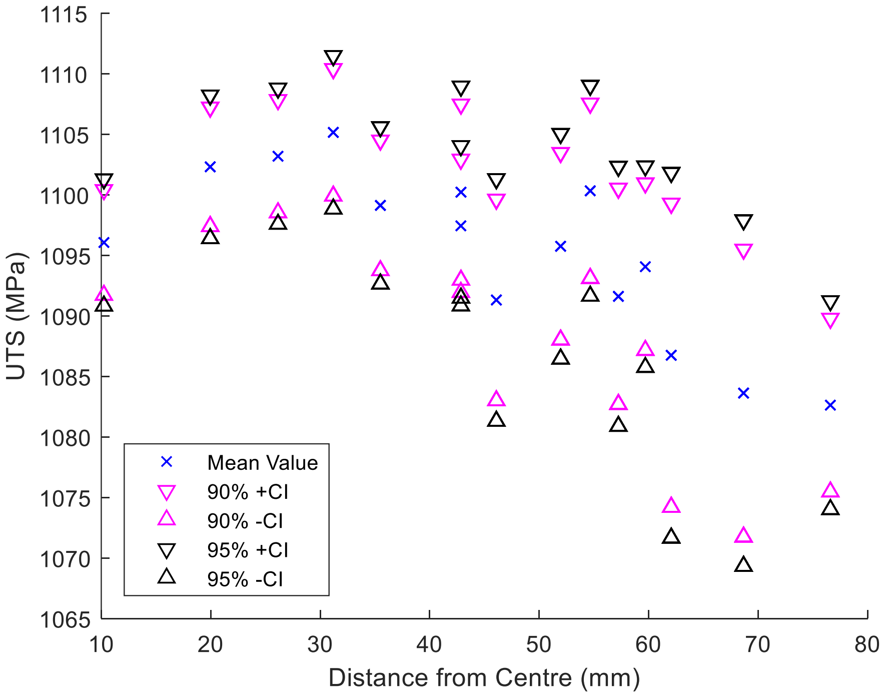

Figure 100: CoCr Base Case UTS

The UTS results from the first build demonstrate the same reduction in performance at the edge of the build plate when compared to the centre, however in this case it is a weaker correlation. This is due to the confidence intervals still overlapping at the 95% significance level. There is a number of possible reasons for this, the foremost for the remaining overlap is that the central sampling group was not the best performing sample group in the UTS data sets. The grouping had a lower mean than the next six groupings. If the initial central region is ignored, then the second to fourth groupings are significantly different from the centre sample grouping. The central grouping does have a confidence interval overlap with the apparently better performing samples. This means that the difference between them may still be within the random variation present in the system, limiting the strength of conclusions that can be made in this case.

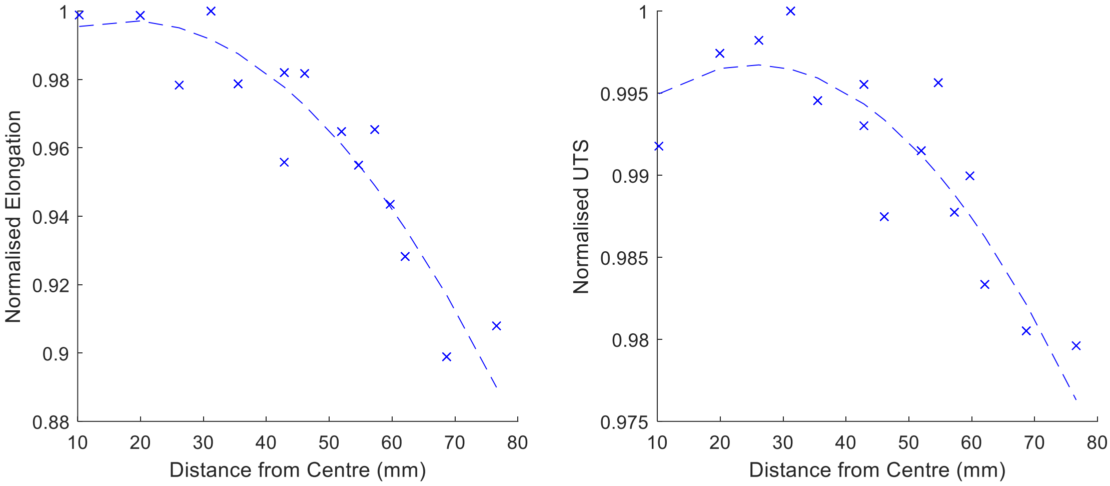

Figure 101: CoCr Base Case Normalised fitted plots

Comparing the two mechanical properties that were examined, it is evident that in this CoCr material, the elongation has a more significant reduction in performance when normalised by the maximum value. The mean elongation for the fitted curve, based on this round of testing, showed a greater than 10% reduction in performance at the corner of the build plate relative to the centre. The UTS only reduced by 2.4%, demonstrating that it is less influenced by the change in location.

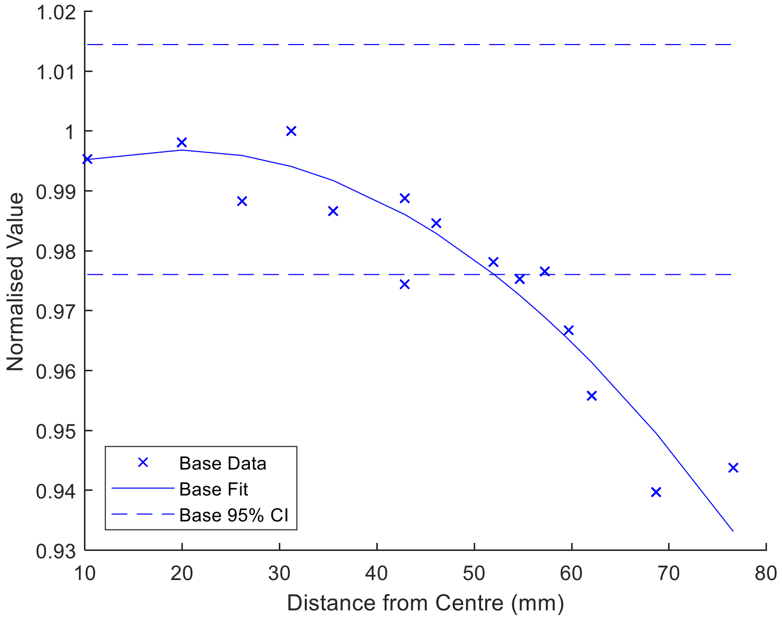

Figure 102: CoCr Base normalised fitted plot with central CI Intercept

Figure 102 shows the effect of combining the normalised mechanical properties, to form an overall indicator of the mechanical properties over distance from the centre. The fit crosses the threshold of the confidence interval set about the central location at 52mm from the centre. This shows that samples further than 52mm away from the centre are likely to have significantly different mean properties. This radius of leads to a significant area of the build plate falling outside this performance envelope. Examining the overall build plate, this 52mm criteria would leave 56.6% of the plate providing poor overall repeatability.

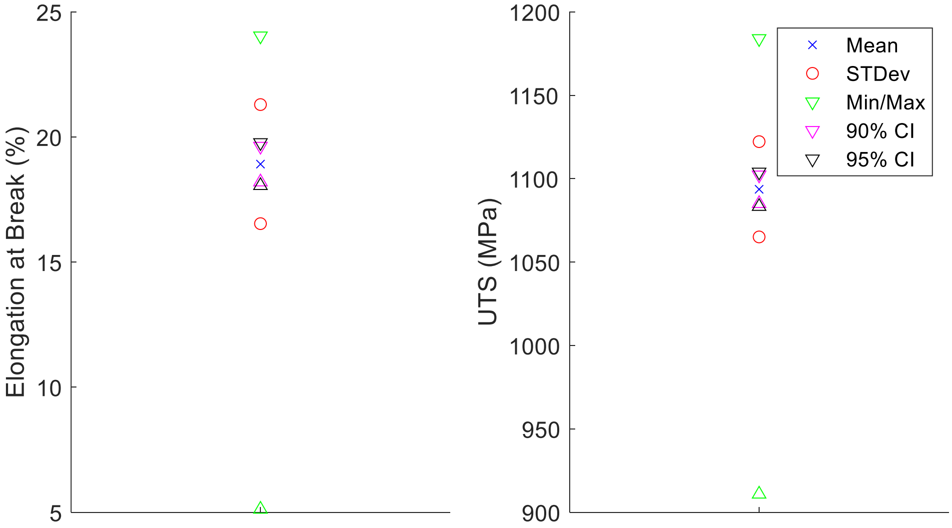

Figure 103: CoCr base case overall build properties

	Mean	STDev	Min	Max	90% CI	95% CI
Elongation (%)	18.91	2.38	5.12	24.04	±0.71	±0.86
UTS (MPa)	1093	28.6	910.9	1184	±8.6	±10.3

Table 12: CoCr Base Overall Build Properties

When evaluating the full build plate, not just the locations, the extent of the repeatability issue can be clearly seen. The full build data is synopsised in Figure 103 and Table 12.

A notable factor present in the data is the large range in the mechanical values, demonstrating significant variation is present beyond what the large standard deviations would suggest. The coefficient of variations for this base case is 0.026 for UTS and 0.126 for elongation.

6.1.2 CoCr corrected parameter set build

The first trial of correcting for the locally variant energy density by using the new energy density equation was also completed in CoCr using the same machine, grade of powder and set up as the original validation.

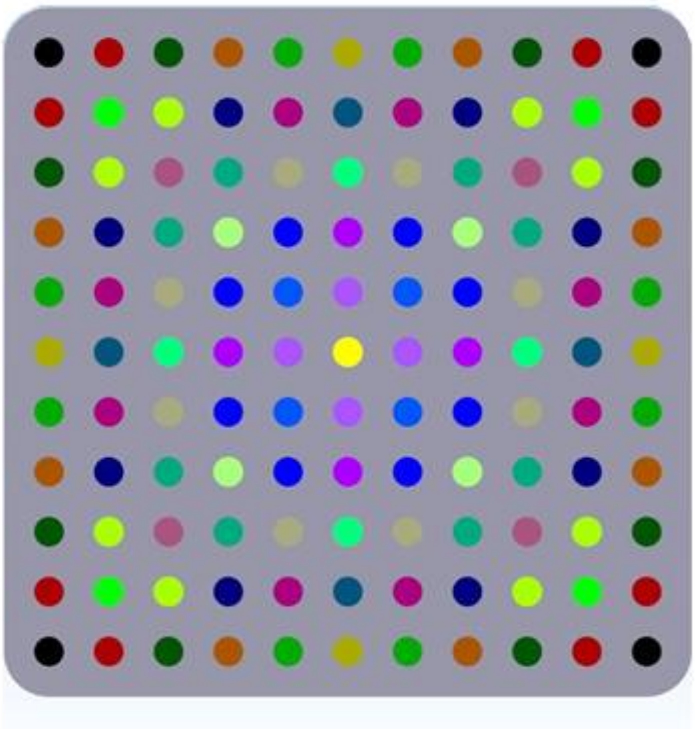

Figure 104: Modified build families

A new set of locally designated process parameters with modified scan speed setpoints distribution from 2400mm/s at the edges to 2500mm/s in the central region was created, hereafter referred to as the corrected case. The process parameter families were named sequentially starting on the top left with “a” and continuing with each new set gaining the next letter finishing at “u” in the central position. The samples are colour coded in Figure 104, to show the different parameter families.

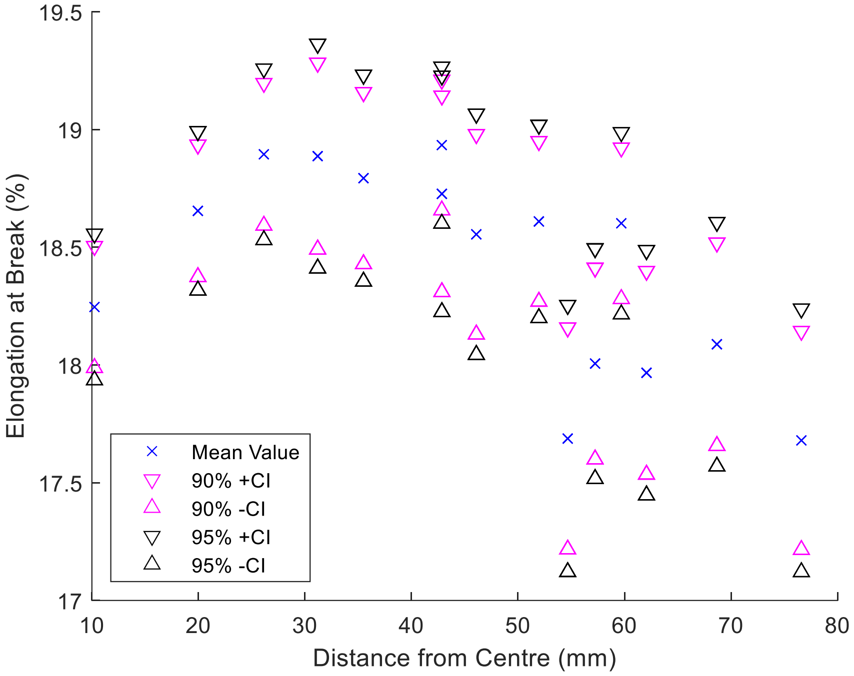

Figure 105: CoCr corrected case elongation

The elongation data from this corrected build is shown in Figure 105. The confidence intervals of the groupings have significant overlap in most cases. This includes the corner grouping and the central grouping not being different in a statistically significant manner. However, there are groupings in the transition between the centre and corner that are statistically different and improved over either the centre or corner cases. This is not predicted by the modified energy density and could be an indication of further sources of variation that are not accounted for currently.

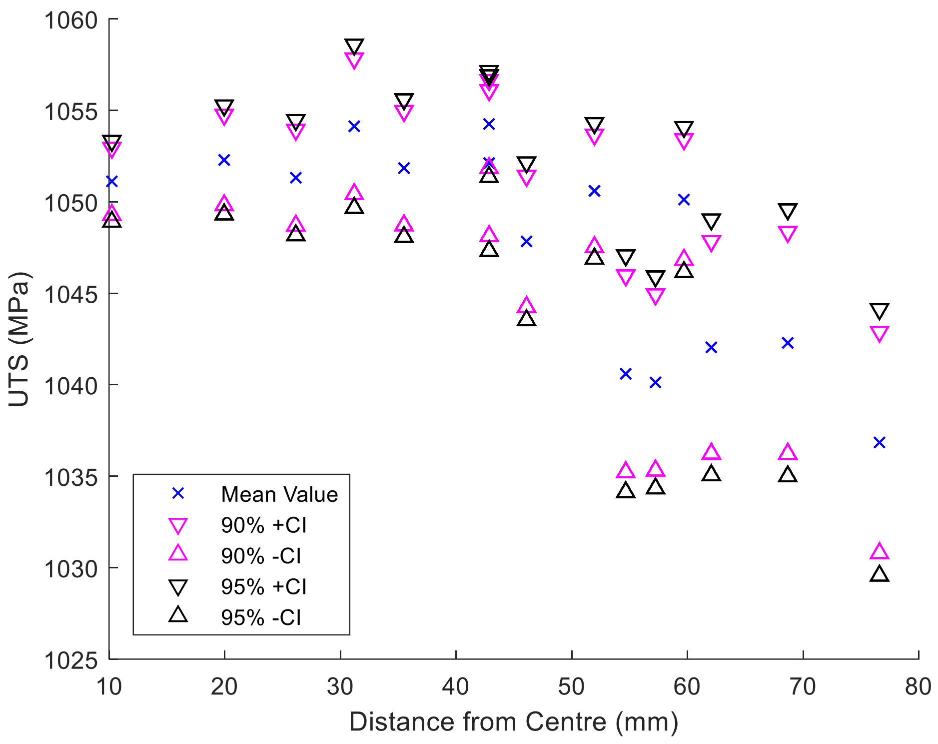

Figure 106: CoCr corrected case UTS

The UTS data however now demonstrates a statistically significant difference in far from centre samples. There is a noticeable reduction in the range of confidence intervals present in this build when compared to the base build. The contracted confidence intervals lead to a greater sensitivity to differences as we can be more confident that the difference is real and not an artefact of the sampling method or uncertainty in the means of the samples taken.

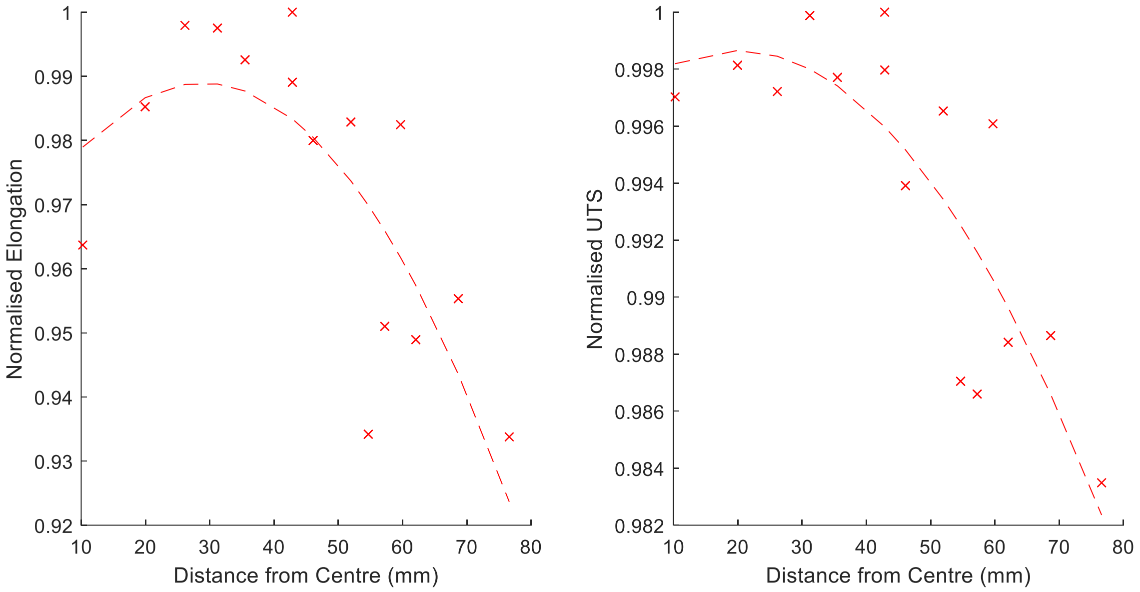

Figure 107: CoCr corrected case normalised fitted plots

Comparing the two mechanical properties once again normalised by the maximum value. The mean elongation for the fitted curve based on this round of testing showed a less than 8% reduction in performance at the corner of the build plate relative to the centre for elongation. The UTS also experienced a reduction of 1.8% again demonstrating that it is less influenced by the change in location.

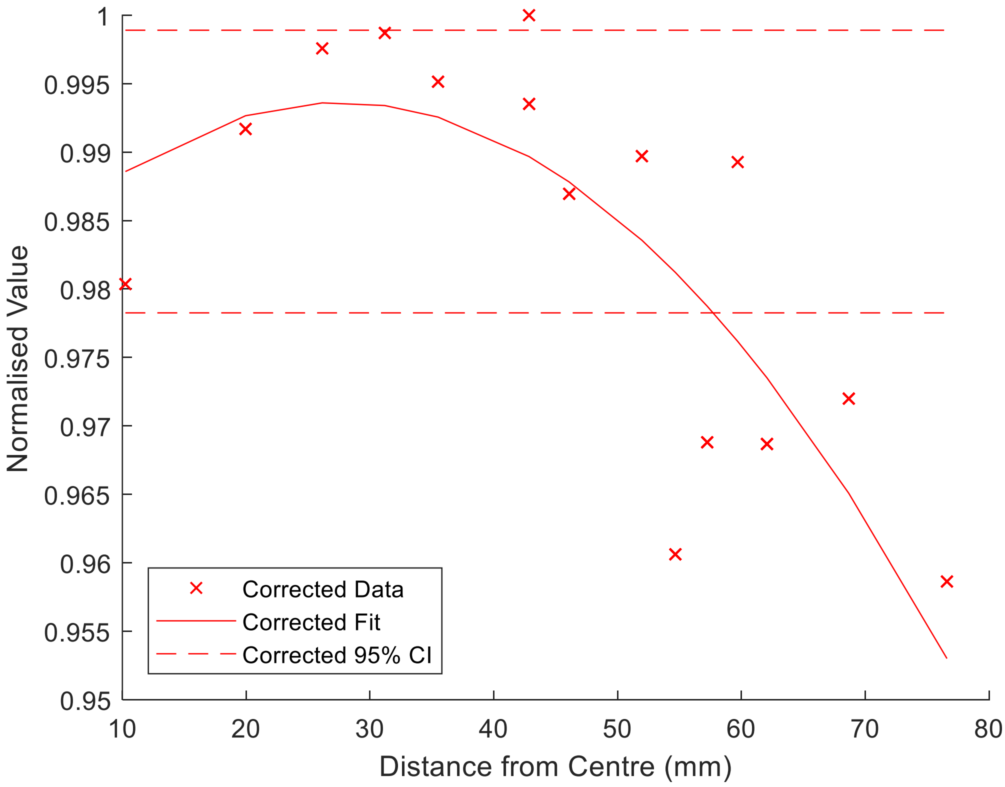

Figure 108: CoCr corrected case normalised fitted plot with central CI intercept

When examining the combined normalised mechanical properties for this build in Figure 108, it is evident that the plotted fit has a weaker correlation than was present in the base build. The fit crosses the threshold of the confidence interval set about the central location of 58mm from the centre. The confidence interval that is being crossed is already smaller (±0.010) than the base build (±0.019). This in effect shows that the corrected build still has some variation affected by location, however it is much reduced. The larger area of within the confidence interval also leads to a decrease in the poor repeatability area to 46.1% of the total build envelope.

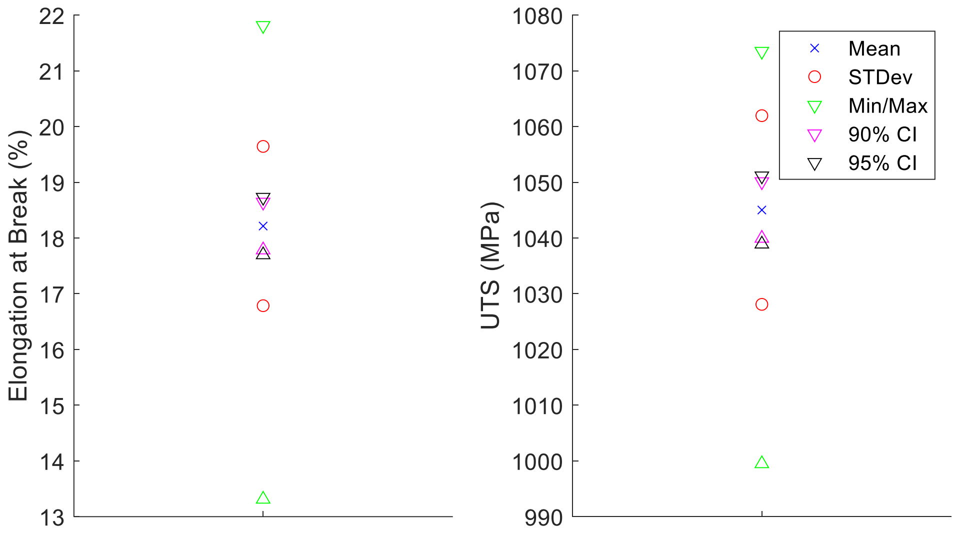

Figure 109: CoCr corrected case overall build properties

	Mean	STDev	Min	Max	90% CI	95% CI
Elongation (%)	18.21	1.43	13.31	21.81	±0.43	±0.52
UTS (MPa)	1045	16.9	999	1073	±5.1	±6.1

Table 13: CoCr corrected case overall build properties

The full build data is synopsised in Figure 109 and Table 13

The synopsised tensile test results for both the base and corrected cases are shown in Figure 110 and further tabulated in Table 14.

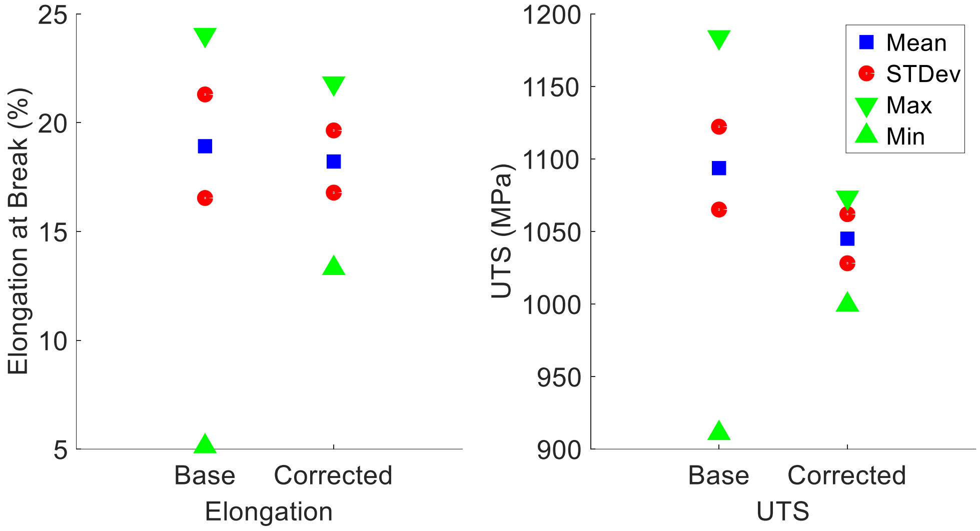

Figure 110: CoCr combined results

	Mean	**STDev**	**Max**	**Min**
Base UTS (MPa)	1093	28.6	1184	910
Base Elongation (%)	18.9	2.4	24.0	5.1
Corrected UTS (MPa)	1045	16.9	1073	999
Corrected Elongation (%)	18.2	1.4	21.8	13.3

Table 14: CoCr combined results

The results show a clear improvement in repeatability for the corrected case compared to the base case. For the corrected sample set, the standard deviation of the mechanical properties was reduced by approximately 40% for both UTS and elongation giving more consistent parts. This is further reinforced when examining the range of these mechanical properties, not just the standard deviation. There exists a significant reduction of the range for the corrected case which demonstrates increased repeatability across the build volume. The range in UTS reduces from 274MPa to 84MPa, while the range of elongation reduces from 18.9% to 8.5%.

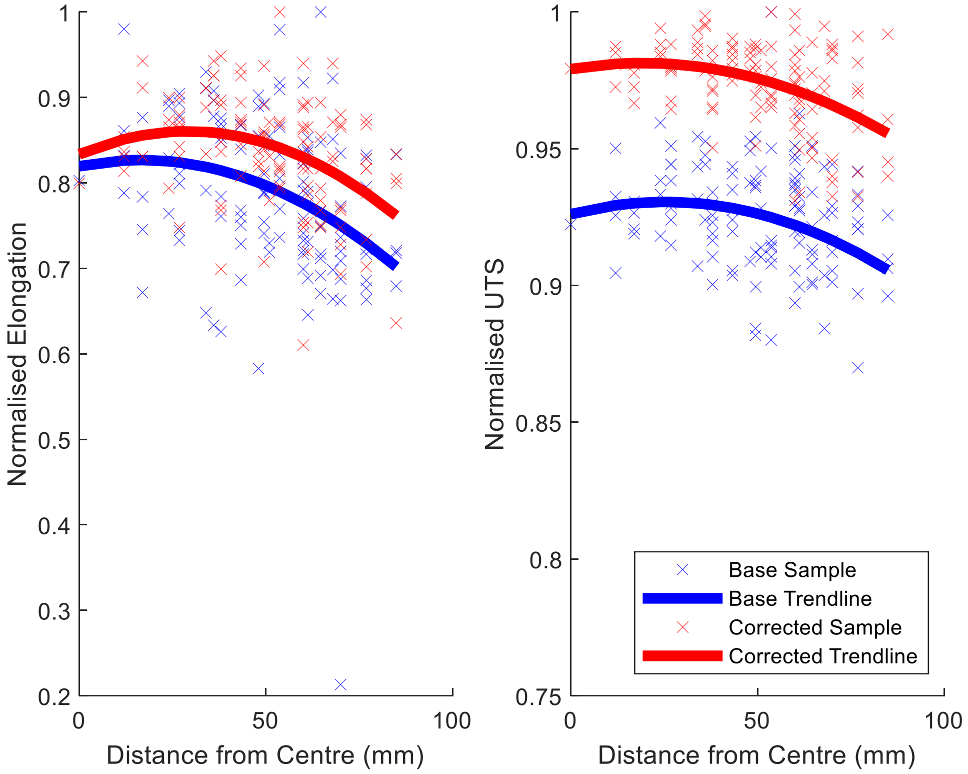

Figure 111: CoCr comparison normalised fitted plots

Examining the normalised mechanical properties of the two builds together is shown in Figure 111. The base case is shown in blue, and the corrected case is shown in red. As we are looking at normalised properties, the plot being closer to 1 would show improved repeatability. It can be seen that in both UTS and elongation cases that the performance loss from the centre to corner is reduced in the corrected build. This improved performance is present over the entire range of samples.

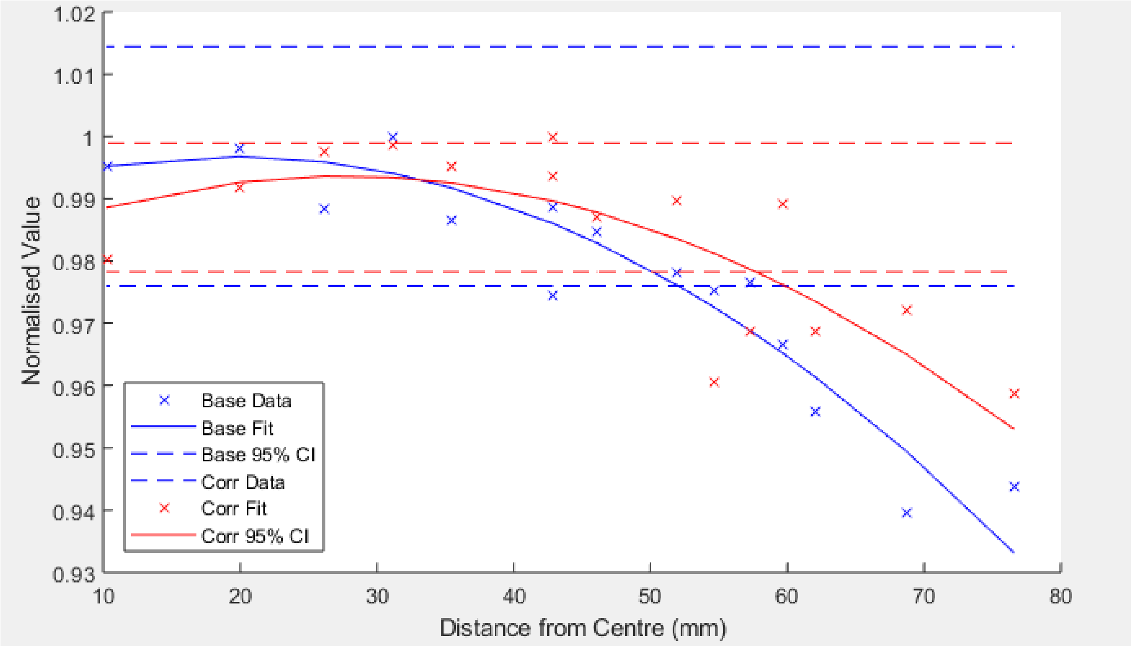

Figure 112: CoCr combined normalised mechanical properties relative to the distance from the centre

Figure 112 shows the combined normalised properties. It can be seen that the mechanical properties decrease far from the centre of the build plate in both cases. The fitted trends show that, while this effect is still evident in the corrected case, the magnitude of the decrease is reduced. The onset of the reduction is also extended; the base case crosses the confidence interval of its central value at 52 mm, whereas the corrected case leaves its already tighter confidence interval at 58 mm. This represents a 24% increase in the area of the build plate providing more consistent mechanical properties.

The difference in performance for the two builds was confirmed by carrying out an F-Test on the data and, independently, both UTS and elongation showed statistically significant improvements. The tests are tabulated below in Tables 5 & 6.

	Base Case	***Corrected Case***
Mean	18.91777	18.21436
Variance	5.66	2.041916
Observations	121	121
df	120	120
F	2.771907	
P(F<=f) one-tail	2.4E-08	
F Critical one-tail	1.351886	

Table 15: F-Test for Elongation CoCr

	Base Case	***Corrected Case***
Mean	1093.674	1045.023
Variance	815.724	286.6356
Observations	121	121
df	120	120
F	2.845857	
P(F<=f) one-tail	1.11E-08	
F Critical one-tail	1.351886	

Table 16: F-Test for UTS CoCr

The coefficient of variation for the corrected cases are 0.016 for UTS and 0.076 for elongation, compared to the base case are 0.026 for UTS and 0.126 for elongation. This, while not reaching the level of repeatability in traditional wrought samples, is a clear improvement in both mechanical properties cases.

6.2 Tensile Testing Results of 316L Builds

To further validate the conclusions and applicability of the new energy density equation, and to guide process parameter selection, a second study was undertaken that followed the same methodology as the CoCr. This repeated experiment shows that the results are repeatable and not an artefact of individual builds, while also demonstrating the universal nature of the improvement to the SLM process as a whole.

To contrast to the hard and brittle nature of CoCr, a softer and more ductile material was used for this experiment. 316L was selected as it is available from the same material supplier and has defined parameters readily available. The key expected mechanical properties of the two materials are shown in Table 17.

	Density (g/cm^3)	**Tensile Strength (MPa)**	**Elongation at Break (%)**
CoCr	8.5-8.8	1200±100	11±3
316L	7.91-7.95	550±50	40±20

Table 17: Mechanical Properties comparison [156]

6.2.1 316L base parameter set build

The first build in 316L was to repeat the verification build carried out in CoCr earlier. The samples were produced in the same ProX DMP 200 machine using 316L powder (3D Systems LaserForm 316L (B)). The purpose of this build was to investigate any material-specific effects that may have been present in the process. The powder morphology between the two is directly comparable with the same D10, D50 and D90 measurements. This allows for the only pertinent change between the two cases to be the material itself.

The first clear indication of differences between the two materials was evident before any tensile testing was carried out. The base build had several individual samples fail during the printing process, which was primarily in the form of delamination and dislocation between the layers in the upper gauge to the grip section.

The failures are likely due to lack of fusion defects such as porosity. This concept will be thoroughly invested in sections 6.5 Microstructure Results and 6.6 Computer Tomography Results. These defects occur when a poor interlayer bond is created. Mukherjee et al. created a calculated lack of fusion index that showed 316L to be particularly vulnerable to this failure when compared to other common AM alloys [157]. Furthermore, this effect is more pronounced at lower energy inputs. This can be seen in Figure 113, where layer fusion (LF) is the depth of melt pool penetration divided by the layer height. This connection to energy input would lead to a higher likelihood of this defect occurring at the edges of the plate where lower energy density is predicted.

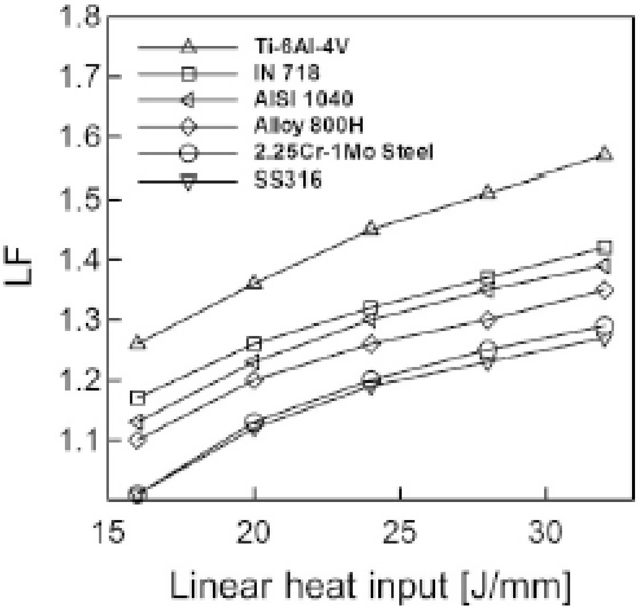

Figure 113: LF against linear heat input, taken from Mukherjee et al.[157]

The location of the dislocation at the gauge to grip transition rendered samples with dislocation unsuitable for comparison with the non-dislocated samples. They were tested as far as possible and found to have on average a 20% lower UTS, 50% lower elongation and standard deviations an order of magnitude larger than the normal samples.

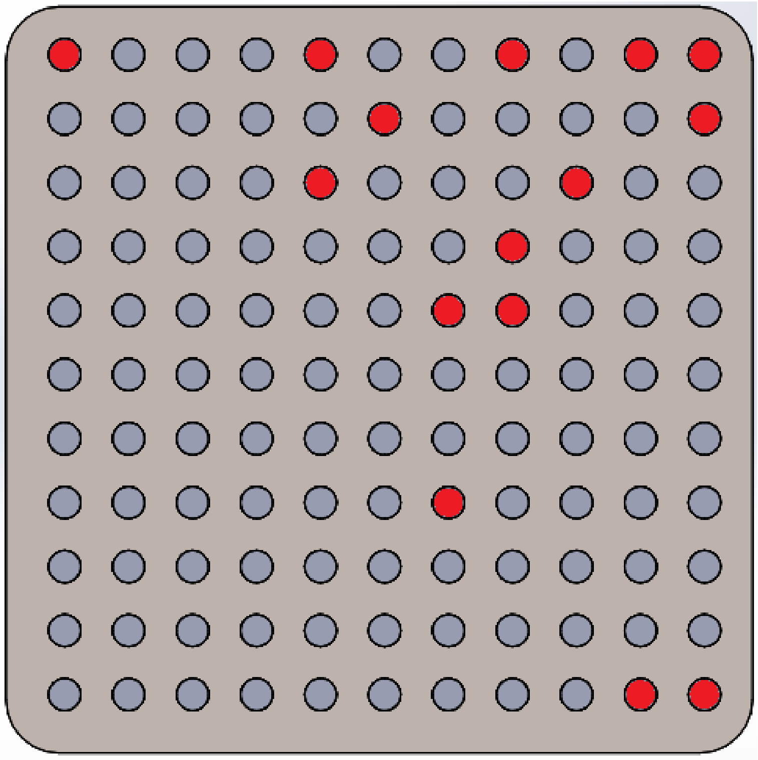

Figure 114: Failed tensile specimens 316L base case

In total, the base build had 15 samples fully discounted from the comparisons. The samples eliminated were spread across the build plate so no one area of the build plate had a complete loss of data, as shown in Figure 114. There was a greater number of samples eliminated away from the centre of the build, however with a greater number of samples present in these areas, no strong conclusions can be drawn from their distribution.

It can be inferred that the samples on the right side are more likely to fail, however, there are failures across the full width of the plate which reduce the likelihood of this being the only reason. This could be due to the layering mechanism where the roller returns over the plate but this effect cannot be separated from the process.

The samples that were adjacent to eliminated samples showed no issues. The spacing between samples was sufficient to prevent any defected samples that intruded into the gaps between samples from interacting with the normally produced samples.

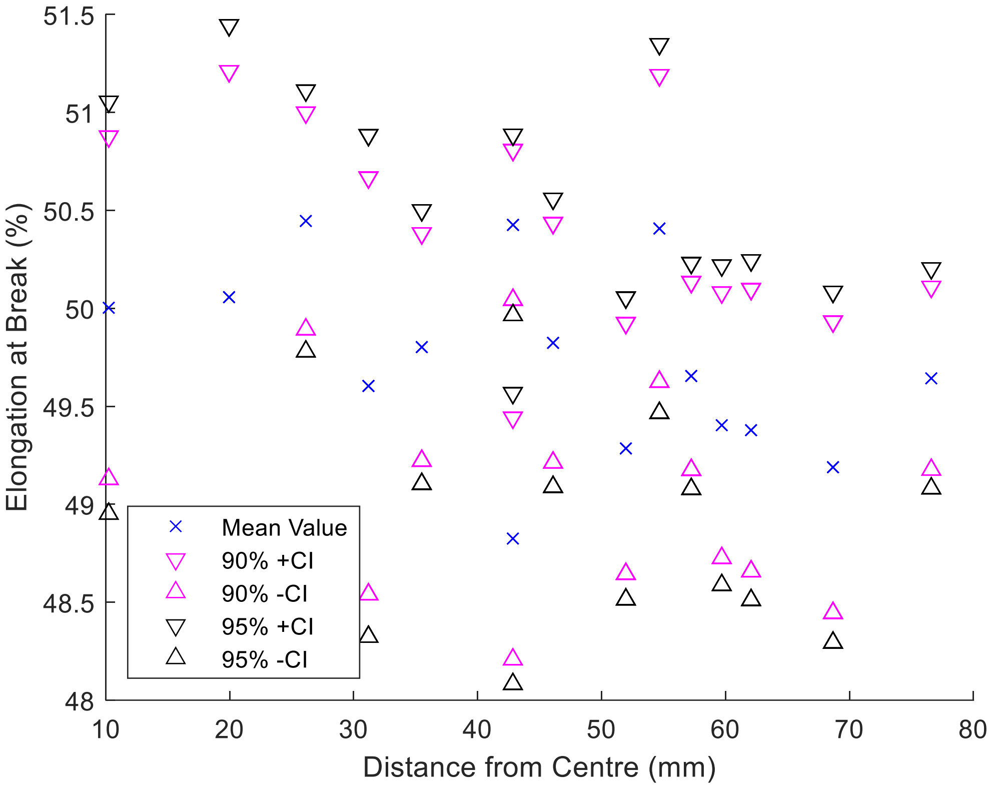

Figure 115: 316L base case elongation

The elongation data at break for the base 316L provided unexpected results. There exists no statistical difference between the centre and the far from centre samples. The confidence intervals for the furthest cases are wholly contained within the confidence interval of the central data grouping. Every data grouping has at least a partial overlap with both the centre and far from centre groupings showing no statistical variation across the build plate in the elongation data.

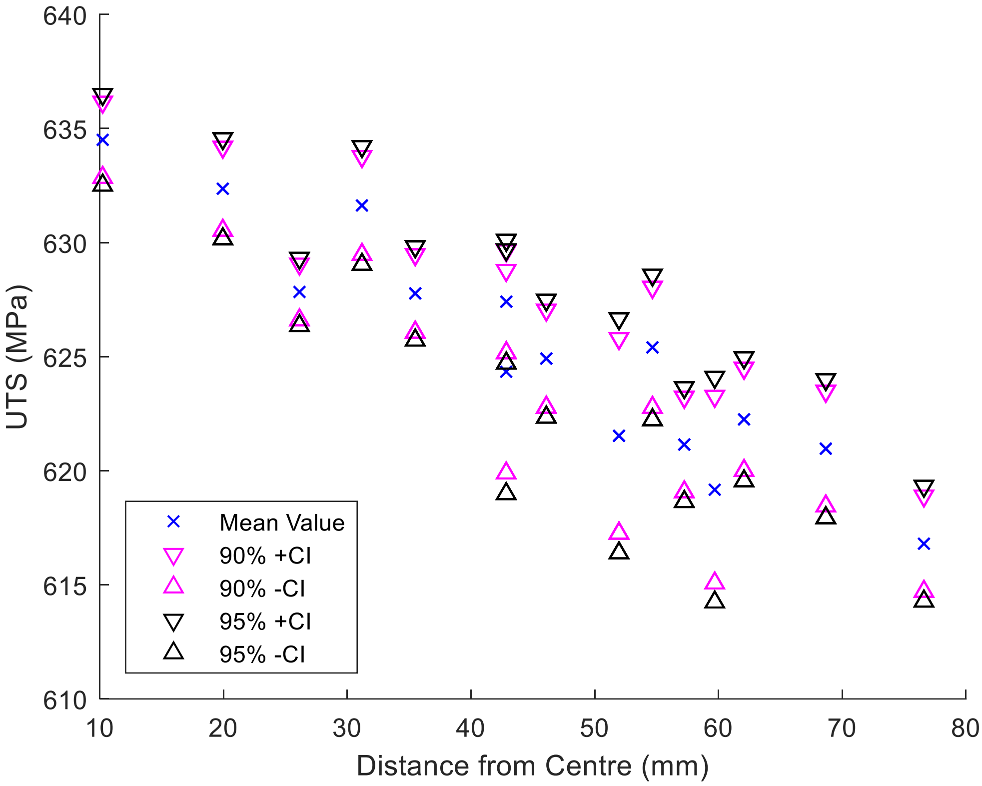

Figure 116: 316L base case UTS

The UTS data is in sharp contrast to the elongation data. There is a very clear progression in the UTS reducing as the samples move further from the centre. While each grouping maintains a confidence interval overlap with its adjacent groupings, the clear steps between the centre and edge show strong statistical difference. This difference is stronger than any previously found in either CoCr case. Statistically, the central grouping is significantly stronger than the 46mm grouping which is in turn significantly stronger than the furthest from the centre case.

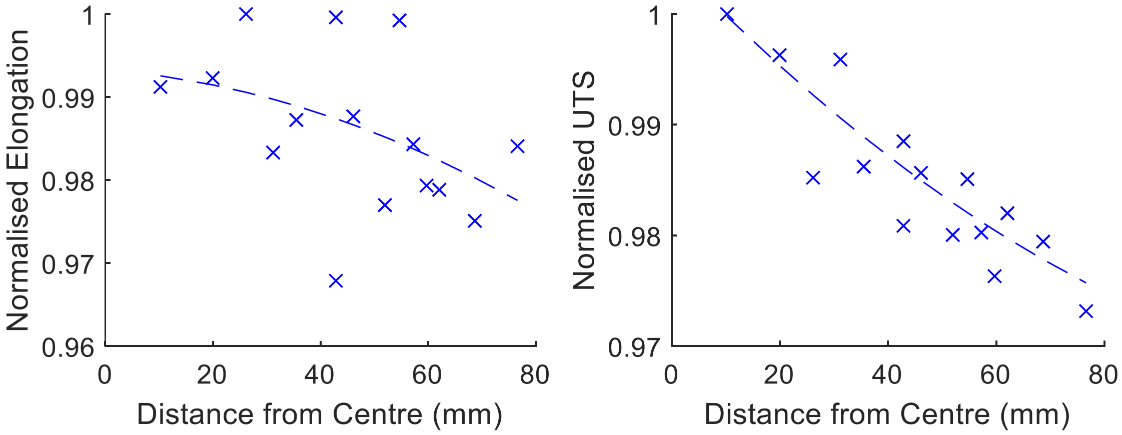

Figure 117: 316L base case normalised fitted plots

The fitted plots for the two mechanical properties show a performance decrease in both of 2.5% from the centre to the corner of the build plate. This decrease is much less than was expected and was present in the CoCr samples. This verified the need for a new validation build for direct comparisons in 316L.

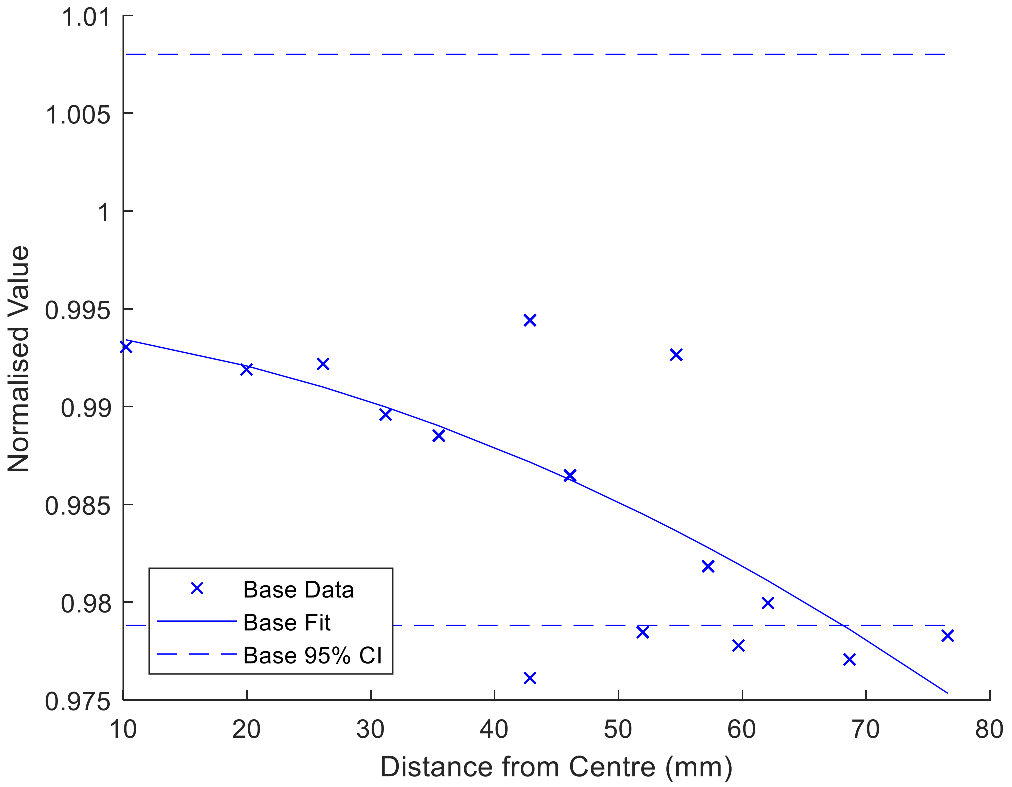

Figure 118: 316L base case normalised fitted plot with central CI intercept

When examining the combined normalised mechanical properties for this build, the combined properties are reduced primarily by the strong decrease in the UTS. The fitted plot remained within the confidence interval of the central grouping dramatically longer than was found in either of the CoCr builds. The fit only exits at the 69mm point.

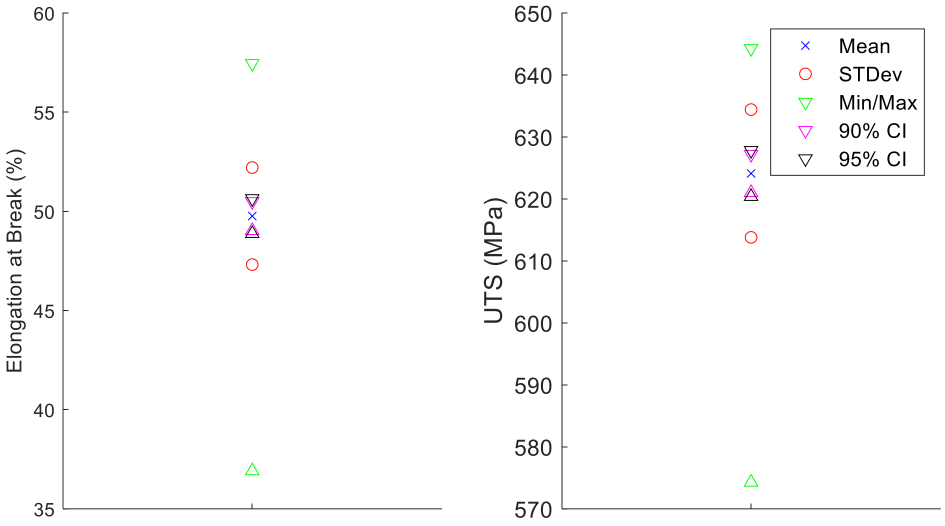

Figure 119: 316L base case overall build properties

	Mean	**STDev**	**Min**	**Max**	**90% CI**	**95% CI**
UTS (MPa)	624	9.8	644	574	±2.94	±3.5
Elongation (%)	49.7	2.39	57.4	36.9	±0.72	±0.86

Table 18: 316L base case overall build properties

The whole build information is synopsised in Figure 119 and Table 18. From this synopsis, it can be seen that even in this base case the mechanical properties for 316L are more consistent than was found in the CoCr cases. This consistency in properties was at the expense of print consistency, as there were part failures in the 316L with no part failures in the CoCr builds. It is possible that what would have been the worst-performing samples in 316L did not reach the testing stage and this would artificially inflate the repeatability of 316L by only measuring the “good samples”. This also gives another metric that can be examined for improved repeatability in 316L that was not available in CoCr for overall print success. The coefficient of variations for this base case is 0.016 for UTS and 0.048 for elongation.

6.2.2 316L corrected parameter set build

The second build in 316L was the build with modified scan speed to attempt to correct the energy density discrepancy anticipated from the base settings similar to the second CoCr build. The experiment used the same machine, grade of powder and set up as the base parameter set validation. The builds were run sequentially to reduce the effect that any other uncontrolled factors may have had on the results.

As was the case in the base parameter set, some samples needed to be excluded from the tensile testing due to localised print failures. There was however a marked difference in the magnitude of failures present.

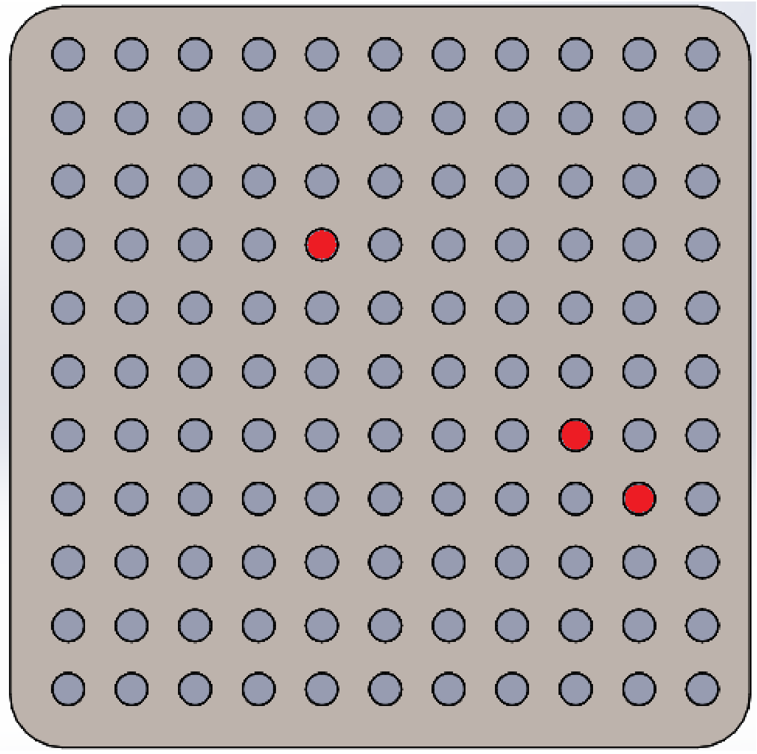

Figure 120: Failed tensile specimens 316L corrected case

Of the 121 samples that were designed to print, only 3 failed under this corrected case, as shown in Figure 120. The file was identical to the base case with only the speed parameter changed. There was no modification to the .stl files or support method. No location failed in both cases meaning that the issue is not symptomatic of a machine or slicing issue. The reduction in failures gives credence to the hypothesis that a reduction in fusion defects was caused by lower energy inputs at the edge in the base case. The reduction in failures also demonstrates a direct improvement in overall process repeatability.

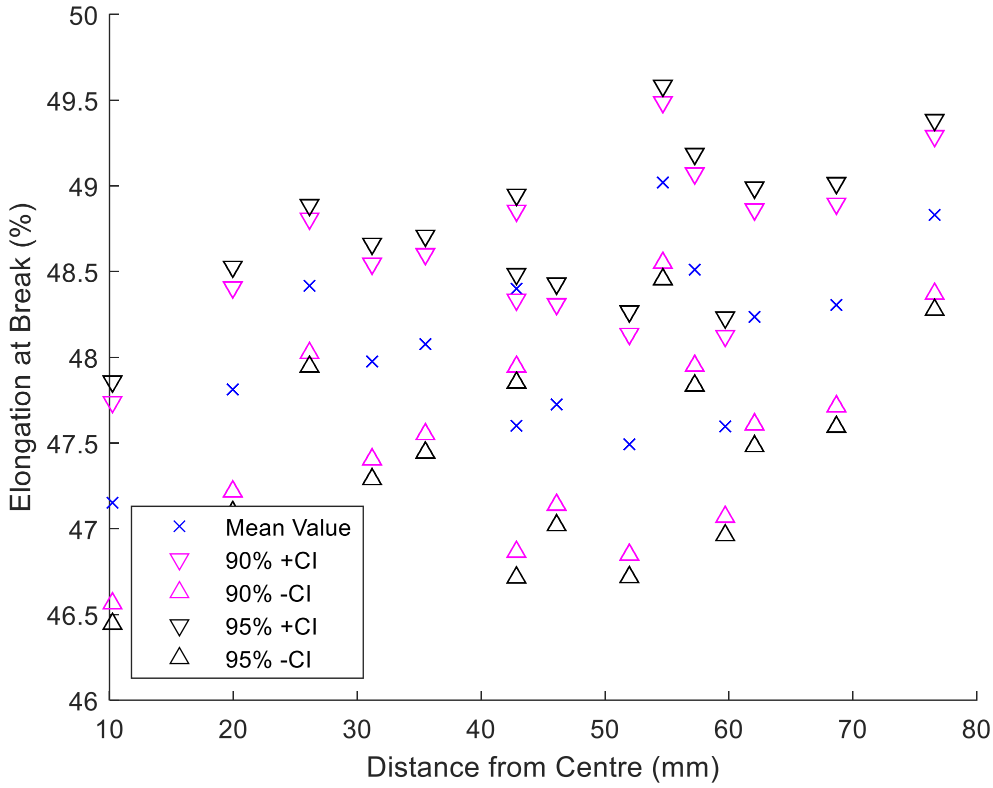

Figure 121: 316L corrected case elongation

The elongation data from the corrected case shows an unexpected result. There is a slight but statistically significant improvement in elongation from the centre to the far from the centre region. While the individual grouping confidence interval has reduced, that does not explain the new gap. One possible answer is that the apparent consistency of the base case was an artefact of the discounted samples hiding the drop in performance, however, it would not be reasonable to use this explanation to disregard the base repeatability or this apparent improvement. The effect of adding the discounted samples would cause the base case to have a significant reduction in apparent repeatability. However, as there were fewer samples discounted in this case and none are in central or the furthest from centre groupings, it would not remove this data trend. This data set shows that there is likely to be other effects governing the elongation mechanical properties beyond the scope of what has been investigated in this study.

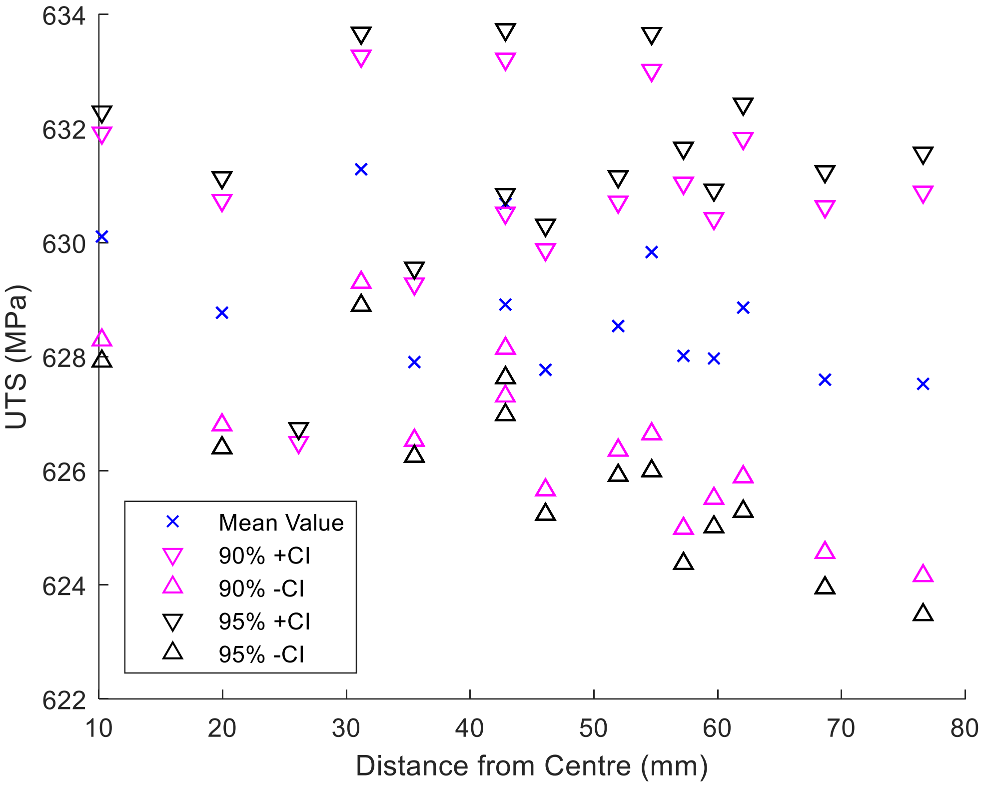

Figure 122: 316L corrected case UTS

The UTS data from the corrected case shows no significant difference between the central and edge regions. Almost all of the data groupings except for the 28mm distance have CI overlap with every other grouping. This is in sharp contrast to the UTS of the base case where a clear downward progression of performance was observed. This shows that in this case, the correction was able to nearly completely eliminate the drop in performance observed in the base case.

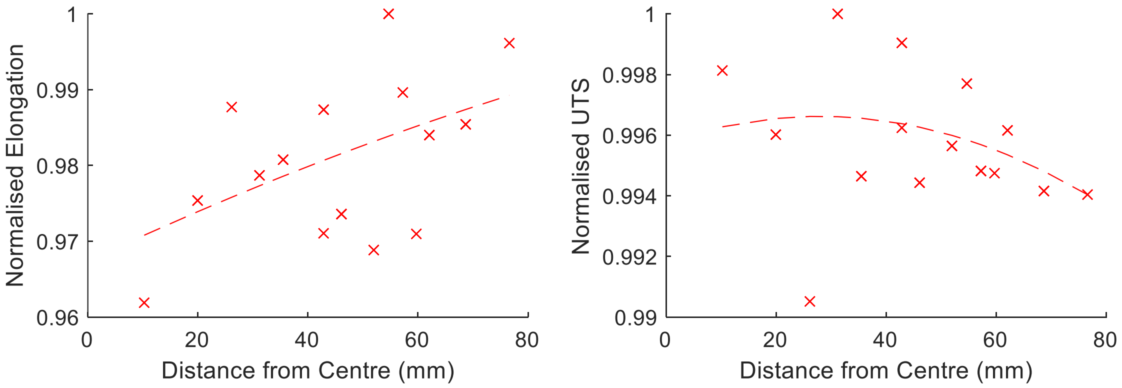

Figure 123: 316L corrected case normalised fitted plots

The normalised fitted plots for the corrected case show a performance increase of 1.9% in the elongation case. When all the data is fitted for the UTS case, there is a drop of 0.2% from the centre to the edge in the line of best fit. This is well within the 0.8% confidence interval for the data. This change can thus be discounted as a fitting artefact rather than an actual drop in performance.

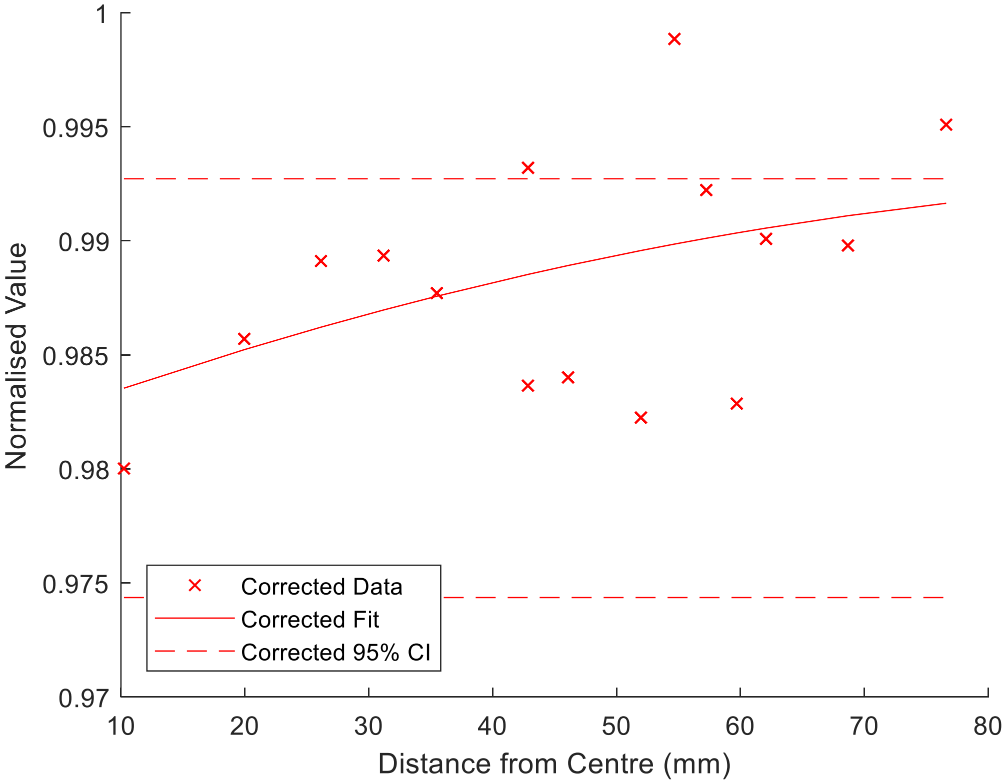

Figure 124: 316L corrected case normalised fitted plot with central CI

The combined normalised mechanical properties when plotted give Figure 124. The fitted plot trends upwards mostly due to the elongation improvement present in the corrected case but this is mediated by the very consistent UTS data. A key finding from this plot is that, over the full range of the build plate, the fitted plot does not exit the CI of the first fitted point. As the sample groupings covered the full range of the build plate, this shows that there is no expected statistically significant change in mechanical properties over the full build plate. This is strong evidence that improved repeatability was achieved using this correction process.

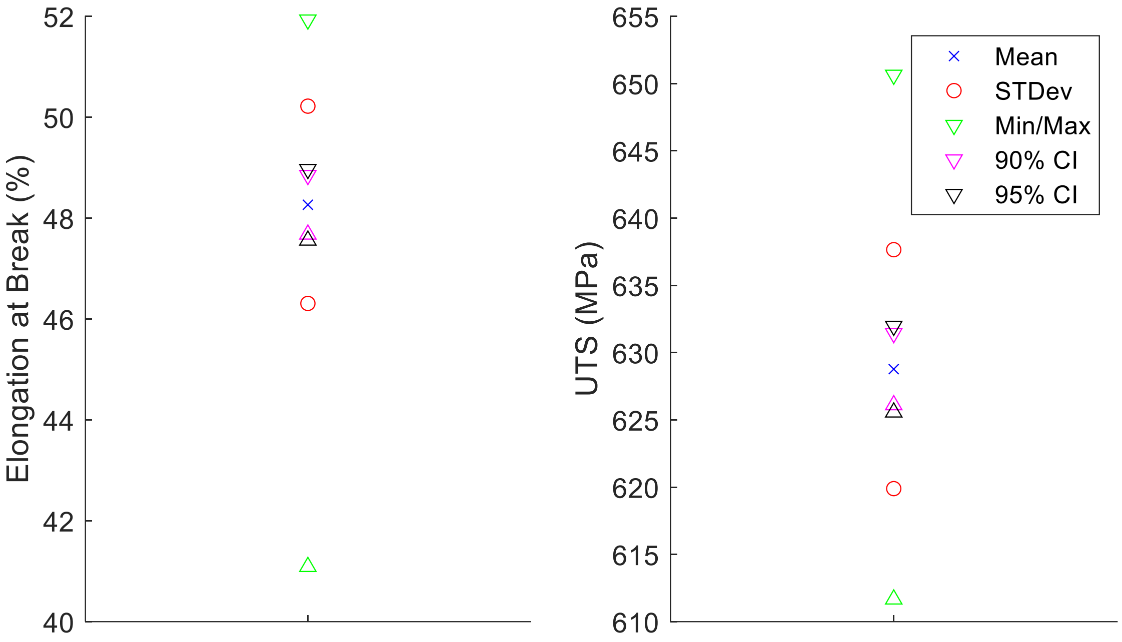

Figure 125: 316L corrected case overall build properties

	Mean	**STDev**	**Min**	**Max**	**90% CI**	**95% CI**
UTS (MPa)	628	8.9	650	611	±2.6	±3.2
Elongation (%)	48.3	1.96	51.9	41.0	±0.59	±0.71

Table 19: 316L corrected case overall build properties

The full build data is synopsised in Figure 125 and Table 19.

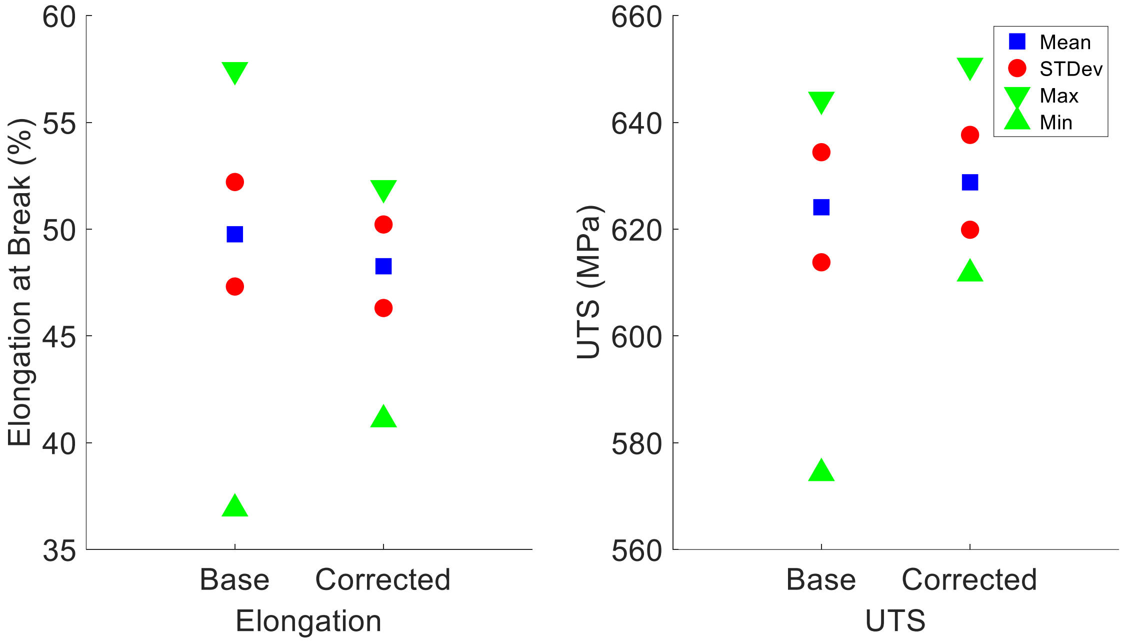

Figure 126: 316L combined results

	Mean	**STDev**	**Max**	**Min**
Base UTS (MPa)	625	9.8	644	574
Base Elongation (%)	49.7	2.39	57.4	36.9
Corrected UTS (MPa)	628	8.9	650	611
Corrected Elongation (%)	48.3	1.96	51.9	41.0

Table 20: 316L combined results

The overall combined results show that in the 316L case there was an improvement in the standard deviation for both mechanical properties investigated by the tensile tests. The improvement was 10% in UTS and 20% in the elongation. This is a lesser improvement than what was found in the CoCr but it is still significant. The 316L samples in the base case were already more consistent than the CoCr base case and thus had less range for improvements to be made. There was a reduction in the range of results in the base to corrected cases from 70 MPa to 39 MPa in the UTS and 20.5% to 10.9% in elongation. The contracted ranges and reduced standard deviations show a significant repeatability improvement by using the corrected parameter set over the base set.

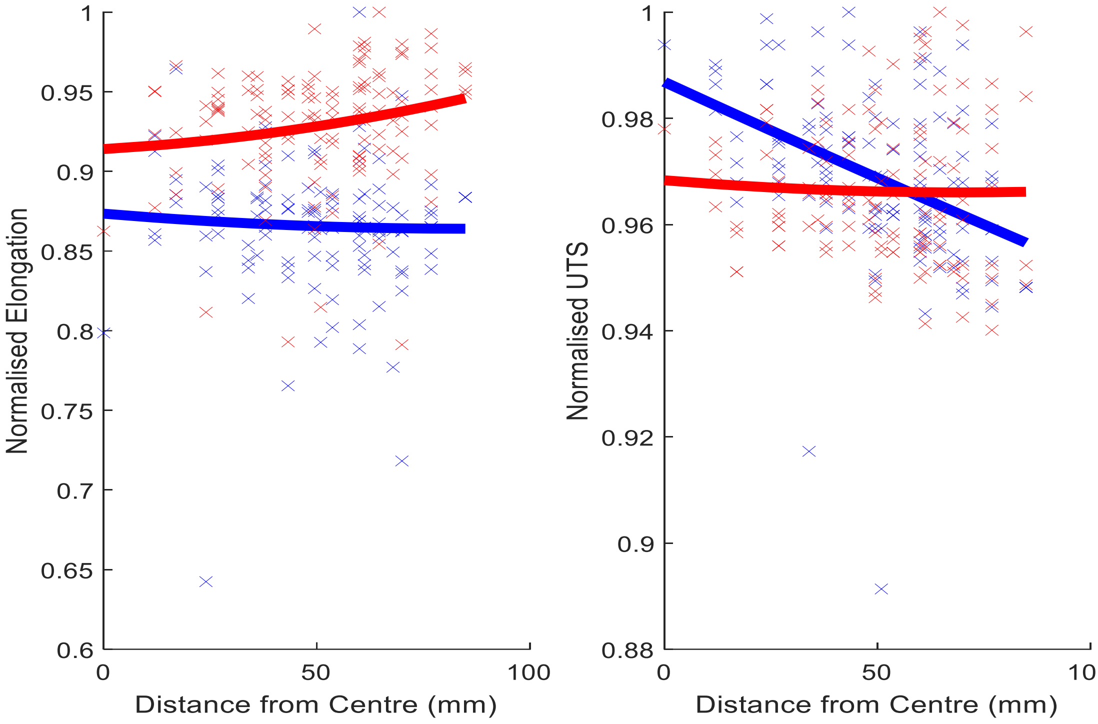

Figure 127: 316L comparison normalised fitted plots

Examining the normalised mechanical properties from both builds shows interesting comparisons. The elongation case has disagreement in the trends, with the base case having a slight reduction in properties away from the centre and the corrected case being the inverse. Following the traditional statistical goodness of fit term of R^2, raises concerns about the data. In the elongation case R^2 values of 0.0819 for the base case and 0.26 for the corrected case. The same R^2 issue occurs when looking at the corrected case for UTS (R^2 of 0.0642). This is due to the R^2 being a determination of its errors compared to a constant-only model, which merely predicts that everything will equal the mean [158]. To effectively understand the data and more importantly if there is a variation across the build plate, an F-test was conducted between the fit and a pure constant model, the results of which are shown in Table 21.

Trial	**R^2**	**F-test verses constant (p-value)**	**Determination**
Base Elongation	0.0819	0.599	Constant
Base UTS	0.889	1.89e-06	Variable
Corrected Elongation	0.26	0.165	Constant
Corrected UTS	0.0642	0.672	Constant

Table 21: F-test of fit against a constant model in 316L

The F-tests show that the elongation in both cases and the UTS in the corrected case do not fall beyond the p-value to reject the hypothesis that they are constant across the build plate. This is likely to lead to the improvement in the elongation to be rendered not statistically significant, which shall be confirmed by further F-test between the cases. The base case UTS meets the criteria determining that it is variable across the build plate. The corrected case UTS, however, has no statistical difference from a constant mechanical properties model across the build plate.

	Base Case	***Corrected Case***
Mean	49.73208333	48.27240466
Variance	6.188469574	3.907443854
Observations	105	118
df	104	117
F	1.58376417	
P(F<=f) one-tail	0.007952286	
F Critical one-tail	1.367749318	

Table 22: F-Test for Elongation 316L

	Base Case	***Corrected Case***
Mean	625.1692495	628.8111544
Variance	75.85827465	80.78121361
Observations	105	118
df	104	117
F	0.939058368	
P(F<=f) one-tail	0.372518208	
F Critical one-tail	0.728663121	

Table 23: F-Test for UTS 316L

The F-Tests for the 316L samples confirm that the improvement in repeatability for elongation was statistically significant. However, the UTS repeatability improvement does not meet the threshold for statistical significance on a global level. This was an unexpected result due to the improvement found in the consistency of the mean across the build plate for UTS already discussed. This rejection for the UTS case shows that while the mean was more consistent, the data was still had a similar level of variation about the mean values.

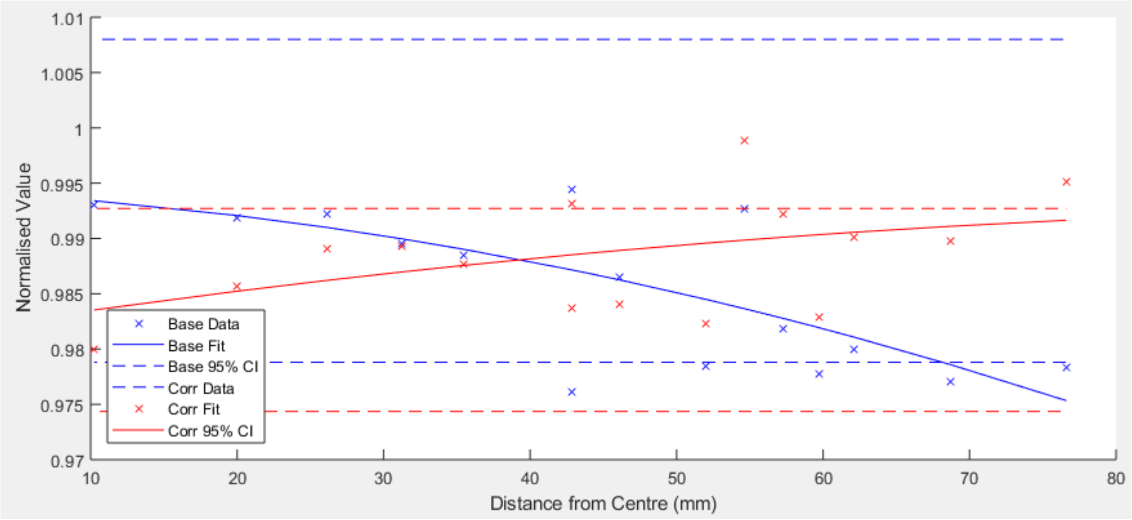

Figure 128: 316L combined normalised mechanical properties relative to the distance from the centre

Taking the combined mechanical properties with the confidence intervals for the central region, as was done in CoCr, we can see that the corrected case does not exit the CI of the centre over the entire build plate, whereas the base case does. This coupled with the F-tests is clear evidence that the corrected case substantially improved the overall consistency across the build plate. This is a clear improvement to the overall build repeatability.

The uncertainty still present for global samples is an area that needs to be further understood. This uncertainty shows that while the new ED equation was able to improve consistency and repeatability in many cases, it will not be a complete answer to the repeatability challenges present in AM.

The coefficients of variation for this corrected case are 0.014 for UTS and 0.041 for elongation.

6.3 Wrought Tensile samples

To allow for a direct comparison between AM produced parts and traditionally produced parts, a series of 10 tensile samples were created for CoCr and 316L. These samples were manufactured by machining wrought stock material to the standard dimensions. These samples were then tested using the same testing system and testing configuration as the AM produced parts.

It was discovered during the CoCr pull test that the clamping jaws of the Instron 8801 were worn and allowed the samples to slip. This caused the elongation data of the CoCr to be widely variable and inaccurate. This also led to two of the samples failing in the grips instead of the gauge and need to be discounted (highlighted below). The clamping jaws were replaced before the resumption of testing with the 316L samples.

CoCr		**316L**	
UTS (MPa)	**Elongation (%)**	**UTS (MPa)**	**Elongation (%)**
1436	25.1	807	58.5
1424	26.0	822	58.5
1436	29.1	811	58.7
1454	33.4	808	58.4
1447	28.9	810	58.0
1467	34.8	810	58.9
1440	29.2	825	59.2
1395	24.9	827	58.6
1260	9.6	807	58.9
772	6.3	835	59.6

Table 24: Wrought tensile sample data

The CoCr data from the remaining 8 samples gave a coefficient of variation of 0.014 for the UTS values which is in line with what was expected from the literature values. The coefficient of variation of the elongation was 0.11, which was significantly above the expected variation from literature. However, even assuming that the variation was not due to the grip issues, the value is still lower than the coefficient calculated for the AM parts.

The 316L data had a coefficient of variation of 0.012 for UTS and 0.007 for elongation. This elongation variation is slightly lower than the expected level based on the literature, but it does illustrate the consistency that is possible from the traditionally wrought materials. The combination of the results, from the AM samples and the wrought samples, clearly verify that the repeatability concern does exist in the AM process. The wrought samples also give a direct comparison point for any improvements that are made.

6.4 Tensile Testing Results Overall

The overall build properties show that on a full build scale there were significant repeatability improvements in both materials. This was shown by a contraction in the ranges for the mechanical properties and also in reductions of the standard deviations over the entire set of testable samples.

The improvements over the entire build are reinforced by examining closely the targeted deviation that was to be removed, which was a variation between the centre and edge regions of the build plate.

A corollary to a repeatable build plate is that it would give rise to the non-reject p-value when examining using the F-test against constant, as was done in the 316L tensile studies. All of the major overall data groupings were tested and the results tabulated in Table 25.

Material	**Trial**	**Property**	**R^2**	**F-test against constant (p-value)**	**Determination**
CoCr	Base	Elongation	0.863	2.41e-06	Variable
CoCr	Base	UTS	0.783	4.86e-05	Variable
CoCr	Base	Combined	0.886	2.18e-06	Variable
CoCr	Corrected	Elongation	0.616	0.00199	Variable
CoCr	Corrected	UTS	0.704	0.000365	Variable
CoCr	Corrected	Combined	0.628	0.00266	Variable
316L	Base	Elongation	0.0819	0.599	Constant
316L	Base	UTS	0.889	1.89e-06	Variable
316L	Base	Combined	0.52	0.0122	Variable
316L	Corrected	Elongation	0.26	0.165	Constant
316L	Corrected	UTS	0.0642	0.672	Constant
316L	Corrected	Combined	0.217	0.231	Constant

Table 25: F-test against constant for all data groupings

In all data groupings, the p-value increased from the base case to the corrected case, showing that overall the results move closer to a consistent value with the corrected process parameters. In the 316L cases, this improvement was sufficient to transition from location variable properties to being location independent (Constant).

Case	UTS	Elongation
Wrought CoCr	0.014	0.11*
Base CoCr	0.026	0.126
Corrected CoCr	0.016	0.076
Wrought 316L	0.011	0.007
Base 316L	0.016	0.048
Corrected 316L	0.014	0.041

Table 26: Coefficients of variation for all data sets

The coefficients of variation for all of the data sets are tabulated in Table 26. The first notable factor is the clear discrepancy between the UTS and elongation in all AM cases. This shows that for all AM cases the elongation is much more variable than the UTS and that this inconsistency is a significant factor in the loss of overall repeatability.

The most important factor for this study is that in all the cases the corrected case is improved when compared to the base case. This clearly shows that the parameter set developed with local ED control, is superior to the global ED control for repeatability. This allows a direct improvement over the previously universally implemented uniform parameter sets used in AM.

The improvement in the consistency of the tensile testing data from the corrected samples does not completely eliminate the repeatability concern. Two factors can be considered when investigating the remaining repeatability issues. The presence of alternative variations that are not accounted for in the energy density equations and the imprecise nature of the control used.

Firstly, we can consider the x-direction factor that is present in the data for both the modified and unmodified builds. This variation is minor relative to the overall variation present with distance from the centre, but it appears to be similar in both builds. This would match with the previous theory of a powder variation in the direction of powder spreading. This effect is more pronounced in the modified build. This would be accounted for by the reduction in the other sources of variation. This allows this variation to be magnified relative to the variable distance from the centre point.

The modified ED equation and its evaluation, also likely under-represents the total number of effects that are diminishing the laser energy. This can be seen in the empirical evidence from the laser beam measurements taken in Section 3.1.3 Angled Incidence. Those measurements showed a drop in the energy of 17% and an increase in beam area of 24%. In the simulation the corresponding changes were 7.2% and 8.4%. The underrepresentation is due to the limited scope of the simulation where only 4 principal sources of energy variation were considered across the build plate. The addition of further sources of variation could bridge the gap between reality and simulation while the existence of stochastic variations will prevent exact convergence.

The control implemented was in modifying the scan speed, however, the modification in the scan speed setpoint does not necessarily correspond exactly to the actual scan speed used. This introduces a variation that cannot be eliminated completely, particularly in the cases of minute changes that are needed when transitioning between similar scan speeds. The lagging of change inherent to any control system can lead to a non-zero error between the scan speed set for the scan and the actual scan speed seen by the material.

The coarse nature of the modifications to the setpoints is also present. The samples are 7mm in diameter and in the modified build each sample was given its own set of speed parameters. This however, still left some level of granularity with the parameters designed for the central coordinates of the sample, resulting in a maximum offset of 3.5mm for the optimum energy density. As the calculated energy density changes more rapidly while further from the centre, this effect also becomes magnified further from the centre, in the simulation; at the edge of the build plate, this means a 1% change in ED across a single part whereas in the central region the change is only 0.02%. This internal gradient of ED could be a factor in still producing the domed mechanical properties mesh and contribute to the lack of repeatability over the build plate.

6.5 Microstructure Results

The etched microstructure images are presented following the naming convention of the first letter is for series (B for Base case and C for Corrected case), the second letter is for build location (C for Centre, E for Edge and O for cOrner), the third letter is for orientation (L for Longitudinal and T for Transverse) and then the material type.

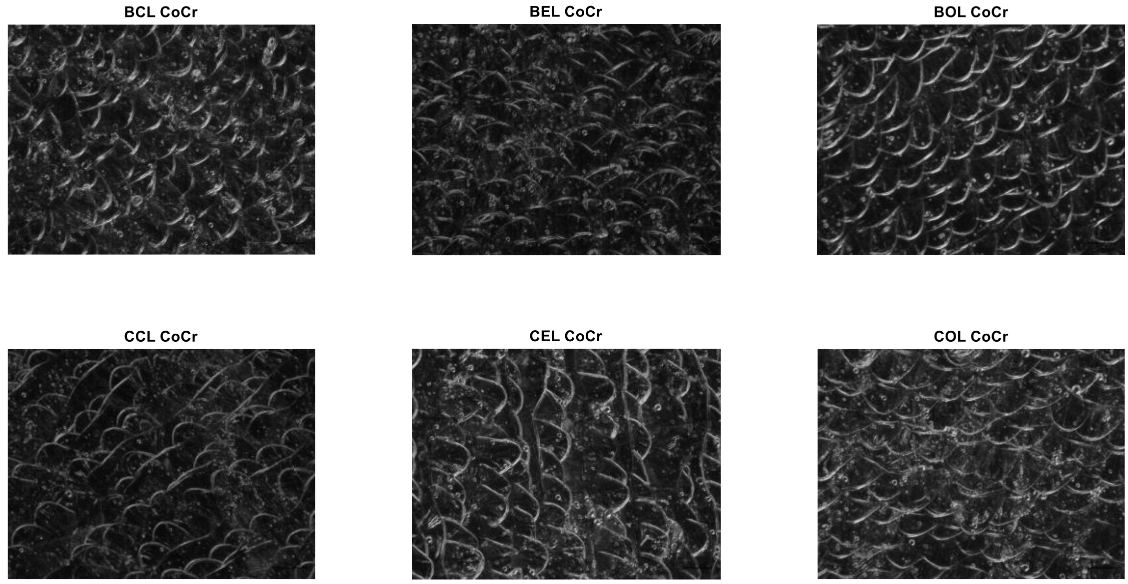
BCL CoCr
BEL CoCr
BOL CoCr
CCL CoCr
CEL CoCr
COL CoCr

Figure 129: CoCr microstructure longitudinal orientation

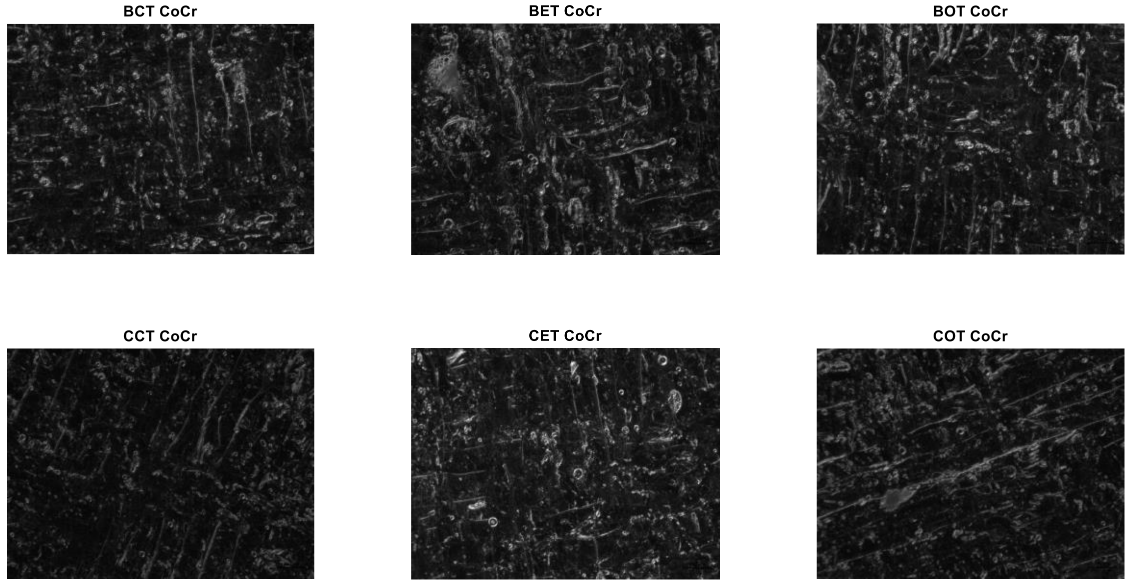
BCT CoCr
BET CoCr
BOT CoCr
CCT CoCr
CET CoCr
COT CoCr

Figure 130: CoCr microstructure transverse orientation

The revealed CoCr microstructure closely matches the expected structure as seen in the paper by Hitzler et al. [159], with no large grains or dendritic structures present. The dominant feature to be observed is the overlapping pattern of individual weld beads from adjacent passes which are most obvious in the longitudinal samples. As the samples were not post-processed, they appear to remain as γ-Co metastable phase as the rapid cooling prevents the transfer to the stable ε-Co phase [160]. Having compared the images for orientation or grain sizes, there was no significant difference found between the samples both along cases and between cases.

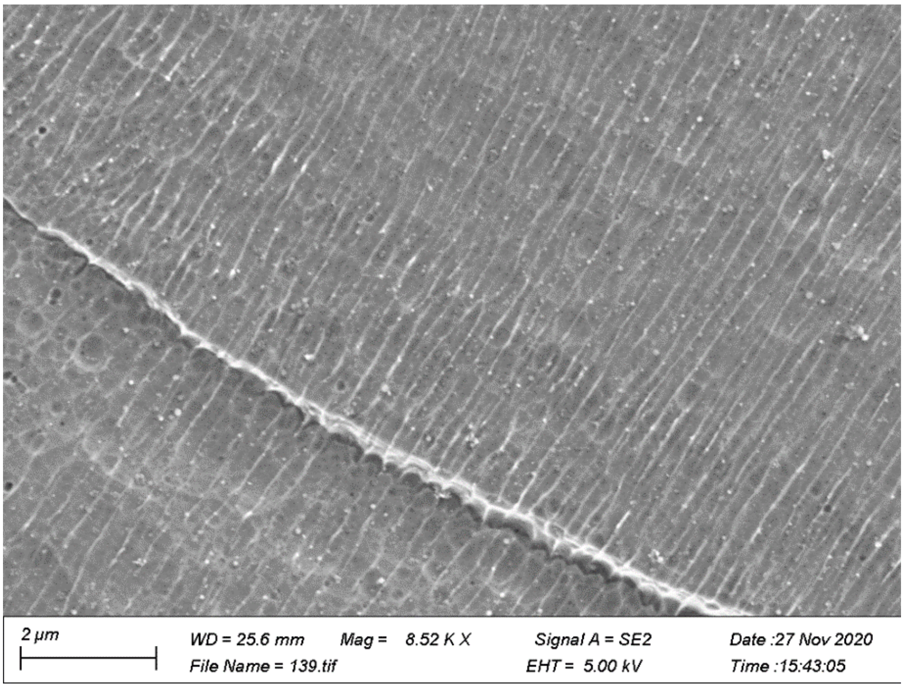

Figure 131: CoCr BCL under SEM

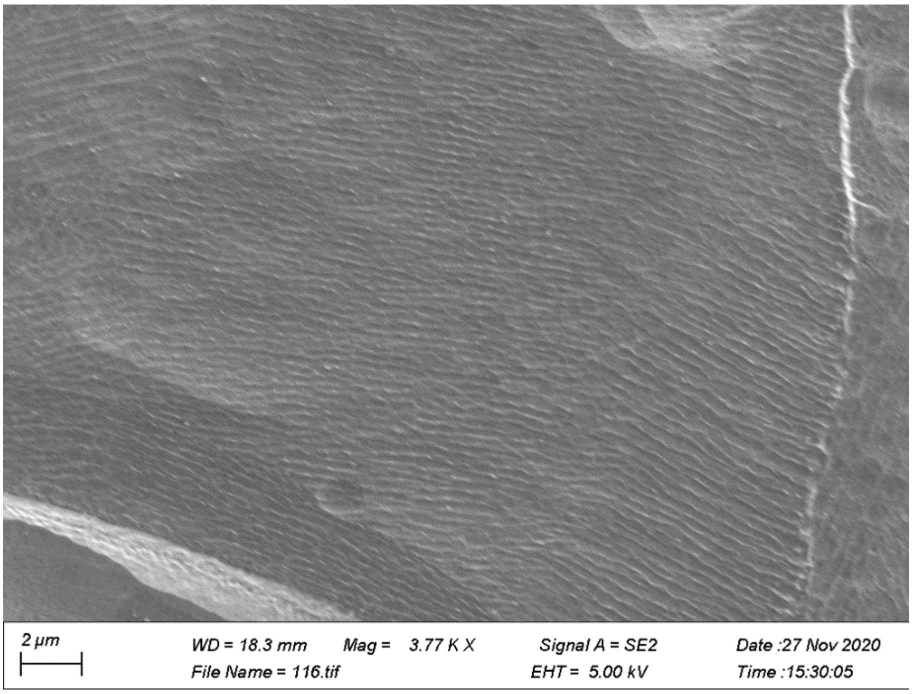

Figure 132: CoCr BOL under SEM

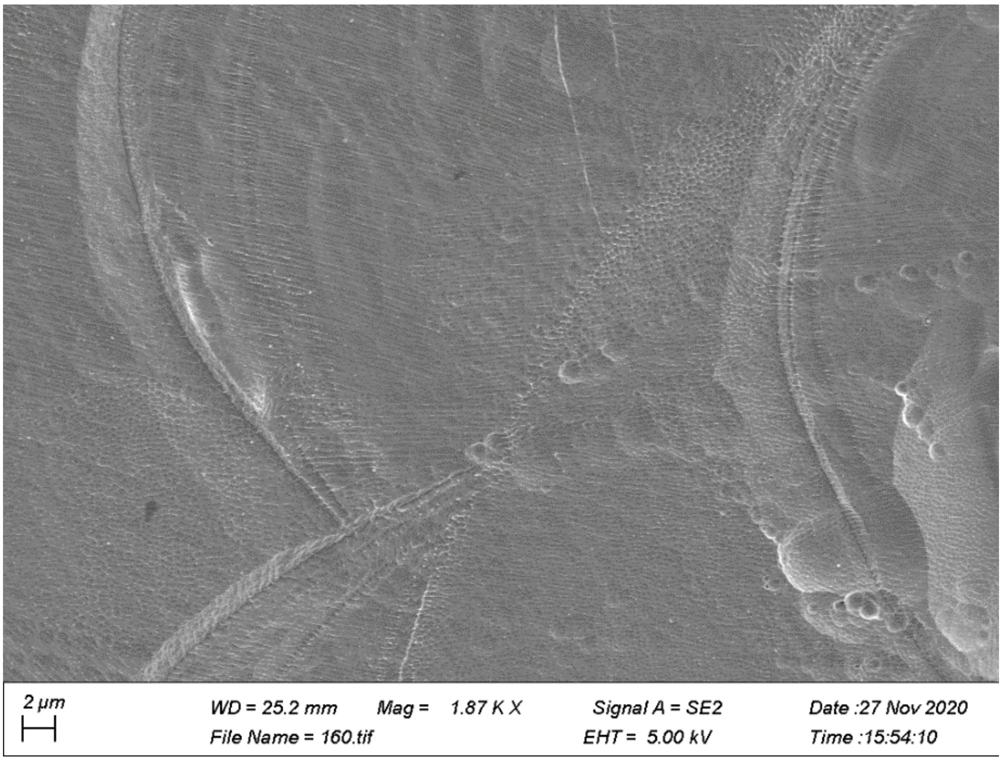

Figure 133: CoCr BEL under SEM

The samples were further examined under a scanning electron microscope (SEM) to investigate any sub-grain features within the laser passes that may not be evident in the optical microscope. The sub-grain images are shown in Figure 131, Figure 132 and Figure 133. The most obvious feature in these sub-scan magnifications is the presence of slender epitaxial columnar cells growing from the interfaces between laser scans. These columns were expected as they closely match the findings by Chen et al. [161]. There is no deviation from the expected microstructure evident in any of the samples, in that all of the cells at the interfaces were consistently in the ~0.25 µm range cell widths.

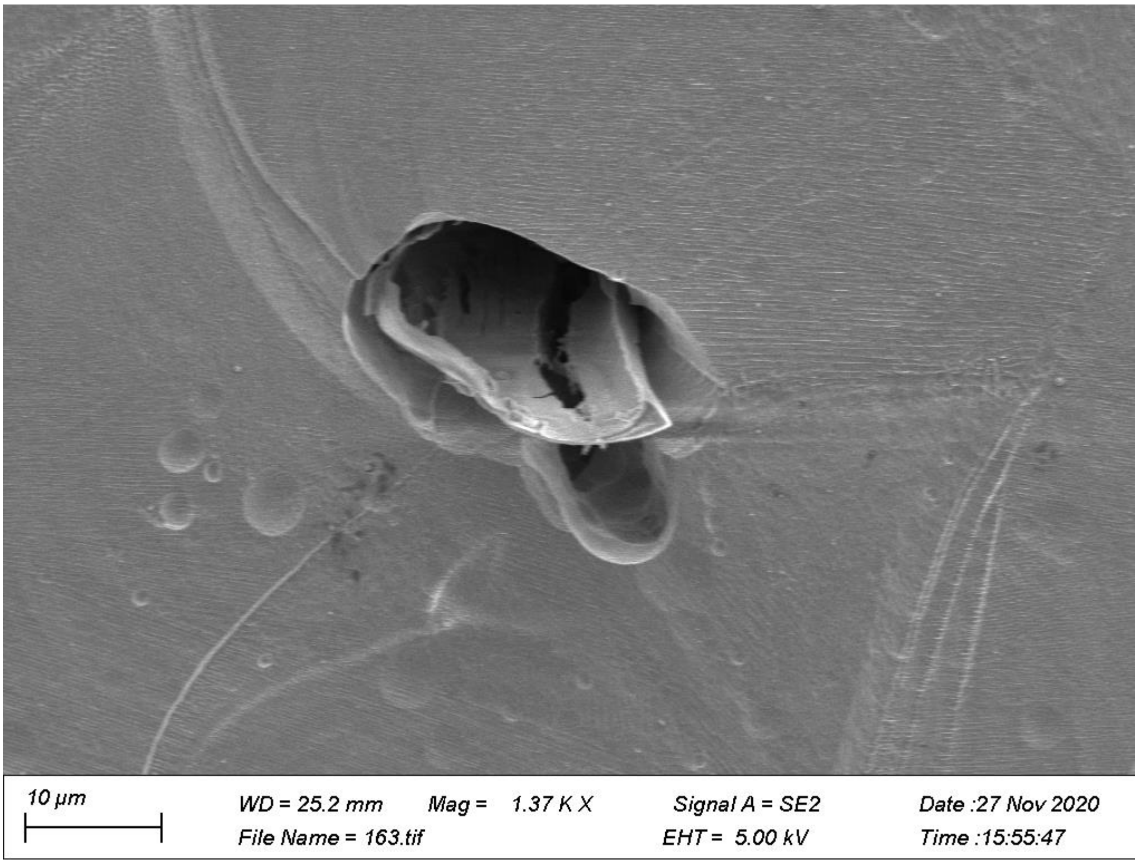

Figure 134: CoCr Porosity from the SEM

The CoCr SEM images have also located some porosity within the sample. The porosity was found to be present at the interface between two scan passes as seen in Figure 134. This would indicate the porosity was caused by an insufficiently large melt pool to overlap with the adjacent solidified melt pool. This would lead to a pore being formed between the melt pools. Alternatively, a void in the powder bed was formed and the material was not able to flow into that void while in the melted state leading to this pore forming. Both these explanations would lend credence to the lack of fusion being a major factor in the creation of porosity.

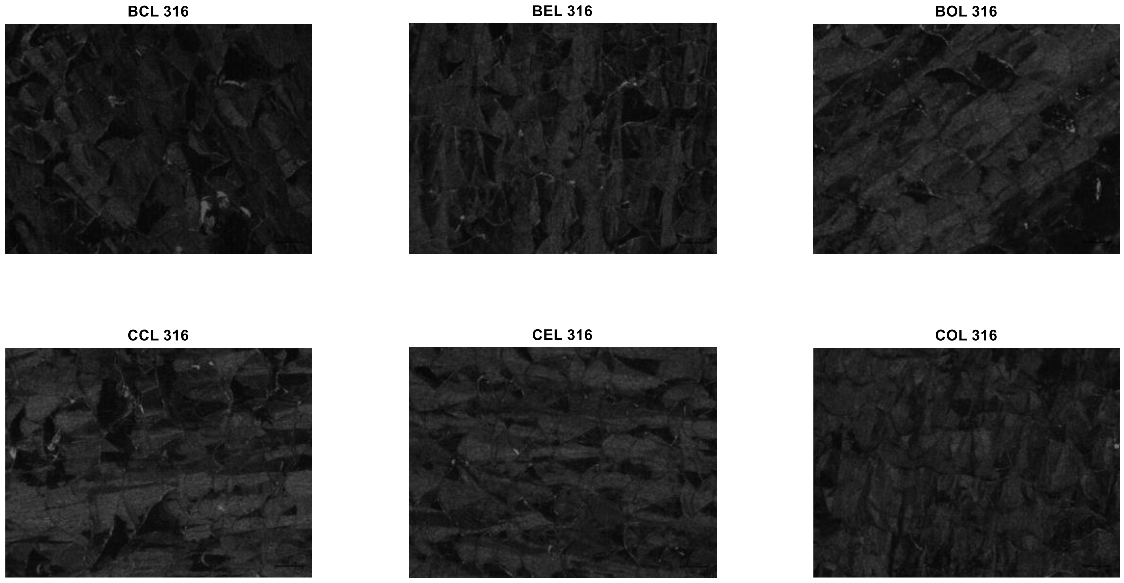

Figure 135: 316L microstructure longitudinal direction

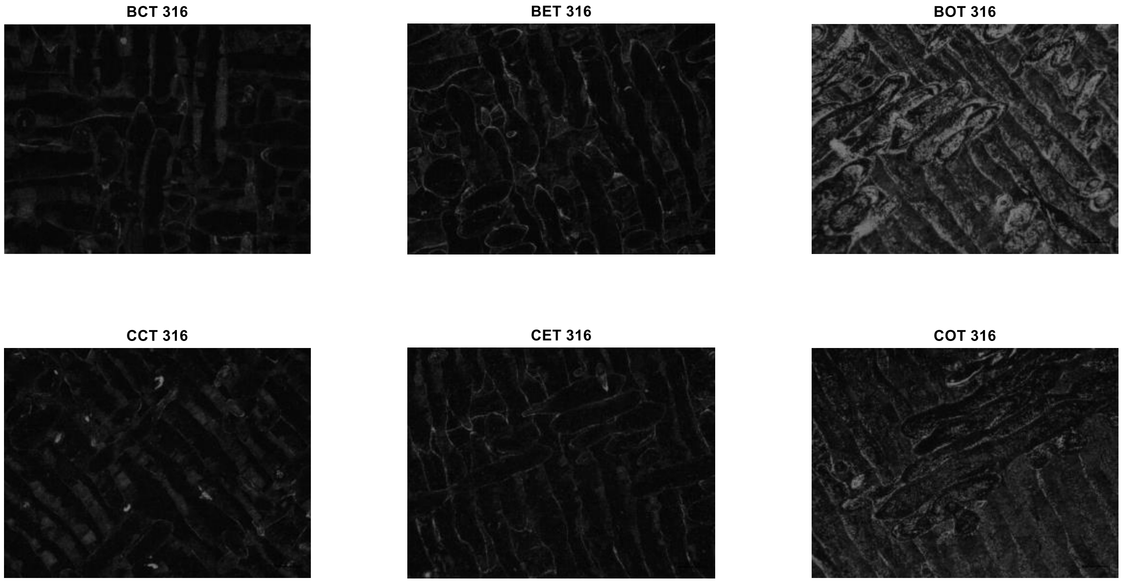

Figure 136: 316L microstructure transverse direction

In the 316L samples, those from the longitudinal direction are close to the expected structure based on the study by Gorsse et al. [162] and by Zhong et al. [50], while those from the transverse direction are more reasonably considered as the overlapping pattern of individual weld beads from adjacent passes as was seen in the CoCr cases. The overall structure appears to be fully austenitic in nature which matches the expected microstructure following the chemical composition ranges supplied from the manufacturer as shown in the red box in the phase diagram displayed in Figure 137.

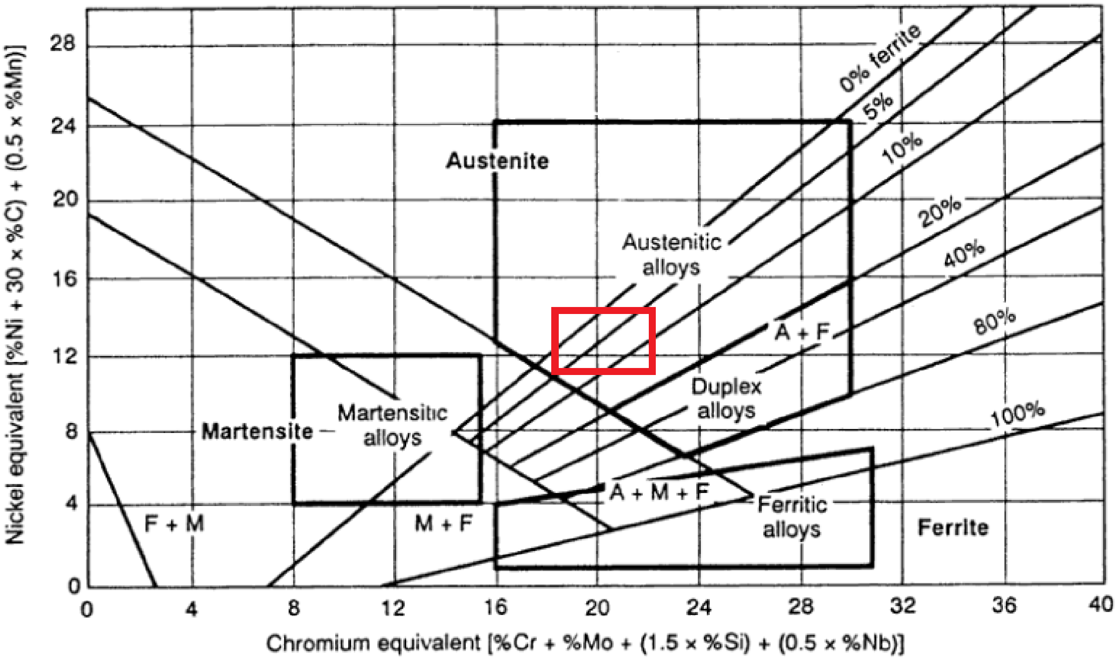

Figure 137: 316L microstructure phase diagram

There is no significant difference found in the longitudinal samples across the cases or locations. In the transverse samples, while there is no significant difference evident between cases, there does appear to be a change in location on the build plate. There appears to be a substantial change in the optical microscopy for the 316L samples in the corner of the build plate. This warranted further investigation and the samples were examined using SEM techniques.

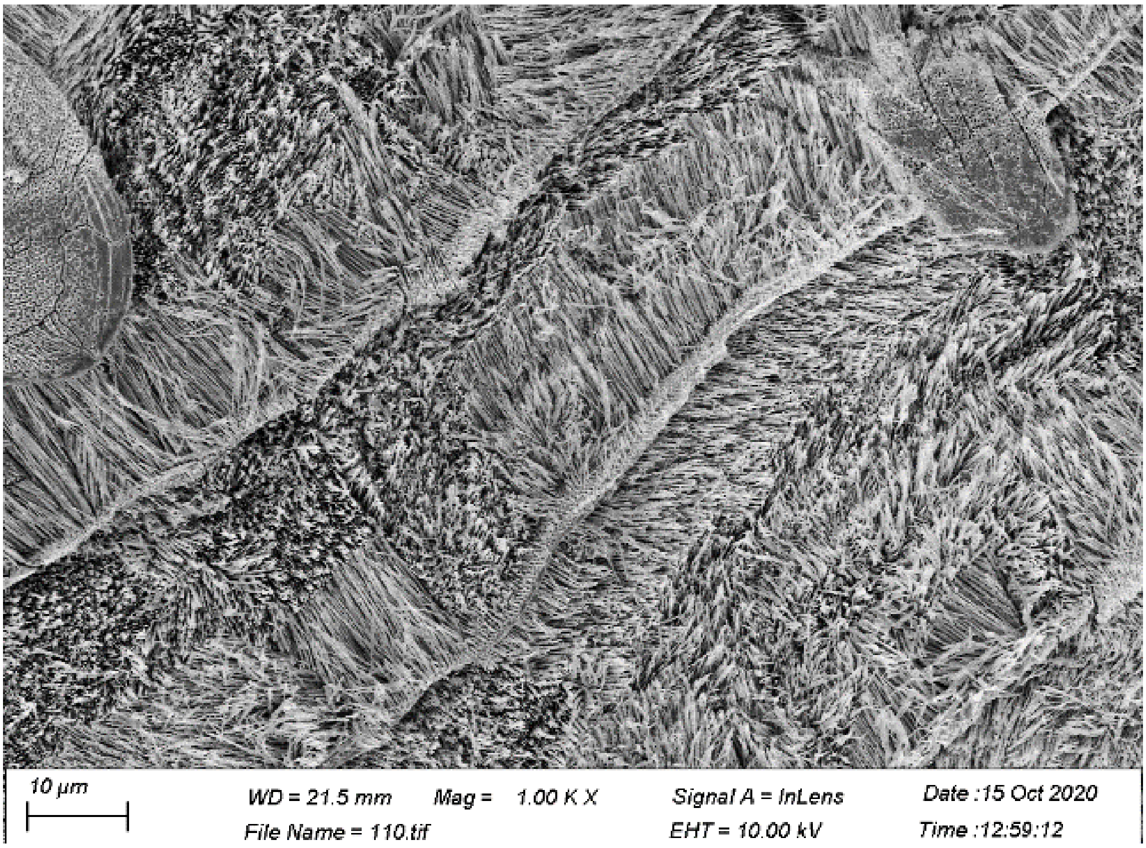

Figure 138: CCT under SEM

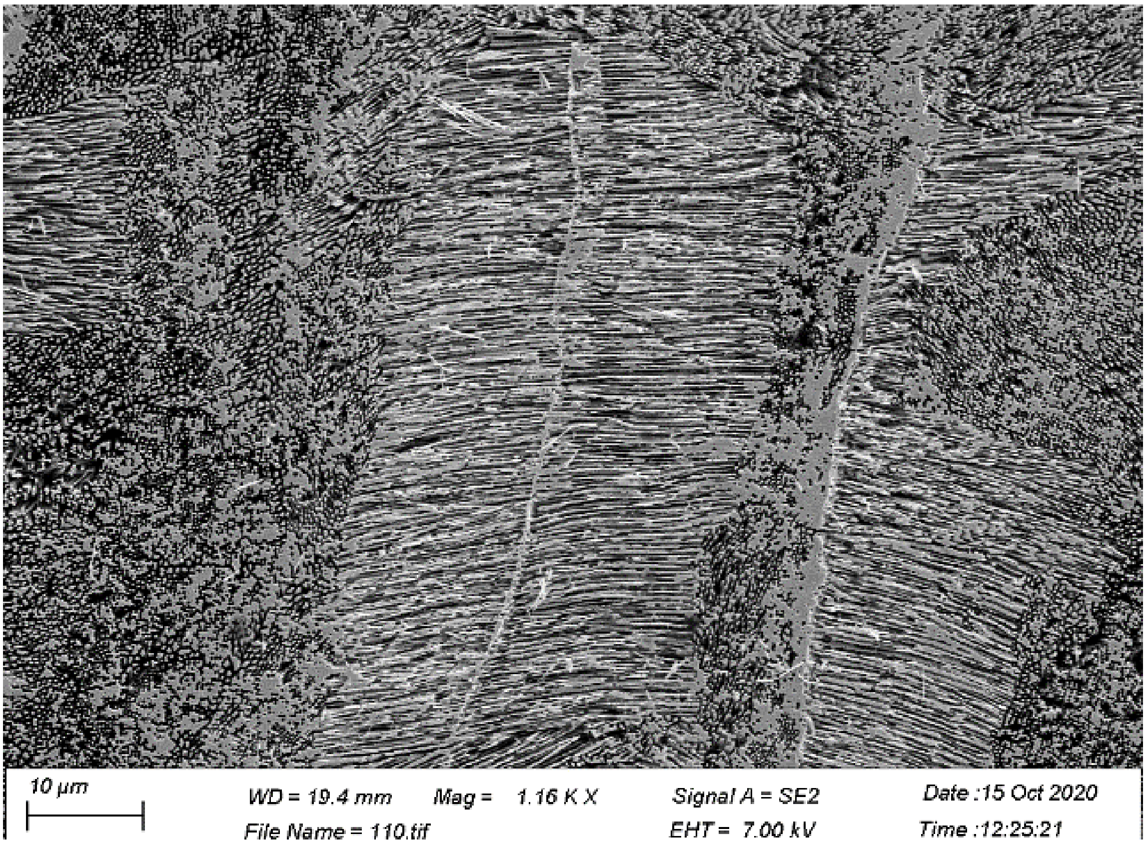

Figure 139: COT under SEM

The SEM images for 316L CCT and COT are shown in Figure 139. The SEM reveals the microstructure to be further comprised of dendritic and cellular structures similar to those found by Chen et al. [163]. The dendrites grow from the interface between scans with the cellular structure covering the rest of the area. The proportion of these two structures remains consistent between the two samples.

Overall, the microstructure analysis shows that the microstructure is non-variant across the sample sets. This would make microstructure difference an unlikely explanation for the evident change in mechanical properties found from the tensile testing.

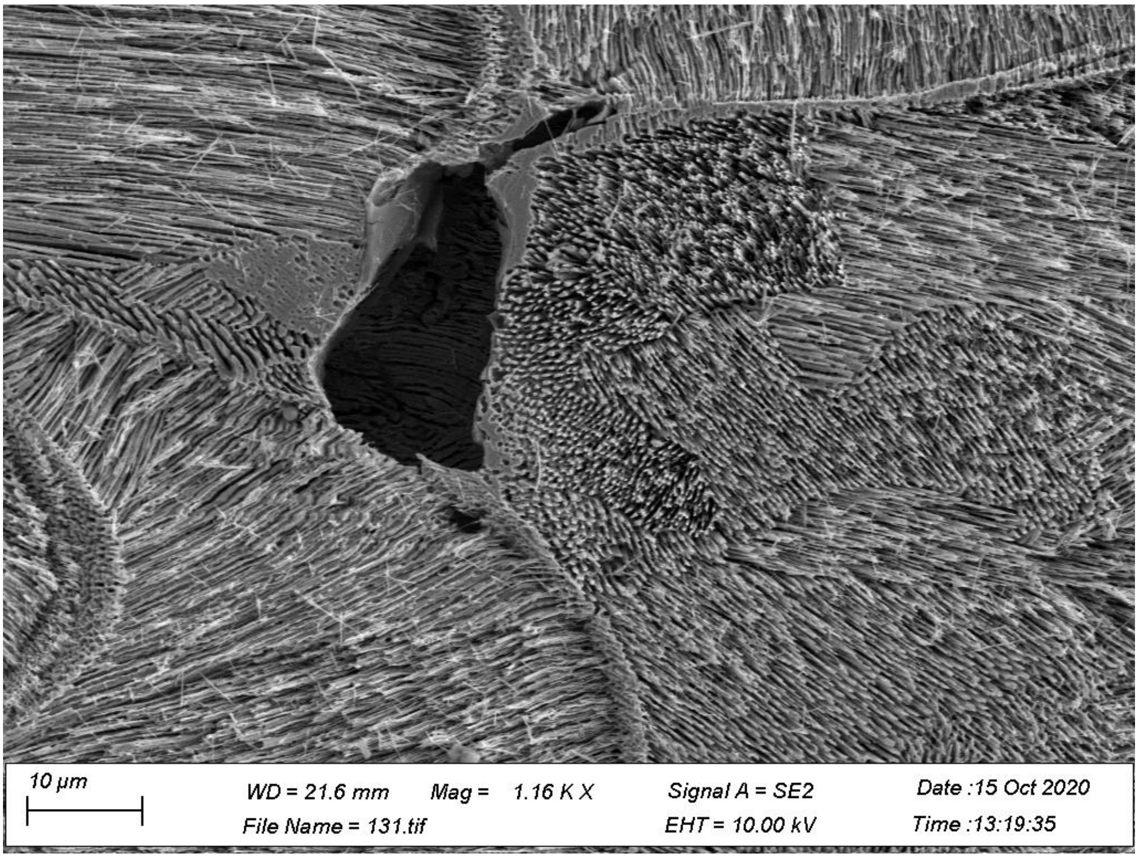

Figure 140: Porosity under SEM

The SEM images were also able to detect some of the porosity in these 316L samples, as seen in Figure 140. The porosity was identified most clearly in the longitudinal samples. From the samples, it is clear that porosity is developed at the interface between layers and the scan passes similarly to the porosity found in the CoCr samples. The porosity seem in this image is more likely due to incomplete melting. The lower layer surface can be clearly seen in the pore. This would strongly suggest that the layer above did not provide sufficient energy for the melt pool to penetrate the previous layer. This would explain the location-based variation. In the base case, the energy density is lower at the edges than the centre and has a correspondingly smaller melt pool. This smaller melt pool would lead to a reduction in the overlap of the adjacent melt pools and a shallower melt pool. Both of these factors allow for more porosity to develop in the layer and scan overlap area. The drop in energy from the centre to far from the centre, while minor, is sufficient to allow porosity to be developed more frequently. This would be a primary driver of the reduction of mechanical properties found in far from centre samples. The porosity will be further investigated using computer tomography to determine if it demonstrates any trends across the builds and locations in a predictable manner. This will allow the full sample to be examined not merely as a single slice of the cross-section.

6.6 Computer Tomography Results

The final porosity from the CT scanning is reported as shown in Figure 141 along with a table of all of the detected pores and their locations in the sample. The region of interest volume and the porosity volume are reported allowing direct comparisons to be made between samples.

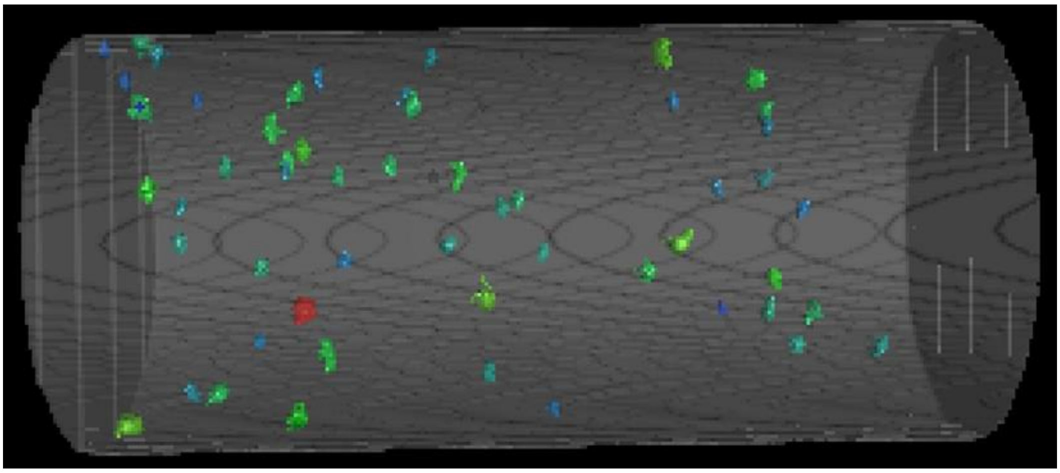

Figure 141: Highlighted entrained porosity

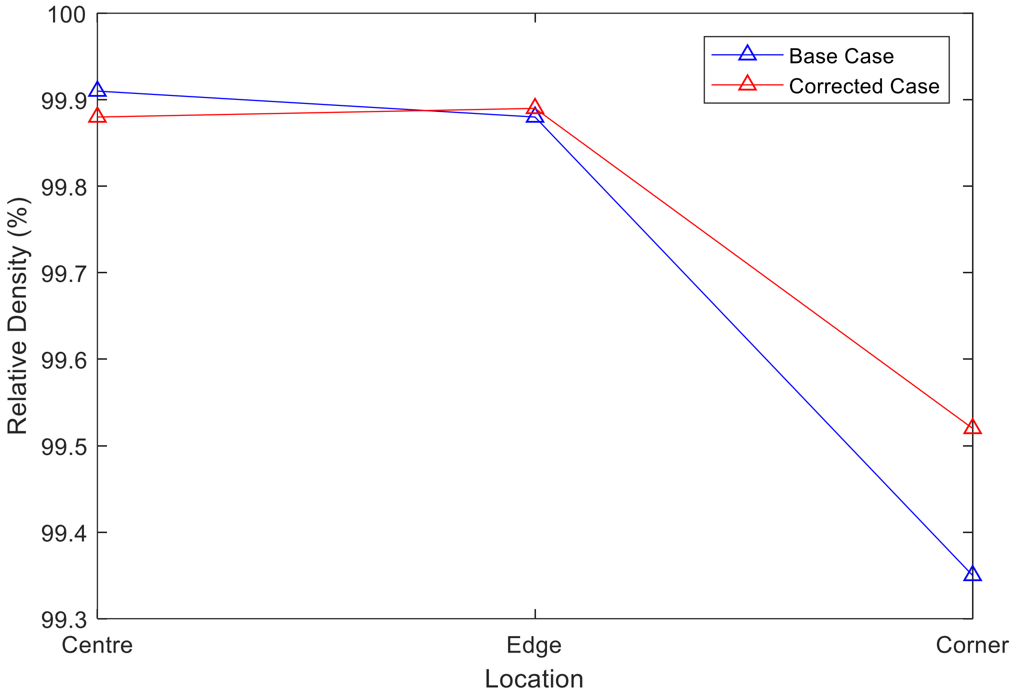

Figure 142: CoCr sample porosity results

The CT results for the Cobalt Chrome samples shows that the parts were near fully dense at the centre and the edge of the build plate but had a significant drop off at the corners of the build plate, as seen in Figure 142. The central and edge regions showed very similar relative densities, which may in part be due to the high specific density of cobalt chrome masking the present porosity at this level. The method for detecting the porosity relies on the x-ray being able to penetrate the material at different rates depending on whether in material or porosity. The CoCr samples due to their dense nature and the limit to energy available in the CT scanner, can have near-complete x-ray opaqueness at the thickest point in the sample. When revolved, this means that the very centre of the sample has only the most powerful x-rays passing through and the porosity does not strongly impact those rays' ability to pass, when compared to the weaker beams capable of passing at the edges. The difference between the base and corrected cases in those two regions are also within the error inherent with the thresholding for what counts as a point of porosity or not in the system.

The corner cases, however, do show a marked difference between the base and corrected case. The base case shows a 0.53% drop in relative density, while the corrected case does still demonstrate a drop in relative density at 0.37%. This drop is likely a contributing factor to location dependant variation still found for the CoCr corrected case in the tensile testing. The correction may not have been aggressive enough to remove all of the defects. This would explain the improvement but not the removal of the location based variation in the CoCr.

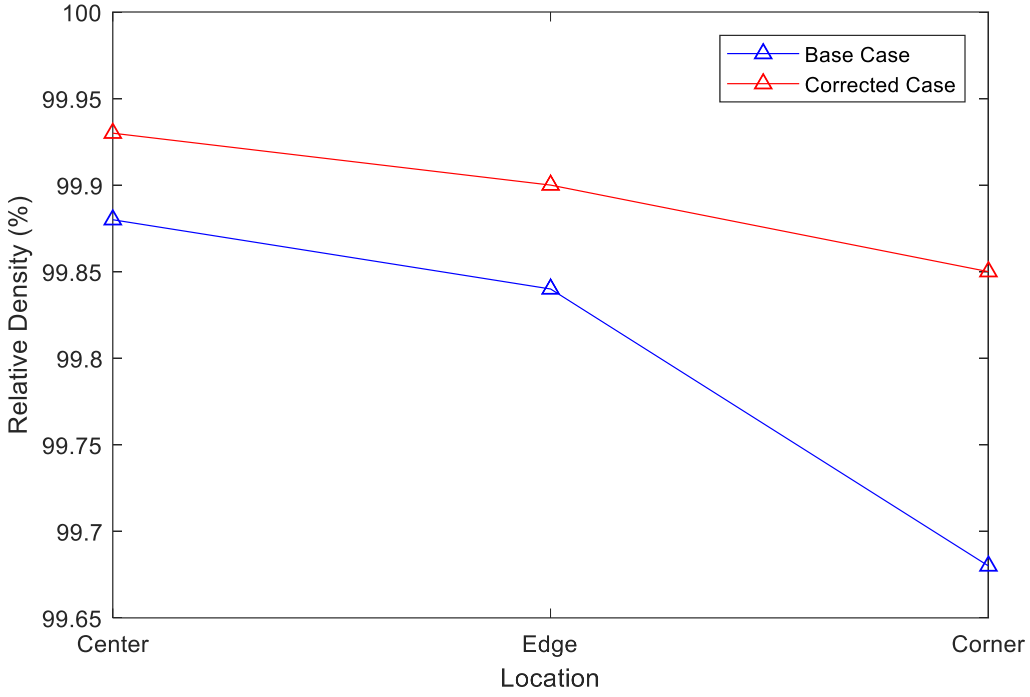

Figure 143: 316L sample porosity results

The results of the CT scanning a representative 316L samples for each region is shown in Figure 143. The samples again were determined to be near fully dense. These results show that a density decrease was present from the centre to corner in both cases. In the base case, the decrease in density was more pronounced and also more rapid than was found in the corrected case. This once again demonstrated an improvement present in the corrected build over the base parameter set.

The combined results for the CT scanning show a density drop as the samples are far from the centre in both cases. This is indicative of a greater number of defects being present in those areas of the build. The corrected case in both materials had a reduced drop in the relative density at the corner than the base settings case. This result gives a plausible reason for the overall improvement in the mechanical properties found for the corrected cases.

Chapter 7: Conclusions and Future Work

7.1 Conclusions

The overall objective of this was to improve the repeatability in metal additive manufacturing. This objective was divided into 4 research questions:

1. Is there a repeatability issue in AM, and how does this compare with traditional manufacturing methods?
2. What are the potential sources of variation causing the repeatability issue?
3. Can the errors or sources of variation be mitigated?
4. Can improved repeatability be achieved in the process?

The conclusions of the project are outlined below:

1. **Is there a repeatability issue in AM, and how does this compare with traditional manufacturing methods?**

   The repeatability issue in SLM and AM, in general, was found to be pervasive both in the literature and in the initial builds. The literature survey showed that the coefficient of variation was found to be higher in AM (UTS of 0.05, Elongation of 0.13) than found in traditional manufacturing methods (UTS of 0.016, Elongation of 0.016). The initial build in CoCr had a coefficient of variation was 0.026 for the UTS and 0.119 for elongation and the initial 316L build had a coefficient of variation was 0.016 for the UTS and 0.049 for elongation, all of which are in the range of the literature values confirming directly the level of the repeatability issue apparent in AM

2. **What are the potential sources of variation causing the repeatability issue?**

   The potential causes of low repeatability and reproducibility were analysed in terms of the pre-process, para-process and post-processing stages. In particular, powder morphology (pre), laser interaction with material (para), and heat treatment, hot isostatic pressing and machining (post) are all potential sources of repeatability issues. Of these potential sources of error, it was determined that the laser interaction with the material is critically important. The laser interaction variation over the build plate was determined to be predominantly due to angled incidence, F-Theta absorption and plume absorption. These were measured and quantified for the level of impact on the ED.

3. **Can the errors or sources of variation be mitigated?**

   A new modified energy density equation was proposed. The equation was evaluated over a full build plate. The evaluation was capable of a reasonable agreement to the reality of the process including the sources of variation present in the overall process. There were discrepancies between the predicted values and reality, however, this was predominantly due to simplifications present by focussing only on the most significant of the major contributing errors. The equation was able to be used to create a set of corrected process parameters to produce more repeatable parts. These parameters focussed on providing a modified scan speed parameter for any location on the build plate, to provide a more uniform energy density.

4. **Can improved repeatability be achieved in the process?**

   The CoCr parts created using the parameter set generated by the repeatability tool, had a coefficient of variation for UTS of 0.016 and Elongation of 0.076. This improvement was verified to be possible also in 316L with the new parameter set creating parts with a coefficient of variation for UTS of 0.014 and Elongation of 0.041. This is a clear and importantly statistically significant improvement in mechanical properties for both material cases, when compared to the initial parts created by the unadjusted parameter sets.

AM, with powder bed fusion process as an exemplar, has a number of inherent flaws. In the research carried out to-date, insufficient focus has been made to systematically address these flaws resulting in poor repeatability in the parts produced. The needs of industry dictate that these flaws need to be more fully addressed and understood at a fundamental level. The fundamental understanding of why the repeatability issue is present has not been thoroughly developed by the research community as a whole. This is in contrast to the high level of research into the exploration of the possible capabilities of AM.

This body of research has created a modified energy density equation to inform locally variable process parameters within a build. These localised parameters were able to achieve up to a 40% reduction in the variation of mechanical properties found over the area of the build. This reduction does not completely remove the variation but does bring it more in line with traditional methods. The reduction in variation also clearly achieves the overall objective of improving the repeatability of SLM process

The comparison between the corrected parameter samples and those from the non-variant parameters also gave a credible explanation for the repeatability losses in metal AM. In both the CT scanning and SEM imaging, more porosity was found in the far from centre regions of the build plate. This porosity is a type of lack of fusion defect. The increased energy provided from the corrected parameters, to counteract the energy losses predicted by the modified energy density equation, helped to eliminate these defects leading to the overall repeatability improvements.

7.2 Future Work

This research was focussed on the para-process issues. An obvious area of further work to be carried out is to look at the pre-process and para process sources of variation in fine detail for a means to correct them and further improve the repeatability. The most important of these is to attempt to address the uncertainty present in the pre-process. As was discussed extensively, the repeatability errors tend to compound and increase so any interventions are best to occur in the earliest possible stage of the AM process.

Another possible avenue of future study is to develop the modified ED equation to include information that currently isn’t available such as the powder bed conditions across the build. The current locally variable power input and process parameters are designed to create a uniform energy density on a generic powder bed. By being able to read the specific powder bed a further fine-tuning of the energy density could be undertaken to improve the build energy density consistency.

A key area for improvement requires restructuring of the manufacturing system, specifically the file format currently the ProX system. Currently, process parameters can only be adjusted on a macro-part level. The tensile and geometric specimens created for this research were only on a small area per part allowing relatively fine control; however the needs of the industry to utilise AM to create larger parts will reduce the ability to control the energy density locally under the current system. The current system does facilitate the automatic subdivision of scan hatches to smaller hexagons to reduce vector scan lengths, introducing a means to define these hexagon subdivisions with local control guided by the proposed modified equation could allow the application of this correction to macro parts and should be investigated.

A key further step in this research is to demonstrate the localised control on a different AM system. The current body of evidence was created on multiple materials showing that the improvements were material agnostic, however, the materials were both utilising the DMP ProX 200 machine. This allowed the same inputs for the variations to be used in both cases simplifying the study and preventing the uncertainties in determining those model inputs from potentially impacting the properties. Such an impact could be misconstrued as a material-specific problem. Now that the improvements been proven to be material independent, the next step towards proving the universal applications of this research to improving the field as a whole, is to apply the improvements to a differing manufacturing system.

Chapter 8: References

[1] Hounshell D (1985) From the American System to Mass Production, 1800-1932: The Development of Manufacturing Technology in the United States. Johns Hopkins University Press

[2] ASTM (2014) Standard Practice for Use of the Terms Precision and Bias in ASTM Test Methods. doi: 10.1520/E0177-14.2

[3] Tapia G, Elwany A (2014) A Review on Process Monitoring and Control in Metal-Based Additive Manufacturing. J Manuf Sci Eng 136:060801 . doi: 10.1115/1.4028540

[4] NIST (2013) Measurement Science Roadmap for Metal-Based Additive Manufacturing

[5] Nakajima S (1988) Introduction to TPM: Total Productive Maintenance. Productivity Press

[6] Weller C, Kleer R, Piller FT (2015) Economic implications of 3D printing: Market structure models in light of additive manufacturing revisited. Int J Prod Econ 164:43–56 . doi: https://doi.org/10.1016/j.ijpe.2015.02.020

[7] Jones DEH (1974) Ariadne. New Sci. 80

[8] Kodama H (2011) Automatic method for fabricating a three-dimensional plastic model with photo-hardening polymer. 1770: . doi: 10.1063/1.1136492

[9] Meiners W, Konrad W, Andres G (1996) Shaped body especially prototype or replacement part production

[10] Nakano T, Ishimoto T (2015) Powder-based additive manufacturing for development of tailor-made implants for orthopedic applications. KONA Powder Part J 75–84 . doi: 10.14356/kona.2015015

[11] Wohlers Associates (2018) Wohlers Report 2018: Additive Manufacturing and 3D Printing State of the Industry

[12] Prakash KS, Nancharaih T, Rao VVS (2018) Additive Manufacturing Techniques in Manufacturing -An Overview. Mater Today Proc 5:3873–3882 . doi: 10.1016/j.matpr.2017.11.642

[13] Yang S, Zhao YF (2015) Additive manufacturing-enabled design theory and methodology: a critical review. Int J Adv Manuf Technol 80:327–342 . doi: 10.1007/s00170-015-6994-5

[14] Friedman T (2013) When Complexity Is Free. New york times

[15] Atzeni E, Salmi A (2012) Economics of additive manufacturing for end-usable metal parts. Int J Adv Manuf Technol 62:1147–1155 . doi: 10.1007/s00170-011-3878-1

[16] Catchpole-Smith S, Sélo RRJ, Davis AW, Ashcroft IA, Tuck CJ, Clare A (2019) Thermal conductivity of TPMS lattice structures manufactured via laser powder bed fusion. Addit Manuf 30:100846 . doi: 10.1016/j.addma.2019.100846

[17] Tyrrell M (2017) A Quantum Leap Forward. Aerosp. Mag. 1–3

[18] Pinkerton AJ (2016) [INVITED] Lasers in additive manufacturing. Opt Laser Technol 78:25–32 . doi: 10.1016/j.optlastec.2015.09.025

[19] Narayan R ASM Handbook Volume 23 Materials for Medical Devices

[20] Orme ME, Gschweitl M, Ferrari M, Madera I, Mouriaux F (2017) Designing for additive manufacturing: Lightweighting through topology optimization enables lunar spacecraft. J Mech Des Trans ASME 139: . doi: 10.1115/1.4037304

[21] Schulz B (2017) Aluminum Material Removal Rate New World Record ? Mod. Mach. Shop

[22] Page I (2018) Desktop Metal Enables Fastest Metal Printer of the World. Spotlight Met.

[23] Franchitti S, Borrelli R, Pirozzi C, Carrino L, Polini W, Sorrentino L, Gazzerro A (2018) Investigation on Electron Beam Melting : Dimensional accuracy and process repeatability. Vacuum 157:340–348 . doi: 10.1016/j.vacuum.2018.09.007

[24] Grasso M, Colosimo BM (2017) Process defects and in situ monitoring methods in metal powder bed fusion : a review. Meas Sci Technol. doi: 10.1088/1361-6501/aa5c4f

[25] Slotwinski JA, Luecke WE, Lass EA (2006) NIST Technical Note 2006 Interlaboratory mechanical-property study for Cobalt-Chromium alloy made by laser powder-bed-fusion additive manufacturing

[26] Lavakumar A (2017) Mechanical properties of materials. Concepts Phys. Metall. 5–22

[27] Takaichi A, Suyalatu, Nakamoto T, Joko N, Nomura N, Tsutsumi Y, Migita S, Doi H, Kurosu S, Chiba A, Wakabayashi N, Igarashi Y, Hanawa T (2013) Microstructures and mechanical properties of Co-29Cr-6Mo alloy fabricated by selective laser melting process for dental applications. J Mech Behav Biomed Mater 21:67–76 . doi: 10.1016/j.jmbbm.2013.01.021

[28] Averyanova M, Bertrand P, Verquin B (2011) Manufacture of Co-Cr dental crowns and bridges by selective laser Melting technology. Virtual Phys Prototyp 6:179–185 . doi: 10.1080/17452759.2011.619083

[29] Song C, Zhang M, Yang Y, Wang D, Jia-kuo Y (2018) Morphology and properties of CoCrMo parts fabricated by selective laser melting. Mater Sci Eng A 713:206–213 . doi: 10.1016/j.msea.2017.12.035

[30] Qian B, Saeidi K, Kvetková L, Lofaj F, Xiao C, Shen Z (2015) Defects-tolerant Co-Cr-Mo dental alloys prepared by selective laser melting. Dent Mater 31:1435–1444 . doi: 10.1016/j.dental.2015.09.003

[31] Lu Y, Gan Y, Lin J, Guo S, Wu S, Lin J (2017) Effect of laser speeds on the mechanical property and corrosion resistance of CoCrW alloy fabricated by SLM. Rapid Prototyp J 23:28–33 . doi: 10.1108/RPJ-07-2015-0085

[32] Kim HR, Jang SH, Kim YK, Son JS, Min BK, Kim KH, Kwon TY (2016) Microstructures and mechanical properties of Co-Cr dental alloys fabricated by three CAD/CAM-based processing techniques. Materials (Basel) 9: . doi: 10.3390/MA9070596

[33] Liverani E, Fortunato A, Leardini A, Belvedere C, Siegler S, Ceschini L, Ascari A (2016) Fabrication of Co-Cr-Mo endoprosthetic ankle devices by means of Selective Laser Melting (SLM). Mater Des 106:60–68 . doi: 10.1016/j.matdes.2016.05.083

[34] Kajima Y, Takaichi A, Kittikundecha N, Nakamoto T, Kimura T, Nomura N, Kawasaki A, Hanawa T, Takahashi H, Wakabayashi N (2018) Effect of heat-treatment temperature on microstructures and mechanical properties of Co–Cr–Mo alloys fabricated by selective laser melting. Mater Sci Eng A 726:21–31 . doi: 10.1016/j.msea.2018.04.048

[35] Zhou Y, Li N, Yan J, Zeng Q (2018) Comparative analysis of the microstructures and mechanical properties of Co-Cr dental alloys fabricated by different methods. J Prosthet Dent 120:1–7 . doi: 10.1016/j.prosdent.2017.11.015

[36] United Performance Metals (2018) CCM Cobalt Chrome Moly - ASTM F1537 Alloy 1

[37] Edwards P, O'Conner A, Ramulu M (2013) Electron Beam Additive Manufacturing of Titanium Components: Properties and Performance. J Manuf Sci Eng 135:061016 . doi: 10.1115/1.4025773

[38] Tang HP, Qian M, Liu N, Zhang XZ, Yang GY, Wang J (2015) Effect of Powder Reuse Times on Additive Manufacturing of Ti-6Al-4V by Selective Electron Beam Melting. Jom 67:555–563 . doi: 10.1007/s11837-015-1300-4

[39] Baufeld B, Biest O Van Der, Gault R (2010) Additive manufacturing of Ti – 6Al – 4V components by shaped metal deposition : Microstructure and mechanical properties. Mater Des 31:S106–S111 . doi: 10.1016/j.matdes.2009.11.032

[40] Welsch G, Boyer R, Collings EW (1993) Materials Properties Handbook: Titanium Alloys. ASM International

[41] Bourell D, Coholich J, Chalancon A, Bhat A (2017) Evaluation of energy density measures and validation for powder bed fusion of polyamide. CIRP Ann - Manuf Technol 66:217–220 . doi: 10.1016/j.cirp.2017.04.128

[42] Yusuf SM, Gao N (2017) Influence of energy density on metallurgy and properties in metal additive manufacturing. Mater Sci Technol 33:1269–1289 . doi: 10.1080/02670836.2017.1289444

[43] Zia Uddin S, Espalin D, Mireles J, Morton P, Terrazas C, Collins S, Murr LE, Wicker R (2016) Laser powder bed fusion fabrication and characterization of crack- free aluminum alloy 6061 using in-process powder bed induction heating. Solid Free Fabr Symp 214–227

[44] Dekking FM, Kraaikamp C, Lopuhaä HP, Meester LE (2005) A Modern Introduction to Probability and Statistics

[45] Humbeeck J Van (2011) Microstructure and mechanical properties of Selective Laser Melted 18Ni-300 steel. 00:

[46] Kempen K, Thijs L, Van Humbeeck J, Kruth JP, Humbeeck J Van, Kruth JP (2012) Mechanical Properties of AlSi10Mg Produced by Selective Laser Melting. Phys Procedia 39:439–446 . doi: 10.1016/j.phpro.2012.10.059

[47] Luecke WE, Slotwinski JA (2014) Mechanical Properties of Austenitic Stainless Steel Made by Additive Manufacturing. J Res Natl Inst Stand Technol 119:398 . doi: 10.6028/jres.119.015

[48] Spierings AB, Levy G (2009) Comparison of density of stainless steel 316L parts produced with selective laser melting using different powder grades. Solid Free Fabr Proc 342–353

[49] Wang X, Keya T, Chou K (2016) Build Height Effect on the Inconel 718 Parts Fabricated by Selective Laser Melting. Procedia Manuf 5:1006–1017 . doi: 10.1016/j.promfg.2016.08.089

[50] Zhong Y, Rännar LE, Liu L, Koptyug A, Wikman S, Olsen J, Cui D, Shen Z (2017) Additive manufacturing of 316L stainless steel by electron beam melting for nuclear fusion applications. J Nucl Mater 486:234–245 . doi: 10.1016/j.jnucmat.2016.12.042

[51] Cervey RR (1974) MECHANICAL PROPERTIES OF Ti-6A1-4V ANNEALED FORGINGS

[52] Clifton F (1969) Strength Variability in Structural Materials Strength Variability in Structural Materials

[53] Hess PE, Bruchman D, Assakkaf IA, Ayyub BM Uncertainties in Material Strength, Geometric, and Load Variables. 1956:1–54

[54] Yadroitsev I (2009) Selective Laser Melting: Direct Manufacturing of 3D-objects by Selective Laser Melting of Metal Powders. Lambert Academic Publishing

[55] Rehme O (2010) Cellular Design for Laser Freeform Fabrication. Cuvillier

[56] Carter LN, Martin C, Withers PJ, Attallah MM (2014) The influence of the laser scan strategy on grain structure and cracking behaviour in SLM powder-bed fabricated nickel superalloy. J Alloys Compd 615:338–347 . doi: 10.1016/j.jallcom.2014.06.172

[57] Tong K (2005) Parametric error modeling and software error compensation for rapid prototyping

[58] Choi SH, Kwok KT (1999) A Memory Efficient Slicing Algorithm for Large STL Files Department of IndustriaFand Manufacturing Systems Engineering ABSTRACT This paper proposes a memory efficient slicing algorithm for Rapid Prototyping (RP) processes . The algorithm is aimed to ove. Proc solid Free Fabr Symp 155–162

[59] Zhu Z, Keimasi S, Anwer N, Mathieu L, Qiao L, Zhu Z, Keimasi S, Anwer N, Mathieu L, Qiao L, Deviation S (2016) Review of Shape Deviation Modeling for Additive Manufacturing

[60] Jiang J, Xu X, Stringer J (2018) Support Structures for Additive Manufacturing: A Review. J Manuf Mater Process 2:64 . doi: 10.3390/jmmp2040064

[61] Leutenecker-Twelsiek B, Klahn C, Meboldt M (2016) Considering Part Orientation in Design for Additive Manufacturing. Procedia CIRP 50:408–413 . doi: 10.1016/j.procir.2016.05.016

[62] Krol TA, Zaeh MF, Seidel C (2012) Optimization of supports in metal-based additive manufacturing by means of finite element models. 23rd Annu Int Solid

Free Fabr Symp - An Addit Manuf Conf SFF 2012 707–718

[63] Oliveira JP, Miranda RM, Braz Fernandes FM (2017) Welding and Joining of NiTi Shape Memory Alloys: A Review. Prog Mater Sci 88:412–466 . doi: 10.1016/j.pmatsci.2017.04.008

[64] Silfvast WT (2008) Laser Fundamentals. Cambridge University Press

[65] Steen WM, Mazumder J (2010) Laser material processing

[66] Boley CD, Mitchell SC, Rubenchik AM, Wu SSQ (2016) Metal powder absorptivity: modeling and experiment. Appl Opt 55:6496 . doi: 10.1364/ao.55.006496

[67] Fischer P, Karapatis N, Romano V, Glardon R, Weber HP (2002) A model for the interaction of near-infrared laser pulses with metal powders in selective laser sintering. Appl Phys A Mater Sci Process 74:467–474 . doi: 10.1007/s003390101139

[68] Fischer P, Romano V, Weber HP, Karapatis NP, Boillat E, Glardon R (2003) Sintering of commercially pure titanium powder with a Nd:YAG laser source. Acta Mater 51:1651–1662 . doi: 10.1016/S1359-6454(02)00567-0

[69] Foroozmehr A, Badrossamay M, Foroozmehr E, Golabi S (2016) Finite Element Simulation of Selective Laser Melting process considering Optical Penetration Depth of laser in powder bed. Mater Des 89:255–263 . doi: 10.1016/j.matdes.2015.10.002

[70] Zeng K, Pal D, Stucker BE (2012) A Review of Thermal Analysis Methods in Laser Sintering and Selective Laser Melting. Proc Solid Free Fabr Symp 796–814

[71] Gong H, Christiansen D, Beuth J, Lewandowski JJ (2014) Melt Pool Characterization for Selective Laser Melting of Ti-6Al-4V Pre-alloyed Powder. Solid Free Fabr Symp 256–267

[72] Gong H, Rafi K, Gu H, Starr T, Stucker B (2014) Analysis of defect generation in Ti-6Al-4V parts made using powder bed fusion additive manufacturing processes. Addit Manuf 1:87–98 . doi: 10.1016/j.addma.2014.08.002

[73] Khairallah SA, Anderson AT, Rubenchik A, King WE (2016) Laser powder-bed fusion additive manufacturing: Physics of complex melt flow and formation mechanisms of pores, spatter, and denudation zones. Acta Mater 108:36–45 . doi: 10.1016/j.actamat.2016.02.014

[74] Qiu C, Panwisawas C, Ward M, Basoalto HC, Brooks JW, Attallah MM (2015) On the role of melt flow into the surface structure and porosity development during selective laser melting. Acta Mater 96:72–79 . doi: 10.1016/j.actamat.2015.06.004

[75] Attar H, Ehtemam-Haghighi S, Kent D, Dargusch MS (2018) Recent developments and opportunities in additive manufacturing of titanium-based matrix composites: A review. Int J Mach Tools Manuf 133:85–102 . doi: 10.1016/j.ijmachtools.2018.06.003

[76] Attar H, Bönisch M, Calin M, Zhang LC, Scudino S, Eckert J (2014) Selective laser melting of in situ titanium-titanium boride composites: Processing, microstructure and mechanical properties. Acta Mater 76:13–22 . doi: 10.1016/j.actamat.2014.05.022

[77] Wang XC, Kruth JP (2000) Energy Absorption and Penetration in Selective Laser Sintering : a Ray Tracing Model. Proc Int Conf Math Model Simul Met Technol 673–683

[78] Presley MA, Christensen PR (2010) Thermal conductivity measurements of particulate materials: 4. Effect of bulk density and particle shape. J Geophys Res 115:E07004 . doi: 10.1029/2009JE003483

[79] Abd-Elghany K, Bourell DL (2012) Property evaluation of 304L stainless steel fabricated by selective laser melting. Rapid Prototyp J 18:420–428 . doi: 10.1108/13552541211250418

[80] Liu B, Wildman R, Tuck C, Ashcroft I, Hague R (2011) Investigation the Effect of Particle Size Distribution on Processing Parameters Optimisation in Selective Laser Melting Process. Sff 227–238 . doi: 10.1017/CBO9781107415324.004

[81] Zou RP, Yu AB (1996) Evaluation of the packing characteristics of mono-sized

non-spherical particles. Powder Technol 88:71–79

[82] Chan C.Y. L, Page NW (1997) Particle fractal and load effects on internal friction in powders. Powder Technol 90:259–266

[83] Dawes J, Langley C, Clayton J (2017) Optimizing Metal Powders for Additive Manufacturing What Makes a Good AM Metal Powder ? Addit. Manuf. Mag. 1–5

[84] Simchi A (2004) The Role of Particle Size on the Laser Sintering of Iron Powder. 35:

[85] NANDWANA P, H. PETER W, DEHOFF RR, LOWE LE, KIRKA MM, MEDINA F, BABU SS (2016) Recyclability Study on Inconel 718 and Ti-6Al-4V Powders for Use in Electron Beam Melting. Metall Mater Trans 47:754–762 . doi: 10.1007/s10884-015-9497-z

[86] Terrassa KL, Haley JC, MacDonald BE, Schoenung JM (2018) Reuse of powder feedstock for directed energy deposition. Powder Technol 338:819–829 . doi: 10.1016/j.powtec.2018.07.065

[87] Engeli R, Etter T, Hövel S, Wegener K (2016) Processability of different IN738LC powder batches by selective laser melting. J Mater Process Technol 229:484–491 . doi: 10.1016/j.jmatprotec.2015.09.046

[88] Kulkarni PA, Berry RJ, Bradley MSA (2010) Review of the flowability measuring techniques for powder metallurgy industry. Proc Inst Mech Eng Part E J Process Mech Eng 224:159–168 . doi: 10.1243/09544089JPME299

[89] Hebert RJ (2016) Viewpoint: metallurgical aspects of powder bed metal additive manufacturing. J Mater Sci 51:1165–1175 . doi: 10.1007/s10853-015-9479-x

[90] Slotwinski JA, Garboczi EJ, Stutzman PE, Ferraris CF, Watson SS, Peltz MA (2014) Characterization of metal powders used for Additive Manufacturing. 119:460–493

[91] Gu H, Gong H, Dilip JJS, Pal D, Hicks A, Doak H, Stucker B (2015) Effects of powder variation on the microstructure and tensile strength of Ti-6Al-4V parts

fabricated by selective laser melting. Int J Powder Metall 51:35–42

[92] Baumers M, Tuck C, Wildman R, Ashcroft I, Rosamond E, Hague R (2012) Combined Build–Time, Energy Consumption and Cost Estimation for Direct Metal Laser Sintering. Proc Twenty Third Annu Int Solid Free Fabr Symp Addit Manuf Conf 53:1689–1699 . doi: 10.1017/CBO9781107415324.004

[93] Ardila LC, Garciandia F, González-Díaz JB, Álvarez P, Echeverria A, Petite MM, Deffley R, Ochoa J (2014) Effect of IN718 recycled powder reuse on properties of parts manufactured by means of Selective Laser Melting. Phys Procedia 56:99–107 . doi: 10.1016/j.phpro.2014.08.152

[94] Decost BL, Jain H, Rollett AD, Holm EA (2017) Computer Vision and Machine Learning for Autonomous Characterization of AM Powder Feedstocks. 69:456–465 . doi: 10.1007/s11837-016-2226-1

[95] Attar H, Prashanth KG, Zhang LC, Calin M, Okulov I V., Scudino S, Yang C, Eckert J (2015) Effect of powder particle shape on the properties of in situ Ti-TiB composite materials produced by selective laser melting. J Mater Sci Technol 31:1001–1005 . doi: 10.1016/j.jmst.2015.08.007

[96] Foster BK, Reutzel EW, Nassar AR, Hall BT, Brown SW, Dickman CJ (2015) Optical, layerwise monitoring of powder bed fusion. In: Solid Freeform Fabrication Symposium, Austin, TX, Aug. pp 10–12

[97] Zhang B, Ziegert J, Farahi F, Davies A (2016) In situ surface topography of laser powder bed fusion using fringe projection. Addit Manuf 12:100–107 . doi: 10.1016/j.addma.2016.08.001

[98] Attar H, Calin M, Zhang LC, Scudino S, Eckert J (2014) Manufacture by selective laser melting and mechanical behavior of commercially pure titanium. Mater Sci Eng A 593:170–177 . doi: 10.1016/j.msea.2013.11.038

[99] Zhu ZG, Nguyen QB, Ng FL, An XH, Liao XZ, Liaw PK, Nai SML, Wei J (2018) Hierarchical microstructure and strengthening mechanisms of a CoCrFeNiMn high entropy alloy additively manufactured by selective laser melting. Scr Mater 154:20–24 . doi: 10.1016/j.scriptamat.2018.05.015

[100] Verlee B, Dormal T (2012) Density and porosity control of sintered 316L stainless steel parts produced by additive manufacturing. Powder Metall 55: . doi: 10.1179/0032589912Z.00000000082

[101] Olakanmi EO, Dalgarno KW, Cochrane RF (2012) Laser sintering of blended Al-Si powders. Rapid Prototyp J 18:109–119 . doi: 10.1108/13552541211212096

[102] Ayoola WA, Suder WJ, Williams SW (2017) Parameters controlling weld bead profile in conduction laser welding. J Mater Process Technol 249:522–530 . doi: 10.1016/j.jmatprotec.2017.06.026

[103] Majumdar JD, Pinkerton A, Liu Z, Manna I, Li L (2005) Microstructure characterisation and process optimization of laser assisted rapid fabrication of 316L stainless steel. Appl Surf Sci 247:320–327 . doi: 10.1016/j.apsusc.2005.01.039

[104] Van Den Avyle JA, Brooks JA, Powell AC (1998) Reducing defects in remelting processes for high-performance alloys. Jom 50:22–25 . doi: 10.1007/s11837-998-0374-7

[105] Yahata T, Ikeda T, Maeda M (1993) Deoxidation of molten titanium by electron-beam remelting technique. Metall Trans B 24:599–604 . doi: 10.1007/BF02673175

[106] Charles C (2008) Modelling microstructure evolution of weld deposited Ti--6Al--4V. P. 76 . doi: 1402-1757

[107] Wang F, Williams S, Colegrove P, Antonysamy AA Microstructure and Mechanical Properties of Wire and Arc Additive Manufactured Ti-6Al-4V. doi: 10.1007/s11661-012-1444-6

[108] Han J, Yang J, Yu H, Yin J, Gao M, Wang Z, Zeng X (2017) Microstructure and mechanical property of selective laser melted Ti6Al4V dependence on laser energy density. Rapid Prototyp J 23:217–226 . doi: 10.1108/RPJ-12-2015-0193

[109] Steen WM, Mazumder J (2010) Basic Laser Optics. Laser Mater Process 79–130 . doi: 10.1007/978-1-84996-062-5_3

[110] He GS, Weder C, Smith P, Prasad PN (1998) Optical power limiting and stabilization based on a novel polymer compound. IEEE J Quantum Electron 34:2279–2285 . doi: 10.1109/3.736090

[111] Moylan S, Jurrens K, Donmez MA, Slotwinski JA, Cooke A (2013) NIST Technical Note 1801 Lessons Learned in Establishing the NIST Metal Additive Manufacturing Laboratory

[112] Kusuma C, Ahmed SH, Mian A, Srinivasan R (2017) Effect of Laser Power and Scan Speed on Melt Pool Characteristics of Commercially Pure Titanium (CP-Ti). J Mater Eng Perform 26:3560–3568 . doi: 10.1007/s11665-017-2768-6

[113] de Oliveira Teixeira PH, Reis AG dos, Janssen A, Teixeira PH de O, Reis AG dos, Janssen A, dos Reis AG, Janssen A (2015) Effect of solid-state laser parameters on the surface's topography formation during texturization of hard metal cutting tools. J Aerosp Technol Manag 7:63–69 . doi: 10.5028/jatm.v7i1.411

[114] Mclouth TD, Bean GE, Witkin DB, Sitzman SD, Adams PM, Patel DN, Park W, Yang J, Zaldivar RJ (2018) The effect of laser focus shift on microstructural variation of Inconel 718 produced by selective laser melting. Mater Des 149:205–213 . doi: 10.1016/j.matdes.2018.04.019

[115] Integrated Optics (2017) Laser Beam Collimation. https://integratedoptics.com/laser-beam-collimation

[116] Mullick S, Agrawal AK, Nath AK (2016) Effect of laser incidence angle on cut quality of 4 mm thick stainless steel sheet using fiber laser. Opt Laser Technol 81:168–179 . doi: 10.1016/j.optlastec.2016.02.006

[117] Roehling TT, Wu SSQ, Khairallah SA, Roehling JD, Soezeri SS, Crumb MF, Matthews MJ (2017) Modulating laser intensity profile ellipticity for microstructural control during metal additive manufacturing. Acta Mater 128:197–206 . doi: 10.1016/j.actamat.2017.02.025

[118] Ali H, Ghadbeigi H, Mumtaz K (2018) Effect of scanning strategies on residual stress and mechanical properties of Selective Laser Melted Ti6Al4V. Mater Sci Eng A 712:175–187 . doi: 10.1016/j.msea.2017.11.103

[119] Thijs L, Verhaeghe F, Craeghs T, Humbeeck J Van, Kruth JP (2010) A study of the microstructural evolution during selective laser melting of Ti-6Al-4V. Acta Mater 58:3303–3312 . doi: 10.1016/j.actamat.2010.02.004

[120] Monroy KP, Delgado J, Sereno L, Ciurana J, Hendrichs NJ (2014) Effects of the Selective Laser Melting manufacturing process on the properties of CoCrMo single tracks. Met Mater Int 20:873–884 . doi: 10.1007/s12540-014-5011-0

[121] Gu H, Gong H, Pal D, Rafi K, Starr T, Stucker B (2013) Influences of Energy Density on Porosity and Microstructure of Selective Laser Melted 17- 4PH Stainless Steel. 24th Int SFF Symp - An Addit Manuf Conf SFF 2013

[122] Demir AG, Previtali B (2017) Investigation of remelting and preheating in SLM of 18Ni300 maraging steel as corrective and preventive measures for porosity reduction. Int J Adv Manuf Technol 93:2697–2709 . doi: 10.1007/s00170-017-0697-z

[123] Vlasea ML, Lane B, Lopez F, Mekhontsec S, Donmez A (2015) TEST BED FOR ENHANCED REAL-TIME PROCESS CONTROL. 527–539

[124] Aminzadeh M (2016) A MACHINE VISION SYSTEM FOR IN-SITU QUALITY INSPECTION IN METAL POWDER-BED ADDITIVE MANUFACTURING

[125] Demir AG, De Giorgi C, Previtali B (2018) Design and Implementation of a Multisensor Coaxial Monitoring System With Correction Strategies for Selective Laser Melting of a Maraging Steel. J Manuf Sci Eng 140:1–14 . doi: 10.1115/1.4038568

[126] Frazier WE (2014) Metal additive manufacturing: A review. J Mater Eng Perform 23:1917–1928 . doi: 10.1007/s11665-014-0958-z

[127] Guesser WL, Souza Pereira F, Boehs L (2016) Surface changes during turning of grey cast iron Wilson Luis Guesser * Fernando Souza Pereira and Lourival Boehs. 18:

[128] Tajima K, Hironaka M, Chen K, Nagamatsu Y, Kakigawa H (2008) Electropolishing of CP Titanium and Its Alloys in an Alcoholic Solution-based Electrolyte. 27:258–

265

[129] Delfs P, Tows M, Schmid H (2016) Optimized build orientation of additive manufactured parts for improved surface quality and build time. 12:314–320 . doi: 10.1016/j.addma.2016.06.003

[130] Moroni G, Syam WP, Petrò S (2015) Functionality-based part orientation for additive manufacturing. Procedia CIRP 36:217–222 . doi: 10.1016/j.procir.2015.01.015

[131] Afkhami S, Dabiri M, Alavi SH, Björk T, Salminen A (2019) Fatigue characteristics of steels manufactured by selective laser melting. Int J Fatigue 122:72–83 . doi: 10.1016/j.ijfatigue.2018.12.029

[132] Mercelis P, Kruth JP (2006) Residual stresses in selective laser sintering and selective laser melting. Rapid Prototyp J 12:254–265 . doi: 10.1108/13552540610707013

[133] Shiomi M, Osakada K, Nakamura K, Yamashita T, Abe F (2004) Residual stress within metallic model made by selective laser melting process. CIRP Ann - Manuf Technol 53:195–198 . doi: 10.1016/S0007-8506(07)60677-5

[134] Wauthle R, Vrancken B, Beynaerts B, Jorissen K, Schrooten J, Kruth JP, Van Humbeeck J (2015) Effects of build orientation and heat treatment on the microstructure and mechanical properties of selective laser melted Ti6Al4V lattice structures. Addit Manuf 5:77–84 . doi: 10.1016/j.addma.2014.12.008

[135] Vrancken B, Thijs L, Kruth J-PP, Van Humbeeck J (2012) Heat treatment of Ti6Al4V produced by Selective Laser Melting: Microstructure and mechanical properties. J Alloy Compd J 541:177–185 . doi: 10.1016/j.msea.2013.10.023

[136] Sames WJ, List FA, Pannala S, Dehoff RR, Babu SS (2016) The metallurgy and processing science of metal additive manufacturing. Int Mater Rev 61:315–360 . doi: 10.1080/09506608.2015.1116649

[137] Leyens C, Peters M, Wenem D, Kaysser WA (1996) Influence of Long-Term Annealing on Tensile Properties and Fracture of Near-a Titanium Alloy Ti-6AI-2 .

75S n-4Z r-0 . 4 M o-0 . 45Si. 27:1709–1717

[138] Strano G, Hao L, Everson RM, Evans KE (2013) A new approach to the design and optimisation of support structures in additive manufacturing. 1247–1254 . doi: 10.1007/s00170-012-4403-x

[139] Hussein A, Hao L, Yan C, Everson R, Young P (2013) Journal of Materials Processing Technology Advanced lattice support structures for metal additive manufacturing. J Mater Process Tech 213:1019–1026 . doi: 10.1016/j.jmatprotec.2013.01.020

[140] Paschotta R (2008) Encyclopedia of Laser Physics and Technology

[141] Yurevich VI, Grimm VA, Afonyushkin AA, Yudin K V., Gorny SG (2015) Optical design and performance of F-Theta lenses for high-power and high-precision applications. Opt Syst Des 2015 Opt Des Eng VI 4:1 . doi: 10.1117/12.2190777

[142] Lacroix D, Jeandel G, Boudot C (2012) Solution of the radiative transfer equation in an absorbing and scattering Nd : YAG laser-induced plume. 2443: . doi: 10.1063/1.368405

[143] Nonhof CJ (1989) MATERIAL PROCESSING WITH Nd-LASERS

[144] Ferrar B, Mullen L, Jones E, Stamp R, Sutcliffe CJ (2012) Gas flow effects on selective laser melting (SLM) manufacturing performance. J Mater Process Technol 212:355–364 . doi: 10.1016/j.jmatprotec.2011.09.020

[145] Ye D, Ying J, Fuh H, Zhang Y, Soon G, Zhu K (2018) The investigation of plume and spatter signatures on melted states in selective laser melting In situ monitoring of selective laser melting using plume and spatter signatures by deep belief networks. ISA Trans 0–1 . doi: 10.1016/j.isatra.2018.07.021

[146] Shcheglov PY, Uspenskiy SA, Gumenyuk A V., Petrovskiy VN, Rethmeier M, Yermachenko VM (2011) Plume attenuation of laser radiation during high power fiber laser welding. Laser Phys Lett 8:475–480 . doi: 10.1002/lapl.201110010

[147] Greses J, Hilton PA, Barlow CY, Steen WM (2002) Plume attenuation under high

power Nd:YAG laser welding. In: International Congress on Applications of Lasers & Electro-Optics

[148] Mumtaz K, Hopkinson N, Mumtaz K, Hopkinson N (2010) Selective laser melting of Inconel 625 using pulse shaping. doi: 10.1108/13552541011049261

[149] Hansen F, Duley WW (2005) Attenuation of laser radiation by particles during laser materials processing. 137:6–13 . doi: 10.2351/1.4745348

[150] Francis Z (2017) The Effects of Laser and Electron Beam Spot Size in Additive Manufacturing Processes

[151] Lahiri A (2016) Basic Optics: Principles and Concepts. Elsevier Science

[152] ASTM (2012) Standard Test Methods for Tension Testing of Metallic Materials

[153] Bagchi TP (1993) Taguchi methods explained: Practical steps to robust design. Prentice-Hall

[154] Al Mangour BA (2017) Additive Manufacturing of High-Performance 316L Stainless Steel Nanocomposites via Selective Laser Melting. 239

[155] Snedecor GW, Cochran WG (1989) Statistical Methods

[156] 3D Systems (2017) Metal Additive Manufacturing with the ProX DMP 3D printers. 3–6

[157] Mukherjee T, Zuback JS, De A, DebRoy T (2016) Printability of alloys for additive manufacturing. Sci Rep 6:1–8 . doi: 10.1038/srep19717

[158] Nau R (2019) What ' s a good value for R-squared ? In: Statistical forecasting: notes on regression and time series analysis. pp 1–10

[159] Hitzeler L, Alifui-Segbaya F, Williams P, Heine B, Heitzmann M, Hall W, Merkel M, Öchsner A (2018) Additive manufacturing of cobalt-based dental alloys: Analysis of microstructure and physicomechanical properties. Adv Mater Sci Eng 2018: . doi: 10.1155/2018/8213023

[160] Li KC, Prior DJ, Waddell JN, Swain M V. (2015) Microstructure, phase content, and thermal stability of a cast Co-Cr dental alloy after porcelain sintering cycles

using electron backscatter diffraction. J Mater Res 30:2188–2196 . doi: 10.1557/jmr.2015.178

[161] Chen ZW, Phan MAL, Darvish K (2017) Grain growth during selective laser melting of a Co–Cr–Mo alloy. J Mater Sci 52:7415–7427 . doi: 10.1007/s10853-017-0975-z

[162] Gorsse S, Hutchinson C, Gouné M, Banerjee R (2017) Additive manufacturing of metals: a brief review of the characteristic microstructures and properties of steels, Ti-6Al-4V and high-entropy alloys. Sci Technol Adv Mater 18:584–610 . doi: 10.1080/14686996.2017.1361305

[163] Chen W, Yin G, Feng Z, Liao X (2018) Effect of powder feedstock on microstructure and mechanical properties of the 316L stainless steel fabricated by selective laser melting. Metals (Basel) 8: . doi: 10.3390/met8090729

Chapter 9: Appendices

9.1 Experimental Data

9.1.1 Base Build (CoCr, Manufacturers Specifications)

Sample	**1**	**2**	**3**	**4**	**5**	**6**	**7**	**8**	**9**	**10**	**11**
Strain (%)	17.33	19.12	18.58	20.38	17.58	17.82	20.17	18.43	20.07	19.91	20.03
UTS (Mpa)	1077	1100	1100	1106	1098	1089	1104	1075	1118	1090	1096
Sample	**12**	**13**	**14**	**15**	**16**	**17**	**18**	**19**	**20**	**21**	**22**
Strain (%)	16.27	15.97	19.02	21.86	18.13	21.38	19.48	18.50	16.81	22.17	15.95
UTS (Mpa)	1093	1047	1107	1082	1111	1128	1108	1125	1112	1117	1115
Sample	**23**	**24**	**25**	**26**	**27**	**28**	**29**	**30**	**31**	**32**	**33**
Strain (%)	15.92	17.33	20.55	20.87	20.50	21.82	21.05	17.52	17.54	19.91	5.12
UTS (Mpa)	1085	1072	1115	1114	1088	1128	1101	1117	1099	1110	911
Sample	**34**	**35**	**36**	**37**	**38**	**39**	**40**	**41**	**42**	**43**	**44**
Strain (%)	16.12	17.70	18.04	22.35	17.89	21.56	19.21	19.02	16.50	23.54	17.11
UTS (Mpa)	1066	1075	1094	1117	1126	1136	1083	1130	1072	1085	1079
Sample	**45**	**46**	**47**	**48**	**49**	**50**	**51**	**52**	**53**	**54**	**55**
Strain (%)	18.99	17.81	20.39	21.48	16.15	23.56	21.07	21.08	15.05	20.28	18.67
UTS (Mpa)	1084	1047	1066	1118	1088	1125	1102	1099	1078	1109	1099
Sample	**56**	**57**	**58**	**59**	**60**	**61**	**62**	**63**	**64**	**65**	**66**
Strain (%)	17.23	14.01	15.23	19.93	20.70	19.30	18.95	18.37	21.55	20.56	20.09
UTS (Mpa)	1100	1076	1094	1111	1096	1092	1071	1087	1122	1124	1126
Sample	**67**	**68**	**69**	**70**	**71**	**72**	**73**	**74**	**75**	**76**	**77**
Strain (%)	15.52	18.98	18.85	21.74	17.92	20.00	18.84	19.49	18.29	21.46	20.51
UTS (Mpa)	1065	1080	1085	1101	1097	1104	1090	1111	1093	1130	1140
Sample	**78**	**79**	**80**	**81**	**82**	**83**	**84**	**85**	**86**	**87**	**88**
Strain (%)	17.23	20.80	20.85	21.89	17.62	21.39	19.75	15.58	18.46	19.36	16.63
UTS (Mpa)	1067	1042	1107	1103	1118	1105	1094	1074	1089	1083	1091
Sample	**89**	**90**	**91**	**92**	**93**	**94**	**95**	**96**	**97**	**98**	**99**
Strain (%)	16.53	17.61	19.01	20.18	20.89	21.10	20.75	18.27	17.28	22.05	17.70
UTS (Mpa)	1067	1058	1082	1098	1106	1118	1096	1070	1078	1122	1072
Sample	**100**	**101**	**102**	**103**	**104**	**105**	**106**	**107**	**108**	**109**	**110**
Strain (%)	17.23	16.79	19.26	20.03	18.94	21.70	18.94	22.05	18.24	20.46	17.37
UTS (Mpa)	1062	1070	1120	1184	1044	1110	1065	1078	1100	1096	1105
Sample	**111**	**112**	**113**	**114**	**115**	**116**	**117**	**118**	**119**	**120**	**121**
Strain (%)	16.33	16.49	17.31	24.04	16.55	19.79	20.09	18.01	17.04	20.01	17.26
UTS (Mpa)	1061	1030	1080	1126	1114	1109	1088	1081	1097	1090	1073

9.1.2 Corrected Build (CoCr, Variable Speed)

Sample	**1**	**2**	**3**	**4**	**5**	**6**	**7**	**8**	**9**	**10**	**11**
Strain (%)	17.56	17.19	18.88	18.63	18.88	18.50	18.38	19.50	18.94	17.81	18.19
UTS (Mpa)	1031	1043	1055	1050	1058	1050	1048	1062	1061	1054	1065
Sample	**12**	**13**	**14**	**15**	**16**	**17**	**18**	**19**	**20**	**21**	**22**
Strain (%)	18.06	19.00	18.81	17.88	18.63	18.25	20.44	21.81	20.50	20.50	19.06
UTS (Mpa)	1028	1042	1046	1040	1048	1055	1061	1074	1073	1068	1064
Sample	**23**	**24**	**25**	**26**	**27**	**28**	**29**	**30**	**31**	**32**	**33**
Strain (%)	16.31	18.13	18.38	20.19	19.56	20.19	16.75	18.44	18.13	18.88	19.19
UTS (Mpa)	1009	1053	1044	1060	1058	1069	1035	1051	1058	1066	1058
Sample	**34**	**35**	**36**	**37**	**38**	**39**	**40**	**41**	**42**	**43**	**44**
Strain (%)	17.00	17.38	17.63	18.19	18.38	17.31	18.81	19.88	19.50	18.94	16.38
UTS (Mpa)	1020	1036	1057	1062	1061	1056	1052	1066	1063	1060	1042
Sample	**45**	**46**	**47**	**48**	**49**	**50**	**51**	**52**	**53**	**54**	**55**
Strain (%)	17.81	15.44	18.25	19.00	18.13	18.63	18.13	18.88	19.44	18.75	17.38
UTS (Mpa)	1031	1021	1042	1053	1044	1060	1038	1052	1048	1053	1038
Sample	**56**	**57**	**58**	**59**	**60**	**61**	**62**	**63**	**64**	**65**	**66**
Strain (%)	17.81	18.63	19.56	18.88	18.13	17.44	18.25	19.63	20.56	17.88	16.31
UTS (Mpa)	1034	1058	1068	1061	1058	1051	1053	1067	1072	1060	1029
Sample	**67**	**68**	**69**	**70**	**71**	**72**	**73**	**74**	**75**	**76**	**77**
Strain (%)	19.50	18.31	16.88	16.31	20.56	17.75	19.88	19.19	18.50	19.44	17.13
UTS (Mpa)	1026	1041	1036	1035	1053	1044	1050	1051	1043	1059	1039
Sample	**78**	**79**	**80**	**81**	**82**	**83**	**84**	**85**	**86**	**87**	**88**
Strain (%)	17.31	17.81	19.00	19.88	19.63	19.06	18.13	19.38	19.06	19.00	16.31
UTS (Mpa)	1016	1038	1046	1057	1050	1058	1038	1059	1059	1052	1035
Sample	**89**	**90**	**91**	**92**	**93**	**94**	**95**	**96**	**97**	**98**	**99**
Strain (%)	15.13	19.44	17.00	18.94	20.69	20.19	15.25	20.38	19.00	17.94	16.75
UTS (Mpa)	1001	1043	1036	1049	1054	1050	1020	1054	1046	1045	1059
Sample	**100**	**101**	**102**	**103**	**104**	**105**	**106**	**107**	**108**	**109**	**110**
Strain (%)	18.94	18.00	16.44	17.31	17.75	18.00	18.69	17.75	19.38	18.13	17.81
UTS (Mpa)	1033	1038	1041	1041	1032	1050	1050	1047	1057	1046	1042
Sample	**111**	**112**	**113**	**114**	**115**	**116**	**117**	**118**	**119**	**120**	**121**
Strain (%)	17.44	16.00	15.88	16.75	15.69	13.31	16.44	17.81	16.81	15.31	13.88
UTS (Mpa)	1015	1011	1007	1024	1003	999	1019	1020	1015	1001	1009

9.1.3 Base Build (316L, Manufacturers Specifications)

Sample	**1**	**2**	**3**	**4**	**5**	**6**	**7**	**8**	**9**	**10**	**11**
Strain (%)	0.00	48.75	49.53	46.84	8.14	57.46	48.35	34.93	48.03	3.10	2.03
UTS (Mpa)	0	624	632	632	448	642	639	637	640	256	46
Sample	**12**	**13**	**14**	**15**	**16**	**17**	**18**	**19**	**20**	**21**	**22**
Strain (%)	48.18	44.65	53.56	46.08	49.33	25.14	48.65	50.91	52.09	50.41	26.95
UTS (Mpa)	631	624	628	631	632	618	636	628	638	631	624
Sample	**23**	**24**	**25**	**26**	**27**	**28**	**29**	**30**	**31**	**32**	**33**
Strain (%)	54.45	49.94	50.97	47.88	39.32	50.11	50.32	43.98	45.55	46.18	49.55
UTS (Mpa)	624	624	624	629	630	642	632	640	574	631	627
Sample	**34**	**35**	**36**	**37**	**38**	**39**	**40**	**41**	**42**	**43**	**44**
Strain (%)	51.08	48.31	48.45	49.05	50.33	36.91	50.86	14.88	50.71	50.40	50.49
UTS (Mpa)	622	620	628	631	629	640	640	591	629	628	625
Sample	**45**	**46**	**47**	**48**	**49**	**50**	**51**	**52**	**53**	**54**	**55**
Strain (%)	48.15	47.49	53.32	51.95	51.41	52.99	55.41	30.77	50.66	49.77	49.70
UTS (Mpa)	617	612	621	624	626	637	621	622	624	620	619
Sample	**56**	**57**	**58**	**59**	**60**	**61**	**62**	**63**	**64**	**65**	**66**
Strain (%)	53.33	50.23	50.79	49.38	49.47	45.89	52.43	48.10	50.73	51.12	49.93
UTS (Mpa)	627	628	633	636	636	640	638	643	637	634	636
Sample	**67**	**68**	**69**	**70**	**71**	**72**	**73**	**74**	**75**	**76**	**77**
Strain (%)	50.90	50.26	49.41	49.46	50.87	49.22	50.58	50.13	51.93	50.34	48.69
UTS (Mpa)	617	618	624	626	624	632	629	628	625	624	620
Sample	**78**	**79**	**80**	**81**	**82**	**83**	**84**	**85**	**86**	**87**	**88**
Strain (%)	52.17	48.66	52.27	47.13	51.74	51.15	10.31	48.50	50.34	47.08	49.60
UTS (Mpa)	616	620	620	622	625	636	427	630	628	620	617
Sample	**89**	**90**	**91**	**92**	**93**	**94**	**95**	**96**	**97**	**98**	**99**
Strain (%)	47.40	50.08	49.61	48.23	49.70	48.68	53.13	50.37	49.94	49.39	48.12
UTS (Mpa)	614	614	618	622	618	626	628	644	620	616	618
Sample	**100**	**101**	**102**	**103**	**104**	**105**	**106**	**107**	**108**	**109**	**110**
Strain (%)	50.28	49.57	49.01	49.66	52.35	49.66	52.46	50.71	50.72	48.80	50.15
UTS (Mpa)	614	613	616	620	612	624	620	620	620	615	612
Sample	**111**	**112**	**113**	**114**	**115**	**116**	**117**	**118**	**119**	**120**	**121**
Strain (%)	50.78	51.23	41.27	49.53	52.55	45.32	49.60	49.29	50.13	5.44	0.00
UTS (Mpa)	611	608	611	618	608	623	616	613	610	488	0

9.1.4 Corrected Build (316L, Variable Speed)

Sample	**1**	**2**	**3**	**4**	**5**	**6**	**7**	**8**	**9**	**10**	**11**
Strain (%)	49.39	45.74	47.17	44.37	48.38	50.28	47.77	49.82	48.04	49.40	50.12
UTS (Mpa)	640	634	642	641	647	647	648	651	649	642	648
Sample	**12**	**13**	**14**	**15**	**16**	**17**	**18**	**19**	**20**	**21**	**22**
Strain (%)	50.76	48.40	49.40	48.80	44.85	49.13	48.59	45.38	48.69	47.40	48.25
UTS (Mpa)	629	632	636	634	636	646	641	644	645	637	639
Sample	**23**	**24**	**25**	**26**	**27**	**28**	**29**	**30**	**31**	**32**	**33**
Strain (%)	50.89	50.37	47.13	48.53	45.14	48.60	46.62	49.26	42.31	47.26	50.62
UTS (Mpa)	628	628	630	628	637	641	632	639	637	636	625
Sample	**34**	**35**	**36**	**37**	**38**	**39**	**40**	**41**	**42**	**43**	**44**
Strain (%)	51.93	45.95	49.68	48.03	13.42	48.37	49.32	49.85	47.95	48.50	49.27
UTS (Mpa)	626	624	633	629	542	639	630	634	635	631	632
Sample	**45**	**46**	**47**	**48**	**49**	**50**	**51**	**52**	**53**	**54**	**55**
Strain (%)	50.57	46.39	47.67	46.18	48.01	49.34	50.19	48.78	48.70	48.41	48.54
UTS (Mpa)	622	616	621	622	619	631	619	629	628	627	632
Sample	**56**	**57**	**58**	**59**	**60**	**61**	**62**	**63**	**64**	**65**	**66**
Strain (%)	49.51	49.57	49.20	42.15	45.56	44.79	49.36	47.76	49.83	49.42	50.83
UTS (Mpa)	631	628	635	637	633	636	635	639	640	639	624
Sample	**67**	**68**	**69**	**70**	**71**	**72**	**73**	**74**	**75**	**76**	**77**
Strain (%)	50.80	45.58	47.34	48.74	46.70	47.94	45.99	49.09	16.27	49.84	50.95
UTS (Mpa)	623	624	628	626	624	627	624	624	608	627	626
Sample	**78**	**79**	**80**	**81**	**82**	**83**	**84**	**85**	**86**	**87**	**88**
Strain (%)	49.93	47.65	47.78	46.97	48.83	48.88	49.94	49.38	49.39	4.92	47.47
UTS (Mpa)	620	621	622	624	624	633	622	628	629	212	625
Sample	**89**	**90**	**91**	**92**	**93**	**94**	**95**	**96**	**97**	**98**	**99**
Strain (%)	48.54	46.75	46.96	41.18	46.22	49.41	48.42	49.40	47.81	48.81	50.55
UTS (Mpa)	620	618	622	624	622	625	624	627	621	621	636
Sample	**100**	**101**	**102**	**103**	**104**	**105**	**106**	**107**	**108**	**109**	**110**
Strain (%)	51.23	49.31	47.24	49.35	51.39	48.51	49.14	49.15	47.07	46.65	46.63
UTS (Mpa)	620	619	622	623	616	625	618	621	624	620	618
Sample	**111**	**112**	**113**	**114**	**115**	**116**	**117**	**118**	**119**	**120**	**121**
Strain (%)	50.00	49.92	49.02	48.73	49.47	46.90	49.66	47.94	41.09	48.83	49.26
UTS (Mpa)	617	615	618	622	612	621	619	620	613	612	620

9.1.5 Hole feature measurements

Sample	**1**	**2**	**3**	**4**	**5**	**6**	**7**	**8**	**9**	**10**	**11**
Nominal 1 mm (mm)	0.845	0.943	0.970	0.952	0.964	0.955	0.958	0.941	0.951	0.945	0.898
Nominal 0.8 mm (mm)	0.707	0.745	0.779	0.761	0.777	0.770	0.772	0.749	0.750	0.750	0.709
Nominal 0.6 mm (mm)	0.494	0.539	0.566	0.554	0.555	0.577	0.576	0.563	0.562	0.560	0.516
Nominal 0.4 mm (mm)	0.318	0.350	0.389	0.363	0.350	0.379	0.383	0.365	0.379	0.369	0.343
Nominal 0.2 mm (mm)	0.084	0.183	0.203	0.183	0.200	0.173	0.219	0.142	0.193	0.179	0.148
Sample	**12**	**13**	**14**	**15**	**16**	**17**	**18**	**19**	**20**	**21**	**22**
Nominal 1 mm (mm)	0.927	0.984	0.980	0.995	0.984	1.010	1.013	1.001	1.007	0.988	0.951
Nominal 0.8 mm (mm)	0.623	0.783	0.788	0.797	0.804	0.796	0.806	0.815	0.802	0.796	0.763
Nominal 0.6 mm (mm)	0.554	0.582	0.583	0.581	0.598	0.593	0.605	0.609	0.607	0.598	0.566
Nominal 0.4 mm (mm)	0.353	0.396	0.398	0.389	0.396	0.396	0.393	0.421	0.411	0.411	0.369
Nominal 0.2 mm (mm)	0.164	0.219	0.238	0.194	0.221	0.229	0.226	0.228	0.250	0.235	0.173
Sample	**23**	**24**	**25**	**26**	**27**	**28**	**29**	**30**	**31**	**32**	**33**
Nominal 1 mm (mm)	0.949	0.988	1.001	0.991	0.999	1.008	1.005	0.992	0.987	0.988	0.952
Nominal 0.8 mm (mm)	0.669	0.802	0.806	0.790	0.790	0.818	0.794	0.792	0.798	0.792	0.760
Nominal 0.6 mm (mm)	0.561	0.580	0.593	0.599	0.584	0.591	0.597	0.580	0.593	0.586	0.562
Nominal 0.4 mm (mm)	0.363	0.407	0.391	0.381	0.405	0.422	0.407	0.408	0.410	0.377	0.360
Nominal 0.2 mm (mm)	0.189	0.201	0.213	0.226	0.201	0.232	0.231	0.226	0.228	0.207	0.185
Sample	**34**	**35**	**36**	**37**	**38**	**39**	**40**	**41**	**42**	**43**	**44**
Nominal 1 mm (mm)	0.962	0.996	0.985	1.005	1.001	1.016	0.991	0.995	0.988	0.995	0.973
Nominal 0.8 mm (mm)	0.764	0.793	0.796	0.804	0.801	0.808	0.801	0.813	0.795	0.790	0.786
Nominal 0.6 mm (mm)	0.573	0.581	0.584	0.603	0.583	0.599	0.594	0.598	0.597	0.589	0.588
Nominal 0.4 mm (mm)	0.366	0.401	0.392	0.384	0.414	0.407	0.423	0.399	0.405	0.399	0.403
Nominal 0.2 mm (mm)	0.190	0.213	0.200	0.224	0.216	0.228	0.248	0.229	0.216	0.212	0.219
Sample	**45**	**46**	**47**	**48**	**49**	**50**	**51**	**52**	**53**	**54**	**55**
Nominal 1 mm (mm)	0.947	0.982	0.976	0.996	1.002	1.017	0.994	0.987	0.999	0.986	0.991
Nominal 0.8 mm (mm)	0.758	0.787	0.797	0.804	0.795	0.808	0.813	0.796	0.788	0.783	0.792
Nominal 0.6 mm (mm)	0.545	0.581	0.592	0.616	0.587	0.596	0.606	0.617	0.592	0.591	0.582
Nominal 0.4 mm (mm)	0.363	0.408	0.398	0.401	0.411	0.395	0.392	0.404	0.402	0.389	0.394
Nominal 0.2 mm (mm)	0.163	0.203	0.218	0.211	0.242	0.236	0.240	0.213	0.222	0.224	0.225
Sample	**56**	**57**	**58**	**59**	**60**	**61**	**62**	**63**	**64**	**65**	**66**
Nominal 1 mm (mm)	0.965	1.001	0.998	1.009	1.009	1.005	1.009	1.010	1.004	0.995	1.001
Nominal 0.8 mm (mm)	0.766	0.801	0.807	0.801	0.816	0.826	0.804	0.801	0.806	0.806	0.799
Nominal 0.6 mm (mm)	0.568	0.597	0.586	0.610	0.610	0.608	0.606	0.599	0.604	0.616	0.589
Nominal 0.4 mm (mm)	0.361	0.401	0.408	0.400	0.415	0.412	0.398	0.417	0.391	0.400	0.390
Nominal 0.2 mm (mm)	0.178	0.226	0.234	0.235	0.223	0.250	0.239	0.242	0.226	0.225	0.189
Sample	**67**	**68**	**69**	**70**	**71**	**72**	**73**	**74**	**75**	**76**	**77**
Nominal 1 mm (mm)	0.966	0.973	0.987	0.982	0.986	0.987	0.996	0.986	0.990	1.003	0.992
Nominal 0.8 mm (mm)	0.772	0.778	0.779	0.778	0.779	0.794	0.790	0.794	0.789	0.800	0.792
Nominal 0.6 mm (mm)	0.551	0.587	0.579	0.591	0.583	0.591	0.585	0.596	0.584	0.606	0.610
Nominal 0.4 mm (mm)	0.365	0.374	0.388	0.391	0.388	0.418	0.400	0.398	0.373	0.407	0.406
Nominal 0.2 mm (mm)	0.209	0.197	0.218	0.184	0.168	0.228	0.231	0.228	0.244	0.222	0.227
Sample	**78**	**79**	**80**	**81**	**82**	**83**	**84**	**85**	**86**	**87**	**88**
Nominal 1 mm (mm)	0.951	0.993	0.989	0.979	0.999	0.999	0.999	0.992	0.989	0.989	0.991
Nominal 0.8 mm (mm)	0.758	0.802	0.790	0.776	0.778	0.795	0.808	0.790	0.784	0.784	0.786
Nominal 0.6 mm (mm)	0.560	0.587	0.590	0.570	0.589	0.601	0.592	0.603	0.582	0.585	0.587
Nominal 0.4 mm (mm)	0.359	0.401	0.384	0.386	0.395	0.393	0.392	0.401	0.393	0.403	0.391
Nominal 0.2 mm (mm)	0.157	0.216	0.204	0.199	0.223	0.216	0.216	0.212	0.218	0.221	0.231

Sample	**89**	**90**	**91**	**92**	**93**	**94**	**95**	**96**	**97**	**98**	**99**
Nominal 1 mm (mm)	0.955	0.986	0.988	0.984	1.012	0.989	0.964	0.963	0.998	0.995	0.985
Nominal 0.8 mm (mm)	0.760	0.783	0.784	0.801	0.807	0.804	0.780	0.769	0.796	0.806	0.790
Nominal 0.6 mm (mm)	0.557	0.592	0.581	0.588	0.601	0.588	0.560	0.579	0.600	0.585	0.581
Nominal 0.4 mm (mm)	0.356	0.366	0.389	0.404	0.401	0.384	0.391	0.378	0.403	0.392	0.406
Nominal 0.2 mm (mm)	0.165	0.210	0.247	0.196	0.226	0.210	0.202	0.218	0.218	0.230	0.239
Sample	**100**	**101**	**102**	**103**	**104**	**105**	**106**	**107**	**108**	**109**	**110**
Nominal 1 mm (mm)	0.967	0.971	0.978	0.974	0.975	0.998	0.998	1.000	1.007	0.992	0.994
Nominal 0.8 mm (mm)	0.756	0.772	0.767	0.767	0.772	0.790	0.790	0.816	0.830	0.784	0.794
Nominal 0.6 mm (mm)	0.564	0.559	0.577	0.563	0.578	0.575	0.588	0.607	0.598	0.595	0.581
Nominal 0.4 mm (mm)	0.364	0.400	0.390	0.371	0.394	0.399	0.412	0.424	0.366	0.399	0.376
Nominal 0.2 mm (mm)	0.175	0.232	0.209	0.194	0.176	0.218	0.204	0.237	0.109	0.238	0.223
Sample	**111**	**112**	**113**	**114**	**115**	**116**	**117**	**118**	**119**	**120**	**121**
Nominal 1 mm (mm)	0.977	0.998	0.981	0.955	0.987	0.978	0.973	0.967	0.972	0.971	0.930
Nominal 0.8 mm (mm)	0.784	0.790	0.793	0.786	0.786	0.802	0.781	0.781	0.771	0.771	0.746
Nominal 0.6 mm (mm)	0.579	0.591	0.582	0.561	0.590	0.582	0.569	0.587	0.590	0.575	0.536
Nominal 0.4 mm (mm)	0.376	0.412	0.386	0.359	0.416	0.406	0.386	0.395	0.396	0.385	0.354
Nominal 0.2 mm (mm)	0.204	0.229	0.190	0.188	0.228	0.227	0.214	0.204	0.236	0.213	0.160

9.1.6 Pin Features (Nominal 1mm)

Sample	**1**	**2**	**3**	**4**	**5**	**6**	**7**	**8**	**9**	**10**	**11**
Diameter (µm)	988	961	933	942	912	922	926	934	928	945	964
Sample	**12**	**13**	**14**	**15**	**16**	**17**	**18**	**19**	**20**	**21**	**22**
Diameter (µm)	970	944	947	944	915	940	924	925	930	973	943
Sample	**23**	**24**	**25**	**26**	**27**	**28**	**29**	**30**	**31**	**32**	**33**
Diameter (µm)	946	946	947	939	932	947	943	913	923	928	936
Sample	**34**	**35**	**36**	**37**	**38**	**39**	**40**	**41**	**42**	**43**	**44**
Diameter (µm)	946	944	928	951	938	892	936	908	907	940	929
Sample	**45**	**46**	**47**	**48**	**49**	**50**	**51**	**52**	**53**	**54**	**55**
Diameter (µm)	934	959	931	940	934	930	906	903	927	931	917
Sample	**56**	**57**	**58**	**59**	**60**	**61**	**62**	**63**	**64**	**65**	**66**
Diameter (µm)	917	948	933	944	945	911	930	894	927	908	917
Sample	**67**	**68**	**69**	**70**	**71**	**72**	**73**	**74**	**75**	**76**	**77**
Diameter (µm)	932	941	937	913	937	920	916	901	915	904	936
Sample	**78**	**79**	**80**	**81**	**82**	**83**	**84**	**85**	**86**	**87**	**88**
Diameter (µm)	964	951	943	947	923	932	918	916	924	954	962
Sample	**89**	**90**	**91**	**92**	**93**	**94**	**95**	**96**	**97**	**98**	**99**
Diameter (µm)	959	948	934	927	923	926	944	913	916	932	935
Sample	**100**	**101**	**102**	**103**	**104**	**105**	**106**	**107**	**108**	**109**	**110**
Diameter (µm)	943	938	927	930	936	937	914	910	924	912	943
Sample	**111**	**112**	**113**	**114**	**115**	**116**	**117**	**118**	**119**	**120**	**121**
Diameter (µm)	952	937	948	956	930	932	949	924	933	938	947

9.2 Engineering Drawings

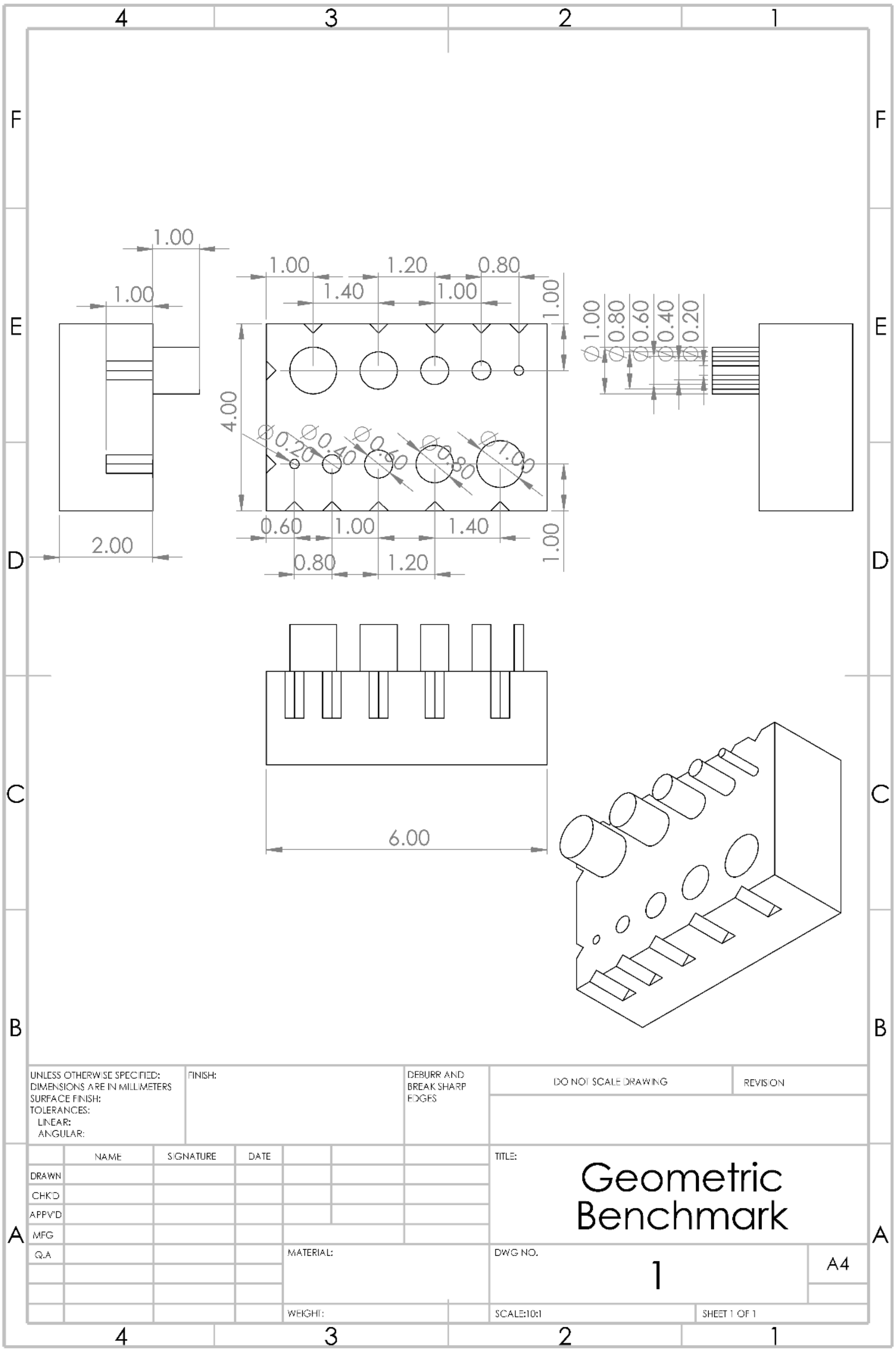

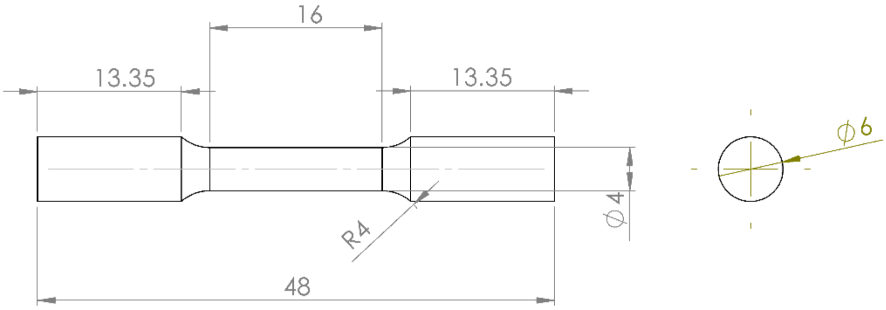

UNLESS OTHERWISE SPECIFIED:
DIMENSIONS ARE IN MILLIMETERS
SURFACE FINISH:
TOLERANCES:
LINEAR:
ANGULAR:

FINISH:

DEBURR AND BREAK SHARP EDGES

DO NOT SCALE DRAWING

REVISION

	NAME	SIGNATURE	DATE
DRAWN			
CHK'D			
APPV'D			
MFG			
Q.A			

MATERIAL:

WEIGHT:

TITLE:

ASTM E8 Dogbone

DWG NO. 2

A4

SCALE:2:1

SHEET 1 OF 1

9.3 MATLab Code

9.3.1 Ray Tracing on a powder bed

```
%% create the bed
clear all;
for w =1:25
    close all;
    clear C R
    w
    xlimit = 400;
    depth = 100;
    % if creating new powder bed
    ab=[xlimit depth]; % rectangle dimensions
    R_min=12.5;      % minimum circle radius 7.5
    R_max=12.5;     % maximum circle radius 17.5
    cnst=true;
    [C,R]=random_circle_packing_rectangle(ab,R_min,R_max,cnst,false);

    %%
    PropSpeed = 0.3;
    Absorbance = 0.7;
    ylim([0 depth*2]);
    for m =65:115
        EscapeEnergy =0;
        m
        clear ray
        for k =1:100
            ray(k,1,:)= [130+k-(round(tand(m-90))) depth*2
PropSpeed*cosd(m) -PropSpeed*sind(m) 1];
            exists = true;
            i=1;
            while exists == true

                if ray(k,i,1) > xlimit || ray(k,i,1) < 0 %check to see
if reflected out of box
                    exists = false;
                    EscapeEnergy = EscapeEnergy + ray(k,i,5);
                end
                if ray(k,i,2) > depth*2 || ray(k,i,2) < 0 %check to
see if reflected into plate or to chamber
                    exists = false;
                    EscapeEnergy = EscapeEnergy + ray(k,i,5);
                end
                if ray(k,i,5) < 0.3 % check if fully absorbed
                    exists = false;
                end

                if exists == true
                    reflection = false;
                    for j=1:length(C)
                        if R(j) > sqrt((power((C(j,1)-
ray(k,i,1)),2))+(power((C(j,2)-ray(k,i,2)),2)))%Check if point it
inside a circle
                            reflection = true;
                            reflectionpoint =j;
                        end
                    end
```

```
                    if reflection == true %if reflected change 
propagation path
                        %Circle Normal Angle
                        X_change =ray(k,i,1)-C(reflectionpoint,1);
                        Y_change =ray(k,i,2)-C(reflectionpoint,2);
                        if X_change >= 0 && Y_change >= 0 %quadrant 1
                            NormalAngle = 
atan(abs(Y_change)/abs(X_change));
                        end
                        if X_change < 0 && Y_change >= 0 %quadrant 2
                            NormalAngle = pi()-
atan(abs(Y_change)/abs(X_change));
                        end
                        if X_change < 0 && Y_change < 0 %quadrant 3
                            NormalAngle = 
pi()+atan(abs(Y_change)/abs(X_change));
                        end
                        if X_change >= 0 && Y_change < 0 %quadrant 4
                            NormalAngle = 2*pi()-
atan(abs(Y_change)/abs(X_change));
                        end

                        XR_change =-ray(k,i,3);
                        YR_change =-ray(k,i,4);
                        %Angle that propagation makes
                        if XR_change >= 0 && YR_change >= 0 %quadrant 
1
                            PropAngle = 
atan(abs(YR_change)/abs(XR_change));
                        end
                        if XR_change < 0 && YR_change >= 0 %quadrant 2
                            PropAngle = pi()-
atan(abs(YR_change)/abs(XR_change));
                        end
                        if XR_change < 0 && YR_change < 0 %quadrant 3
                            PropAngle = 
pi()+atan(abs(YR_change)/abs(XR_change));
                        end
                        if XR_change >= 0 && YR_change < 0 %quadrant 4
                            PropAngle = 2*pi()-
atan(abs(YR_change)/abs(XR_change));
                        end

                        IncidenceAngle=NormalAngle-PropAngle;
                        NewPropAngle = PropAngle +(2*IncidenceAngle);

                        ray(k,i,3)=PropSpeed*cos(NewPropAngle);
                        ray(k,i,4)=PropSpeed*sin(NewPropAngle);
                        ray(k,i,5)=ray(k,i,5)*Absorbance;
                    end
                    i=i+1;
                    ray(k,i,1)=ray(k,i-1,1)+ray(k,i-1,3);
                    ray(k,i,2)=ray(k,i-1,2)+ray(k,i-1,4);
                    ray(k,i,3)=ray(k,i-1,3);
                    ray(k,i,4)=ray(k,i-1,4);
                    ray(k,i,5)=ray(k,i-1,5);
                end
            end

        end
```

```
        storem(m)=EscapeEnergy;
    end
    storewc(1:length(C),1:2,w)=C;
    storewr(1:length(R),w)=R;
    storewm(:,w)=storem;
end
figure();idx = storewr > 0;hist(2*storewr(idx));
```

9.3.2 New ED equation calculator

```
h = 300; %mm distance from build plate to laser source
p = 218/91.5305; %131,174,218 power in watts
v = 2500; %1500, 2000, 2500 start speed
t = 0.03; % layer thickness
ssc = 0.001213; % spot size at source 0.1213,0.1323,0.1401
asc = 3.14*power(ssc,2); %spot at centre of circle

for i =-70:1:70 %no Changes
    for j = -70:1:70
        ft(i+71,j+71)=FTmap(i,j);
        if isnan(ft(i+71,j+71))
            ft(i+71,j+71) = 1;
        end
    end
end

d =zeros(141);
l =zeros(141);
ang =zeros(141);
ssl =zeros(141);
asl =zeros(141);
psl =zeros(141);
ti =zeros(141);
ed =zeros(141);



%%
for i =-70:1:70 %all sources included
    for j = -70:1:70
        d(i+71,j+71) = sqrt((power(i,2)+power(j,2)));
        l(i+71,j+71) = sqrt((power(d(i+71,j+71),2)+power(h,2)));
        ang(i+71,j+71) = atan(h/d(i+71,j+71));
        ssl4(i+71,j+71) = sqrt((power(ssc,2)+power(ssc*tan((pi()/2)-
ang(i+71,j+71)),2)));
        asl(i+71,j+71) = (pi()*ssc*ssl4(i+71,j+71))*ft(i+71,j+71);
        att(i+71,j+71) = exp(-3.46*0.05*(1*(sin(ang(i+71,j+71)))));
        rfl(i+71,j+71) = (-
0.00004*rad2deg(ang(i+71,j+71))*rad2deg(ang(i+71,j+71)))+(0.0078*rad2d
eg(ang(i+71,j+71)))+(0.622);
        psl(i+71,j+71) =
(4*p.*att(i+71,j+71).*rfl(i+71,j+71))/asl(i+71,j+71);
        ti(i+71,j+71) = ((ssl4(i+71,j+71)+ssc)/2)/v;
        ed4(i+71,j+71) = psl(i+71,j+71)*ti(i+71,j+71);
    end
end
%%
figure; mesh(ed4);
xticks(1:20:141);xticklabels(-70:20:70);xlim([1 141]);xlabel('Distance
(mm)');
```

```
yticks(1:20:141);yticklabels(-70:20:70);ylim([1 141]);ylabel('Distance
(mm)');
zlabel('ED (W/mm^2)')

goalED = ed4(71,71);
basev = 2500;

correctedv = zeros(141);

for i =-70:1:70 %attenuation included
    for j = -70:1:70
        correctedv(i+71,j+71) = (ed4(i+71,j+71)./goalED)*basev;
        d(i+71,j+71) = sqrt((power(i,2)+power(j,2)));
        l(i+71,j+71) = sqrt((power(d(i+71,j+71),2)+power(h,2)));
        ang(i+71,j+71) = atan(h/d(i+71,j+71));
        ssl4(i+71,j+71) = sqrt((power(ssc,2)+power(ssc*tan((pi()/2)-
ang(i+71,j+71)),2)));
        asl(i+71,j+71) = (pi()*ssc*ssl4(i+71,j+71))*ft(i+71,j+71);
        att(i+71,j+71) = exp(-3.46*0.05*(1*(sin(ang(i+71,j+71)))));
        rfl(i+71,j+71) = (-
0.00004*rad2deg(ang(i+71,j+71))*rad2deg(ang(i+71,j+71)))+(0.0078*rad2d
eg(ang(i+71,j+71)))+(0.622);
        psl(i+71,j+71) =
(4*p.*att(i+71,j+71).*rfl(i+71,j+71))/asl(i+71,j+71);
        ti(i+71,j+71) =
((ssl4(i+71,j+71)+ssc)/2)/correctedv(i+71,j+71);
        correctedED(i+71,j+71) = psl(i+71,j+71)*ti(i+71,j+71);
    end
end

figure;hold on;
mesh(ed4);mesh(correctedED);colorbar;
xticks(1:10:141);xticklabels(-70:10:70);xlim([1 141]);xlabel('Distance
(mm)');
yticks(1:10:141);yticklabels(-70:10:70);ylim([1 141]);ylabel('Distance
(mm)');
```

9.4 Published Work

Several papers were published during the course of this PhD either directly related to the core work on metal additive manufacturing or related to studies as part of the aerialist project.

The most important published paper is the review which makes up the core of chapter 2. A Review of Critical Repeatability and Reproducibility Issues in Powder Bed Fusion: Published in the Journal of Materials & design DOI: 10.1016/j.matdes.2019.108346

A number of papers from the AERIALIST project have significant contributions on repeatability of additive manufacturing in the context of acoustic metamaterials. Primarily: The influence of additive manufacturing processes on the performance of a periodic acoustic metamaterial: Published in the International Journal of Polymer Science. DOI: 10.1155/2019/7029143 and Design of a Kelvin cell acoustic metamaterial: Published in Journal of Sound and Vibration DOI: 10.1016/j.jsv.2019.115167

As a branching topic of research beyond metal additive manufacturing, a study of the material properties of SLA was also published. Investigations of the mechanical properties on different print orientations in SLA 3D printed resin: Proceedings of the Institution of Mechanical Engineers Part C Journal of Mechanical Engineering Science DOI: 10.1177/0954406220904106.This paper shows that the findings of inconsistent properties are systemic across additive manufacturing in general and not merely in SLM

Outside of journal publications components of this body of work was also presented at a number of conferences.

The use of a benchmark periodic metamaterial to inform numerical modelling and additive manufacturing approaches: Presented at the ISMA conference

Repeatability in additive manufacturing for metamaterials: Presented at both the CEAS conference and International Graduate Summer School (IGSS) in Aeronautics and Astronautics held at Beihang University, Bejing.

Repeatability in Additive Manufacturing: Developing tools for process improvement. Presented at the IMC36 conference, where it won the prize of best presentation.

Materials and Design 186 (2020) 108346

Contents lists available at ScienceDirect

Materials and Design

journal homepage: www.elsevier.com/locate/matdes

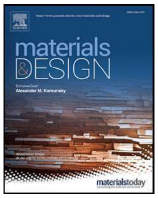

A review of critical repeatability and reproducibility issues in powder bed fusion

L. Dowling, J. Kennedy, S. O'Shaughnessy, D. Trimble [*]

Department of Mechanical & Manufacturing Engineering, Trinity College Dublin, Ireland

HIGHLIGHTS

- An overview on the current state-of-the-art research regarding the repeatability issues in powder bed fusion processes
- In-depth study of potential sources of variation that give rise to the lack of repeatability in metal 3D printing
- Addresses the pre-process, para-process and post-process effects in the process and areas of future research

GRAPHICAL ABSTRACT

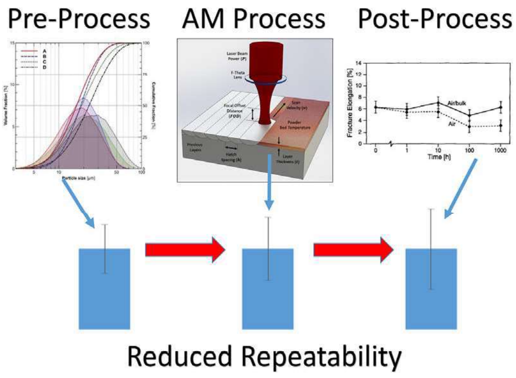

ARTICLE INFO

Article history:
Received 12 September 2019
Received in revised form 6 November 2019
Accepted 8 November 2019
Available online 17 November 2019

Keywords:
Repeatability
Reproducibility
Additive manufacturing
Selective laser melting
Electron beam melting
Process parameters

ABSTRACT

Due to the many advantages associated with metal additive manufacturing (AM) processes, research into these technologies has grown significantly over the last number of years. However, repeatability and reproducibility are critical issues in AM when compared to traditional manufacturing processes. This work reviews the current state of repeatability/reproducibility in metal additive manufacturing, specifically in powder bed fusion technologies such as selective laser melting (SLM) and electron beam melting (EBM). The repeatability issues present in these AM processes is shown to be pervasive across the available literature. The additive manufacturing process is separated into pre-process, para-process and post-process stages and a critical review of the causes and impact of repeatability found at these stages is conducted. Key parameters of these stages: powder properties, laser characteristics and post-processing are studied in depth as sources of variation that can diminish repeatability. An understanding of the limitations of analysing repeatability from the current literature is developed and areas for further research towards the improvement of repeatability are identified.

Contents

---

[*] Corresponding author.
E-mail address: dtrimble@tcd.ie (D. Trimble).

https://doi.org/10.1016/j.matdes.2019.108346

1. Introduction

Research of metal additive manufacturing (AM) processes such as selective laser melting (SLM) and electron beam melting (EBM) has been accelerating over the past few years as seen in Fig. 1. Both are powder bed fusion processes whereby a part is built by selectively melting areas of powder layers using an energy source [1]. The processes can be described as follows; upon irradiation, the powder material is heated and melts to form a liquid pool, known as the melt pool, which solidifies and cools down rapidly. After the cross-section of the part is scanned, the building platform is lowered by a pre-defined distance and a new layer of powder is deposited. This process is repeated until the part is completed [2].

The growth in research focused on metal AM can be partially attributed to the many advantages associated with the process. For example, AM techniques do not have the same extent of design constraints that limit conventional processes [3], thus AM allows a far greater degree of geometrical freedom enabling mass customisation of parts. Furthermore, savings in time, energy and material using AM can reduce the cost per part substantially compared to traditional manufacturing techniques [4,5].

Reviews in the field of additive manufacturing processes and its potential applications in industry have been carried out to discover why this technology has not been widely adopted given its many benefits. Tapia et al. [6] demonstrated a consensus among experts and stakeholders in the aerospace, healthcare, and automotive fields that metallic AM parts are still not sufficient to meet their stringent requirements. The most important requirements are Overall Equipment Effectiveness (OEE), which needs to be greater than 70% with scrap rates of less than 1000 ppm. These requirements are compared to existing world-class automotive production which has an OEE of 85%. However, current AM production is significantly below this target with an OEE measured at approximately 30% [7]. Weller et al. [8] further demonstrated this consensus in a comprehensive economic review on the implications and limitations of AM in industry. The greatest barrier to a manufacturer's investment in AM systems was the limited reproducibility of parts, which is a factor when calculating the OEE.

To date, a significant volume of research has focused on the capabilities of AM, but there is a lack of research focused on its repeatability and reproducibility. These are defined in ASTM E117 as follows; Repeatability is precision under the conditions where independent test results are obtained with the same method on identical test items in the same laboratory by the same operator using the same equipment within short intervals of time. Reproducibility is similar however the test can be carried out in different laboratories, with different operators, and using different equipment [9].

The limited number of studies focused on repeatability in metal AM to date is more concerned with geometric accuracy and defect generation rather than mechanical properties. For example, Franchitti et al. [10] examined the effect of different parameters (orientation, build location, build height) on the dimensional accuracy of Ti6Al4V rectangular parts fabricated using EBM. Dimensional accuracy was determined by measuring the sample thickness. The authors reported that the most significant factors affecting accuracy was the sample orientation and build location. Grasso and Colosimo [11] published a review of the current state-of-the-art in-situ monitoring methods available to reduce process defects in powder bed fusion processes such as EBM and SLM.

The aim of this research is to conduct a critical review of repeatability and reproducibility issues in the powder bed fusion process with respect to mechanical properties. To accomplish this, the manuscript first presents evidence of repeatability/reproducibility by analysing data available in the current literature. The paper then examines some of the causes of the lack of repeatability/reproducibility in the pre-process, para-process and post-processing areas. In particular, powder

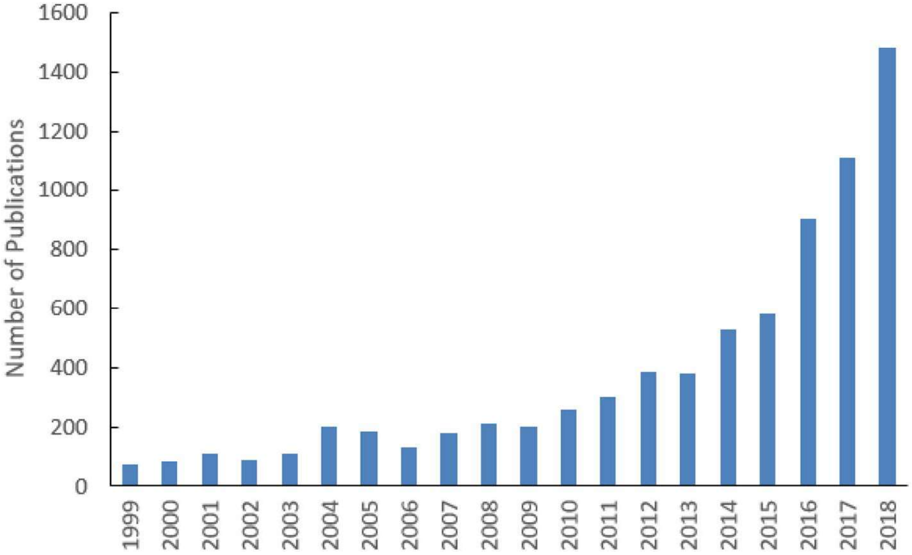

Fig. 1. Number of publications with keywords selective laser melting or electron beam melting. (Scopus, 26 March 2019).

morphology (pre), laser interaction with material (para), and heat treatment, hot isostatic pressing and machining (post). At the end of each section, the paper will address the current state-of-the-art techniques that have been implemented to improve repeatability/reproducibility and the areas of future work for investigation.

2. Evidence of repeatability issues

Despite the lack of literature available specifically focused on repeatability in additive manufacturing, it is possible to draw some information from the published data. Commonly, the results of experimentation are presented including their standard deviations, demonstrating the statistical significance of these results in order to draw strong conclusions. The standard deviation can be taken as an indicator of repeatability in a single data point. Reproducibility information can be taken from comparing studies using identical machines between different research groups or in the form of inter-laboratory tests [12].

The most important mechanical properties considered are the ultimate tensile strength and elongation [13]. The materials with the most focus in powder bed fusion research are cobalt-chrome (CoCr) and titanium alloy (Ti64), the data from some of this research is shown in Fig. 2A & B. There is a large variation of the mean UTS and elongation for each data set. This is expected as each data set represents different operating parameters. However, the error bars represent the standard deviation on each data set which gives a measure of the process repeatability. For example, Takaichi et al. [14] fabricated Co—29Cr samples for mechanical testing using SLM over a range of different energy densities (300 to 800 J/mm^3). The authors recorded standard deviations of up to 75 MPa for UTS and up to 2.9% for elongation which is significantly larger than wrought parts (shown in a different colour). The increase in standard deviations and wide range in values recorded for AM parts demonstrates that a repeatability issue is present.

The literature also can be examined for reproducibility information. The energy density or specific energy input is commonly used as a defining variable in laser-based additive manufacturing [28–30]. Fig. 3 shows the UTS results from different studies carried out at the same energy density in cobalt chrome and shows they have divergent mean values and standard deviations. The two-tailed P value equals 0.0014 for the 100 J/mm^3 case and the two-tailed P-value is less than 0.0001 for the 115 J/mm^3 case. Both are statistically significant differences and show the lack of reproducibility present in the process.

In order to compare the level of repeatability across a number of materials and manufacturing processes, both additive and traditional in nature, this paper uses the coefficient of variation as a comparison metric. The coefficient of variation is the ratio of the standard deviation to the mean for a population or sample [9].

In the case of UTS, AM produced materials have a slightly higher coefficient of variation to the traditionally produced counterparts shown in Fig. 4A. When looking at the elongation case, the variation in the AM materials is up to an order of magnitude larger than that of traditionally manufactured materials as seen in Fig. 4B. This variation transcends the individual material selection or set of process parameters used, demonstrating that repeatability is a systematic issue across powder bed fusion-based additive manufacturing.

3. Pre-process effects

The most important pre-process parameter is the morphology of the powder being used. Powder morphology covers the particle size distribution of the powder and the shape characteristics of the individual particles such as their sphericity and uniformity. The powder morphology is a critical factor in determining the optical penetration depth [40,41], thermal conductivity and packing density of the powder bed.

Optical penetration depth indicates the depth that the energy will penetrate the powder, which is intrinsically linked to the formation of the melt pool [42]. Optical penetration depth is defined as the depth at which the intensity of the radiation inside the material falls to 1/*e* of the original value. A graphical representation of the optical penetration depth in powder is shown in Fig. 5 adapted from Zeng et al. [43]. The graph shows a 1 mm square section of the powder bed. The intensity of the laser is reduced by reflections and absorption of the powder particles. At 0.6 mm from the surface level on the graph, only one of the trace beams continues propagating through the material resulting in a drop below the 1/*e* energy level. A variation in penetration depth can cause a corresponding variation in the melt pool depth. If the melt pool depth becomes greater than the layer height, this can add melting-solidification cycles to underlying formed layers. This variation leads to quality issues such as defects and thus affects the mechanical properties. This was shown in the study by Gong et al. [44] which characterised the melt pool in Ti64 as a means for process parameter selection.

The thermal conductivity of the powder bed determines the size and cross-section of the melt pool generated. The size and shape of the melt pool have been shown to affect the mechanical properties of a completed part due to the formation of pores and rough surfaces. This has been demonstrated by a number of authors in both simulations of the melt pool and experimental measurements [45–47]. Varying powder morphology can affect the conductivity by changing the level of connection between particles and changing the gaps between the particles. The thermal conductivity may also be changed due to the varying composition of the powder, particularly in the case of titanium-based matrix composites [48]. The melting point of the ceramics are significantly higher than those of the metal component of the matrix [49], potentially leading to a variation in melt pool dependant on ceramic concentration both in a build and between builds as the material is processed.

The packing density of the powder bed can directly affect the optical penetration [50] and thermal conductivity [51] as already discussed. Separate from these effects, low packing density can cause voids in the powder bed. This can lead to an unstable melt flow which can cause the formation of defects [47]. The study by Abd-Elghany and Bourell [52] characterised the packing density of 304 L stainless steel powder at various layer thicknesses and the effect this had on the material properties, the results of which are shown in Fig. 6. The conclusion from the study is that a more densely packed powder bed leads to better part ultimate tensile strength.

The packing density of a powder is related to its flowability [53], which is a complex phenomenon. The factors that are important in its characterisation are the shape of the particles and the powder size distribution. As spherical powder flows better than one with an angular shape, this is due to the reduced particle interlocking and the free rotation of the powder [54,55].

The size distribution is an important factor in determining the size of voids. Small satellite particles connected to large particles can impact the packing density by reducing flowability due to increased mechanical interlocking [56]. Fig. 7 has combined data for different powder size distributions in cobalt chrome taken from a series of studies [14,17,18,20,22]. The figure shows a difference in UTS with powder variation but also a larger uncertainty moving from a standard deviation of 24 MPa to 44 MPa to 59 MPa as the powder size increased. The larger particles appear to result in stronger parts however the repeatability of these parts is reduced. This cross publication conclusion reinforces the findings of Simchi [57] who investigated a wide range of iron powder sizes and found that fine powder agglomerates can have increased reflectivity, reducing absorbed energy.

The particle size distribution of the powder used in additive manufacturing follows a statistical distribution both within a single container [58] and across batches of produced powder [59]. This can be seen in Fig. 8, taken from the study of IN738LC powder batches by Engeli et al. [60]. The inherent variability in the powder leads to variations in powder conditions, as multiple batches of powder are used in a single build. This is both an in-build and build-to-build concern for

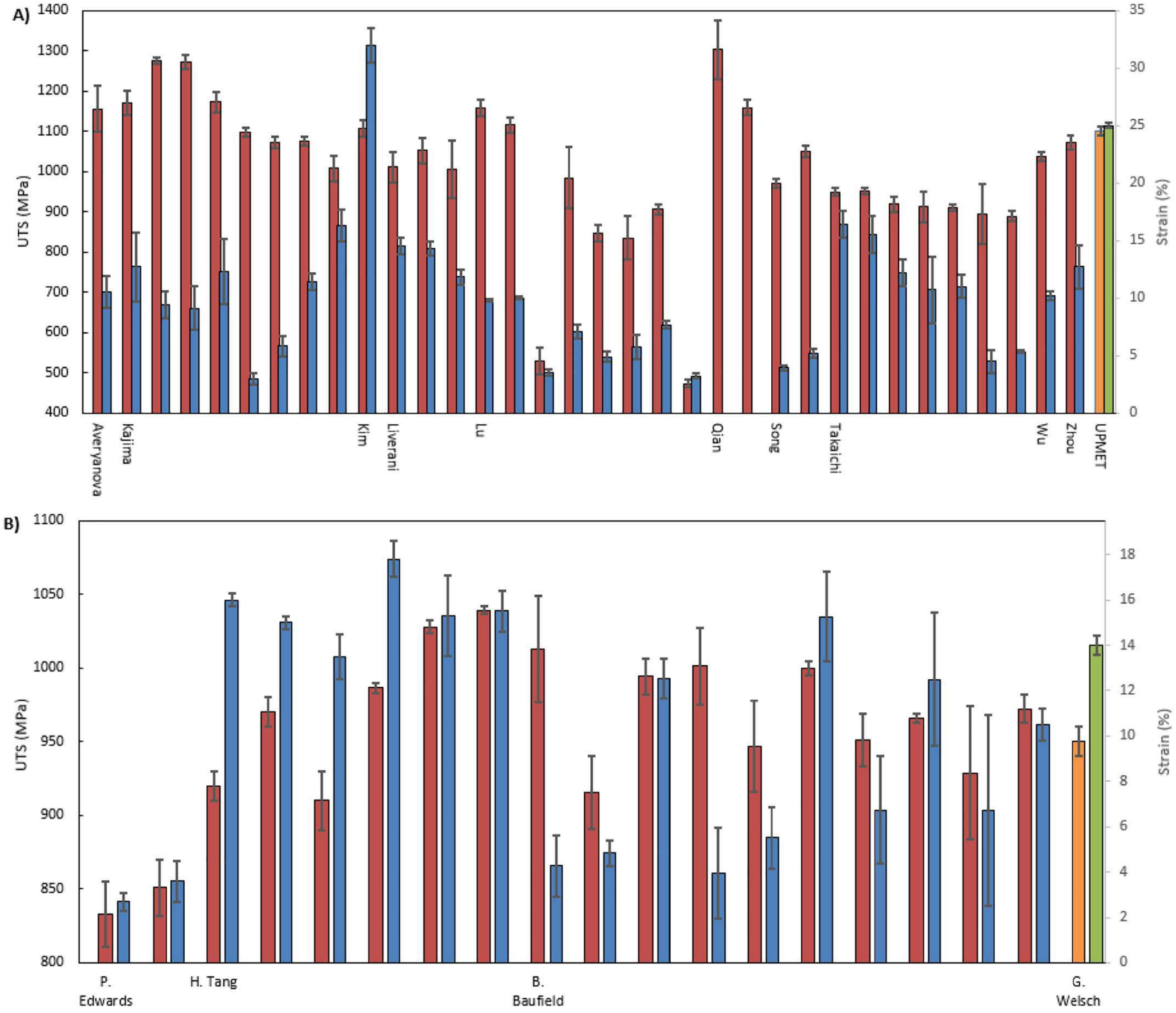

Fig. 2. UTS and Elongation of CoCr (A) [14–23] and Ti64 (B) [24–27].

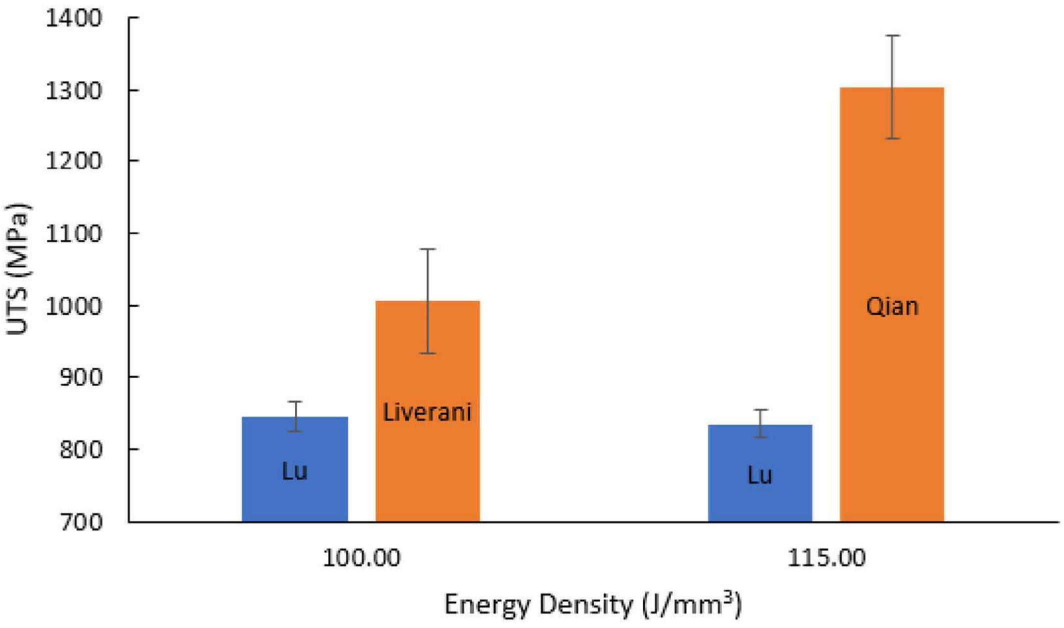

Fig. 3. Reproducibility comparison at two energy densities [17,18,20].

repeatability. The in-build repeatability is of greater concern as the layering mechanism leads to a stratified set of properties [35]. Coupling these stratified properties with a variation in powder properties due to powder feedstock being also stratified gives rise to a potentially greater variation in physical properties. Kulkarni et al. [61] found that "a very small change in the particle size distribution, span, or the wall friction properties can influence the flowability", which has already been noted to impact packing density. The sensitive nature of flowability can impact part properties which contribute to a build-to-build variation.

Slotwinski et al. [62] conducted a study on the powder properties in an individual layer of a build in additive manufacturing, their findings showed that larger particles are preferentially transported across the build plate, leading to a graded distribution of particle sizes across the build plate. It is therefore possible within a layer that this variable powder size could lead to changed properties across a build plate.

Research into the effects of using different powder sources and grades provides empirical evidence of the powder variation affecting the final properties [34]. An example is shown in Fig. 9, adapted from Gu et al. [63]. The study investigated both the shape and size distribution of the Ti6Al4V powder. The process parameters were held consistent across the powders: Trial A processed all the powders following the settings recommended by Raymor, one of the suppliers, whereas Trial B processed all powders using optimal parameters based on modelling of melt pool overlap. The different powders showed significant changes in the standard deviation values of the yield strength and UTS between the different suppliers in both trial cases. This reinforces the repeatability concern as any change in powder supplier can have a dramatic difference in the material properties produced by the process.

A variation of powder morphology can also be created as a function of the process. The nature of the SLM process gives rise to ejected material which can settle on the powder bed ahead of the laser scan. This material ejection is in the form of small particle size material, which is seen as sparks or splatter [46]. The addition of small particles to the powder bed from this splatter can skew the particle size distribution from normal and can give an uneven surface between layers leading to porosity development [47].

The powder is commonly recycled from build to build as the majority of powder forming the bed is not fused. Even under maximum build plate usage conditions, less than 20% of the volume is melted [64]. The process requires material to be supplied to create the powder bed beyond what is melted to form the parts. The unused powder is recycled and reintroduced into the process. However, its properties may have deviated from the virgin material due to this recycling [59]; most commonly in size distribution but also in becoming less spherical [25,62,65]. A clear example of this is shown in the study by Tang et al. [25], in which a series of tests on reused Ti64 powder processed by EBM were conducted, the results can be seen in Fig. 10. The measured

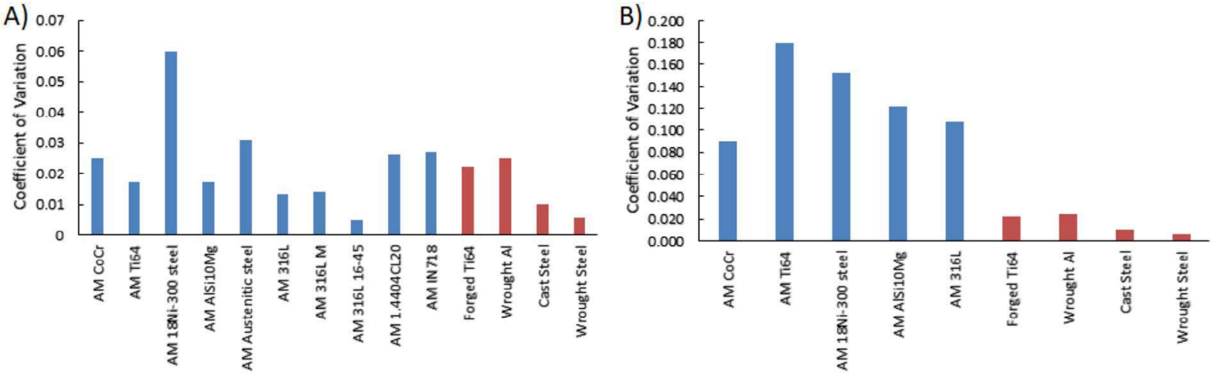

Fig. 4. Coefficient of Variation of UTS (A) and Elongation (B) for AM materials [2–14,16–21] and traditionally produced materials [37–39].

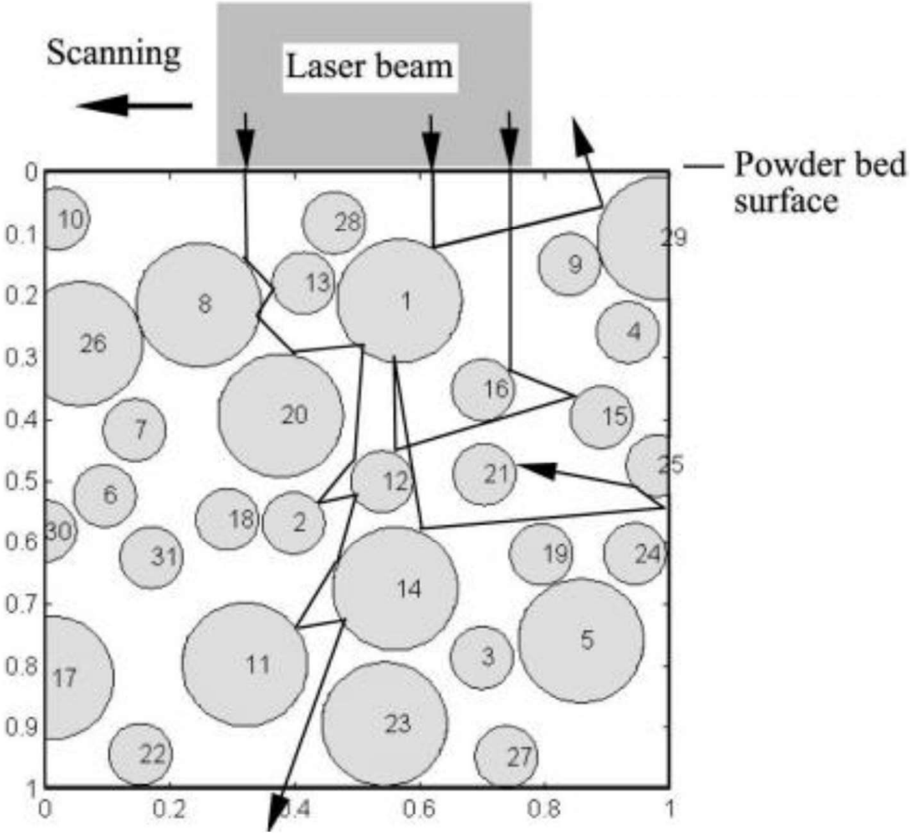

Fig. 5. Optical penetration depth.
Adapted from Zeng et al. [43].

changes could be deemed beneficial to a produced set of parts and beneficial to the process in general due to improved mechanical properties and reduced variation. The authors of the study concluded, "Reused powder showed no measurable undesired influence". However, any influence whether desirable or not changes repeatability, specifically in a build-to-build case. The parts produced by the same machine using the same parameters have a significant variation in mechanical properties which correlates to the number of times the powder has been recycled.

The pre-process powder properties can be affected by a number of factors including supplier, the specific batch from a supplier and

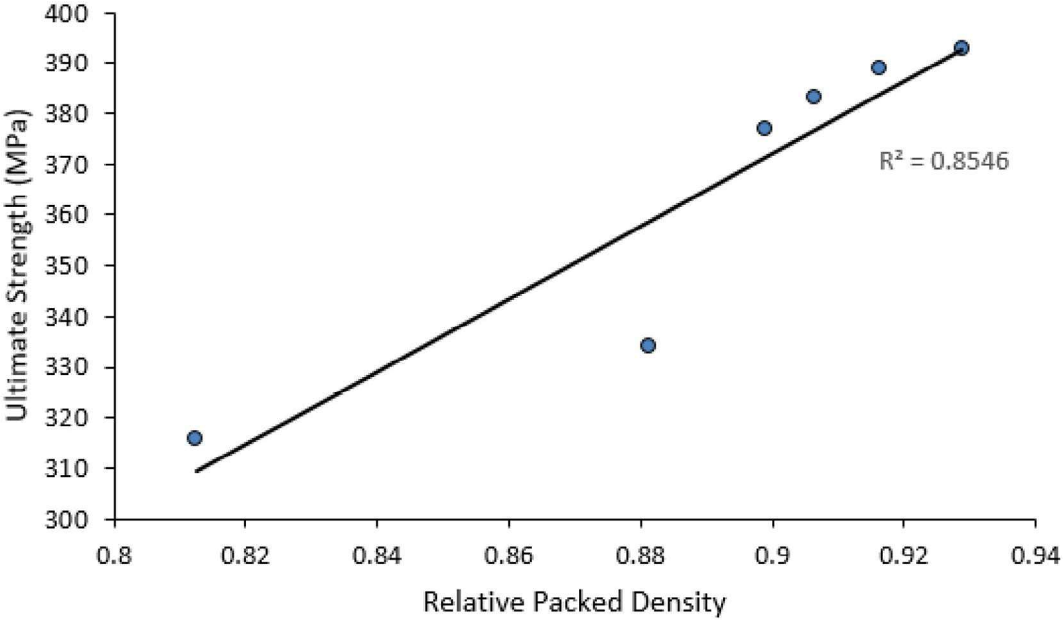

Fig. 6. Packed Density against Ultimate Strength.
Adapted from [52].

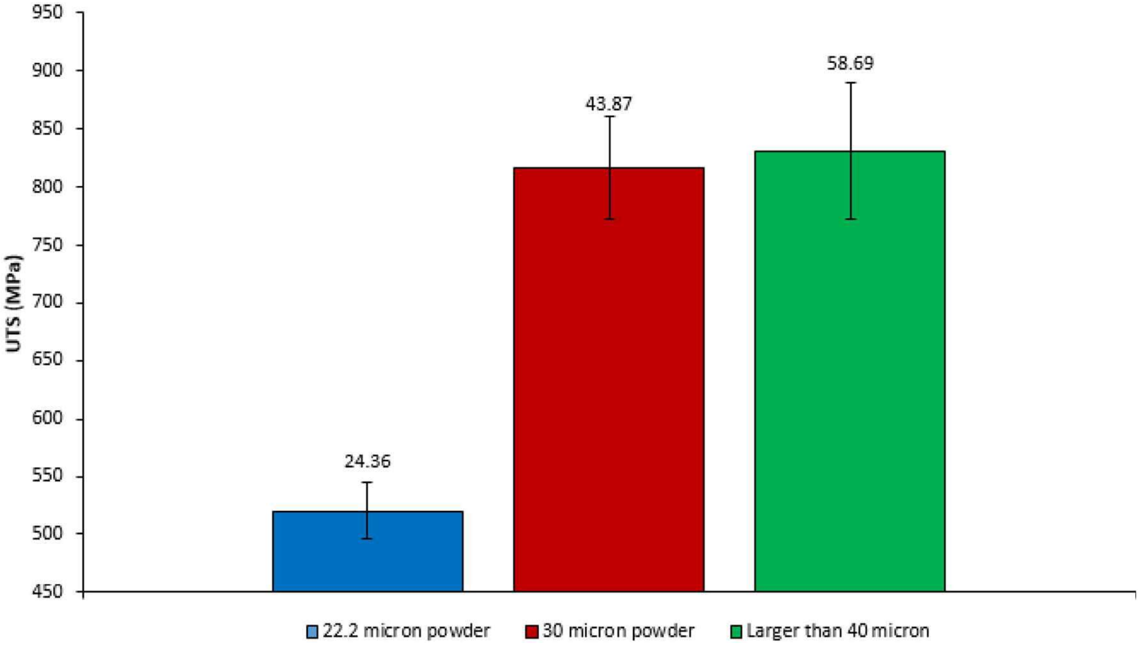

Fig. 7. Powder size and UTS data taken from studies [14,17,18,20,22].

the re-usage cycle of the powder. The powder properties have been shown to directly impact the mechanical properties of produced parts and also indirectly impact the part quality due to defect generation.

Methods to improve the repeatability due to the powder effects include controlling the feedstock leading to reproducibility issues, and monitoring the produced powder bed for inhomogeneity that could lead to repeatability concerns. For example, accurately characterising the powder in order to use the correct processing parameters for the specific feedstock rather than for a generic feedstock. Decost et al. [66] developed a system to classify both representative and atypical powders. This was achieved by using computer vision and machine learning. A significant advantage of their approach is that it is autonomous, objective and repeatable. The ability to classify the full powder morphology being used could significantly improve reproducibility as the variation in feedstock would be reduced. Alternative means to control the powder morphology such as ball milling prior to production has also been investigated by Attar et al. [67] that indicate possible improvements to the repeatability of the process.

4. Para-process effects

The most important factor considered in the entire process is the laser interaction with the powder bed. The interaction of the laser and the powder is a complex phenomenon due to multiple phase changes and variable absorbance based on the temperature of the material. These interactions happen on rapid timescales due to the focused nature of a laser spot on microscopic spatial scales. Operating on these small scales means even minor perturbations can have a significant effect.

The energy density or specific energy input is used as a primary comparison variable in laser-based additive manufacturing [28–30] to

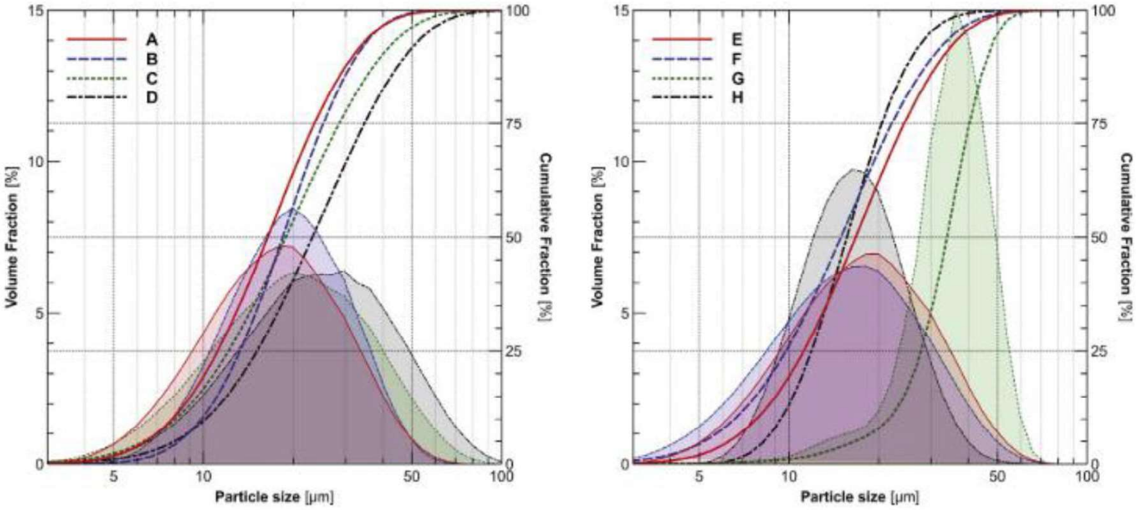

Fig. 8. Powder size distribution of multiple batches of powder.
Taken from [60].

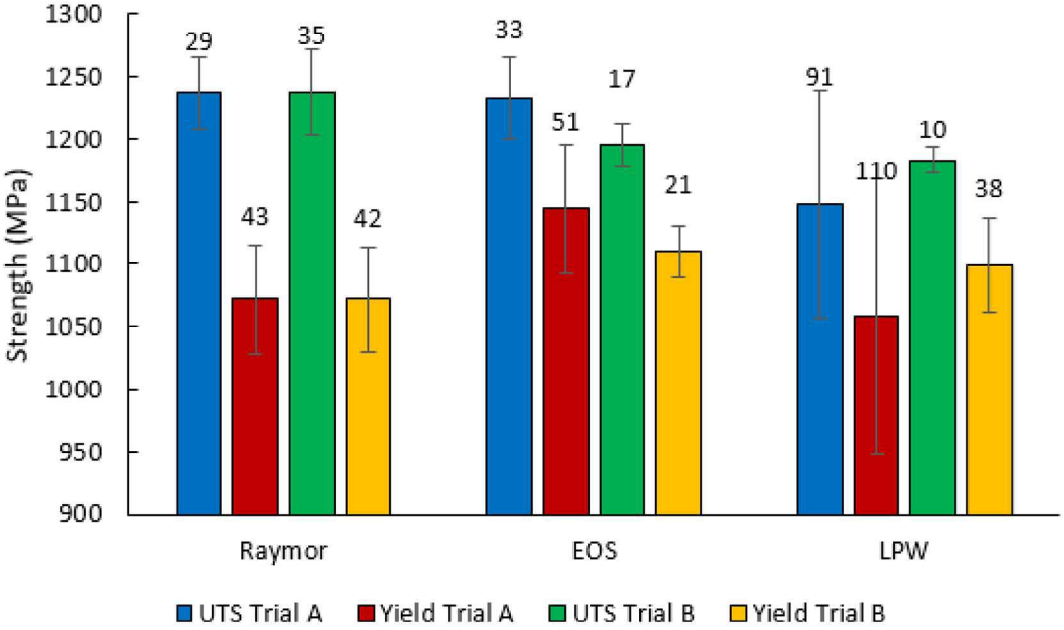

Fig. 9. Ti64 powder variation effect on properties.
Adapted from [63].

encapsulate all the laser characteristics in a single variable. The energy density is used to generate relationships with relative density [16,68,69] which is further connected to strength and elongation [70]. Energy Density is commonly formulated as

$$\psi = \frac{P}{v * h * d} \tag{1}$$

where ψ is the energy density (J/mm^3), P is laser Power (W), v is the scan speed (mm/s), h is the scan spacing (mm) and d is the depth of powder (mm) [71]. An alternative means of calculating energy density has also been used in some studies to explicitly include the time interaction of the laser.

$$\psi = P_d * t_i \tag{2}$$

$$P_d = \frac{4P}{\pi D_b^2} \tag{3}$$

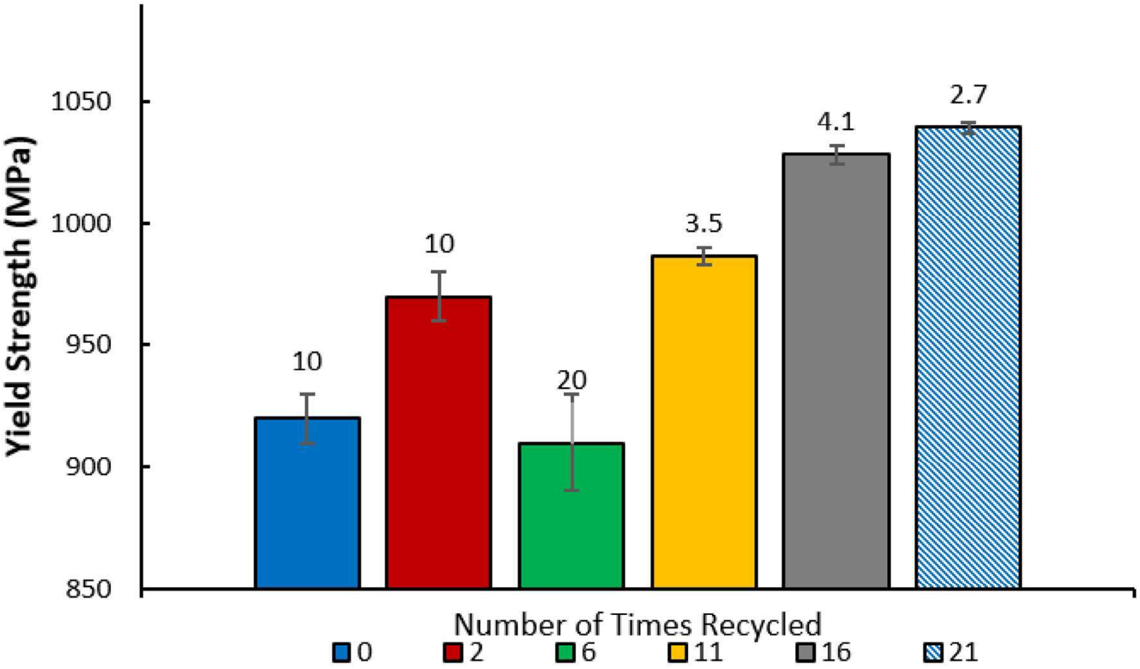

Fig. 10. Ultimate Tensile Strength against the level of recycling.
(Adapted from [25]).

$$t_i = \frac{D_b}{v} \quad (4)$$

The additional terms are the power density P_d, the beam diameter D_b, and the interaction time t_i [72]. The scan spacing and beam diameter are related variables. In order to accurately control the level of remelting the scan spacing and thus beam diameter must be considered to define the overlap of the scan passes. Re-melting can have a significant effect on the final microstructure [73] and thus mechanical properties in both a positive and negative way. For example, studies by Van Den Avyle et al. [74] and Yahata et al. [75] demonstrated that remelting was found to reduce defects in Inconel and deoxidify titanium respectively, thus improving their properties. However, if excess remelting occurs then the microstructure can become undesirable as shown by Charles [76] wherein a banded microstructure was discovered to form in Ti64 due to the reheating cycle, not the original quench. This banded microstructure has been shown by Wang et al. [77] to introduce anisotropy to the mechanical properties and affect the mechanical properties relative to samples without this banded microstructure. Any variation in these laser characteristics would modify the energy density and thus impact the parts directly making it a critical factor for repeatability.

The beams used in modern lasers use diffraction-limited optics to provide a tight focus [78]. The laser source, however, is not perfect, with inherent power fluctuations particularly at higher power levels used in the manufacturing process [79], as shown in Fig. 11. The fluctuation of power can lead to repeatability issues as inconsistent melt pool effects such as excess vaporisation could occur from the transient higher energy levels.

There has been a discussion among authors on the effect the "Balling" phenomenon which has been shown to occur over a range of energy densities [80–82] and gives rise to bad layer deposition, cracking or even process failure [2]. Balling defects has been shown to reduce the overall relative density of the produced part [83]. The balling features also affect the viscosity of the melt pool, potentially changing its size, shape and stability [47,84,85]. This effect can be a contributing factor to a lack of repeatability while not being its underlying cause.

The fluctuations of energy reaching the build plate are further increased by transmission variations due to plume development and accumulation of process by-products in the process chamber [86]. The fluctuations can impact part quality, raising a repeatability concern as the energy density may not remain constant during the entire process. This can be seen clearly in Fig. 12 adapted from Kusuma et al. [87] which shows the percentage standard deviations of measured track widths at different laser powers. Both the standard deviation of the track width measurements and the spread of the data are observed to increase with laser power.

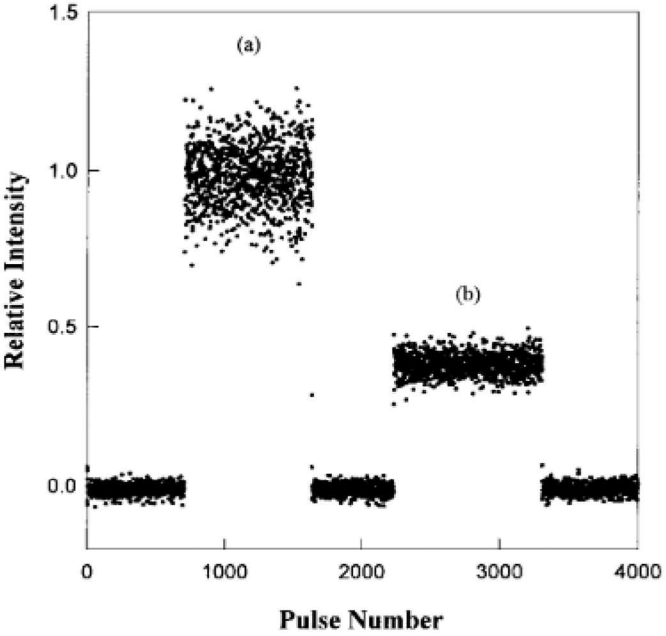

Fig. 11. Relative intensity of laser pulses [79].

The spot size of a laser can be calculated in a number of different ways including full-width half-maximum (FWHM), D4σ method and $1/e^2$ method. The derivation of these methods is based on the intensity profile of the beam and is inherently independent of power variation. These calculations for spot size do not intrinsically have a power relationship, however, we are not interested in the scientific spot size of the beam. In additive manufacture, the effective spot size is a more useful measurement. When the effective spot size is defined as the minimum irradiance required to melt the powder, if the power is increased with all other parameters kept constant, an identical Gaussian profile upshifted on the irradiance axis is generated as seen in Fig. 13. This leads to a greater section of the beam contributing to the melting process, increasing the effective spot size [88]. The effect of laser spot size on the resultant microstructure of an additively manufactured part was studied by McLouth et al. [89], whose study was carried out on Inconel 718 parts produced by SLM. The spot size of the laser was modified by changing the manufacturing focal offset without modifying any other processing parameters. They concluded that an offset focus or larger spot size gave rise to "coarser microstructure and stronger crystallographic and morphological textures in both the as-built and fully heat-treated conditions". These microstructure changes would introduce changes in the mechanical properties and could potentially add a repeatability concern due to the stochastic nature of power fluctuations in the laser system.

It is possible the beam may become out of focus at certain points in the build due to immovable or transient optical effects. An out of focus beam gives a greater beam diameter and the cross-sectional shape of the beam may become more elliptical as it moves out of focus [90]. The beam diameter can also be increased when the beam becomes elliptical in shape as its angle of incidence on the plate is changed [91]. It has been shown that the shape of the beam, specifically studied by Roehling et al. [92], can have a direct impact on the mechanical properties of a produced part. The experimental results found by Roehling et al. were supported by a series of ALE3D simulations of the process. The results show clear evidence of a scan directional dependence created by an elliptical spot not present in a circular spot. This dependence leads to narrower melt tracks and higher peak temperatures in the melt pool as seen in Fig. 14. These narrower tracks could change the conditions present in adjacent scans and the higher temperatures can introduce melt pool variability and excess particle ejection or vaporisation, the effects of which are described in the work by Qiu et al. [47], wherein the role of melt flow is extensively addressed in both modelling and experimentally with respect to Ti64. They found that unstable melt flow gives rise to porosity defects and increased surface roughness.

The effect of the change in melt pool formation is shown clearly in Fig. 15. The longitudinal elliptical beams lead to greater ejected material and the development of internal porosity. The scan vector used in additive manufacturing is commonly rotated between layers [93,94]. This leads to a variation between longitudinal and transverse elliptical passes through a part, which can lead to variable porosity and mechanical properties in each layer.

As the size and shape of the laser spot is location dependant, the physical and geometric properties of the part are also location dependent. This dependency gives rise to a significant repeatability challenge.

The laser parameters used for producing parts are usually found empirically and thus can be unreliable when applied in locations and systems other than there formulation system. The empirical values are found for a specific system and cannot be taken to be ideal for all possible systems used in additive manufacturing. The level of power required

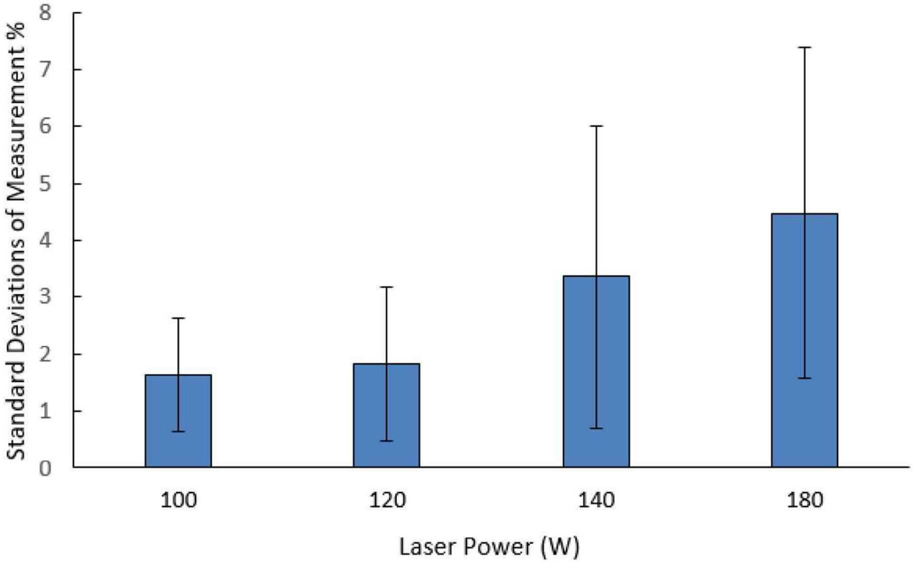

Fig. 12. Percentage standard deviations of track widths at different powers.
Adapted from Kusmana et al. [87].

for the process is commonly considered in ranges. The process is an optimisation problem with a vast number of potential control points. The optimisation is also based on a specifically targeted characteristic. For example, designing for particular microstructure or density can require very different parameters sets for the same material [16,95]. This has been shown clearly in the study by Gu et al. [85], where the influence of energy density on porosity and microstructure was evaluated in 17-4PH stainless steel. They showed that different parameter sets such as changes in scan speed gave rise to varying physical properties but the properties do not reach maximums at the same location, as seen in Fig. 16. The selection of process parameters in order to get a desired property can be a repeatability issue without the understanding of interconnectedness present in the properties. For example, one cannot assume that a part would exhibit the same microstructure when the parameters are modified to produce a denser part. It is also noticeable that the standard deviations present at each setting vary across the parameter sets. Selecting the process parameters with the best resulting part properties can give rise to repeatability issues as the spread in the part properties is not constant while changing process parameters.

The effect that scanning strategy has on the resulting part has also been studied by Demir and Previtali [96]. The study showed the impact on the part quality. Variations in scan strategy were shown to impact the magnitude of the residual stresses, surface roughness and geometric accuracy of the produced parts. It was noted in the study that the remelting scan strategies also increased the dimensional errors of the parts produced [96]. The scan strategy can also affect the repeatability, as shown in Fig. 17. The strategies investigated were based on secondary passes over the workpiece. The second pass options were as follows: no second pass, full-strength second pass, reduced strength second pass, focally offset pass. It is noticeable that not only is the density changing

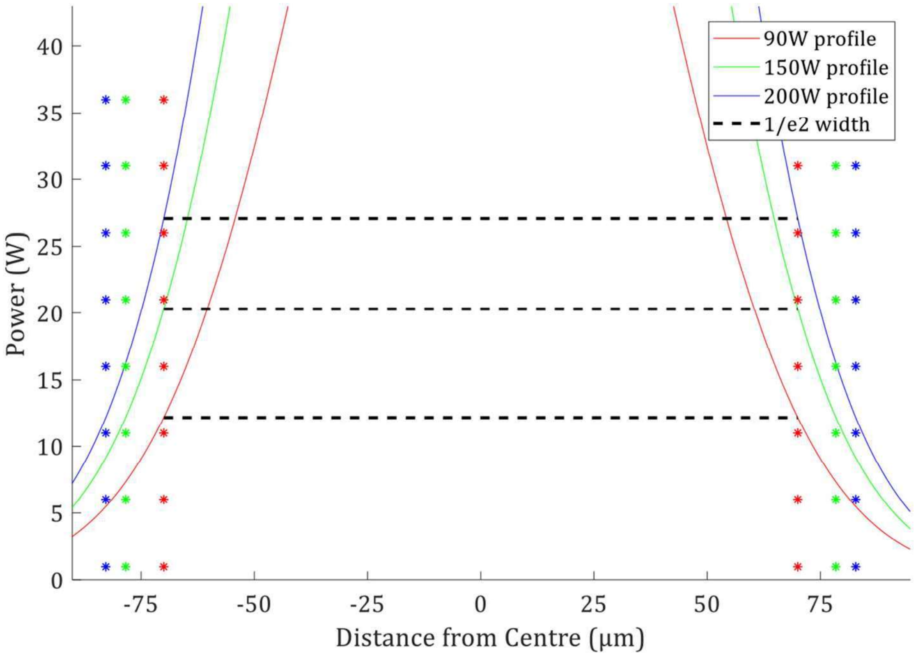

Fig. 13. Laser spot size with respect to power.

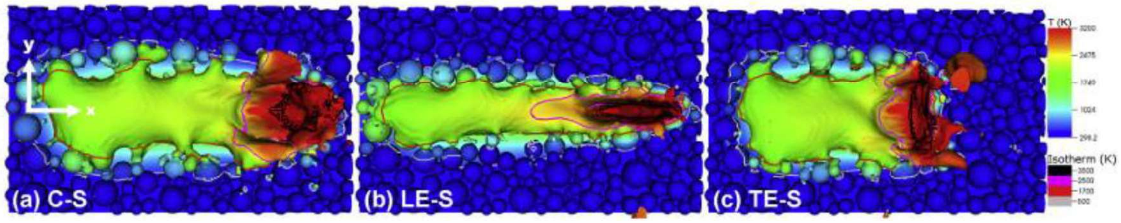

Fig. 14. Beam shape effect on the melt pool [92].

as the scan pattern changes but also the magnitude of the errors changes, with the final polishing strategy having the spread of results halved compared to the no second pass condition [96]. The effect of correcting the scan strategy for a single variable can cause unintended quality reductions elsewhere, this is one of the cruxes of the additive manufacturing repeatability issue in that the optimum settings for one property are not optimum for all properties.

The effect of scan strategy was further investigated by Ali et al. [93], who found that the standard scan strategy used in the production of Ti6Al4V parts produced the lowest residual stresses as shown in Fig. 18. The spread of the residual stresses, however, was greater for the standard strategy than the 2 × 2 case. In selecting the lowest stress for the standard, a less repeatable strategy was selected.

The common theme across the laser characteristics used in additive manufacturing is selecting parameters that give the best physical properties [2,97] but not necessarily the optimum parameters for repeatability. The systemic selection for material properties over repeatability could be a major contributing factor in the lack of repeatability in additive manufacturing in general. The lack of explicit information about how certain physical properties were optimised for and how the

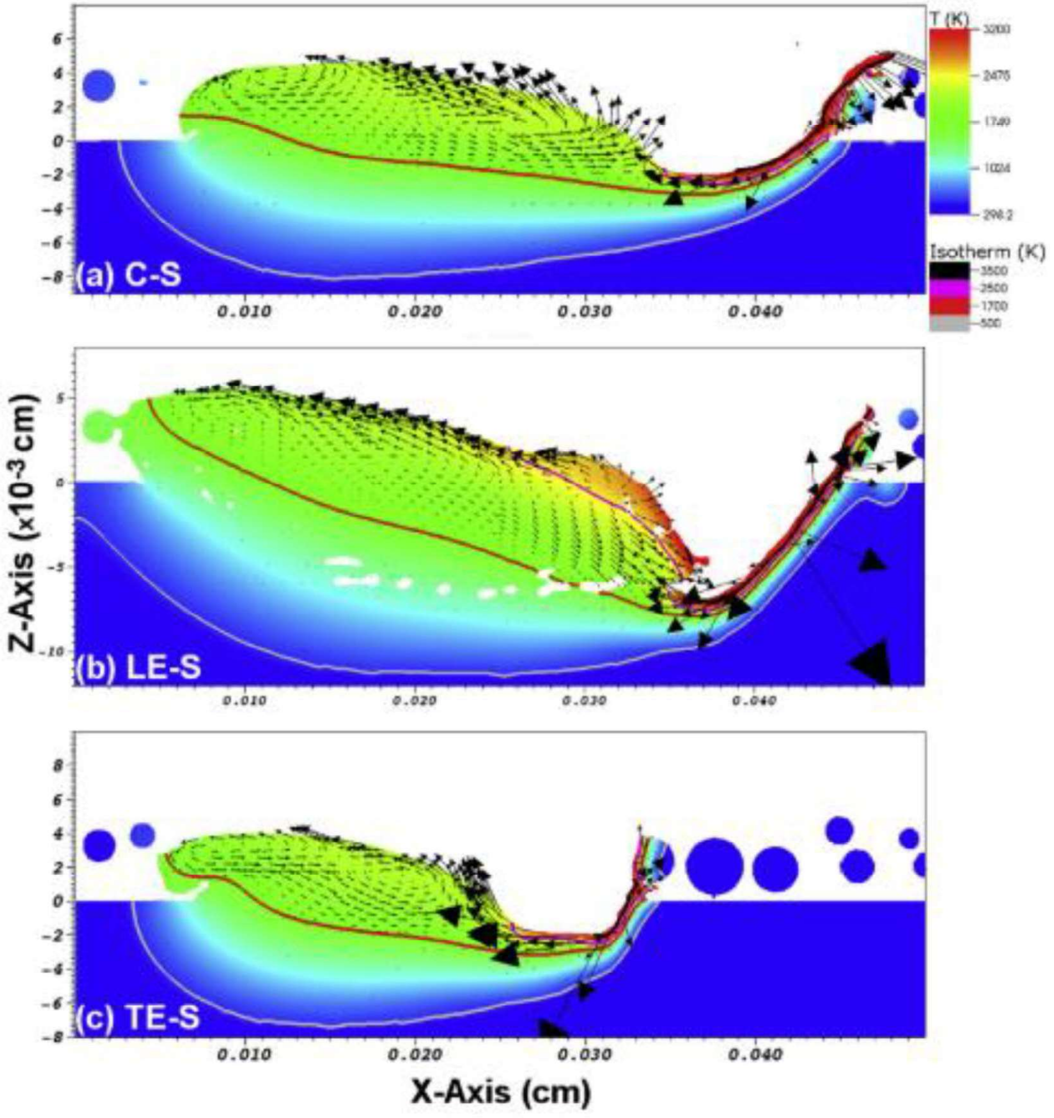

Fig. 15. Melt track formation [92].

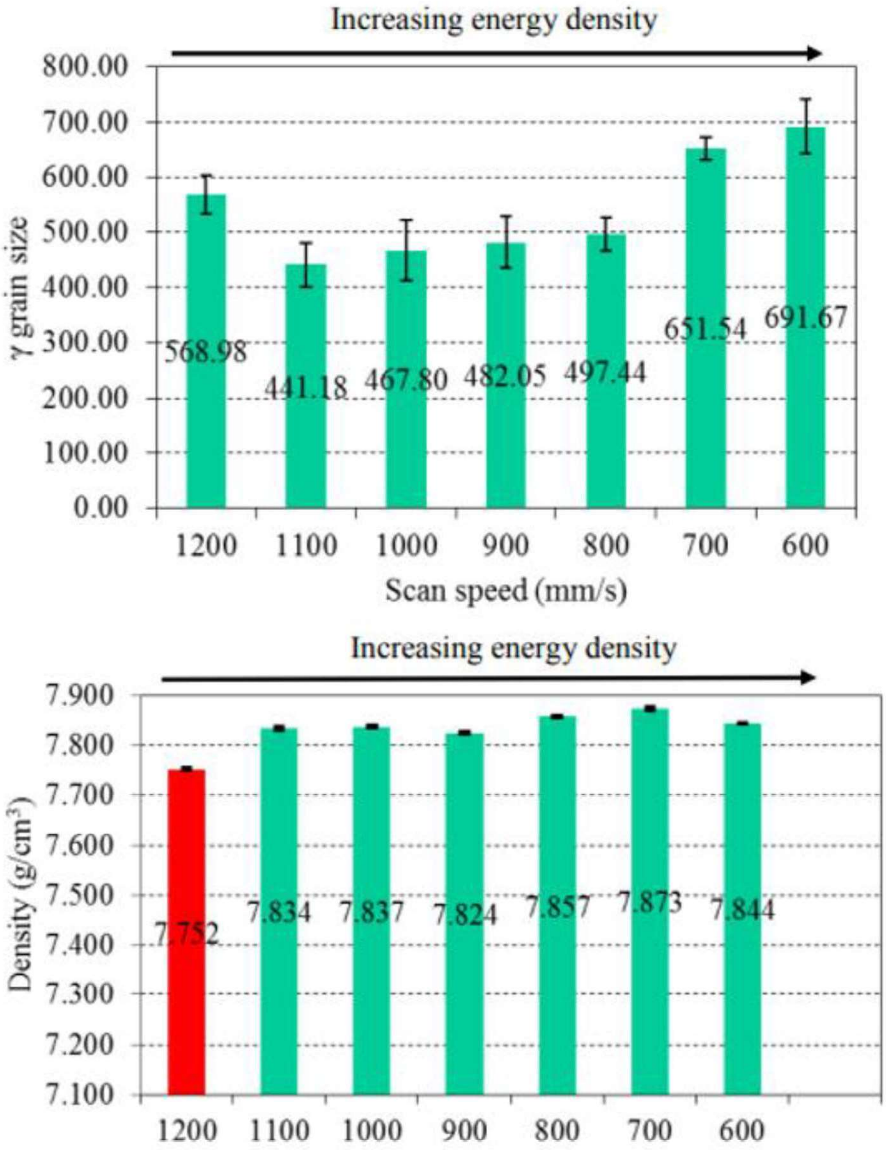

Fig. 16. Density and grain size against scan speed.
Adapted from [85].

process parameters were selected by these optimisations give rise to a number of claimed optimum process parameters for the same physical property. This lack of information can lead to the selection of suboptimal parameter sets when repeatability is the desired property.

5. Post-processing effects

Confusion is created around the properties of additive manufactured parts as the level of post-processing can give rise to different properties. The post-processing of additively manufactured parts could hide issues inherent in the process. The most common post-processing carried out is machining to give a better surface finish and to remove supports, stress relief or annealing.

The surface of an additively manufactured part is frequently rough. The surface roughness values for as-built additively manufactured parts [98] is an order of magnitude greater than those made of cast [99] or wrought [100] similar materials. This roughness is due to the layered nature of the parts' construction creating a stair-stepping effect which is heavily dependent on part orientation [101]. The use of supports on overhanging surfaces also gives rise to localised roughness peaks [102]. Additively manufactured parts are commonly machined to improve surface roughness in order to increase fatigue life [103].

The process of powder bed fusion gives rise to residual stresses in the part. The stress is created by the large thermal gradients created in the laser scan, as the laser passes over an area the powder rapidly heats to melting and then back to solidification [104].

Stress relief reduces the residual stresses left in the part from manufacturing and can have a significant impact on the mechanical properties, surface quality and microstructure of a produced part. This can also lead to a change in the repeatability of the measurements. This can be observed in tighter standard deviations from more consistent part post-processing or a greater spread due to additional processes with their own inherent errors creating a larger deviation. Fig. 19 shows the effect of post-processing and build orientation of titanium parts produced using SLM from a study conducted by Wauthle et al. [105]. It can be seen that the post-processing improved the consistency of the maximum strength values but increased the spread in the elongation comparisons. The trend in standard deviation is clear with a reduced deviation found in the UTS case as the level of post-processing increased with heat treating and then further HIP treatment. However, this trend

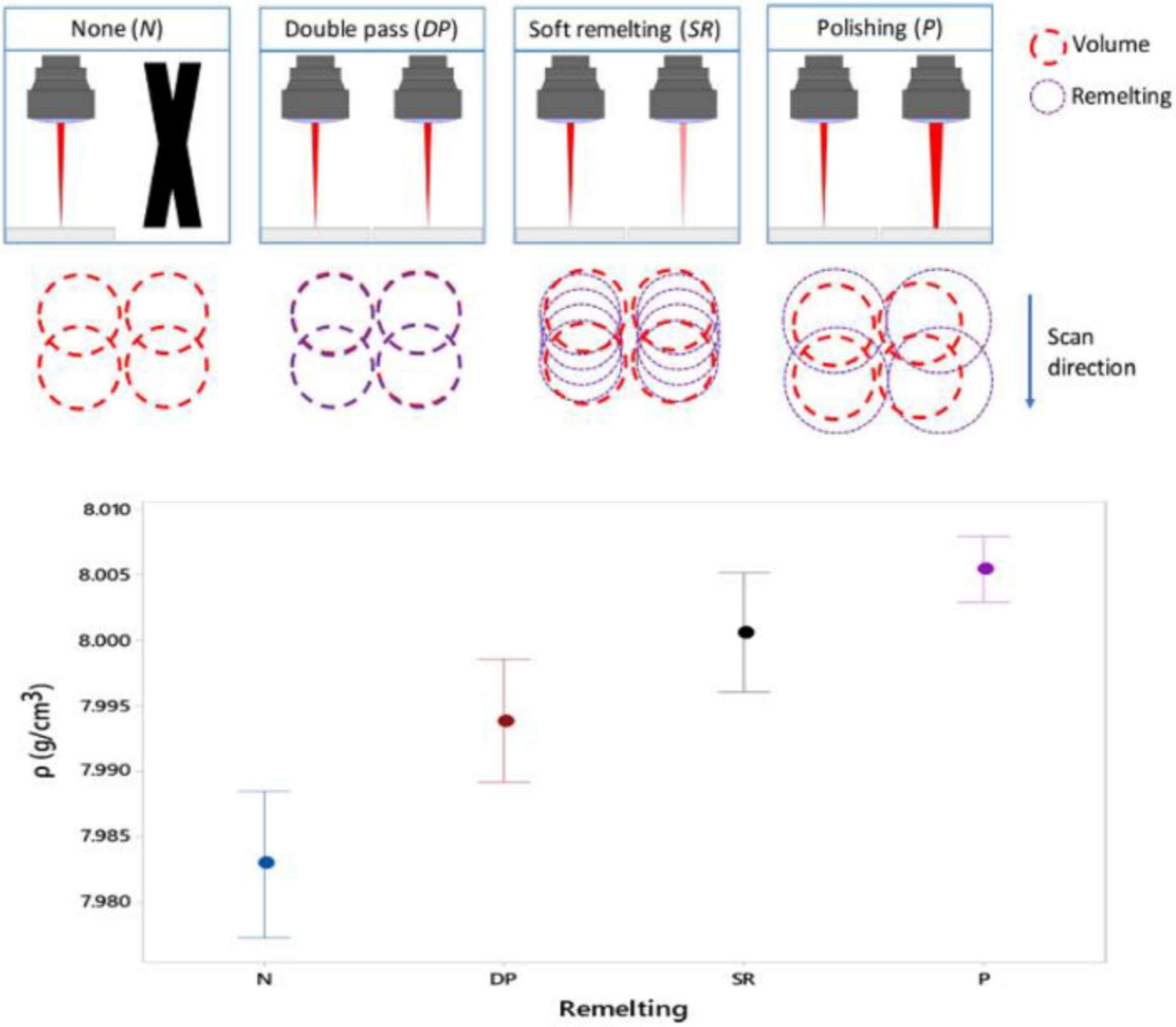

Fig. 17. Effect of scan strategy on density.
Adapted from [96].

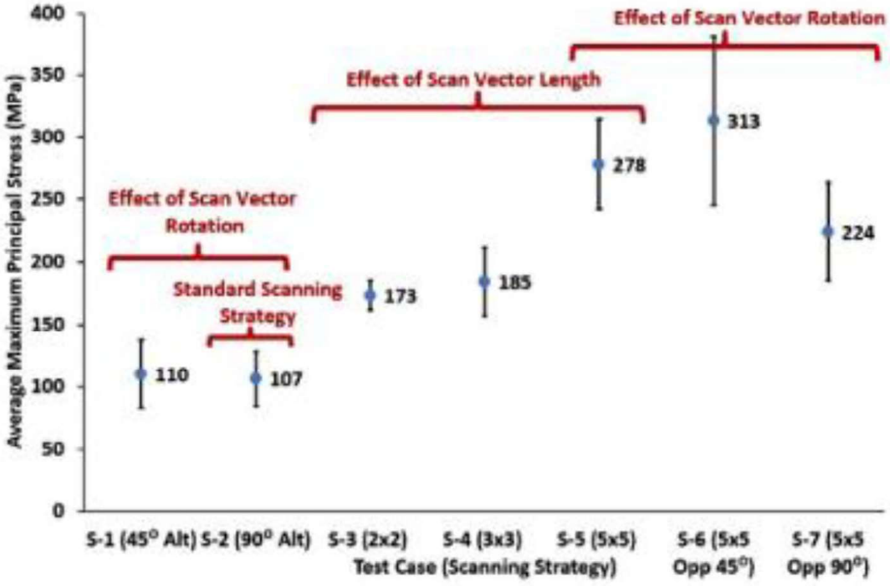

Fig. 18. Principal stresses for different scan strategies [93].

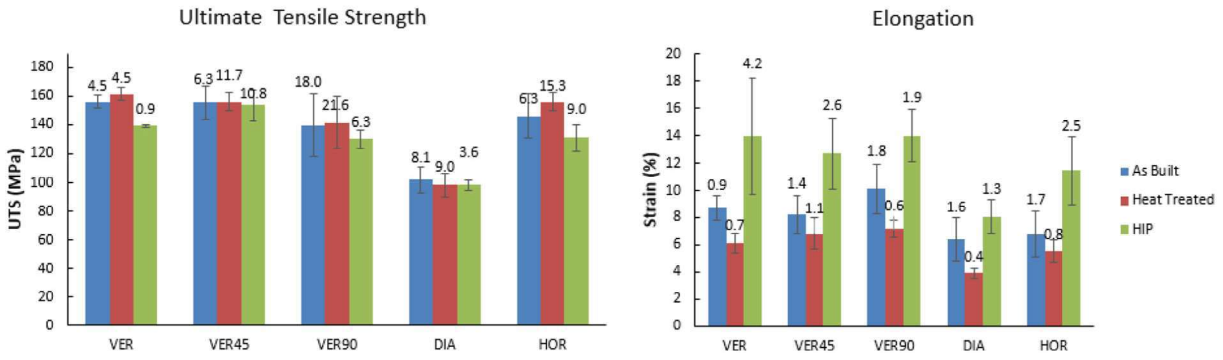

Fig. 19. Effect of post-process and orientation on UTS and elongation of Ti64 SLM parts. Adapted from Wauthle et al. [105].

is not consistent as can be seen when the elongation is considered as the heat-treated parts have a tighter distribution but the HIP samples have a wider spread compared to even the as-built samples. The post-processing gave rise to improved mechanical properties but at the cost of a more variation between samples in some cases.

An example of how post-processing can affect the variability in mechanical properties can be seen in Fig. 20 which shows the UTS and elongation for SLM Ti64 parts which have undergone different heat treatment cycles. Data is adapted from the study by Vrancken et al. [106]. It can be seen that after heat treating, in general, the elongation improves and the UTS decreases as expected. The more important factor from a repeatability point of view is the spread of results. In all UTS cases, the standard deviation of the results is larger when samples underwent heat treatment compared to as-built samples. A similar trend can be seen for elongation in most cases. The act of post-processing the parts, while improving the physical properties for certain applications, has a detrimental impact upon repeatability.

In general, the post-processing of a part will change its properties significantly. The selection of the correct post-processing to apply to as-built microstructure is not a simple task in additive manufacturing, as starting microstructure can vary significantly in the as-built part based on process parameters [107]. When homogenous and consistent wrought material undergoes post-processing, the standard deviations of its mechanical properties remain consistent across the treatment. This can be seen in studies of varying heat treatments of wrought material such as those carried out by Leyens et al. [108] shown in Fig. 21 It can be seen that all the treatments while giving different property values had similar relative errors.

Vrancken et al. [106] summarise one of the issues found in post-processing AM parts as: "Application of standard heat treatments shows that these treatments do not lead to the usual or expected results, SLM produced parts need to be treated differently to bulk alloys". Specific desired properties need varying and targeted treatments, the incorrect application of post-processing leads to the creation of undesired microstructures. The unexpected and unusual results give rise to inconsistency which hampers repeatability. The improper application of bulk-determined heat treating can lead to an increased spread of results. This is further expanded due to the different effects the post-processing has on a given microstructure which may be batch-specific, leading to a build-to-build variation.

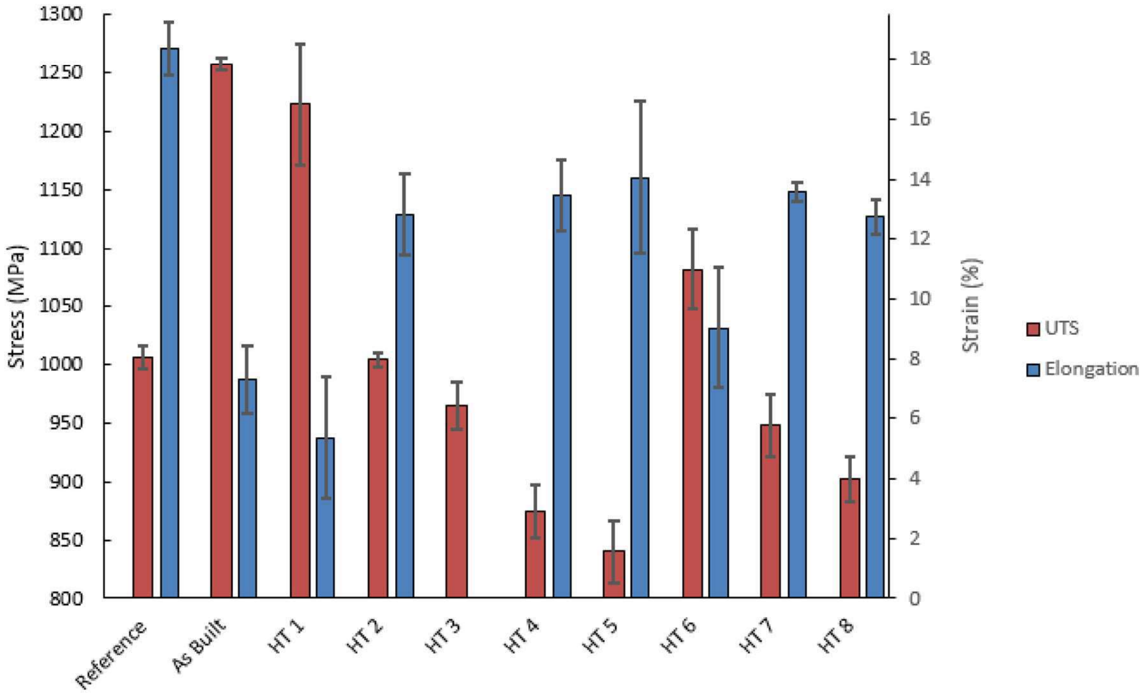

Fig. 20. Effect of different heat treatments of SLM Ti64 parts. Adapted from Vrancken et al. [106].

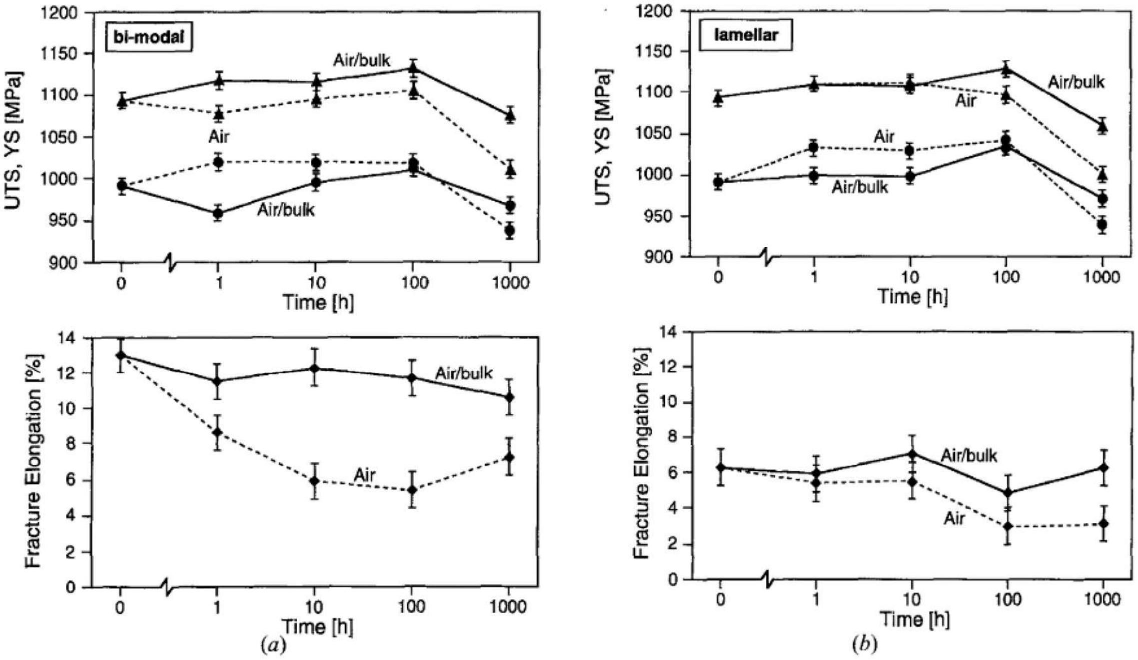

Fig. 21. The effect on mechanical properties of Ti64 under different annealing times and different solution heat treatment temperatures of (a) 990 °C and (b) 1060 °C. Adapted from [108].

6. Future research and outlook

The outlook for the powder bed fusion method of additive manufacturing is of increased repeatability capabilities in the near future. The current technological usage for the generating once-off prototypes has been moved to a more mass production setting of tailored individual parts and complex geometries driving the needs for repeatable and reproducible parts. The need for concerted focus in the field towards improvements in the repeatability of the process has become more apparent. The areas of future work including addressing the pre-process, para-process and post-process sources of error outlined in this work and mitigating their effect on the final produced parts.

Examining the produced powder bed for variations is a means by which repeatability could be improved. Methods of this in-situ analysis have been developed and proposed by Foster et al. [109] and Zhang et al. [110]. Both studies suggest the use of camera systems to image the powder bed before and after scanning a layer. This will allow the potential development of closed-loop process control. The ability to recognise variations in the powder bed enables remedial action to be taken, such as recoating or dynamically modifying the processing parameters to fit the powder bed generated, and not an idealised general powder bed. This could improve the repeatability of parts in a single build by accounting for any powder variations. Some research has focused on investigating the in-situ monitoring of the powder bed fusion process. For example, the National Institute of Standards and Technology (NIST) is developing a focused testbed for enhanced process control [111]. This testbed will allow in-situ continuous feedback control to be developed to improve repeatability. The research by Aminzadeh [112] demonstrated the ability to detect defects as they are forming using a visual camera for quality inspection focusing on porosity occurrence. Work by Demir et al. [113] monitored the process using co-axial measurements with the processing laser. The monitoring consisted of using a visible light camera to monitor the stability of the melt pool and near-infrared camera to monitor thermal effects. The ability to detect defects forming during the process would allow the targeted use of corrective scan strategies such as the polishing-type remelting pass used by Demir et al. [96] to reduce or remove these defects improving part quality and importantly improve the repeatability.

The means to improve the repeatability and reproducibility at the post-processing level are multifaceted, focussing on two key steps, the elimination of the need of the post-processing and improvements of the consistency of the parts before post-processing. The latter will be accomplished by improvements found in pre- and para-process techniques. The former could be found by improving the surface roughness using techniques such as optimised support to reduce the support requirements with associated roughness [114,115] and reducing the layer thicknesses to reduce the staircase effect found due to the layering system.

7. Conclusion

There exists scant research focused on repeatability or reproducibility in metal AM, despite the growing field. Repeatability/reproducibility in additive manufacturing is an area of underdeveloped research. There is a body of evidence, that repeatability/reproducibility issues are pervasive across techniques, materials and machine systems. The complexity of the process leads to critical information such as powder morphology, laser characteristics and scan pattern being omitted or insufficiently addressed. This is further compounded by other information like the build orientation, thermal history, post-processing and test specimen nature being excluded from some publications. The level of complexity and interconnectedness between parameters leads to difficulty in improving the repeatability/reproducibility of AM processes.

The powder morphology has been shown to be a critical factor in the mechanical properties of parts produced by additive manufacturing. The powder properties directly affect the melt pool characteristics by modifying the packing density of the powder bed, its thermal conductivity and response to the laser input. The use of recycled feedstock gives rise to a significant variation of powder properties which in turn can modify the level of repeatability. Studies have shown an improvement in repeatability as the number of recycles increases. The ability to classify the full powder morphology being used could significantly improve repeatability/reproducibility as the variation in feedstock would be reduced. The development of closed loop process control to recognise the powder variations present could enable remedial action. For example, recoating or dynamically modifying the processing parameters to fit the powder bed generated instead of an idealised general bed.

The laser-powder interactions during the process are a complex phenomenon due to multiple phase changes and variable absorbance based on the temperature of the material. These interactions happen on rapid timescales due to the focused nature of a laser spot on microscopic spatial scales. Operating on these small scales means even minor perturbations can have a significant effect. The process can be spatially varying across the build plate or temporally varying during a build leading to reductions in repeatability. The process parameters for a particular material are usually developed empirically for a specific system and cannot be taken to be ideal for all possible systems. This leads to the selection of suboptimal parameter sets in terms of repeatability/reproducibility. The ability to monitor the stability of the melt pool and thermal effects can increase process control to account for perturbations, however, this needs to be developed further. Also, the ability to detect defects forming during the process can enable the targeted use of corrective scan strategies such as the polishing-type remelting pass to further improve repeatability/reproducibility.

Parts produced by additive manufacturing have a staircase structure on the surface from the discrete layers present. This gives rise to a rough surface that is anisotropic depending on build direction. This, coupled with the requirement to have support structures attached to parts, increases the variation in surface roughness values. This variation can reduce repeatability/reproducibility and also increase the amount of machining required. The requirement of post-processing of additively manufactured parts gives rise to repeatability/reproducibility issues as the standard heat treatments for traditional manufactured parts do not lead to the usual or expected results. The errors present in the process stages propagate and increase the variations in each step, significantly reducing the repeatability/reproducibility. The improvements in part repeatability/reproducibility after post-processing will require improvements in the as built conditions to occur.

CRediT authorship contribution statement

L. Dowling: Investigation. **J. Kennedy:** Project administration. **S. O'Shaughnessy:** Review & editing. **D. Trimble:** Supervision, Conceptualization.

Declaration of competing interest

The authors declare that they have no known competing financial interests or personal relationships that could have appeared to influence the work reported in this paper.

Acknowledgments

This work was funded through the AERIALIST project no: 723367 European Union H2020-EU.3.4. SOCIETAL CHALLENGES - Smart, Green And Integrated Transport.

References

[1] I. Gibson, D.W. Rosen, B. Stucker, Additive Manufacturing Technologies: Rapid Prototyping to Direct Digital Manufacturing, 1st ed. Springer Publishing Company, Incorporated, 2009.

[2] H. Shipley, D. McDonnell, M. Culleton, R. Coull, R. Lupoi, G. O'Donnell, D. Trimble, Optimisation of process parameters to address fundamental challenges during selective laser melting of Ti-6Al-4V: a review, Int. J. Mach. Tools Manuf. 128 (2018) 1–20, https://doi.org/10.1016/j.ijmachtools.2018.01.003.

[3] S.L. Sing, J. An, W.Y. Yeong, F.E. Wiria, Laser and electron-beam powder-bed additive manufacturing of metallic implants: a review on processes, Materials and Designs (2015) https://doi.org/10.1002/jor.23075.

[4] J. Kruth, B. Vandenbroucke, J. Van Vaerenbergh, P. Mercelis, Benchmarking of Different SLS/SLM Processes As Rapid Manufacturing Techniques, 2005.

[5] M. Brandt, S. Sun, M. Leary, S. Feih, J. Elambasseril, Q. Liu, High-Value SLM Aerospace Components: From Design to Manufacture High-Value SLM Aerospace Components: From Design to Manufacture, 2013https://doi.org/10.4028/www.scientific.net/AMR.633.135.

[6] G. Tapia, A. Elwany, A review on process monitoring and control in metal-based additive manufacturing, J. Manuf. Sci. Eng. 136 (2014), 060801. https://doi.org/10.1115/1.4028540.

[7] NIST, Measurement Science Roadmap for Metal-based Additive Manufacturing, 2013.

[8] C. Weller, R. Kleer, F.T. Piller, Economic Implications of 3D Printing: Market Structure Models in Light of Additive Manufacturing Revisited, 3, 2015 303–312.

[9] ASTM, Standard Practice for Use of the Terms Precision and Bias in ASTM Test Methods, (n.d.). doi:https://doi.org/10.1520/E0177-14.2.

[10] S. Franchitti, R. Borrelli, C. Pirozzi, L. Carrino, W. Polini, L. Sorrentino, A. Gazzerro, Investigation on electron beam melting: dimensional accuracy and process repeatability, Vacuum 157 (2018) 340–348, https://doi.org/10.1016/j.vacuum.2018.09.007.

[11] M. Grasso, B.M. Colosimo, Process defects and in situ monitoring methods in metal powder bed fusion: a review, Meas. Sci. Technol. (2017) https://doi.org/10.1088/1361-6501/aa5c4f.

[12] J.A. Slotwinski, W.E. Luecke, E.A. Lass, NIST Technical Note 2006 Interlaboratory mechanical-property study for Cobalt-Chromium alloy made by laser powder-bed-fusion additive manufacturing, NIST Technical Note 2006 Interlaboratory Mechanical-Property Study for Cobalt-Chromium Alloy Made By Laser, 2006.

[13] A. Lavakumar, Mechanical properties of materials, Concepts Phys. Metall. (2017) 5–22, https://doi.org/10.1088/978-1-6817-4473-5ch5.

[14] A. Takaichi, Suyalatu, T. Nakamoto, N. Joko, N. Nomura, Y. Tsutsumi, S. Migita, H. Doi, S. Kurosu, A. Chiba, N. Wakabayashi, Y. Igarashi, T. Hanawa, Microstructures and mechanical properties of Co-29Cr-6Mo alloy fabricated by selective laser melting process for dental applications, J. Mech. Behav. Biomed. Mater. 21 (2013) 67–76, https://doi.org/10.1016/j.jmbbm.2013.01.021.

[15] M. Averyanova, P. Bertrand, B. Verquin, Manufacture of Co-Cr dental crowns and bridges by selective laser melting technology, Virtual Phys. Prototyp. 6 (2011) 179–185, https://doi.org/10.1080/17452759.2011.619083.

[16] C. Song, M. Zhang, Y. Yang, D. Wang, Y. Jia-kuo, Morphology and properties of CoCrMo parts fabricated by selective laser melting, Mater. Sci. Eng. A 713 (2018) 206–213, https://doi.org/10.1016/j.msea.2017.12.035.

[17] B. Qian, K. Saeidi, L. Kvetková, F. Lofaj, C. Xiao, Z. Shen, Defects-tolerant Co-Cr-Mo dental alloys prepared by selective laser melting, Dent. Mater. 31 (2015) 1435–1444, https://doi.org/10.1016/j.dental.2015.09.003.

[18] Y. Lu, Y. Gan, J. Lin, S. Guo, S. Wu, J. Lin, Effect of laser speeds on the mechanical property and corrosion resistance of CoCrW alloy fabricated by SLM, Rapid Prototyp. J. 23 (2017) 28–33, https://doi.org/10.1108/RPJ-07-2015-0085.

[19] H.R. Kim, S.H. Jang, Y.K. Kim, J.S. Son, B.K. Min, K.H. Kim, T.Y. Kwon, Microstructures and mechanical properties of Co-Cr dental alloys fabricated by three CAD/CAM-based processing techniques, Materials (Basel) 9 (2016) https://doi.org/10.3390/MA9070596.

[20] E. Liverani, A. Fortunato, A. Leardini, C. Belvedere, S. Siegler, L. Ceschini, A. Ascari, Fabrication of Co-Cr-Mo endoprosthetic ankle devices by means of Selective Laser Melting (SLM), Mater. Des. 106 (2016) 60–68, https://doi.org/10.1016/j.matdes.2016.05.083.

[21] Y. Kajima, A. Takaichi, N. Kittikundecha, T. Nakamoto, T. Kimura, N. Nomura, A. Kawasaki, T. Hanawa, H. Takahashi, N. Wakabayashi, Effect of heat-treatment temperature on microstructures and mechanical properties of Co–Cr–Mo alloys fabricated by selective laser melting, Mater. Sci. Eng. A 726 (2018) 21–31, https://doi.org/10.1016/j.msea.2018.04.048.

[22] Y. Zhou, N. Li, J. Yan, Q. Zeng, Comparative analysis of the microstructures and mechanical properties of Co-Cr dental alloys fabricated by different methods, J. Prosthet. Dent. (2018) 1–7, https://doi.org/10.1016/j.prosdent.2017.11.015.

[23] United Performance Metals, CCM Cobalt Chrome Moly - ASTM F1537 Alloy 1, https://www.upmet.com/products/cobalt/cobalt-chrome-moly 2018.

[24] P. Edwards, A. O'Conner, M. Ramulu, Electron beam additive manufacturing of titanium components: properties and performance, J. Manuf. Sci. Eng. 135 (2013) 61016, https://doi.org/10.1115/1.4025773.

[25] H.P. Tang, M. Qian, N. Liu, X.Z. Zhang, G.Y. Yang, J. Wang, Effect of powder reuse times on additive manufacturing of Ti-6Al-4V by selective electron beam melting, Jom 67 (2015) 555–563, https://doi.org/10.1007/s11837-015-1300-4.

[26] B. Baufeld, O. Van Der Biest, R. Gault, Additive manufacturing of Ti – 6Al – 4V components by shaped metal deposition: microstructure and mechanical properties, Mater. Des. 31 (2010) S106–S111, https://doi.org/10.1016/j.matdes.2009.11.032.

[27] G. Welsch, R. Boyer, E.W. Collings, Materials Properties Handbook: Titanium Alloys, ASM International, 1993. https://books.google.ie/books?id=x3rToHWOcD8C.

[28] D. Bourell, J. Coholich, A. Chalancon, A. Bhat, Evaluation of energy density measures and validation for powder bed fusion of polyamide, CIRP Ann. - Manuf. Technol. 66 (2017) 217–220, https://doi.org/10.1016/j.cirp.2017.04.128.

[29] S.M. Yusuf, N. Gao, Influence of energy density on metallurgy and properties in metal additive manufacturing, Mater. Sci. Technol. 33 (2017) 1269–1289, https://doi.org/10.1080/02670836.2017.1289444.

[30] S. Zia Uddin, D. Espalin, J. Mireles, P. Morton, C. Terrazas, S. Collins, L.E. Murr, R. Wicker, Laser powder bed fusion fabrication and characterization of crack- free aluminum alloy 6061 using in-process powder bed induction heating, Solid Free. Fabr. Symp. (2016) 214–227.

[34] A.B. Spierings, G. Levy, Comparison of density of stainless steel 316L parts produced with selective laser melting using different powder grades, Solid Free. Fabr. Proc. (2009) 342–353.

[35] X. Wang, T. Keya, K. Chou, Build height effect on the Inconel 718 parts fabricated by selective laser melting, Procedia Manuf. 5 (2016) 1006–1017, https://doi.org/10.1016/j.promfg.2016.08.089.

[37] R.R. Cervey, Mechanical Properties of Ti-6A1-4V Annealed Forgings, 1974.

[38] F. Clifton, Strength Variability in Structural Materials Strength Variability in Structural Materials, 1969.

[39] P.E. Hess, D. Bruchman, I.A. Assakkaf, B.M. Ayyub, Uncertainties in Material Strength, Geometric, and Load Variables, vol. 1956 (n.d.) 1–54.

[40] P. Fischer, N. Karapatis, V. Romano, R. Glardon, H.P. Weber, A model for the interaction of near-infrared laser pulses with metal powders in selective laser sintering, Appl. Phys. A Mater. Sci. Process. 74 (2002) 467–474, https://doi.org/10.1007/s003390101139.

[41] P. Fischer, V. Romano, H.P. Weber, N.P. Karapatis, E. Boillat, R. Glardon, Sintering of commercially pure titanium powder with a Nd:YAG laser source, Acta Mater. 51 (2003) 1651–1662, https://doi.org/10.1016/S1359-6454(02)00567-0.

[42] A. Foroozmehr, M. Badrossamay, E. Foroozmehr, S. Golabi, Finite element simulation of selective laser melting process considering optical penetration depth of laser in powder bed, Mater. Des. 89 (2016) 255–263, https://doi.org/10.1016/j.matdes.2015.10.002.

[43] K. Zeng, D. Pal, B.E. Stucker, A review of thermal analysis methods in laser sintering and selective laser melting, Proc. Solid Free. Fabr. Symp. (2012) 796–814. http://utwired.engr.utexas.edu/lff/symposium/proceedingsArchive/pubs/Manuscripts/2012/2012-60-Zeng.pdf%5Cnhttp://utwired.engr.utexas.edu/lff/symposium/proceedingsArchive/pubs/Tableof Contents/2012_TOC.cfm.

[44] H. Gong, D. Christiansen, J. Beuth, J.J. Lewandowski, Melt Pool characterization for selective laser melting of Ti-6Al-4V pre-alloyed powder, Solid Free. Fabr. Symp. (2014) 256–267.

[45] H. Gong, K. Rafi, H. Gu, T. Starr, B. Stucker, Analysis of defect generation in Ti-6Al-4V parts made using powder bed fusion additive manufacturing processes, Addit. Manuf. 1 (2014) 87–98, https://doi.org/10.1016/j.addma.2014.08.002.

[46] S.A. Khairallah, A.T. Anderson, A. Rubenchik, W.E. King, Laser powder-bed fusion additive manufacturing: physics of complex melt flow and formation mechanisms of pores, spatter, and denudation zones, Acta Mater. 108 (2016) 36–45, https://doi.org/10.1016/j.actamat.2016.02.014.

[47] C. Qiu, C. Panwisawas, M. Ward, H.C. Basoalto, J.W. Brooks, M.M. Attallah, On the role of melt flow into the surface structure and porosity development during selective laser melting, Acta Mater. 96 (2015) 72–79, https://doi.org/10.1016/j.actamat.2015.06.004.

[48] H. Attar, S. Ehtemam-Haghighi, D. Kent, M.S. Dargusch, Recent developments and opportunities in additive manufacturing of titanium-based matrix composites: a review, Int. J. Mach. Tools Manuf. 133 (2018) 85–102, https://doi.org/10.1016/j.ijmachtools.2018.06.003.

[49] H. Attar, M. Bönisch, M. Calin, L.C. Zhang, S. Scudino, J. Eckert, Selective laser melting of in situ titanium-titanium boride composites: processing, microstructure and mechanical properties, Acta Mater. 76 (2014) 13–22, https://doi.org/10.1016/j.actamat.2014.05.022.

[50] X. Wang, J. Kruth, Energy absorption and penetration in selective laser sintering: a ray tracing model, Proc. Int. Conf. Math. Model. Simul. Met. Technol. (2000) 673–683. http://www.ariel.ac.il/sites/conf/mmt/MMT-2000/papers/673-682.doc.

[51] M.A. Presley, P.R. Christensen, Thermal conductivity measurements of particulate materials: 4. Effect of bulk density and particle shape, J. Geophys. Res. 115 (2010), E07004. https://doi.org/10.1029/2009JE003483.

[52] K. Abd-Elghany, D.L. Bourell, Property evaluation of 304L stainless steel fabricated by selective laser melting, Rapid Prototyp. J. 18 (2012) 420–428, https://doi.org/10.1108/13552541211250418.

[53] B. Liu, R. Wildman, C. Tuck, I. Ashcroft, R. Hague, Investigation the Effect of Particle Size Distribution on Processing Parameters Optimisation in Selective Laser Melting Process, Sff, 2011 227–238, https://doi.org/10.1017/CBO9781107415324.004.

[54] R.P. Zou, A.B. Yu, Evaluation of the packing characteristics of mono-sized non-spherical particles, Powder Technol. 88 (1996) 71–79.

[55] L. Chan C.Y., N.W. Page, Particle fractal and load effects on internal friction in powders, Powder Technol. 90 (1997) 259–266.

[56] J. Dawes, C. Langley, J. Clayton, Optimizing metal powders for additive manufacturing what makes a good AM metal powder? Addit. Manuf. Mag. (2017) 1–5.

[57] A. Simchi, The Role of Particle Size on the Laser Sintering of Iron Powder, 2004 35.

[58] P. NANDWANA, W.H. PETER, R.R. DEHOFF, L.E. LOWE, M.M. KIRKA, F. MEDINA, S.S. BABU, Recyclability study on Inconel 718 and Ti-6Al-4V powders for use in electron beam melting, Metall. Mater. Trans. 47 (2016) 754–762, https://doi.org/10.1007/s10884-015-9497-z.

[59] K.L. Terrassa, J.C. Haley, B.E. MacDonald, J.M. Schoenung, Reuse of powder feedstock for directed energy deposition, Powder Technol. 338 (2018) 819–829, https://doi.org/10.1016/j.powtec.2018.07.065.

[60] R. Engeli, T. Etter, S. Hövel, K. Wegener, Processability of different IN738LC powder batches by selective laser melting, J. Mater. Process. Technol. 229 (2016) 484–491, https://doi.org/10.1016/j.jmatprotec.2015.09.046.

[61] P.A. Kulkarni, R.J. Berry, M.S.A. Bradley, Review of the flowability measuring techniques for powder metallurgy industry, Proc. Inst. Mech. Eng. Part E J. Process Mech. Eng. 224 (2010) 159–168, https://doi.org/10.1243/09544089JPME299.

[62] J.A. Slotwinski, E.J. Garboczi, P.E. Stutzman, C.F. Ferraris, S.S. Watson, M.A. Peltz, Characterization of Metal Powders Used for Additive Manufacturing, 119, 2014 460–493.

[63] H. Gu, H. Gong, J.J.S. Dilip, D. Pal, A. Hicks, H. Doak, B. Stucker, Effects of powder variation on the microstructure and tensile strength of Ti-6Al-4V parts fabricated by selective laser melting, Int. J. Powder Metall. 51 (2015) 35–42.

[64] M. Baumers, C. Tuck, R. Wildman, I. Ashcroft, E. Rosamond, R. Hague, Combined build–time, energy consumption and cost estimation for direct metal laser sintering, Proc. Twenty Third Annu. Int. Solid Free. Fabr. Symp. Addit. Manuf. Conf. 53 (2012) 1689–1699, https://doi.org/10.1017/CBO9781107415324.004.

[65] L.C. Ardila, F. Garciandia, J.B. González-Díaz, P. Álvarez, A. Echeverria, M.M. Petite, R. Deffley, J. Ochoa, Effect of IN718 recycled powder reuse on properties of parts manufactured by means of Selective Laser Melting, Phys. Procedia 56 (2014) 99–107, https://doi.org/10.1016/j.phpro.2014.08.152.

[66] B.L. Decost, H. Jain, A.D. Rollett, E.A. Holm, Computer Vision and Machine Learning for Autonomous Characterization of AM Powder Feedstocks, 69, 2017 456–465, https://doi.org/10.1007/s11837-016-2226-1.

[67] H. Attar, K.G. Prashanth, L.C. Zhang, M. Calin, I.V. Okulov, S. Scudino, C. Yang, J. Eckert, Effect of powder particle shape on the properties of in situ Ti-TiB composite materials produced by selective laser melting, J. Mater. Sci. Technol. 31 (2015) 1001–1005, https://doi.org/10.1016/j.jmst.2015.08.007.

[68] H. Attar, M. Calin, L.C. Zhang, S. Scudino, J. Eckert, Manufacture by selective laser melting and mechanical behavior of commercially pure titanium, Mater. Sci. Eng. A 593 (2014) 170–177, https://doi.org/10.1016/j.msea.2013.11.038.

[69] Z.G. Zhu, Q.B. Nguyen, F.L. Ng, X.H. An, X.Z. Liao, P.K. Liaw, S.M.L. Nai, J. Wei, Hierarchical microstructure and strengthening mechanisms of a CoCrFeNiMn high entropy alloy additively manufactured by selective laser melting, Scr. Mater. 154 (2018) 20–24, https://doi.org/10.1016/j.scriptamat.2018.05.015.

[70] B. Verlee, T. Dormal, Density and porosity control of sintered 316L stainless steel parts produced by additive manufacturing, Powder Metall. 55 (2012) https://doi.org/10.1179/0032589912Z.00000000082.

[71] E.O. Olakanmi, K.W. Dalgarno, R.F. Cochrane, Laser sintering of blended Al-Si powders, Rapid Prototyp. J. 18 (2012) 109–119, https://doi.org/10.1108/13552541211212096.

[72] W.A. Ayoola, W.J. Suder, S.W. Williams, Parameters controlling weld bead profile in conduction laser welding, J. Mater. Process. Technol. 249 (2017) 522–530, https://doi.org/10.1016/j.jmatprotec.2017.06.026.

[73] J.D. Majumdar, A. Pinkerton, Z. Liu, I. Manna, L. Li, Microstructure characterisation and process optimization of laser assisted rapid fabrication of 316L stainless steel, Appl. Surf. Sci. 247 (2005) 320–327, https://doi.org/10.1016/j.apsusc.2005.01.039.

[74] J.A. Van Den Avyle, J.A. Brooks, A.C. Powell, Reducing defects in remelting processes for high-performance alloys, Jom 50 (1998) 22–25, https://doi.org/10.1007/s11837-998-0374-7.

[75] T. Yahata, T. Ikeda, M. Maeda, Deoxidation of molten titanium by electron-beam remelting technique, Metall. Trans. B 24 (1993) 599–604, https://doi.org/10.1007/BF02673175.

[76] C. Charles, Modelling Microstructure Evolution of Weld Deposited Ti–6Al–4V, 2008 76 (doi:1402-1757).

[77] F. Wang, S. Williams, P. Colegrove, A.A. Antonysamy, Microstructure and Mechanical Properties of Wire and Arc Additive Manufactured Ti-6Al-4V, (n.d.). doi: https://doi.org/10.1007/s11661-012-1444-6.

[78] W.M. Steen, J. Mazumder, Basic laser optics, Laser Mater. Process. (2010) 79–130, https://doi.org/10.1007/978-1-84996-062-5_3.

[79] G.S. He, C. Weder, P. Smith, P.N. Prasad, Optical power limiting and stabilization based on a novel polymer compound, IEEE J. Quantum Electron. 34 (1998) 2279–2285, https://doi.org/10.1109/3.736090.

[80] J.P. Kruth, L. Froyen, J. Van Vaerenbergh, P. Mercelis, M. Rombouts, B. Lauwers, Selective laser melting of iron-based powder, J. Mater. Process. Tech. 149 (2004) 616–622, https://doi.org/10.1016/j.jmatprotec.2003.11.051.

[81] B.C. Hauser, M. Engineering, Selective Laser Sintering of a Stainless, 2003.

[82] E. Olakanmi, R. Cochrane, K. Dalgarno, A Review on Selective Laser Sintering/Melting of Aluminium Alloy Powders: Processing, Microstructure, and Properties, 2015.

[83] A.M. Khorasani, I. Gibson, A.H. Ghasemi, A. Ghaderi, A comprehensive study on variability of relative density in selective laser melting of Ti-6Al-4V, Virtual Phys. Prototyp. (2019) 2759, https://doi.org/10.1080/17452759.2019.1614198.

[84] R. Li, J. Liu, Y. Shi, L. Wang, Balling Behavior of Stainless Steel and Nickel Powder During Selective Laser Melting Process, 2012 1025–1035, https://doi.org/10.1007/s00170-011-3566-1.

[85] H. Gu, H. Gong, D. Pal, K. Rafi, T. Starr, B. Stucker, Influences of energy density on porosity and microstructure of selective laser melted 17- 4PH stainless steel, 24th Int. SFF Symp. - An Addit. Manuf. Conf. SFF 2013, 2013.

[86] S. Moylan, K. Jurrens, M.A. Donmez, J.A. Slotwinski, A. Cooke, NIST Technical Note 1801 Lessons Learned in Establishing the NIST Metal Additive Manufacturing Laboratory, 2013.

[87] C. Kusuma, S.H. Ahmed, A. Mian, R. Srinivasan, Effect of laser power and scan speed on melt pool characteristics of commercially pure titanium (CP-Ti), J. Mater. Eng. Perform. 26 (2017) 3560–3568, https://doi.org/10.1007/s11665-017-2768-6.

[88] P.H. De Oliveira Teixeira, A.G. dos Reis, A. Janssen, P.H. de O. Teixeira, A.G. dos Reis, A. Janssen, Effect of solid-state laser parameters on the surface's topography formation during texturization of hard metal cutting tools, J. Aerosp. Technol. Manag. 7 (2015) 63–69, https://doi.org/10.5028/jatm.v7i1.411.

[89] T.D. Mclouth, G.E. Bean, D.B. Witkin, S.D. Sitzman, P.M. Adams, D.N. Patel, W. Park, J. Yang, R.J. Zaldivar, The effect of laser focus shift on microstructural variation of Inconel 718 produced by selective laser melting, Mater. Des. 149 (2018) 205–213, https://doi.org/10.1016/j.matdes.2018.04.019.

[90] Integrated Optics, Laser Beam Collimation, https://integratedoptics.com/laser-beam-collimation 2017.

[91] S. Mullick, A.K. Agrawal, A.K. Nath, Effect of laser incidence angle on cut quality of 4 mm thick stainless steel sheet using fiber laser, Opt. Laser Technol. 81 (2016) 168–179, https://doi.org/10.1016/j.optlastec.2016.02.006.

[92] T.T. Roehling, S.S.Q. Wu, S.A. Khairallah, J.D. Roehling, S.S. Soezeri, M.F. Crumb, M.J. Matthews, Modulating laser intensity profile ellipticity for microstructural control during metal additive manufacturing, Acta Mater. 128 (2017) 197–206, https://doi.org/10.1016/j.actamat.2017.02.025.

[93] H. Ali, H. Ghadbeigi, K. Mumtaz, Effect of scanning strategies on residual stress and mechanical properties of Selective Laser Melted Ti6Al4V, Mater. Sci. Eng. A 712 (2018) 175–187, https://doi.org/10.1016/j.msea.2017.11.103.

[94] L. Thijs, F. Verhaeghe, T. Craeghs, J. Van Humbeeck, J.P. Kruth, A study of the microstructural evolution during selective laser melting of Ti-6Al-4V, Acta Mater. 58 (2010) 3303–3312, https://doi.org/10.1016/j.actamat.2010.02.004.

[95] K.P. Monroy, J. Delgado, L. Sereno, J. Ciurana, N.J. Hendrichs, Effects of the Selective Laser Melting manufacturing process on the properties of CoCrMo single tracks, Met. Mater. Int. 20 (2014) 873–884, https://doi.org/10.1007/s12540-014-5011-0.

[96] A.G. Demir, B. Previtali, Investigation of remelting and preheating in SLM of 18Ni300 maraging steel as corrective and preventive measures for porosity reduction, Int. J. Adv. Manuf. Technol. 93 (2017) 2697–2709, https://doi.org/10.1007/s00170-017-0697-z.

[97] S. Scudino, C. Unterdörfer, K.G. Prashanth, H. Attar, N. Ellendt, V. Uhlenwinkel, J. Eckert, Additive manufacturing of Cu-10Sn bronze, Mater. Lett. 156 (2015) 202–204, https://doi.org/10.1016/j.matlet.2015.05.076.

[98] W.E. Frazier, Metal additive manufacturing: a review, J. Mater. Eng. Perform. 23 (2014) 1917–1928, https://doi.org/10.1007/s11665-014-0958-z.

[99] W.L. Guesser, F. Souza Pereira, L. Boehs, Surface Changes During Turning of Grey Cast Iron Wilson Luis Guesser * Fernando Souza Pereira and Lourival Boehs, 2016 18.

[100] K. Tajima, M. Hironaka, K. Chen, Y. Nagamatsu, H. Kakigawa, Electropolishing of CP Titanium and Its Alloys in an Alcoholic Solution-based Electrolyte, 27, 2008 258–265.

[101] P. Delfs, M. Tows, H. Schmid, Optimized Build Orientation of Additive Manufactured Parts for Improved Surface Quality and Build Time, 12, 2016 314–320, https://doi.org/10.1016/j.addma.2016.06.003.

[102] G. Moroni, W.P. Syam, S. Petrò, Functionality-based part orientation for additive manufacturing, Procedia CIRP 36 (2015) 217–222, https://doi.org/10.1016/j.procir.2015.01.015.

[103] S. Afkhami, M. Dabiri, S.H. Alavi, T. Björk, A. Salminen, Fatigue characteristics of steels manufactured by selective laser melting, Int. J. Fatigue 122 (2019) 72–83, https://doi.org/10.1016/j.ijfatigue.2018.12.029.

[104] P. Mercelis, J.P. Kruth, Residual stresses in selective laser sintering and selective laser melting, Rapid Prototyp. J. 12 (2006) 254–265, https://doi.org/10.1108/13552540610707013.

[105] R. Wauthle, B. Vrancken, B. Beynaerts, K. Jorissen, J. Schrooten, J.P. Kruth, J. Van Humbeeck, Effects of build orientation and heat treatment on the microstructure and mechanical properties of selective laser melted Ti6Al4V lattice structures, Addit. Manuf. 5 (2015) 77–84, https://doi.org/10.1016/j.addma.2014.12.008.

[106] B. Vrancken, L. Thijs, J.-P. Kruth, J. Van Humbeeck, Heat treatment of Ti6Al4V produced by Selective Laser Melting: microstructure and mechanical properties, J. Alloy. Compd. J. 541 (2012) 177–185, https://doi.org/10.1016/j.msea.2013.10.023.

[107] W.J. Sames, F.A. List, S. Pannala, R.R. Dehoff, S.S. Babu, The metallurgy and processing science of metal additive manufacturing, Int. Mater. Rev. 61 (2016) 315–360, https://doi.org/10.1080/09506608.2015.1116649.

[108] C. Leyens, M. Peters, D. Wenem, W.A. Kaysser, Influence of Long-Term Annealing on Tensile Properties and Fracture of Near-a Titanium Alloy Ti-6Al-2. 75S n-4Z r-0. 4 M o-0. 45Si, 27, 1996 1709–1717.

[109] B.K. Foster, E.W. Reutzel, A.R. Nassar, B.T. Hall, S.W. Brown, C.J. Dickman, Optical, layerwise monitoring of powder bed fusion, Solid Free. Fabr. Symp 2015, pp. 10–12 , Austin, TX, Aug.

[110] B. Zhang, J. Ziegert, F. Farahi, A. Davies, In situ surface topography of laser powder bed fusion using fringe projection, Addit. Manuf. 12 (2016) 100–107, https://doi.org/10.1016/j.addma.2016.08.001.

[111] M.L. Vlasea, B. Lane, F. Lopez, S. Mekhontsec, A. Donmez, Test Bed for Enhanced Real-time Process Control, 2015 527–539.

[112] M. Aminzadeh, A Machine Vision System for In-situ Quality Inspection in Metal Powder-bed Additive Manufacturing, 2016.

[113] A.G. Demir, C. De Giorgi, B. Previtali, Design and implementation of a multisensor coaxial monitoring system with correction strategies for selective laser melting of a Maraging steel, J. Manuf. Sci. Eng. 140 (2018) 1–14, https://doi.org/10.1115/1.4038568.

[114] G. Strano, L. Hao, R.M. Everson, K.E. Evans, A New Approach to the Design and Optimisation of Support Structures in Additive Manufacturing, 2013 1247–1254, https://doi.org/10.1007/s00170-012-4403-x.

[115] A. Hussein, L. Hao, C. Yan, R. Everson, P. Young, Advanced lattice support structures for metal additive manufacturing, J. Mater. Process. Tech. 213 (2013) 1019–1026, https://doi.org/10.1016/j.jmatprotec.2013.01.020.

Hindawi
International Journal of Polymer Science
Volume 2019, Article ID 7029143, 11 pages
https://doi.org/10.1155/2019/7029143

Research Article

The Influence of Additive Manufacturing Processes on the Performance of a Periodic Acoustic Metamaterial

John Kennedy, Lara Flanagan, Luke Dowling, G. J. Bennett, Henry Rice, and Daniel Trimble

Department of Mechanical Engineering, Trinity College Dublin, Ireland

Correspondence should be addressed to John Kennedy; jkenned5@tcd.ie

Received 8 February 2019; Revised 8 May 2019; Accepted 10 June 2019; Published 24 July 2019

Guest Editor: Jean-Philippe Groby

Advancements in 3D print technology now allow the printing of structured acoustic absorbent materials at the appropriate microscopic scale and sample sizes. The repeatability of the fundamental cell unit of these metamaterials provides a pathway for the development of viable macro models to simulate built-up structures based on detailed models of the individual cell units; however, verification of such models on actual manufactured structures presents a challenge. In this paper, a design concept for an acoustic benchmark metamaterial consisting of an interlinked network of resonant chambers is considered. The form chosen is periodic with cubes incorporating spherical internal cavities connected through cylindrical openings on each face of the cube. This design is amenable to both numerical modelling and manufacture through additive techniques whilst yielding interesting acoustic behaviour. The paper reports on the design, manufacture, modelling, and experimental validation of these benchmark structures. The behaviour of the acoustic metamaterial manufactured through three different polymer-based printing technologies is investigated with reference to the numerical models and a metal powder-based print technology. At the scale of this microstructure, it can be seen that deviations in surface roughness and dimensional fidelity have a comparable impact on the experimentally measured values of the absorption coefficient.

1. Introduction

The European COST action DENORMS (Designs for Noise Reducing Materials and Structures) has the stated goal of providing a framework for efficient information exchange, avoiding duplication of research effort, and channelling the work of groups involved towards the common goal of designing multifunctional, light, and compact noise-reducing treatments. As part of this effort, there is a need for benchmark designs and materials which can be used to cross-check and validate new numerical approaches as well as experimental measurements and manufacturing technologies. The group has recently proposed a design for a benchmark periodic metamaterial which was amenable to numerical modelling, manufacture, and experimental testing [1, 2]. This paper reports on initial results for the proposed design where the "end-to-end" process of simulation, manufacture, experimental testing, and validation was performed.

1.1. 3D Print Technology. The recent surge in metamaterial research has been facilitated by a number of advances in enabling technologies. Advances in numerical modelling also have enabled viable simulations of metabehaviour under realistic conditions. This has led to proposals for effective designs; however, until recently, these were often unrealisable. In particular, development of advanced additive manufacturing technologies has opened the door to complex geometries that are not suited to traditional manufacturing techniques. At present, there are a number of additive manufacturing technologies available and these include

(i) stereolithography (SLA)
(ii) jetting systems
(iii) direct light processing (DLP)
(iv) laser metal deposition

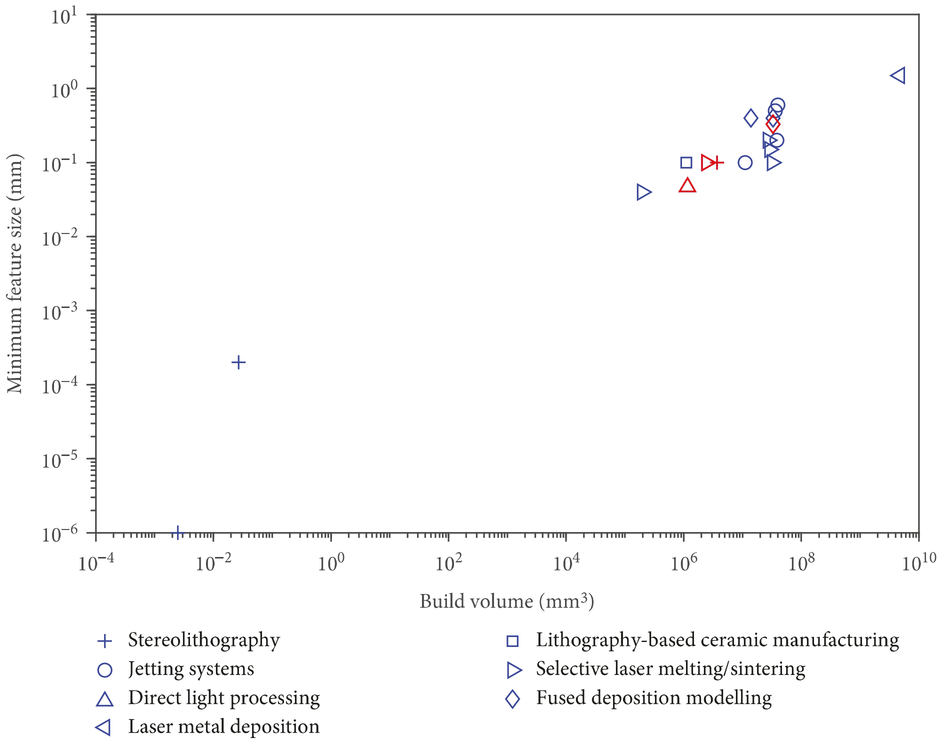

Figure 1: Build volume and minimum feature size for commercial additive manufacturing systems based on manufacturer data (the machines used in this research are identified by red symbols).

(v) electron beam melting

(vi) lithography-based ceramic manufacturing

(vii) selective laser melting/sintering (SLM)

(viii) fused deposition modelling (FDM)

The various technologies provide different capabilities in terms of resolution and build volumes. These limit the scale and quantity of the metamaterial that can be produced. The different processes also make use of different materials with FDM [3], SLA [4], and DLP [5] print technologies being based exclusively on polymers while other technologies also offer the possibility of manufacture in ceramics and metals. The design and manufacturing processes from conception through to realisation of a metamaterial is also of vital importance as is it currently unknown to what extent manufacturing tolerances or defects will impact the targeted metabehaviour. Therefore, the correct selection of the manufacturing process and assessment of the quality of the performance of the produced material are topics which require research.

A survey of the state of the art in terms of additive manufacturing technologies reveals the capabilities currently available to metamaterial researchers. The key capabilities of build volume and minimum feature size have been graphed in Figure 1. The graph shows a clear relationship between the build volume and minimum feature size and shows the overlap in the capabilities of the various technologies considered. As a general rule, an increase in build volume is matched by a corresponding increase in the minimum feature size which can be achieved. There were four printing technologies used for this research which extend from low cost desktop printers to state-of-the-art machines.

A question of interest when considering a benchmark validation material is what level of geometric accuracy and quality of surface finish is required to closely match the numerical models. A second question of interest is what is the lowest cost technology which can achieve this level of accuracy.

One of the most widely used low cost (approx. e3k) desktop printers is the FDM Ultimaker series highlighted by a red 5 on the plot. The Formlabs Form 2 is a relatively low cost SLA desktop printer (approx. e5k) highly suited to laboratory research of metamaterials as it allows a reduction of roughly one order of magnitude in minimum feature size possible over FDM machines and is highlighted with a red + on the plot. The Anycubic Photon is a very low cost (approx. e500) DLP machine and is highlighted with a red 4 on the plot.

At a fundamental level, the process of manufacturing polymers by SLA and DLP is an identical process. Both processes occur by a photomonomer reacting to light in a polymerisation reaction which results in a high level of crosslinking which generates a solid object. The source of light in each case is different. The SLA process relies on a laser light source scanning in a raster pattern. The DLP process is either a LCD screen or an array of LEDs which illuminate the entire layer at the same time. In both cases, the wavelength of light used is typically in the violet or near-UV spectrum.

The obvious difference between the use of a laser and a broad focus illumination is a dramatic difference in the

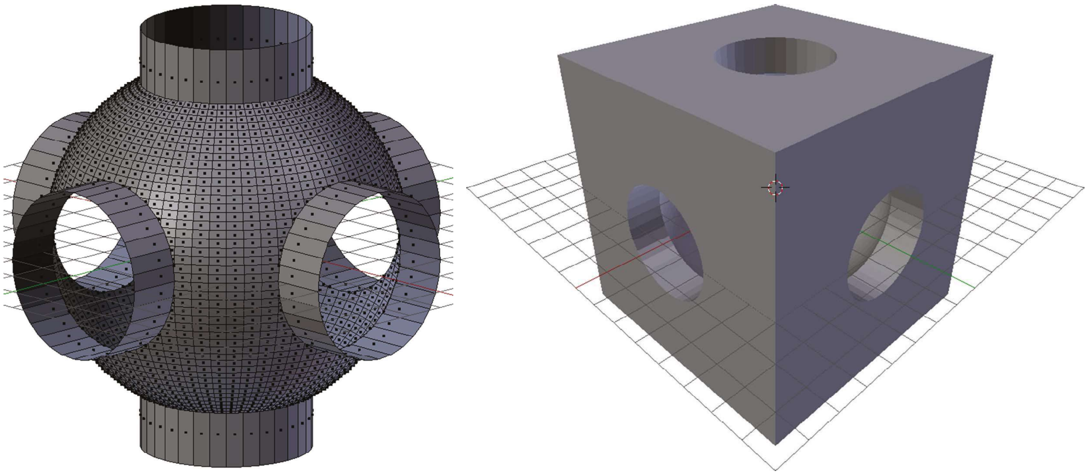

Figure 2: DENORMS benchmark design.

power density on the photopolymer. This power density difference can be a factor in the level of polymerisation that occurs and what form of reaction in the photopolymer occurs. The material used in both processes is typically an acrylic or methacrylic monomer with photoinitiators; the exact initiator and the ratio of monomer to initiator are usually proprietary information limiting the research into the area and preventing direct comparisons between the source materials.

The gaps between layers in both processes are a connection of semireacted photopolymers joining together. The polymerisation between layers can also be weaker in both technologies than those within a layer, theoretically leading to minor anisotropy. This is similar to the anisotropy found in FDM printed parts [6] but not at the same level. An effect shown in the DLP process that does not appear in SLA is the voxel effect. As the DLP process relies on pixel controlled granularity, its parts inherently have a staircase-like structure; this increases the surface roughness when compared to the smooth finish from SLA which will be more continuous in nature.

The three polymer-based print technologies have a material cost ranging from e30 (FDM) to e50 (DLP) and e170 (SLA) per kilo. The 3D Systems Prox DMP 200, highlighted by the red B symbol, is an SLM machine [7] which can print in titanium, cobalt chrome, aluminium, and stainless steel. This is a state-of-the-art machine (approx. e450k), and this work was used to manufacture in cobalt chrome at a cost of e200 per kilo of powder.

1.2. Design. The DENORMS benchmark design consists of a periodic structure of cubes with spherical internal cavities connected through cylindrical openings on each face of the cube. This design is defined by a small number of parametric features which can be varied to alter the acoustic performance of the periodic cellular material. It is also amenable to manufacture at different scales with the sphere and cylinder diameter easily varied within a cell of a given size.

In this work, a single 5 mm cubed cell size was used with fixed interior spherical cavities of radius 2.1 mm with interconnecting cylinders of radius 1 mm from all faces of the cell. These parameters were chosen in the first instance to allow for a successful manufacture of the structure in multiple print technologies. Figure 2 shows the design of the unit cell. In this work, the unit cell was used to form a lattice up to 10 layers deep and samples were made for impedance tube testing to investigate the acoustic performance.

While the DENORMS cell does not correspond closely to many of the wide range of acoustic metamaterial designs currently published in the literature, the lessons learned for the manufacture, simulation, and testing are still widely applicable to other materials. For example, recent papers on optimal sound absorber design [8], ultrathin metasurfaces [9], and space coiling metamaterials [10–12] have all utilised periodic structures realised through additive manufacturing.

There is considerable potential for acoustic metamaterials to operate at a subwavelength thickness through the use of concepts such as space coiling and labyrinthine structures. In this paper, the suitability of the DENORMS unit cell to incorporate these behaviours was also investigated through the designs shown in Figure 3. Figure 3(a) shows a labyrinthine modification to the basic structure which effectively doubles the number of resonators in a given depth, from two deep to four deep in the figure. Figure 3(b) has a mixed length design with channels of four, six, eight, and ten resonators, all contained within a depth of seven cells.

1.3. Manufacturing Considerations. Most low cost commercial 3D printers make use of fused deposition modelling (FDM) which is a 3D printing process that uses a continuous filament of a thermoplastic polymer, for example, the Ultimaker desktop printers. The resolution of these machines is potentially insufficient to accurately manufacture the spherical internal cavities and circular openings of the connecting cylinders which are included in this material's design. Additionally, these "fuzzy" internal surfaces may influence the achieved acoustic performance, potentially leading to an enhanced broadband performance [11] due to additional losses caused by the spurs. It is not a trivial task to quantify the influence of these manufacturing defects on the achieved acoustic performance of the DENORMS material; therefore, FDM samples may be unsuitable for the validation of

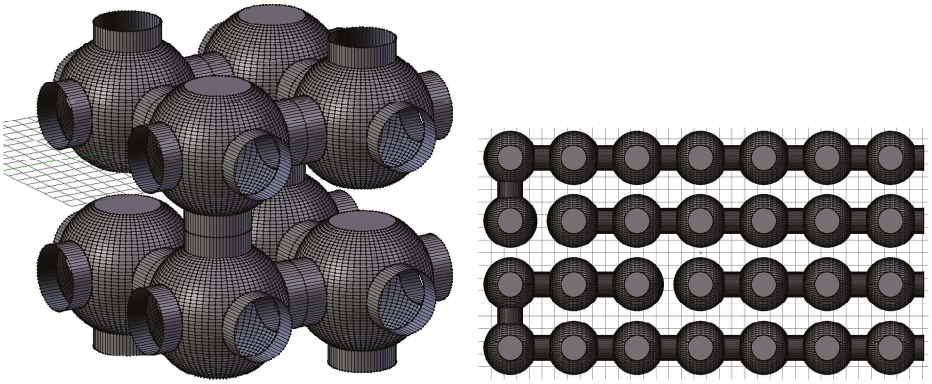
(a) (b)

Figure 3: DENORMS design variations: (a) labyrinth; (b) space coiling mixed length.

numerical codes. In this work, all FDM samples are manufactured in PLA.

The Formlabs Form 2 printer, which is based on stereolithography (SLA), can achieve a resolution which is conservatively four to ten times smaller than FDM technology while still being a low cost desktop printer. This technology uses a UV laser to cure layers of photopolymer resin with a resolution dependent on the laser spot size. It is to be hoped that the more accurate manufacturing will lead to greater agreement with the numerical simulations of the acoustic behaviour. The Anycubic Photon is a very low cost machine based on a competing technology to SLA known as digital light processing (DLP). This technology uses a UV light source and a digital LCD to cure layers of photopolymer resin by opening and closing pixels within the LCD. The resolution of the DLP printers is dependent on the pixel size in the LCD which imparts a step-like finish to the surface.

Finally, the 3D Systems Prox DMP 200, based on selective laser melting/sintering (SLM), uses a laser to form the part from a bed of metal powder. This system can achieve the smoothest surfaces with the best resolution and will be the closest to the ideal benchmark material sample. Figure 4 shows microscopy images of the four printed samples used in this work; the images were taken using a Leica S6E system under 56x magnification. The figure includes an assessment of the dimensional accuracy of the cylindrical openings and the distances between openings on the front face of the sample. The FDM prints have many defects including filaments bridging the openings and holes that are elliptical rather than circular with significant eccentricity as seen Figure 4(a). The tolerances of the other three print technologies are comparable. The surface features of the SLA and SLM technologies are related to the laser spot size and print direction. The voxel effect, unique to the DLP technology, is shown in Figure 5.

Manufacture with these four different technologies essentially introduces defects into the design which are inherent to the technology chosen. There are however significant disadvantages to all of these technologies when considering a periodic cellular design. For the SLA-based printers, the entrainment of the resin material inside the cells leads to blockages which are more difficult to remove deeper in the material. This limits the number of layers of cells which can be manufactured in a single piece. While the DLP printers suffer a similar limitation, the viscosity of the resin is generally much lower than the SLA printers and therefore easier to remove from within the part. This problem is not encountered in FDM printers as there is no excess material to be entrained inside the cells.

In this work, the Form 2 SLA printer was unable to print the DENORMS cell design to a depth of ten layers due to the entrained resin. Attempts were made to remove the entrained resin material through compressed air cleaning, ultrasonic baths, and manual evacuation. A decision was made to print the cells on the Form 2 in high resolution single and dual layers which could be combined for testing. This introduces a new complication in that it is possible to have air gaps between layers of the cells, the effect of which may be very significant on the acoustic performance. A move to selective laser melting/sintering in metals avoids all of the above issues; however, this technology can no longer be considered low cost.

In order to achieve the desired material properties, the manufactured components must be post-processed. The SLA and DLP printers use photopolymers which require additional curing under UV light following the printing process. Completed prints undergo a rigorous inspection procedure. The initial inspection is a visual inspection after print removal. This stage of inspection checks for large scale defects such as support failures, missing or damaged cells, and layer disconnects. These macro defects usually necessitate a new print or support redesign. The first quantitative check is to verify that all faces are level. This ensures that the print is not warped or twisted. It is possible that uneven curing causes the print to curl inwards on the more cured side; this is due to entrapped and entrained liquid leaving the material and causing a modest amount of shrinkage. To avoid this, prints are rotated regularly over the curing period to achieve an even curing.

The next visual inspection is to check that all corners are complete and undamaged. As some of the printing processes include a wiper passing over the print, it is possible, at the exposed corners, for a wiper crash to cause damage. The corners are also where any damage in inserting the print into the test apparatus is likely to be noticed as they are the weakest

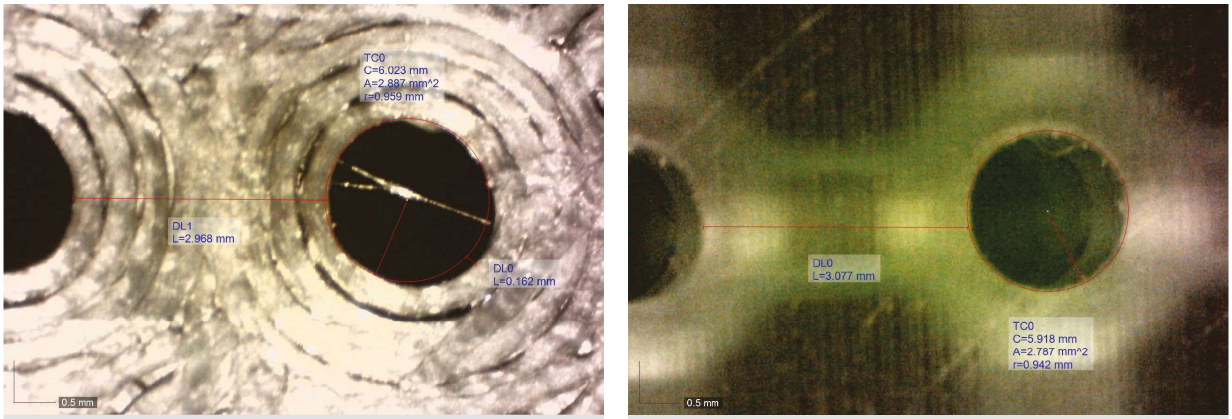

(a) FDM (b) DLP

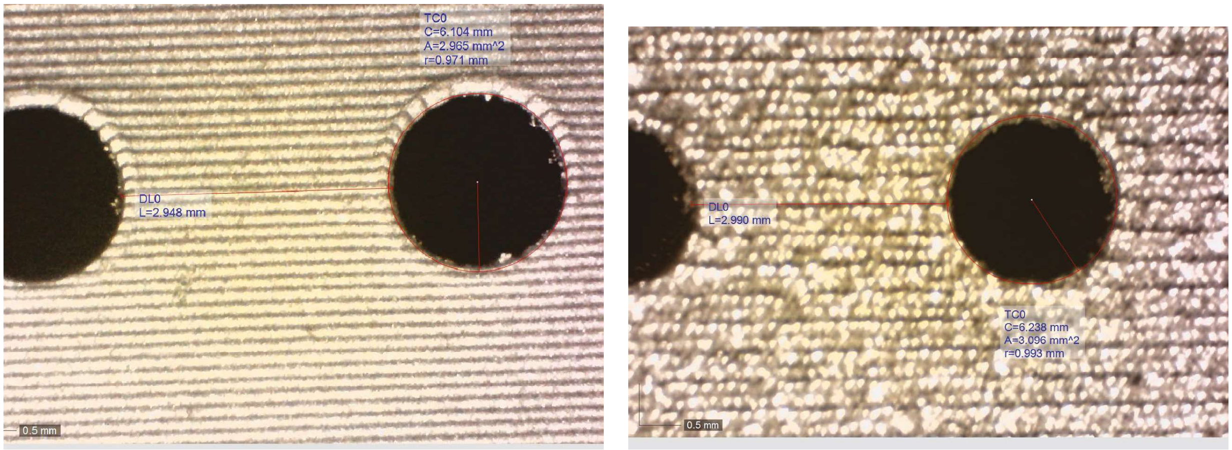

(c) SLA (d) SLM

Figure 4: Microscopy images detailing the dimensional accuracy of the 3D print technologies.

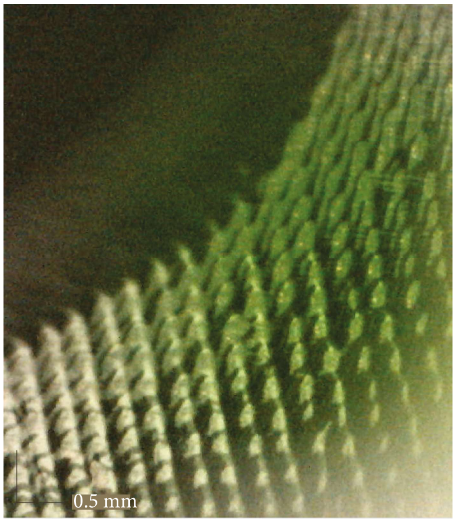

Figure 5: Microscopy image of the DLP printed components showing the voxel effect on the surface finish.

points. This weakness is due to fewer neighbouring cells being available to dissipate force without deforming. The final element of the visual inspection is to check that all designed channels are formed and clear. The DENORMS cell design has a series of cylindrical channels where air passes through. Any internal defects can usually be seen through these regular channels such as debris being embedded in the material or residue from a support spur failing into the channel.

2. Numerical Modelling

A 3D numerical model of the DENORMS cell was developed using a commercial finite element software COMSOL Multiphysics. Numerical models of the basic cell up to ten layers deep were developed in COMSOL as well as the labyrinthine and space coiling variations. The acoustic module within COMSOL 5.4 includes a full viscothermal acoustic module capable of modelling the dissipation from viscous shear and thermal conduction. However, as full viscothermal formulation comes at a high computational cost, reduced order models are often required to model complex systems [13, 14]. In this study, we restricted the analysis to full viscothermal modelling to remove any potential error associated with model simplification.

2.1. Linearised Navier-Stokes Equations. The full viscothermal acoustic model implements the linearised version of

Table 1: Properties of air used in all models.

Symbol	Value	Unit
T_0	343.2036	K
p_0	101325	Pa
ρ_0	1.2043	kg/m^3
μ	1.8140e-05	Pa·s
μ_b	0	Pa·s
C_p	1005.4	J/(kgK)
k	0.0258	W/(mK)

the Navier-Stokes equations. These equations are given in time harmonic form $+e^{j\omega t}$ represented by the convention $j\omega$, which solve for the acoustic pressure p, the variation of velocity field components $\mathbf{u}$, and the acoustic temperature variation T.

$$j\omega\rho_0\mathbf{u}=-\nabla p+\nabla\cdot\left(\mu\left[\nabla\mathbf{u}+(\nabla\mathbf{u})^T\right]-\left[\frac{2}{3}\mu-\mu_b\right][\nabla\cdot\mathbf{u}]I\right), \tag{1}$$

the equation of mass conservation,

$$j\omega\rho+\rho_0\nabla\mathbf{u}=0, \tag{2}$$

and the energy equation in the frequency domain,

$$j\omega\rho_0C_pT=\nabla\cdot(k\nabla T)+j\omega pT_0\alpha_0, \tag{3}$$

where ρ_0, μ, μ_b, I, C_p, k, and α_0 are the fluid equilibrium density, dynamic viscosity, bulk viscosity, unit tensor, heat capacity at constant pressure, thermal conductivity, and isobaric coefficient of thermal expansion, respectively. The dynamic viscosity, μ_b, is neglected and set to zero [15]. ω is the angular frequency.

The three preceding relationships are finally closed with a statement of the ideal gas law:

$$\frac{\rho}{\rho_0}=\frac{p}{p_0}-\frac{T}{T_0}, \tag{4}$$

where ρ, T_0, and p_0 are the fluid density, equilibrium temperature, and pressure, respectively.

At the fluid/solid interface, a no-slip isothermal condition is applied: $\mathbf{u}=0$ and $T=0$. The fluid parameters assumed in the study are listed in Table 1.

2.2. Finite Element Modelling. Within COMSOL, the equation systems were discretised using second order Lagrangian elements with quadratic shape function interpolation for the three velocity and temperature nodal variables and linear interpolation for the pressure variable [16]. The system was excited using an inlet manifold with a unit plane wave pressure excitation p_i and the depth of the manifold was 3.5 mm; the initial section is modeled using a lossless Helmholtz model with a transition to a full viscothermal model at 2 mm. And a hard backing wall was placed at the end of the series of cells.

From the average velocity reported at the inlet $\bar{u}$, a system impedance can be estimated:

$$Z=\frac{p_i}{\bar{u}}, \tag{5}$$

from which the absorptivity can be reported using

$$\alpha=1-\left|\frac{Z-\rho_0c}{Z+\rho_0c}\right|^2, \tag{6}$$

where c is the sonic speed:

$$c=\sqrt{\frac{\gamma P_0}{\rho_0}}, \tag{7}$$

and the ratio of specific heats γ is set at 1.41.

The viscothermal model requires special attention to meshing near the boundaries. Kirchoff [17] and Rayleigh [18] provided solutions for sound propagation through infinitely long narrow tubes and determined frequency-dependent boundary layer thicknesses based on the following:

$$\begin{aligned}\delta_{visc}&=\sqrt{\frac{2\mu}{\omega\rho_0}}\\ \delta_{therm}&=\sqrt{\frac{2k}{\omega\rho_0C_P}}\end{aligned} \tag{8}$$

In air, the Prandtl number is the ratio of these penetration depths $P_r=\delta_{\text{visc}}^2/\delta_{\text{therm}}^2$ and is ~0.7. [19] which enables the viscous boundary layer to be used as a meshing control parameter at the boundaries. For the largest space coiling system, this was set using automatic boundary layer settings under COMSOL, and absorptivity results were compared to user-specified boundary layer thicknesses at every 500 Hz step. It should be noted that (expected) surface roughness will increase the acoustic boundary layer thicknesses [20] and thus have an effect on the absorptivity, but this increase was not modelled in this paper as no definitive roughness measurements were available. In general, a five element per wavelength with the parameterised boundary layer meshing is the default setting used by COMSOL. However, in the case of the largest space coiling system, this was reduced by increasing the maximum element size parameter (2.1 mm) for viable run times. A number of convergence studies showed the reported absorptivity to be relatively insensitive to further refinement. Depending on the system being considered, half or quarter section symmetries were also taken advantage of to reduce model size. For the other models, a quarter section was used. The maximum element size was kept at five elements per wavelength, and boundary layer thicknesses were changed for every 500 Hz increment.

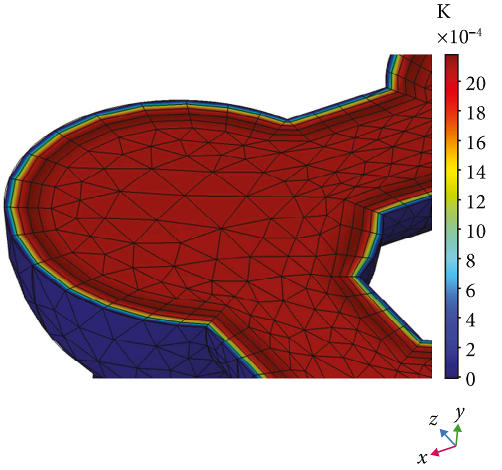

Figure 6: Temperature variation (K) unit cell at $f = 500$ Hz.

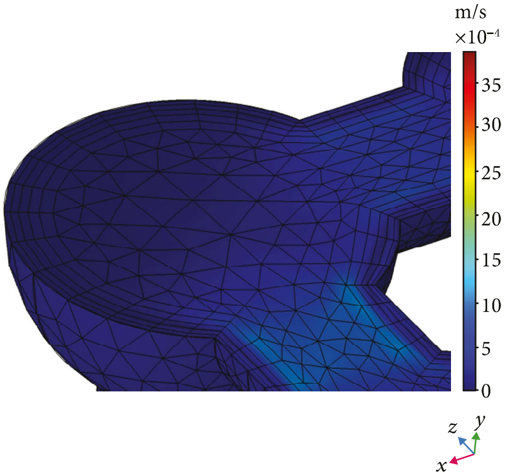

Figure 7: Axial component of velocity (m/s) unit cell, at $f = 500$ Hz.

In addition, Padé-based frequency sweeps were availed of to deliver a resolution of 50 Hz for the mixed length space coiling and 10 Hz for the other models with run times of 24 hours using a modest workstation (Xeon CPU 14 Core, 2.6 GHz, and 64 Gb RAM).

The mesh structure for some sample temperature and velocity plots at 500 Hz are presented in Figures 6 and 7.

3. Experimental Testing

The primary lab-based acoustic validation of the material performance is the measurement of the complex surface acoustic impedance leading to an absorptivity α. This can also be compared with the numerical predictions using the methods described above.

The measurements used here all followed the ISO 10534-2:2001 which describes the test rig and procedures for estimating the complex acoustic impedance of a material under normal incidence using the two-microphone or transfer function method. This leads to an estimate of the reflection coefficient R at the target surface which then yields the absorptivity coefficient α from

Figure 8: Impedance tube rig.

$$\alpha = 1 - |R|^2, \tag{9}$$

which is completely analogous to equation 6. Values of the α absorption coefficient vary with frequency and range between 0 and 1, with 1 representing complete absorption.

In these tests, the sample is placed in an impedance tube and is backed by a hard, reflective termination. A custom rig, shown in Figure 8, with a 40 mm internal diameter was used for these tests with an upper frequency limit of 4000 Hz. The lower limit is determined by the speaker and is in the region of 300 Hz. On the left hand side of Figure 8, we can see the BMS 4591 speaker which is driven by the output signal of a National Instruments DAQ which has been amplified by a power amplifier. The speaker bolts on to the end of the tube to provide a tight seal with little leakage of sound. The square section on the right of Figure 8 is the sample holder which opens to hold cylindrical samples of 40 mm diameter up to 50 mm deep. In the experimental rig, the hard termination is provided by a 20 mm thick piece of aluminium which can be bolted on the end of the tube.

GRAS 40PL array microphones were chosen to instrument the rig as they have a frequency response (±1 dB) in the region of 50 Hz–5 kHz and upper limit of the dynamic range of 142 dB re 20 μPa allowing for testing up to high pressure amplitudes. The microphones are connected to the National Instruments DAQ, and the signals were recorded using a MATLAB interface. The microphones were calibrated using the switching methods described in ISO 10534-2:2001.

During the test procedure, band-limited white noise at 90 dB was presented through the speaker and the sound pressures were measured by the two microphones. In this work, the resulting spectral resolution of the tests was 2 Hz with 1000 averages used for the estimation of the frequency response functions required to generate R and Z. All measurements were repeated three times with complete dismounting of the sample between measurements to insure repeatability of the test procedure.

The reflection and absorption coefficients are also affected by factors such as porosity and surface finish of the material. If the material is compressible, energy can also be lost to internal friction in the material as it is loaded and unloaded by the incident pressure wave. In addition, material thermal conductivity may account for further losses. These additional losses will be influenced by both the print quality and material used in the manufacture.

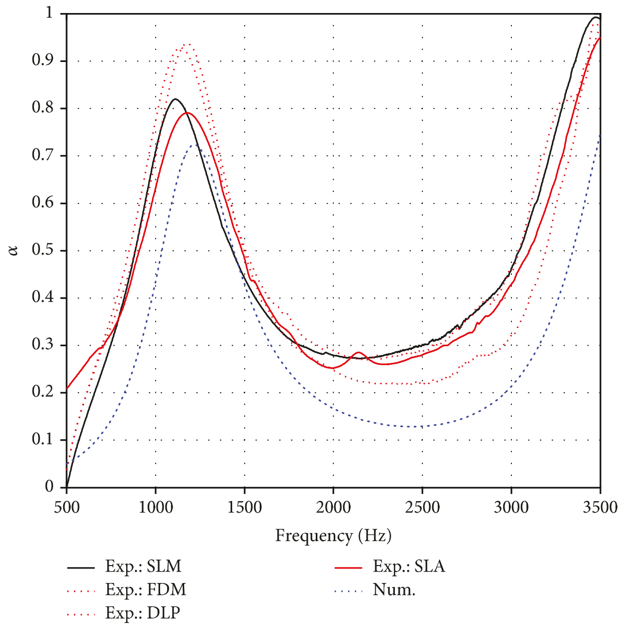

Figure 9: Absorption coefficient for four different prints of the 10-layer-deep DENORMS cell.

4. Results

Figures 9–13 report the experimental and numerical results for the cases considered. The results for the baseline ten-layer-deep design are shown in Figure 9. From all four prints, there is a double peak in the absorptivity in the regions of 1150 Hz and 3500 Hz. Experimentally, the results for the cobalt-chrome SLM sample produced using the 3D Systems machine is considered the best standard of geometric accuracy and surface finish, and this is shown as a black line in the figure. The three low-cost polymer-based experimental results are shown in red on the plot. The full viscothermal numerical model is plotted in blue. The numerical model underpredicts the absorption across the full frequency range, a fact most likely related to the lack of any surface roughness considerations in the numerical approach. The same colour conventions are used for subsequent plots.

There is good agreement between the SLM sample and the SLA sample produced on the Form 2 for the location and amplitude of the first peak. The FDM and DLP prints, manufactured on the Ultimaker and Photon machines, produce peaks in the absorption at roughly the same frequency but at high amplitudes. The increase in absorptivity can likely be attributed to the remaining spurs and low quality surface finish of the sample introducing additional losses within the channels. For the DLP technology, the increase in absorption may be attributed to the increased surface roughness due to the voxel effects which prevent as smooth a finish as the SLA and SLM technologies. The numerical model underpredicts losses as it assumes a completely smooth surface. An allowance for surface roughness by adjustment, for example, of the viscosity to model the thicker boundary layers would move these plots closer particularly to the SLM and SLA data.

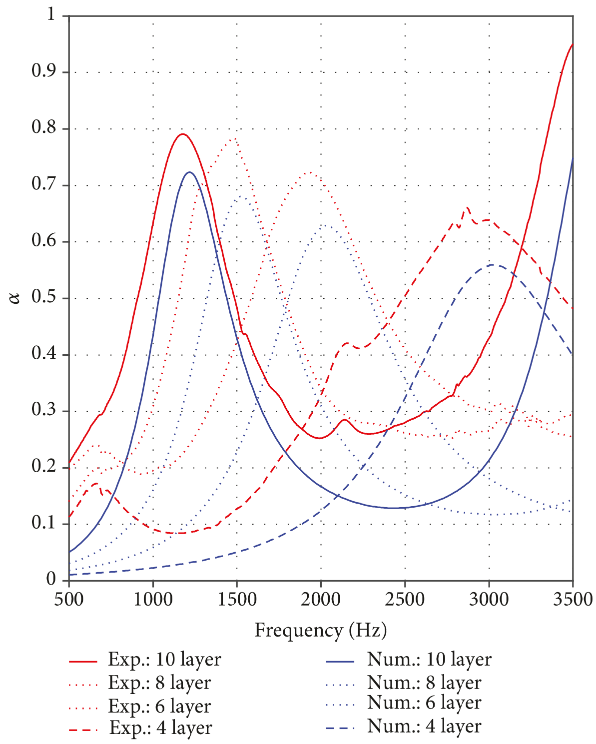

Figure 10: Absorption coefficient for 4, 6, 8, and 10 layers deep of the DENORMS cell printed on the SLA Form 2 (red: experimental results; blue: numerical results).

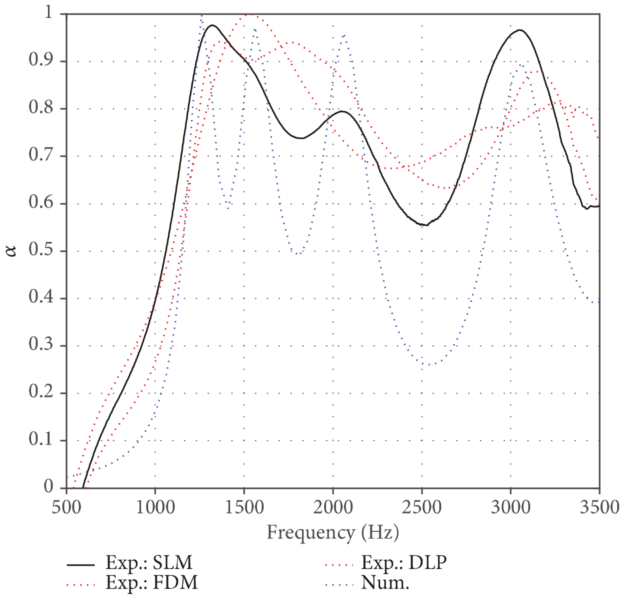

Figure 11: Absorption coefficient for combined 4-, 6-, 8-, and 10-layer depths of the DENORMS cell.

It appears from these results that any errors associated with the manual positioning of the SLA polymer disks are of less importance than the quality of the interior geometry, and from this, we can conclude that the Form 2 may be a viable, low cost system suitable for producing a sample for comparison to numerical models. The divergence

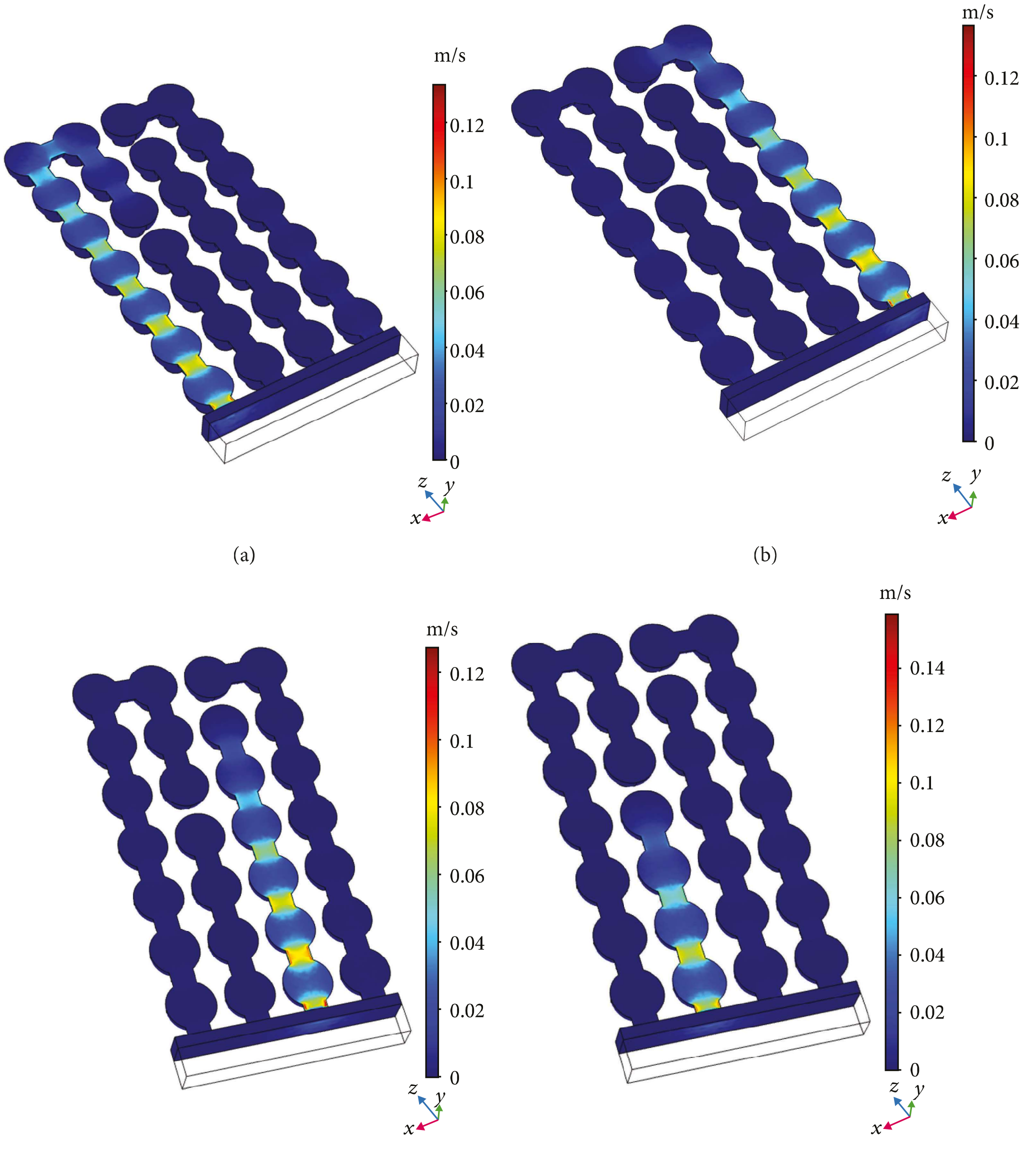

(a)

(b)

(c)

(d)

Figure 12: Axial component of velocity (m/s) within the lattice: (a) $f = 1250$ Hz; (b) $f = 1550$ Hz; (c) $f = 2050$ Hz; (d) $f = 3050$ Hz.

of the Ultimaker samples from the 3D systems sample is likely too great to allow it to be used for validation purposes. As the DLP technology improves through increased pixel count and variable exposure times, the voxel effect will reduce and it may therefore become a lower cost alternative to the SLA and SLM print technologies.

Due to the necessity to limit manufacture to single and dual layer disks on the Form 2, it was also possible to test other combinations of disks to produce different numbers of layers. Figure 10 reports the experimental and numerical results for four, six, eight, and ten layers deep. A same trend can be seen in the location and magnitude of the peaks. As the number of layers decreases, the location of both peaks shift to higher frequencies and the magnitude of the absorptivity drops with the numerical model under predicting absorbency and shifting slightly higher in frequency. This result provides the inspiration for the mixed length design as a combination of lengths is likely to provide a broadband absorption as these separate resonant peaks merge.

Figure 11 reports the experimental and numerical results for the 10-8-6-4 mixed length samples. The samples were produced using SLM, DLP, and FDM technologies. An SLA sample could not be produced using the Form 2 as the resin viscosity was too high for the entrained resin to be removed from within the sample. The numerical model produces a good estimation of the combination behaviour of the design; however, it assumes fully vacated cross-channels and smooth surfaces neither of which existed in the manufactured samples. Distinct peaks are thus reported and are confirmed by the peak frequency snapshots of the acoustic velocity at 1250 Hz, 1550 Hz, 2050 Hz, and 3050 Hz as shown in Figure 12. The behaviour of the FDM-produced sample is different to that predicted by the numerical model, and there is a more broadband behaviour without clear resonant peaks.

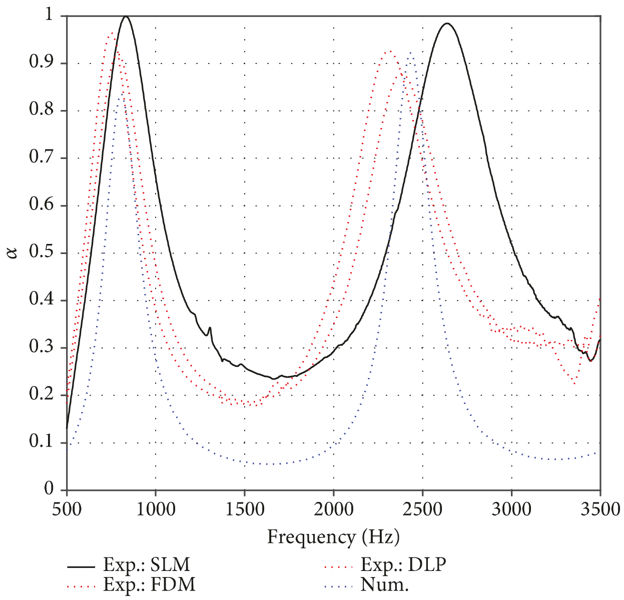

Figure 13: Absorption coefficient for a 10-layer depth of the labyrinth DENORMS cell (equivalent to a 20-layer depth).

The DLP and SLM samples have a close match to the numerical predictions, and the locations of multiple resonant peaks are visible within these experimental results. This design has achieved relatively high broadband absorption with a low thickness of 35 mm.

The final results shown are the experimental and numerical results for the labyrinthine concept. In this case, the "S"-shaped path of the resonators doubles the number of cavities within a given depth. The cross-linking side branches were required in order to allow the resin to be removed from the DLP sample and aid the removal of metal powder from the SLM sample. In this instance, there was a partial failure of the SLM sample which led to a slight eccentricity in the sample necessitating some post-processing to insure a clean fit inside the sample holder. Due to time and financial constraints, a second sample could not be produced.

The SLM, FDM, and DLP samples have similar locations for the frequency of the first peak in absorption, but the SLM sample deviates for the frequency of the second peak. This deviation may be the result of the original eccentricity in the print. In this case, the numerical model again captures well the location and amplitude of the peaks in the absorption coefficient.

5. Conclusion

This work has reported on the design of a periodic acoustic metamaterial that is suitable for use as a benchmark validation case. The design was realised through four different additive manufacturing technologies which ranged from low cost desktop printers to state-of-the-art machines. While all print technologies provide a reasonable match to the numerical results, there are deviations which are clearly due to geometric tolerances and surface roughness which become more pronounced in geometries where cross-channels may become difficult to clear after manufacture. Three polymer-based print technologies were investigated, namely, FDM, DLP, and SLA. Experimentally, the SLA sample was closest to the high quality SLM sample produced in cobalt-chrome. This demonstrates the potential of the SLA technology to accurately produce complex interior geometries with a smooth surface finish. Both the SLA and SLM samples were in very close agreement with the numerical models in terms of the locations of the peaks in absorption. The SLA and SLM samples still had a generally higher absorption value than was predicted numerically possibly due to their surface finish.

These results indicated that the manufacture of a benchmark validation material may be possible at relatively low cost using the current polymer-based SLA technologies. However, there is considerable difficulty in using this technology with designs resulting in large quantities of entrained resin as these become difficult to remove.

The use of a FDM Ultimaker printer highlighted the potential for low quality prints to significantly influence the achieved performance; this is considered an obstacle for the production of validation data using this type of printer technology should designs at the fineness of scale required to induce significant flow resistivity be attempted. The DLP printer was capable of producing geometrically accurate samples, but there was evidence to suggest that the increased roughness over the SLA samples due to voxel effects led to increased levels of absorption. The DLP technology is a promising approach for the production of very low cost validation materials in polymers.

Clear trends as a function of depth were identified in the experimental and numerical results. The results were the inspiration for two modifications to the design to incorporate both space coiling and labyrinthine elements. These modifications successfully demonstrated increased broadband behaviour and the ability to shift the resonant behaviour to a lower frequency for the same sample thickness. The DENORMS design is therefore highly suitable for use as a benchmark and validation tool in the development of acoustic metamaterials.

The current scale of the design is at the limit of the low cost additive manufacturing technologies, but finer scales can readily be achieved in the state-of-the-art machines. The viscosity of the DLP and SLA polymer resins poses a significant challenge to producing finer scale parts using these technologies. The lower viscosity of the DLP resin allows for easier extraction of the entrained material in samples at the scale produced here.

Data Availability

The CAD design and absorption coefficient data used to support the findings of this study are included within the article.

Conflicts of Interest

There are no conflicts of interest with this research or the data presented herein.

Acknowledgments

This work was partially funded through the AERIALIST project no: 723367 EU H2020-EU.3.4. Societal Challenges Smart, Green And Integrated Transport. The authors wish to acknowledge the COST Action DENORMS (CA 15125) and in particular Dr. Tomasz G. Zielinski, Department of Intelligent Technologies, Institute of Fundamental Technological Research of the Polish Academy of Sciences, who proposed the design of the unit DENORMS cell. The authors wish to acknowledge the AMBER Additive Research Lab in facilitating the manufacturing of our metal test specimens and the AR Lab staff on providing training and guidance on the manufacturing process. The AR Lab has been enabled by a €3.3M award from the Science Foundation Ireland as part of their research infrastructure program and an additional €1M investment from the European Research Council.

References

[1] K. C. Opiela, M. Rak, and T. G. Zielinski, "A concept demonstrator of adaptive sound absorber/insulator involving microstructure-based modelling and 3Dprinting," in *Proceedings of ISMA2018 Including USD2018*, Leuven, Belgium, September 2018.

[2] L. Flanagan, H. Rice, D. Trimble, L. Dowling, and J. Kennedy, "The use of a benchmark periodic metamaterial to inform numerical modelling and additive manufacturing approaches," in *Proceedings of ISMA2018 Including USD2018*, Leuven, Belgium, September 2018.

[3] S. H. Masood, "Intelligent rapid prototyping with fused deposition modelling," *Rapid Prototyping Journal*, vol. 2, no. 1, pp. 24–33, 1996.

[4] M. N. Cooke, J. P. Fisher, D. Dean, C. Rimnac, and A. G. Mikos, "Use of stereolithography to manufacture critical-sized 3d biodegradable scaffolds for bone ingrowth," *Journal of Biomedical Materials Research Part B: Applied Biomaterials*, vol. 64, no. 2, pp. 65–69, 2003.

[5] I. Cooperstein, M. Layani, and S. Magdassi, "3d printing of porous structures by UV-curable O/W emulsion for fabrication of conductive objects," *Journal of Materials Chemistry C*, vol. 3, no. 9, pp. 2040–2044, 2015.

[6] S.-H. Ahn, M. Montero, D. Odell, S. Roundy, and P. K. Wright, "Anisotropic material properties of fused deposition modeling abs," *Rapid Prototyping Journal*, vol. 8, no. 4, pp. 248–257, 2002.

[7] M. Agarwala, D. Bourell, J. Beaman, H. Marcus, and J. Barlow, "Direct selective laser sintering of metals," *Rapid Prototyping Journal*, vol. 1, no. 1, pp. 26–36, 1995.

[8] M. Yang, S. Chen, C. Fu, and P. Sheng, "Optimal sound-absorbing structures," *Materials Horizons*, vol. 4, no. 4, pp. 673–680, 2017.

[9] Y. Zhu, X. Fan, B. Liang, J. Cheng, and Y. Jing, "Ultrathin acoustic metasurface-based Schroeder diffuser," *Physical Review X*, vol. 7, no. 2, article 021034, 2017.

[10] R. Ghaffarivardavagh, J. Nikolajczyk, R. Glynn Holt, S. Anderson, and X. Zhang, "Horn-like space-coiling metamaterials toward simultaneous phase and amplitude modulation," *Nature Communications*, vol. 9, no. 1, article 1349, 2018.

[11] C. Chen, Z. Du, G. Hu, and J. Yang, "A low-frequency sound absorbing material with subwavelength thickness," *Applied Physics Letters*, vol. 110, no. 22, article 221903, 2017.

[12] Y. Xie, B.-I. Popa, L. Zigoneanu, and S. A. Cummer, "Measurement of a broadband negative index with space-coiling acoustic metamaterials," *Physical Review Letters*, vol. 110, no. 17, article 175501, 2013.

[13] H. Tijdeman, "On the propagation of sound waves in cylindrical tubes," *Journal of Sound and Vibration*, vol. 39, no. 1, pp. 1–33, 1975.

[14] J.-L. Auriault, C. Boutin, and C. Geindreau, *Homogenization of Coupled Phenomena in Heterogenous Media*, vol. 149, John Wiley & Sons, 2010.

[15] J. Allard and N. Atalla, *Propagation of Sound in Porous Media: Modelling Sound Absorbing Materials 2e*, John Wiley & Sons, 2009.

[16] COMSOL Multiphysics, *Acoustics Module User Guide Version 4.2. Users Manual*, COMSOL AB, Stockholm, 2011.

[17] G. Kirchhoff, "Ueber den Einfluss der Wärmeleitung in einem Gase auf die Schallbewegung," *Annalen der Physik und Chemie*, vol. 210, no. 6, pp. 177–193, 1868.

[18] John William Strutt Baron Rayleigh, *Theory of Sound*, Macmillan and co., London, 1877.

[19] G. P. Ward, R. K. Lovelock, A. R. J. Murray, A. P. Hibbins, J. R. Sambles, and J. D. Smith, "Boundary-layer effects on acoustic transmission through narrow slit cavities," *Physical Review Letters*, vol. 115, no. 4, article 044302, 2015.

[20] S. Y. Song, X. H. Yang, F. X. Xin, S. W. Ren, and T. J. Lu, "Modeling of roughness effects on acoustic properties of micro-slits," *Journal of Physics D: Applied Physics*, vol. 50, no. 23, article 235303, 2017.


The Scientific World Journal

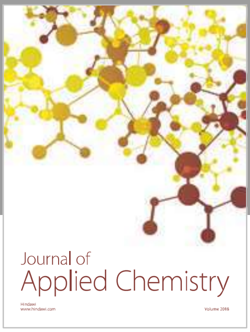
Journal of
Applied Chemistry

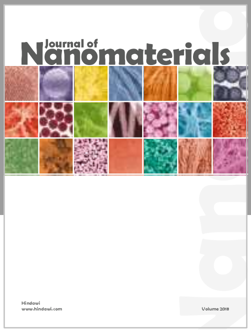
Journal of
Nanomaterials


Scientifica


International Journal of
Polymer Science

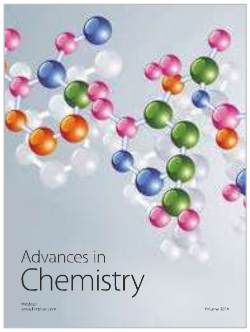
Advances in
Chemistry

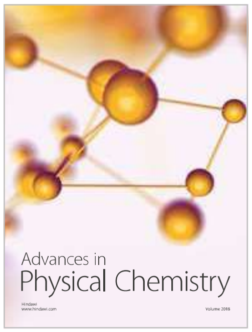
Advances in
Physical Chemistry

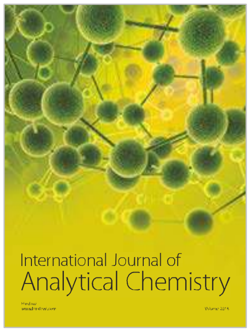
International Journal of
Analytical Chemistry

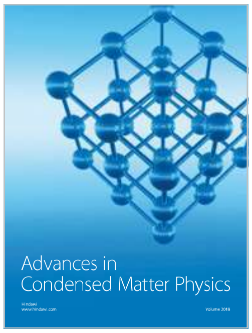
Advances in
Condensed Matter Physics


Journal of
Chemistry


International Journal of
Biomaterials

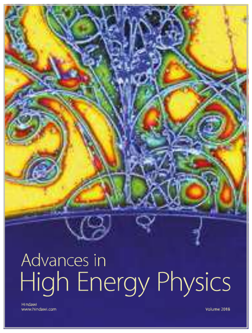
Advances in
High Energy Physics


Journal of
Engineering

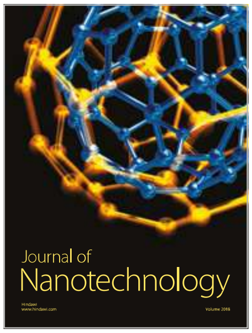
Journal of
Nanotechnology

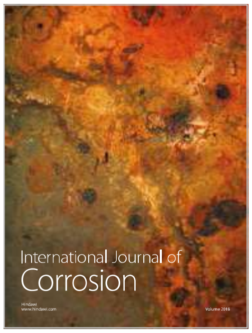
International Journal of
Corrosion


Journal of
Materials


BioMed
Research International

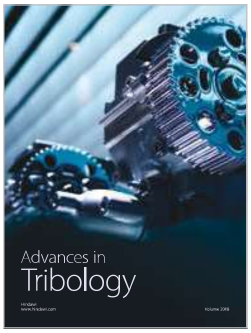
Advances in
Tribology

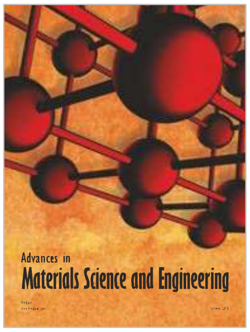
Advances in
Materials Science and Engineering

Journal of Sound and Vibration 472 (2020) 115167

Contents lists available at ScienceDirect

Journal of Sound and Vibration

journal homepage: www.elsevier.com/locate/jsvi

Special Issue at the occasion of the ISMA2018 International Noise and Vibration Conference

Design of a Kelvin cell acoustic metamaterial

H.J. Rice [a], J. Kennedy [a,*], P. Göransson [b], L. Dowling [a], D. Trimble [a]

[a] Trinity College Dublin, Department of Mechanical Engineering, Ireland
[b] KTH Royal Institute of Technology, Aeronautical & Vehicle Engineering, 100 44, Stockholm, Sweden

ARTICLE INFO

Article history:
Received 9 March 2019
Revised 29 November 2019
Accepted 22 December 2019
Available online 20 January 2020
Handling Editor: I. Trendafilova

Keywords:
Acoustic metamaterial
Noise control
Additive manufacture
3D printing

ABSTRACT

Advancements in 3D print technology now allow the printing of structured acoustic absorptive materials at appropriate microscopic scales and sample sizes. Optimisation of parameter sets associated with a Kelvin Cell structure have the potential to develop various metabehaviours in the associated acoustic responses. The repeatability of the fundamental cell unit also provide a route for the development of viable macro models to simulate built up structures based on detailed models of the individual cell units. This paper describes a process to model, print and test such a sample. Manufacturing restraints will initially guide the optimised design and introduce response uncertainties associated with surface finishes and critical geometric dimensions. A “micro to macro” model is developed using a full visco thermal acoustic model of a single cell to develop a frequency dependent cell transfer matrix. The transfer matrices for the repeated cells may then be combined until sufficient material depth is achieved and efficiently generate an absorptivity for the material layer. Two prints using different processes (digital light processing (DLP) and selective laser melting (SLM)) of nominally the same kelvin cell structure. For the metal print the model predicts the absorptivity well once an allowance is made for the surface roughness. The DLP has a smoother finish with a lower geometric fidelity; however the DLP sample is still well modelled by the process.

1. Introduction

The capabilities of additive manufacturing technologies now allowed previously unmanufacturable structures to be produced in numerous materials and at small scales. While terminology and definitions around metamaterials are evolving the authors are using following definition from the EU H2020 funded AERIALIST project: A metamaterial is a human-made compound, a structured material engineered to achieve a response not available in nature and for which the model of an equivalent continuum can be defined. In this context a metabehaviour is the response which characterises the material as a metamaterial. Efficient, low computational costs design tools are required to enable the development of targeted noise control solutions using acoustic metamaterials. One potential route for the design of acoustic metamaterials are absorptive materials with repeated inner structures rather than foams or fibrous structures where the inner geometries are randomised by the solidification processes. Whereas homogenisation is the route to developing macroscopic acoustic property prediction for the latter, the former can be modelled by building up a macro model from a detailed repeatable cell analysis. The design of periodic structures for benchmark materials useful for validation of numerical codes is also a topic of interest at present [1,2]. Recent papers on optimal sound absorber design (and experimental testing) using these strategies include [3], ultra thin metasurfaces [4] and space coiling metamaterials [5–7]. These papers demonstrate the potential for additive manufacturing to realise complex metamate-

---

[*] Corresponding author.
E-mail address: jkenned5@tcd.ie (J. Kennedy).

https://doi.org/10.1016/j.jsv.2019.115167

rial designs however the influence of the manufacturing tolerances on the material performance still needs to be assessed [2]. The Kelvin cell structure reported upon in this paper requires state of the art additive manufacturing capabilities to realise the micro-structure and the details of the lattice are such that the computational costs of producing and slicing the files in preparation for printing are at the limits of what can be achieved with commercial software. A very recent paper [8] uses the periodicity potential of printed foams to build up an efficient homogenised macroscopic acoustic model from a detailed analysis of the individual cell dynamics. The cell acoustics were captured from a combination of numerical static flow and electro static analyses which mimic bulk experimental test processes as advanced in Ref. [9]. The efficiency introduced here through individual cell modelling is an essential step to the eventual development of design processes. A similar overall approach using an individual cell modelling strategy has also been demonstrated in Ref. [10] where a full viscothermal cell model incorporating an efficient WCAWE frequency sweep [11] was reported on to inform an Low Reduced Frequency (LRF) macroscopic model [12]. In the present paper the overall modelling concept is similar except the Kevlin Cell structure is built from primary solid components. A full viscothermal cell WCAWE model is used to drive a macroscopic model based on transfer matrix approach similar to the approach reported in, for example [13], and the results are verified against experimental data where sensitivity to geometric uncertainties caused primarily by the printing approach at this scale can be assessed.

1.1. Background models

The lossy acoustics in a fine absorptive medium can be modelled by linearised viscothermal fluid mechanical models. These are governed by the equation system given for example in Nijhof et al. [14]. Assuming a Stoksian assumption the linearised equations, assuming Stokesian behaviour, can be written as

$$\rho_0(\nabla.\boldsymbol{v}) + j\omega\rho = 0 \tag{1}$$

$$j\omega\rho_0\boldsymbol{v} = -\nabla p + \mu(\nabla.\nabla\boldsymbol{v} + \frac{1}{3}\nabla\nabla.\boldsymbol{v}) \tag{2}$$

$$j\omega\rho_0 C_p T = \kappa\Delta T + j\omega p \tag{3}$$

$$p = R(\rho_0 T + \rho T_0) \tag{4}$$

where $\boldsymbol{v}, p, \rho, T, \mu, R, \rho_0, T_0, \kappa$ and C_p are the acoustic harmonic velocity, pressure, density, temperature, dynamic viscosity, gas constant, static density, static temperature, thermal conductivity, and specific heat at constant pressure. A finite element model implementing the above can be constructed using a mixed weak formulation following [14] and Zienkiewicz et al. [15] which can present the system in the matrix form

$$[\mathbf{K} + j\omega\mathbf{M}]\mathbf{a} = \mathbf{F} \tag{5}$$

As the density variable may be eliminated using the equation of state, Equation (4), each node will have five degrees of freedom including three velocity components, temperature and pressure stored in **a**. The forcing vector **F** then models boundary pressure loads, material injection and heat flux. **K** and **M** were constructed following the procedures for mixed formulations outlined in Ref. [15]. In order to develop a stable mixed model it is critical to use shape functions of one order less for the pressure and its related weighting functions. In this work quadratic 10 noded tetrahedral elements were used with linear functions for pressure and quadratic functions for the velocity and temperature. The redundant mid-side nodal pressure degrees of freedom were decoupled from the formulation and 2nd order volumetric and spatial integrations were used.

The general equation system in Section 1.1 has also shown itself to be amenable over the frequency ranges of interest to efficient Padé type frequency sweeps such as the WCAWE method proposed by Slone et al. [11]. In the cell system modelled in this work, it the equation system required full solution only at a single centre frequency. The rest of the frequency range of interest was generated by WCAWE extrapolation based on derivatives up to order 12. The cell model with adequate mesh density to model the boundary layers which generated of the order of 12,000 nodes was thus easily solvable on a standard laptop computer.

1.2. From micro to macro:visco-thermal model to transfer matrix

Despite the efficiencies introduced by the individual cell modelling considerations above, solution of the full system equations is extremely expensive and is effectively impractical for any optimisation studies of built up systems of multiple conjoined cells. Clearly a model reduction strategy leading to a macro model is required.

A transfer matrix approach provides a key to building up full depth absorbent models from individual modelled test data. If the cell is considered a two port network using averaged pressure $\overline{p}(\omega)$ and velocity $\overline{u}(\omega)$ as the (frequency dependent) interface data, then we can write

$$\begin{bmatrix} \overline{p}_{inlet} \\ \overline{u}_{inlet} \end{bmatrix} = \begin{bmatrix} T_{11} & T_{12} \\ T_{21} & T_{22} \end{bmatrix} \begin{bmatrix} \overline{p}_{outlet} \\ \overline{u}_{outlet} \end{bmatrix} \tag{6}$$

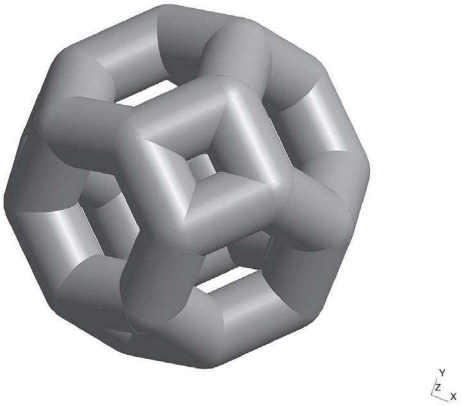

Fig. 1. The unit Kelvin Cell design defined within a cubic tessellation.

where $\mathbf{T}(\omega)$ is the cell transfer matrix. The individual elements of the matrix can be determined by for example driving the system at inlet (a plane wave forcing was used in the present case) and then imposing an open ($p_{outlet} = 0$) followed by a closed boundary condition ($u_{outlet} = 0$). The open cell simulation then delivers

$$T_{12} = p_{inlet}/u_{outlet}; T_{22} = u_{inlet}/u_{outlet}; \tag{7}$$

whereas the closed cell simulation yields

$$T_{11} = p_{inlet}/p_{outlet}; T_{21} = u_{inlet}/p_{outlet}; \tag{8}$$

The overall multicell system response matrix $\mathbf{T}_{sys}(\omega)$ for n cells can then be quickly calculated from

$$\mathbf{T_{sys}} = \mathbf{T^n} \tag{9}$$

from which the surface impedance for a system with a closed backing can be determined using

$$Z = \frac{T_{sys_{11}}}{\phi T_{sys_{21}}} \tag{10}$$

where ϕ is the surface porosity. This can be estimated directly from the geometric model ($\phi = 0.571$ for the present case). Alternatively the porosity could be set to one and transfer matrix prefixed to the system calculation to model the inlet manifold in detail. Other backing conditions can be also readily calculated using other combinations of the system transfer matrix entities. Finally the full depth absorptivity α can be assessed using

$$R = \frac{Z - \rho_0 c}{Z + \rho_0 c} \tag{11}$$

$$\alpha = 1 - |R|^2 \tag{12}$$

where c is the external sonic speed.

2. Visco-thermal Kelvin cell model

In this study an absorptive layer 20 cells deep was considered with the cell form shown in Fig. 1.

The nominal lengths of the individual struts shown are 375 μm with diameters 400 μm. A one eight model of the complementary acoustic cavity was geometrically modelled and meshed using gmsh 4.1.5 [16]. This had an open or closed outlet with a forced pressure inlet and a symmetry condition applied to the side walls. No slip and zero acoustic temperature conditions were applied to the curved wetted surface areas. Sample results for the temperature and axial velocity (open end condition) are shown in Fig. 2(a) and (b) for the system running at 1000 Hz.

Note that in addition to the high number of degrees of freedom required per node (5) there is also a further requirement to locally refine the meshes within the boundary layers particularly as the frequencies rise. The indicative meshes shown here (12,028 nodes) gave converged results. A further feature to note on the plots is the small aperture in the cell which generate significant local activity. In some of the manufactured models this tends to close. Simulations with it closed can be conveniently performed by simply placing a wall boundary conditions at that section of the inlet produced minor effects on averaged inlet and outlet data. For transfer matrix calculations we elected to close the apertures.

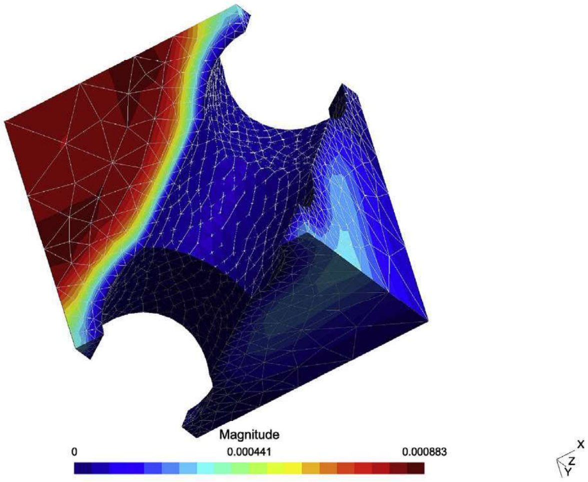

(a) Acoustic Temperature

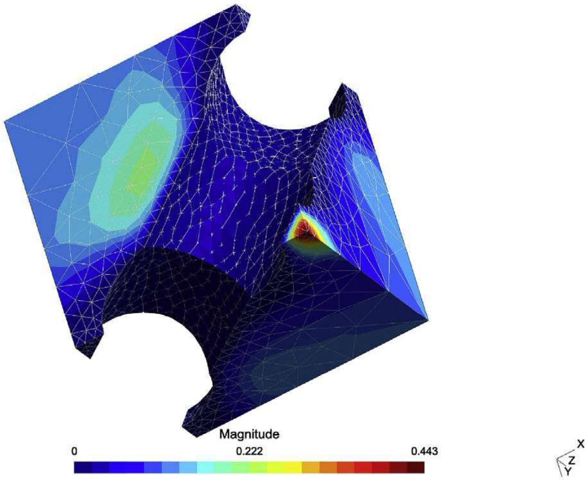

(b) Axial Velocity

Fig. 2. Example cell simulations - Open exit boundary conditions'.

3. Multi-cell macro model

The next stage is then to model the full 20 cell structure using the efficient Helmholtz model using the transfer matrix approach described above. Although nominally set at 400 μm the cell models were rerun with appropriate strut diameters for the various materials. Space averaged pressure and normal velocity data were gathered with estimate of the porosity at the inlet. Once the cell transfer matrix was estimated the system matrix was formed by raising it to a power of 40 which could then modelled a hard-backed structure 30 mm deep. The entire laptop computation takes approximately 30 s. Simulation results are presented against experimental data in the two cases under study at the end of section 4.

4. Experimental measurements

The relevant ISO standard for the measurement of the acoustical properties of the material is ISO 10534–2:2001. This standard describes the test rig and procedures for estimating the complex acoustic impedance of a material under normal incidence using the “two-microphone” or “transfer function” method. This methodology was used to calculate the reflection and absorption coefficients which are the usual measures used to quantify the performance of an acoustic material.

In order to facilitate impedance tube testing samples were manufactured using additive techniques. Due to the high resolution and precision required for the Kelvin cell material there are limited options available for additive manufacture of the samples. Selective laser melting (SLM) [17] and digital light processing (DLP) [18,19] were chosen for manufacture of the samples. The SLM samples were manufactured with the 3D Systems Prox DMP 200 and in this work was used to manufacture in cobalt chrome. The machine has the following capabilities:

- Resolution: x = 100 μm; y = 100 μm; z = 20 μm
- Material: metals - Titanium, CoCr, Aluminium, SS
- Build Volume: x = 140 mm; y = 140 mm; z = 125 mm
- Wall Thickness: 150 μm
- Surface Roughness: Up to 5 Ra μm

The DLP samples were manufactured with an Anycubic Photon. The DLP process utilises a photomonomer reacting to light in a polymerisation reaction which results in a high level of crosslinking thus generating a solid object. The DLP process uses a LCD screen with a UV lamp, the LCD screen is used to illuminate and cure an entire layer with UV light. The machine has the following capabilities:

- Resolution: x = 47 μm; y = 47 μm; z = 25–100 μm
- Material: polymer
- Build Volume: x = 115 mm; y = 65 mm; z = 155 mm

For both technologies entrained material must be removed which requires a combination of ultrasonic and compressed air cleaning. This process of cleaning limited the number of layers of Kelvin cells that could be manufactured at this scale to ten cells deep.

In normal incidence impedance tube tests the sample is backed by a hard, reflective termination. The custom rig used for this work is also shown in Fig. 3. In the experimental rig, the hard termination is provided by a 20 mm thick piece of aluminium which can be bolted on the end of the tube.

The cut-on frequency for this tube means that it is only possible to perform tests reliably up to 3800 Hz. The lower limit is determined by the speaker and is in the region of 500 Hz. On the left hand side of Fig. 3 we can see the BMS 4591 speaker which is driven by the output signal of a National Instruments DAQ which has been amplified by a power amplifier. The speaker bolts on to the end of the tube to provide a tight seal with little leakage of sound. The square section on the right of Fig. 3 is the sample holder which opens to hold cylindrical samples of 40 mm diameter and up to 50 mm thick.

GRAS 40 PH array microphones were chosen to instrument the rig as they have a frequency response of ±1 dB within 50–5000 Hz and upper limit of the dynamic range of 135 dB re 20 μPa allowing for testing up to high pressure amplitudes. The microphones are connected to the National Instruments DAQ and the signals are recorded in Matlab. The microphones are calibrated using the switching methods described in the standards to achieve a calibration transfer function which corrects for any differences in the behaviour of the microphones.

The impedance tube requires samples of a 40 mm diameter but due to the periodic structure of the Kelvin cell material a disk of this material will include many partial cells at the edges. These partial cells are impossible to manufacture due to unsupported overhangs in the print. To avoid these overhangs the entire sample was printed within a hard wall supporting ring. This hard wall ring was designed to have an inner diameter of 40 mm so as to allow an exact flush fit with the walls of the impedance tube. Custom sample holders were designed to enable this flush fit with the walls of the tube.

Fig. 4(a) shows the STL file of the sample. This file consists of a mesh with 8,825,219 vertices with a file size of 875 MB which is approaching the limit of what can be achieved on a standard desktop PC and processed by the printer's slicing software. The unit cell design is specified in the commercial nTopology Element software and then this software is used to generate the lattice of cells within the specified sample volume. The unit cell is specified within a cubic tessellation of 1.5 mm and with strut diameters of 0.4 mm. The samples and holder are shown in Fig. 5. Each disk consists of ten layers of 1.5 mm cells for a total depth of 15 mm and for the tests two disks were stacked in the sample holder to give a total depth of twenty layers.

The produced samples were then inspected using a Leica S6E stereomicroscope under 127× magnification. Images were captured and dimensioned with a dino-eye eyepiece camera and associated software. Fig. 6 reports the locations where the three dimensions were taken from each microscopy image. Thirty two images were taken for each print process at various locations in the samples to give a total of ninety six measured values for each print process. The average dimensions are given in Table 1. The SLM process produces a dimension for the struts which is 95% of that specified within the STL file. The DLP process

Fig. 3. Impedance tube rig designed in compliance with ISO 10535-2.

(a) CAD of impedance tube sample

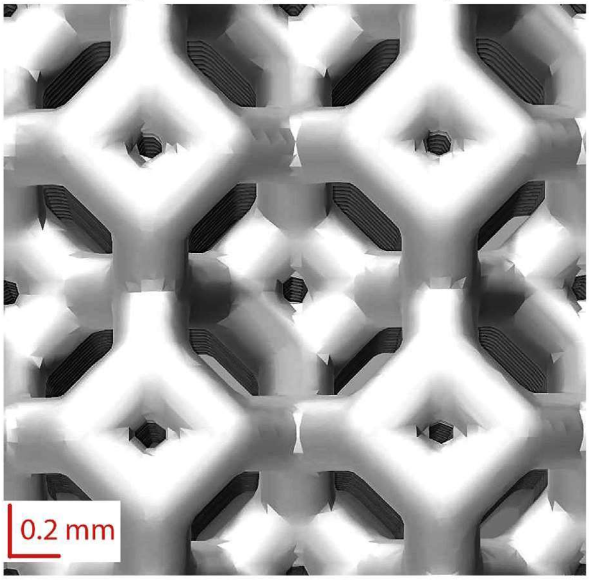

(b) View of lattice structure

Fig. 4. Computer aided design images.

produces a dimension for the struts which is 118% of that specified within the STL file. The extra width within the DLP print process may be due to lateral curing within the vat as the UV light disperses within the resin.

Fig. 7 shows the results for the SLM (a) and DLP (b) samples. As can be seen from the images there is greater variability in the strut diameters than in the original STL file and the printers are not capable of regularly producing the smallest hole in the Kelvin cell lattice. The SLM print process includes some of these small holes but the DLP print processes entirely seals this feature due to entrained resin which subsequently cures.

The surface roughness is also visible particularly in the SLM sample on account of the particle driven process. In the DLP sample the LCD screen pixel size will also generate roughness through a voxel effect. From these observations the working effective strut diameter for the numerical model was assessed to be 0.4 mm as incorporated into the models presented earlier.

To ensure repeatability of the testing and to investigate the impact of the manufacturing imperfections on the measurements each material was tested three times. During tests disks were mounted and dismounted between tests in order to be stacked in both front/back combinations. Fig. 8 reports the mean and standard deviation of the absorption coefficient, α, for both the DLP (a) and SLM (b) samples. As can be seen from Fig. 8 both print processes provided a very precise result with negligible deviations

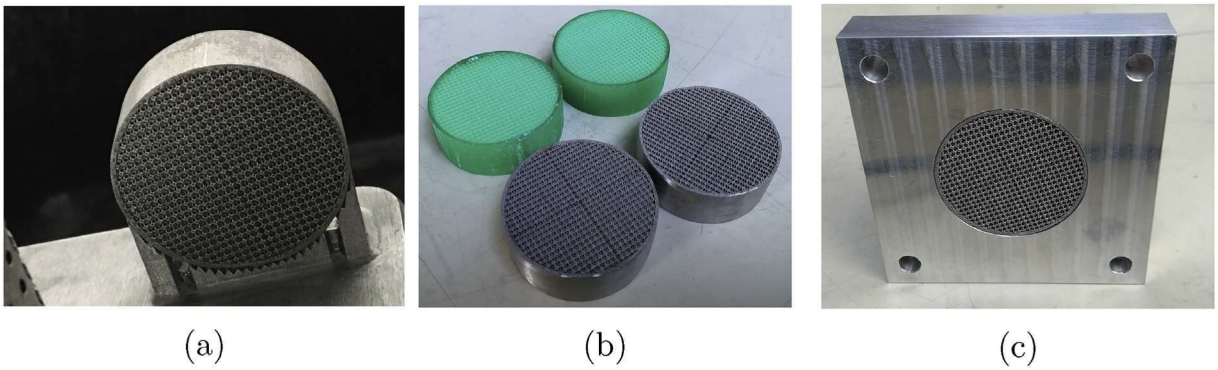

Fig. 5. (a) Sample attached to build plate manufactured with a 3D Systems Prox DMP 200 (b) SLM and DLP sample disks (c) SLM sample in holder for impedance tube testing.

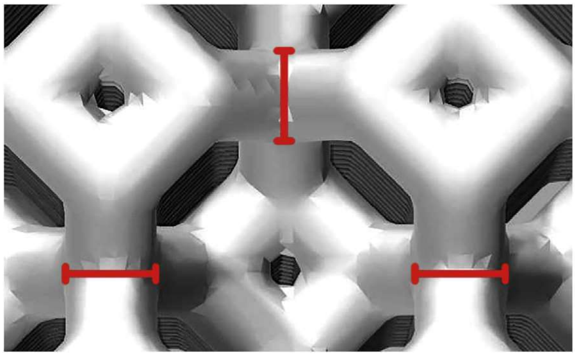

Fig. 6. Dimensioned locations in the lattice.

Table 1
Mean strut dimensions and standard error for SLM and DLP printed samples.

	Average (mm)	Standard Error (mm)	Porosity[a]
SLM	0.381	0.016	0.606
DLP	0.474	0.020	0.515

[a] Estimated from the numerical cell model.

between tests. It is likely that the partially sealed openings and the differing strut diameters are responsible for the different frequency behaviour between the two manufactured samples. The peak in the average α values of the SLM samples is below that of the DLP samples, perhaps as a result of the smoother surface finish in these samples.

A comparison of the experimental and numerical results for both samples with modelled using the geometries summarised in Table 1 are presented in Fig. 9. Although the numerical predictions underestimate the loss, they are positioned well on the frequency axis and show the expected mild sub-wavelength behaviour with a similar sensitivity to the mean geometric deviations between the two experimental samples. In both cases there is a tendency of the samples to develop struts which slightly neck. Relatively speaking this may generate greater error in the numerical model for the SLM sample which uses narrower mean strut diameters. As no account was taken of surface effects, which are clearly evident in the microscopy images in Fig. 7, tentative predictions are also included with a doubled viscosity which give very encouraging results.

5. Discussion

The scale of the Kelvin cell material design presented here clearly pushes current additive manufacturing technologies to their limit in terms of resolution and precision. The experimental acoustic testing reveals the difference in print quality and precision between a state of the art SLM machine and the low cost desktop DLP machine. However there is promising agree-

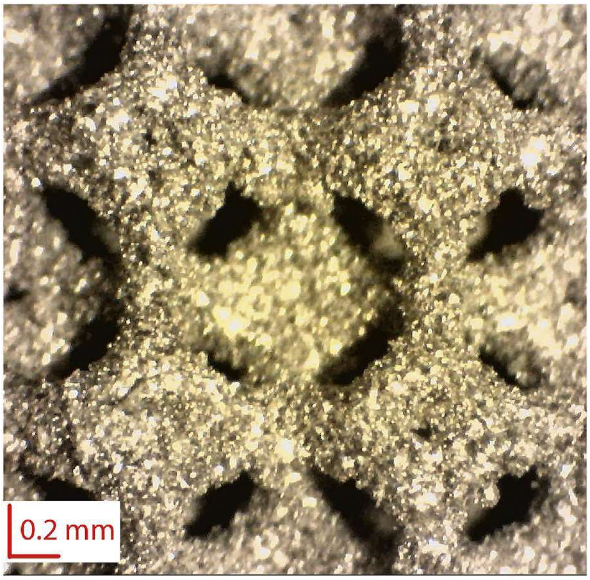

(a) Microscopy image of the SLM produced sample

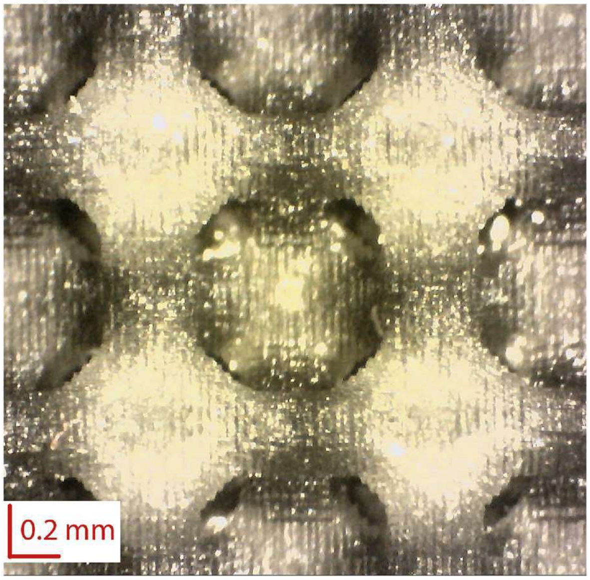

(b) Microscopy image of the DLP produced sample

Fig. 7. Test sample images.

ment between the experimental measurement and the efficient micro-macro numerical simulation procedure. Notwithstanding experimental error, clear uncertainties in the modelling process also include those associated with dimensional estimates of narrower sections and the modelling of surface finish which is the clear differentiator of loss estimates associated with the granular SLM sample over the "voxelated" DLP sample.

6. Conclusions

The proposed structures were realised using state of the art additive manufacturing technologies and when used at the scale presented here, have highlighted the acoustic sensitivity to geometric and surface finish uncertainty.

The use of efficient viscothermal models at a cell level provides a direct route via the transfer matrix approach to modelling built up cellular acoustically absorptive structures.

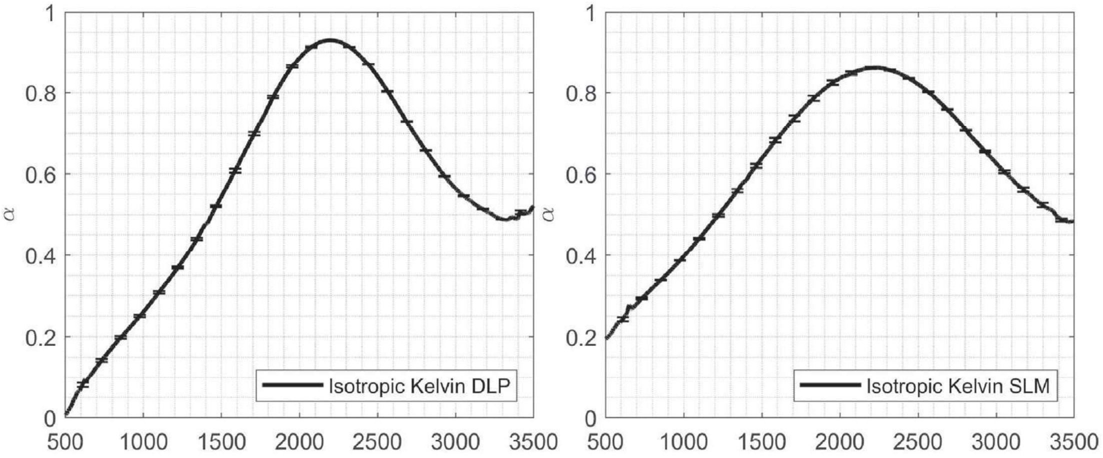

Fig. 8. Mean and Standard deviation of the absorption coefficient α (a) DLP samples (b) SLM samples.

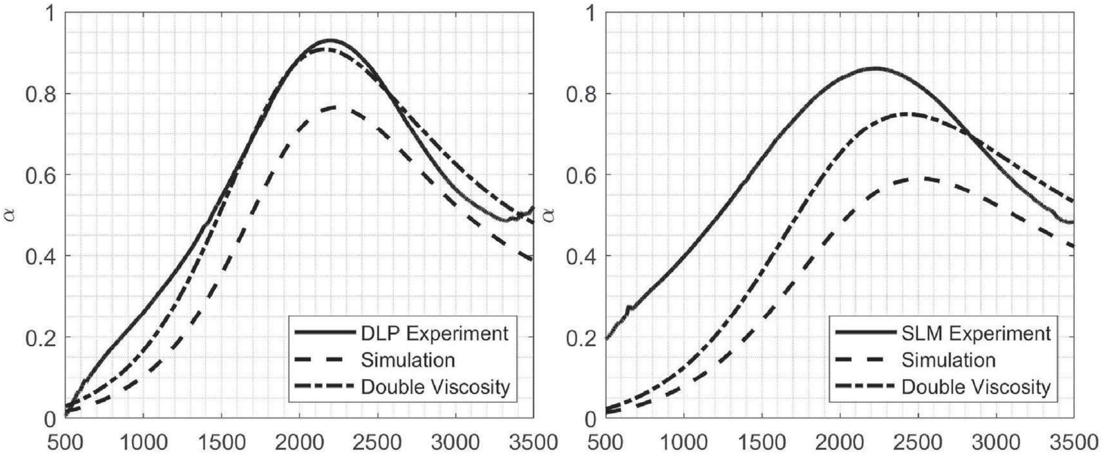

Fig. 9. Experimental vs numerical estimates for absorption coefficient.

Acknowledgements

This work was funded through the AERIALIST project no: 723367 European Union H2020-EU.3.4. SOCIETAL CHALLENGES - Smart, Green And Integrated Transport. The authors also acknowledge the support of the European Union COST Action CA15125. Designs for Noise Reducing Materials and Structures (DENORMS).

The authors would like to acknowledge the support of nTopology through their Element software platform.

In addition, the authors wish to acknowledge the AMBER Additive Research Lab in the facilitating of the manufacturing of our metal test specimens and the AR Lab staff on providing training and guidance on the manufacturing process. The AR-Lab has been enabled by a € 3.3 M award from Science Foundation Ireland as part of their Research Infrastructure program and an additional € 1 M investment from the European Research Council.

References

[1] K.C. Opiela, M. Rak, T.G. Zielinski, A concept demonstrator of adaptive sound absorber/insulator involving microstructure-based modelling and 3dprinting, in: Proceedings of ISMA2018 Including USD2018, Leuven, Belgium, September 2018.

[2] J. Kennedy, L. Flanagan, L. Dowling, G.J. Bennett, H. Rice, D. Trimble, The influence of additive manufacturing processes on the performance of a periodic acoustic metamaterial, Int. J. Polym. Sci. 2019 (2019) 11, https://doi.org/10.1155/2019/7029143.

[3] M. Yang, S. Chen, C. Fu, P. Sheng, Opti mal sound-absorbing structures, Mater. Horiz. 4 (4) (2017) 673–680, https://doi.org/10.1039/C7MH00129K, http://pubs.rsc.org/en/content/articlelanding/2017/mh/c7mh00129k.

[4] Y. Zhu, X. Fan, B. Liang, J. Cheng, Y. Jing, Ultrathin acoustic metasurface-based Schroeder diffuser, Phys. Rev. X 7 (2) (2017) 021034https://doi.org/10.1103/PhysRevX.7.021034.

[5] R. Ghaffarivardavagh, J. Nikolajczyk, R.G. Holt, S. Anderson, X. Zhang, Horn-like space-coiling metamaterials toward simultaneous phase and amplitude modulation, Nat. Commun. 9 (1) (2018) 1349, https://doi.org/10.1038/s41467-018-03839-z, https://www.nature.com/articles/s41467-018-03839-z.

[6] C. Chen, Z. Du, G. Hu, J. Yang, A low-frequency sound absorbing material with subwavelength thickness, Appl. Phys. Lett. 110 (22) (2017) 221903, https://doi.org/10.1063/1.4984095.
[7] Y. Xie, B.-I. Popa, L. Zigoneanu, S.A. Cummer, Measurement of a broadband negative index with space-coiling acoustic metamaterials, Phys. Rev. Lett. 110 (17) (2013) 175501, https://doi.org/10.1103/PhysRevLett.110.175501.
[8] S. Deshmukh, H. Ronge, S. Ramamoorthy, De sign of periodic foam structures for acoustic applications: concept, parametric study and experimental validation, Mater. Des. 175 (2019) 107830, https://doi.org/10.1016/j.matdes.2019.107830.
[9] J.F. Allard, N. Atalla, Propagation of Sound in Porous Media. Modelling Sound Absorbing Materials, second ed., John Wiley & Sons, 2009.
[10] H. Rice, P. Gransson, J. Kennedy, Design of a kelvin cell acoustic metamaterial, in: Proceedings of ISMA2018 Including USD2018 Paper Number 514, Leuven, Belgium, September 2018.
[11] R. Slone, R. Lee, J. Lee, Well conditioned asymptotic waveform evaluation for finite elements, IEEE Trans. Antenn. Propag. 51 (9) (2003) 2442–2447.
[12] H. Tidjerman, On the propagation of sound waves in cylindrical tubes, J. Sound Vib. 39 (1975) 1–33.
[13] D.H. Lee, Y.P. Kwon, Estimation of the absorption performance of multiple layer perforated panel systems by transfer matrix method, J. Sound Vib. 278 (4) (2004) 847–860, https://doi.org/10.1016/j.jsv.2003.10.017.
[14] M. Nijhof, Y. Wijnant, A. de Boer, An Acoustic Finite Element Including Viscothermal Effects, ICSV14, Cairns, Australia, 9-12 July, 2007, pp. 1–8.
[15] O. Zienkiewicz, R. Taylor, J. Zhu, The Finite Element Method: its Basis and Fundamentals, sixth ed., Elsevier Butterworth Heinmann, 2005.
[16] C. Geuzaine, J.-F. Remacle, Gmsh: A 3-d finite element mesh generator with built-in pre-and post-processing facilities, Int. J. Numer. Methods Eng. 79 (11) (2009) 1309–1331.
[17] H. Marcus, J. Barlow, J. Beaman, D. Bourell, M. Agarwala, Dir ect selective laser sintering of metals, Rapid Prototyp. J. 1 (1) (1995) 26–36, https://doi.org/10.1108/13552549510078113.
[18] I. Cooperstein, M. Layani, S. Magdassi, 3d printing of porous structures by UV-curable O/W emulsion for fabrication of conductive objects, J. Mater. Chem. C 3 (9) (2015) 2040–2044, https://doi.org/10.1039/C4TC02215G, https://pubs.rsc.org/en/content/articlelanding/2015/tc/c4tc02215g.
[19] M.N. Cooke, J.P. Fisher, D. Dean, C. Rimnac, A.G. Mikos, Use of stereolithography to manufacture critical-sized 3d biodegradable scaffolds for bone ingrowth, J. Biomed. Mater. Res. Part B Appl. Biomater. 64 (2) (2003) 65–69, https://doi.org/10.1002/jbm.b.10485.

Institution of MECHANICAL ENGINEERS

Journal of MECHANICAL ENGINEERING SCIENCE

Original Article

Proc IMechE Part C:
J Mechanical Engineering Science
0(0) 1–15
© IMechE 2020
Article reuse guidelines:
sagepub.com/journals-permissions
DOI: 10.1177/0954406220904106
journals.sagepub.com/home/pic
SAGE

Investigations of the mechanical properties on different print orientations in SLA 3D printed resin

JS Saini[1], Luke Dowling[2], John Kennedy[2] and Daniel Trimble[2]

Abstract

3D printing has been recognized as the future manufacturing technique by different industries. The properties of products manufactured using this technique depend upon large number of factors, with print orientation being one among the most important factors. Currently, there is no standard for the build orientation of the printed component. To date, the analysis of material properties is conducted by testing specimens printed in different orientations. The present work explores the effect of layer orientations on the different mechanical properties of an SLA manufactured polymer material. Five different orientations, i.e. 0°, 22.5°, 45°, 67.5° and 90° were used to print the specimens for the analysis of mechanical properties of the material. Tensile, compression, flexural, impact, fatigue and vibration analysis are the different mechanical tests that were conducted as per their respective standards. It was found that the print orientation plays a significant role in the behaviour of the respective mechanical property. The maximum tensile and compressive load are being taken by the specimens printed at an angle of 22.5° and 67.5°, respectively. The specimen printed at 67.5° orientation again have highest flexural strength, whereas the specimen printed at 0° have higher impact and fatigue strength.

Keywords

Additive manufacturing, print orientations, polymers, stereolithography apparatus, mechanical properties

Date received: 2 January 2019; accepted: 13 January 2020

Introduction

3D printing also referred to as rapid prototyping or additive manufacturing is a stratified process of joining materials to build a 3D object. It usually begins with a surface tessellation language (STL) file which is generated by a computer aided design (CAD) software. It contains the 2D sliced build data which are sent to the 3D printing machine.[1] The accessibility of 3D printers for both industrial and general public has grown drastically in the past decade.[2] This is due to the fact that open source 3D printers are available to fabricate the components with properties comparable to those of commercially available printers.[3–5] Additive processes can produce complex parts, have freedom of design and have tool-less fabrication as compared to conventional production processes.[6]

Presently, various techniques such as fused deposition modeling (FDM),[7] stereolithography apparatus (SLA),[8] selective laser sintering (SLS),[9] continuous liquid interface production (CLIP)[10] and digital light processing (DLP)[11] have been developed to build components with complex geometries. These techniques have their own advantages, disadvantages and applications.

SLA is one of these techniques which can be used for polymer materials, which are now being produced with a wider range of properties.[12] The main advantage of SLA printing technology is the ability to print parts with high resolution and accuracy.[1] Along with the required accuracy, the mechanical properties of 3D printed polymer materials are an important consideration for their application. Different process parameters in the printing affect the mechanical properties of the build components. Among these parameters, the component's build direction is an important consideration in additive manufacturing.[13,14]

Several researchers have considered the different build parameters in polymer materials for their effects on the

---

[1]Department of Mechanical Engineering, Thapar Institute of Engineering and Technology, Patiala, Punjab, India
[2]Department of Mechanical and Manufacturing Engineering, Trinity College, Dublin-2, Ireland

Corresponding author:
JS Saini, Department of Mechanical Engineering, Thapar Institute of Engineering and Technology, Bhupindra Road, Patiala-147004, Punjab, India.
Email: jsaini@thapar.edu

mechanical properties using different 3D printing techniques. Lee et al.[15] reported that the diagonal-printed specimens had higher compressive strengths as compared to axial and transverse 3D printed specimens. Vega et al.[16] evaluated the effect of layer orientations on the mechanical strength and toughness of the coated polymer specimens manufactured using inkjet printing. The mechanical strength was evaluated using tensile testing and three-point bend testing. The toughness was evaluated by Izod impact testing. Sood et al.[17,18] focused on the influence of orientation, layer thickness, raster angle, raster width and air gap on the tensile, compressive, flexural and impact strength of the FDM manufactured components. Durgun and Ertan[19] studied the influence of orientation and raster angle on the tensile and flexural strengths of FDM-printed components. Mueller et al.[20] investigated the impacts of print table position, number of intersections between layers and nozzles orthogonal to the load-direction, the exposure time to ultraviolet light and the expiry date of the raw material on the mechanical properties of the inkjet 3D printed components.

Torrado and Roberson[21] related the tensile strength of the 3D FDM-printed component to the build orientation and raster pattern. Rankouhi et al.[22] studied the tensile strength of parts manufactured out of acrylonitrile butadiene styrene (ABS) using FDM for different layer thickness and orientations. Tensile test results showed that samples printed with 0.2 mm layer thickness exhibited higher elastic modulus and ultimate strength compared with 0.4 mm layer thickness. Cantrell et al.[23] performed the tensile and shear characterizations of ABS and PC 3D printed parts to determine the extent of anisotropy present in the material. Specimens were printed with varying raster and build orientations to determine the directional properties of the materials. Wang et al.[24] investigated the effect of layer height and plate temperature on the Izod impact strength of FDM-printed PLA components. Zaldivar et al.[25] showed the significant effect of the print orientations on the macrostructure, the mechanical and thermal properties of FDM-printed components. Song et al.[26] investigated the mechanical properties of the FDM 3D printed blocks. Specimens were cut from the printed blocks along different material directions using conventional machining and were tested for tensile and compressive strengths. Turk et al.[27] investigated the thermo-mechanical creep properties of additive-manufactured acrylonitrile butadiene styrene ABSplus-P430 (ABS) for applications in fused deposition modeling (FDM), polyamide 12 (PA12) and DuraForm HST Composite (HST) made by SLS for in- and out-of-plane building orientations.

SLA parts are built by bonding layers of polymer onto the previous layer. This gives rise to planes of weakness in the part where the layers join. The disparate layers join together in an imperfect manner giving rise to the anisotropy exhibited by SLA parts. A secondary set of weakness within layers is created in the overlap between adjacent passes of the laser. The reduction in laser exposure decreases the level of crosslinking which further reduces the bonding of the part. More work is required to investigate the anisotropy of the SLA 3D printed parts. Moreover, there is very limited literature available for the fatigue and vibration analysis of the 3D printed polymer components which are very important properties of the materials for its different applications. The present work aims to fill the gap in the already published literature and produce a dataset to aid product designers.

Material and methods

The specimens were printed on the SLA Form 2 Formlabs advanced desktop 3D printer. It was equipped with 405 nm violet and 250 mW laser and $145 \times 145 \times 175\,\text{mm}^3$ build volume. The specimens were printed with 50 µm layer thickness and 140 µm laser spot size.

Clear photopolymer resin was the material used to print the specimens. Clear resin produces strong plastic parts ideal for a wide variety of applications and is specifically designed for Form 2 printers. The material was supplied by Formlabs, USA. Table 1 shows the material properties of the clear resin in green condition as per the data sheet provided by the company.

The specimens were prepared for five different orientations, i.e. 0°, 22.5°, 45°, 67.5° and 90°, which are shown in Figure 1. The specimens for different mechanical properties were printed as per specification given by the respective ASTM or ISO standard as per the available testing facilities.

All the printed specimens were cleaned in alcohol to remove the resin. The parts were then kept for an hour for isopropyl alcohol to fully evaporate after washing. Thereafter, the specimens were cured by gradual heating to 60 °C for 30 min and then cooling to room temperature.

The specimens with different print orientations were subjected to tensile, compression, flexural, fatigue, impact and vibrational testings to evaluate the effect of print orientations on mechanical properties.

ASTM D638 was used as a reference to prepare the specimens for the tensile testing used in the present work. The specimens were having the dimensions of 165 mm length, 57 mm gauge length, 19 mm width, 13 mm gauge width and 3.2 mm thick. Five specimens for each print orientation were used in the present

Table 1. Properties of the clear resin.

Properties	Ultimate tensile strength	Young's modulus	Elongation at failure	Flexural modulus	Notched Izod
Values	38 MPa	1.6 GPa	12%	1.25 GPa	16 J/m

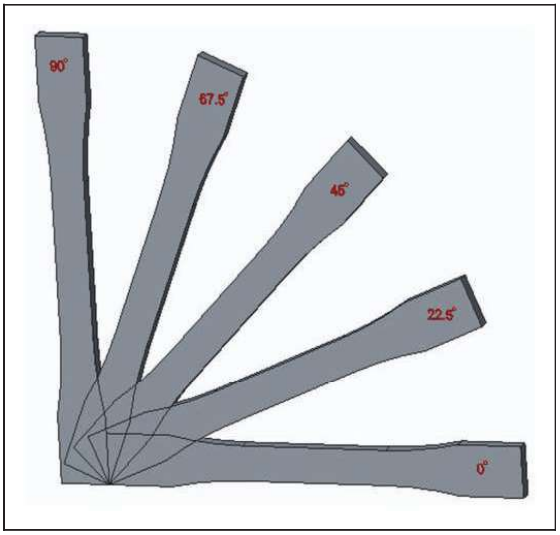

Figure 1. Different vertical print orientations.

work. Instron 3366 testing machine with the load capacity of 10 kN and a constant run test at 5 mm/min was used in the work.

The specimens for compression testing were prepared as per ASTM D695. The specimens were manufactured as blocks of 12.7 × 12.7 × 25.4 mm. Five specimens for each print orientation were used in the present work. Instron 5589 testing machine with the load capacity of 100 kN and a constant run test at 2 mm/min were used for the testing.

The specimens for flexural testing were prepared as per ASTM D790. The specimens were tested flatwise on the support span, with the support span-to-depth ratio of 16:1. Instron 3366 testing machine with the load capacity of 10 kN with the flexural testing setup was used in the work.

The notched specimens for the Charpy impact testing were prepared in accordance with ISO179 standard. The specimens were prepared with 'A' type of notches. Charpy impact tests were conducted using a pendulum impact tester of Jinjian make with XJJD-5 Series. A 0.5 J hammer was sufficient to break all the specimens.

Fatigue testing was performed on the specimens as per ASTM D7791. Cyclic fatigue tests were carried out on Instron 8801 machine operating under load controlled mode with a sinusoidal waveform. Tests were done at room temperature at a frequency of 1 Hz. The frequency was kept low to prevent the thermal effects on the fatigue life of the specimens. To evaluate the durability of the material, the specimens used for cyclic testing were subjected to 50% of their ultimate tensile strength.

Vibration testing of a clamped-free cantilever beam was conducted in order to calculate the modulus of elasticity according to Euler–Bernoulli beam theory. The clamped-free cantilever geometry was chosen which was similar to the test procedure followed in previously published works[28,29] to calculate the dynamic properties of materials from a cantilever beam. This theory is well described in numerous textbooks[30–32] and well summarised by Han et al.[33] The Euler Beam theory approach was selected for simplicity as it allowed for the calculation of frequency dependent Young's Modulus and damping behaviour.

Tests were conducted at room temperature in a custom test rig consisting of National Instruments DAQ, a PCB SmartShaker, a Polytec PDV-100 Portable Digital Vibrometer and custom software for signal generation, data acquisition and analysis through Matlab. Beams of 10.0 × 3.00 × 160 mm were produced and clamped in the SmartShaker to give a free length of 148 mm. Sample dimensions and masses were measured to insure uniformity between samples of different print orientations.

Results and discussions

The following section discusses the results to evaluate the effect of print orientations on the different mechanical properties.

Tensile testing

The experimental setup for tensile testing on Instron 3366 machine for one of the orientation is shown in Figure 2. The typical stress–strain curves for all the orientations are shown in Figure 3.

It can be seen from the figure that the failure load increases from 0° to 22.5° orientation. It is due to the fact that the print layer is at an angle to the direction of the loading. There is decrease in the failure load from 22.5° to 45° orientation. This variation is due to the fact that the print layer is in an off-axis direction with respect to the applied load direction. This promotes a shear failure to occur along the weaker build layer direction. The load decreases further from the 45° orientation to the 67.5° orientation due to the increase in the inclination of the layer with respect to the load direction. The failure load is a minimum for the 90° print orientation as the print layer is perpendicular to the direction of the applied load. When the specimen build was entirely along the direction parallel to the applying of tensile force, the part exhibited flexible but strong bonding. Specimens that were built perpendicular to the tensile test direction demonstrated lower mechanical properties in line with work reported by Durgun and Ertan.[19] There is also significant effect of print orientations on the strain or the extension in the specimens. As can be seen from Figure 3, the extension in the specimens during the tensile test increases from 0° to 45° orientation. This is due to the fact that the print layers are in the direction of the applied load. Due to the elastic properties of the material, there is an extension of the specimens with maximum for 45° print orientations. With the print orientations of 67.5°, the print layer

Figure 2. Experimental setup for the tensile testing.

in the specimen is aligning in the direction perpendicular to the applied load. The extension decreases with increase in the print orientation from 45° to 67.5° and further decreases and is minimum at 90° orientation.

The maximum tensile loads taken by all the different orientations are shown in Figure 4(a). Figure 4(b) shows the tensile modulus for different print orientations. The failure of the specimens with 22.5°, 45° and 67.5° is along their print orientations as can be seen from Figure 5. The failure of the specimens with 0° and 90° print orientations is along the cross section of the specimens.

Figure 6 shows the optical images of the fracture surfaces for the different print orientations. The images were taken with a Zeiss AX10 optical microscope using its extended depth of focus (EDF) feature. It can be seen from Figure 6(a) that the failure in specimen with 0° print orientation is along the interface of the different layers. There is shear failure among the different printed layers as the layers are along the direction of the applied load in the tensile test. Figure 6(b) to (d) shows that the failure of the specimens is along the layers which are printed at a particular angle. The cracks begin to progress along the direction of the printing of the layer within the particular specimen. Figure 6(e) shows the failure in the specimen printed at 90° orientation. It can be seen from Figure 6(e) that the specimen fails with the complete removal of one layer from the adjoining layer as

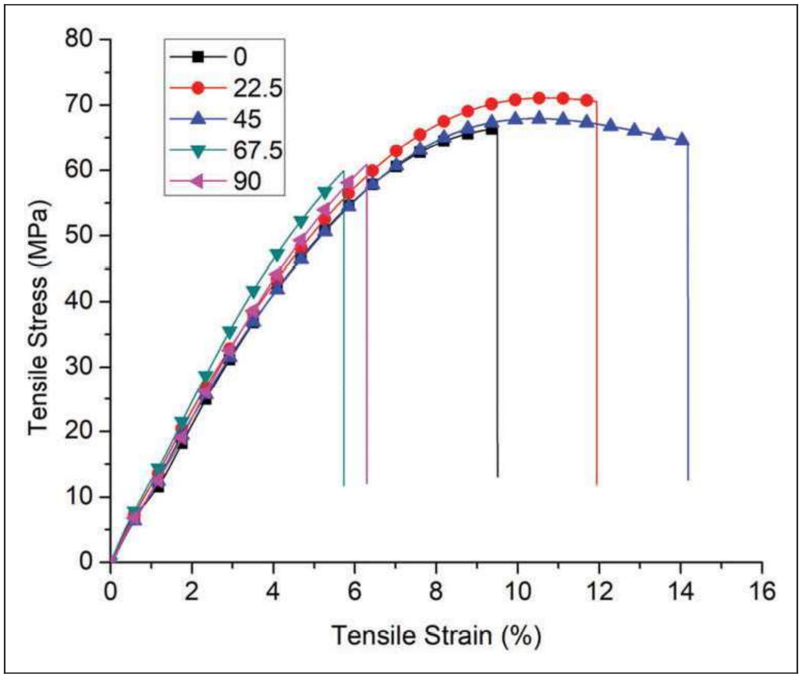

Figure 3. Stress–strain curves during tensile testing for all the print orientations.

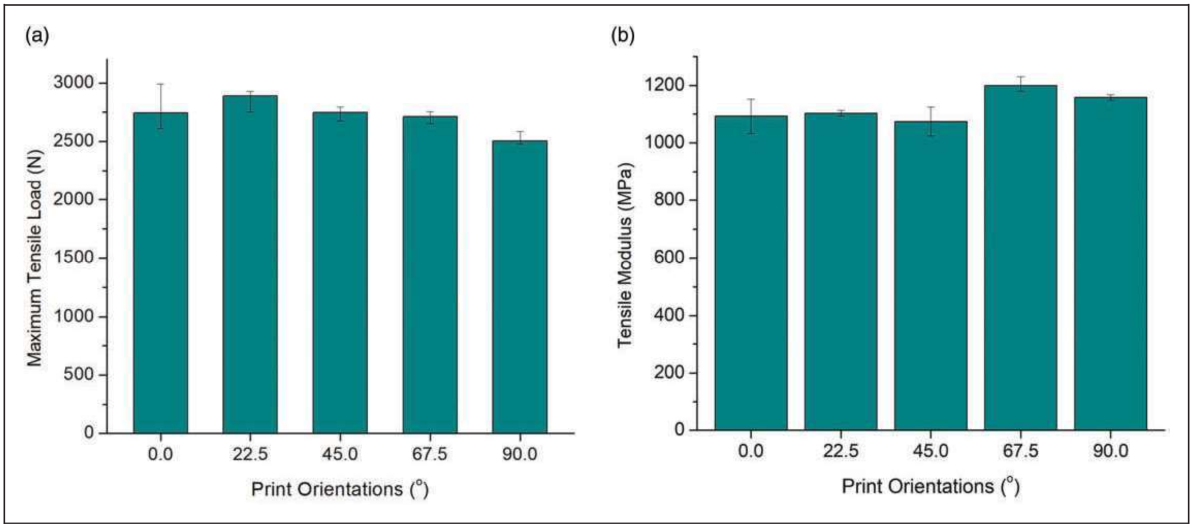

Figure 4. Tensile testing results with respect to print orientation. (a) Maximum tensile load. (b) Tensile modulus.

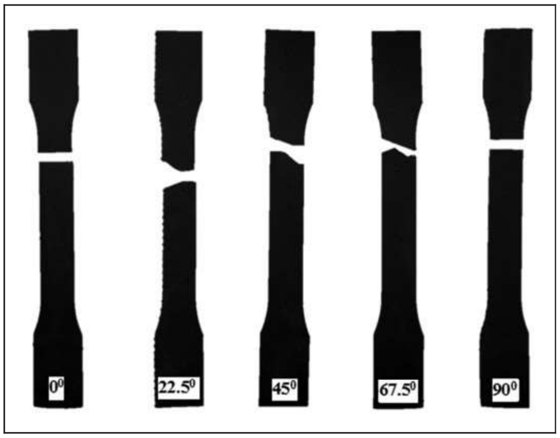

Figure 5. Failure modes in different print orientations.

the layers are in perpendicular direction to the applied tensile load. It can be seen from Figure 6 that the print orientations of the layers in the specimens play a vital role in the propagation of cracks and failure of the components.

Compression testing

A high load capacity machine was used to study the complete failure of the specimens under compressive loading. The experimental setup for compression testing on Instron 5589 machine for one of the orientation is shown in Figure 7. The different print orientations for preparation of compression specimens are shown in Figure 8. Figure 9 shows the direction of loading for the compression testing for two different orientations. The stress–strain curves during compression testing for all the printed part orientations are shown in Figure 10. It can be seen from Figure 10 that the material is having a high compressive strength, with compressive strain at about 55%.

The variation of maximum compressive strength with respect to print orientation is shown in Figure 11. It can be seen from the figure that the compressive strength increases with increase in orientation with the maximum compressive strength at 67.5° orientation. The specimen with 0° orientation is weakest in compressive strength due to the fact that the plane in which the material is added in 0° orientation is parallel to the direction of loading. With the increase in print orientation, the plane in which the material is added kept on inclining with respect to the direction of applied load and thus resisting more compressive load. There is a decrease in the compressive load for 90° print orientation as the printing plane is perpendicular to the direction of load, so the specimen fails by bulging out from all its four side faces. The results of compression testing are in line with Lee et al.[15] which says that the inclined printed specimens have higher compressive strength as compared to axial and transverse 3D printed specimens. To measure the maximum compressive load taken by the specimens, the load given by the UTM machine was increased resulting in the bulging out of the specimens from all of its side faces till the complete failure of the specimens due to crack propagation.

Flexural testing

Figure 12 shows the three-point bending test setup on the Instron 3366 machine. The bending test was done with the attachment such that the specimens were pulled upwards resulting in the three-point bending of the specimens.

In the bending tests, the stress that occurred in the specimen is more complex than that for the tensile

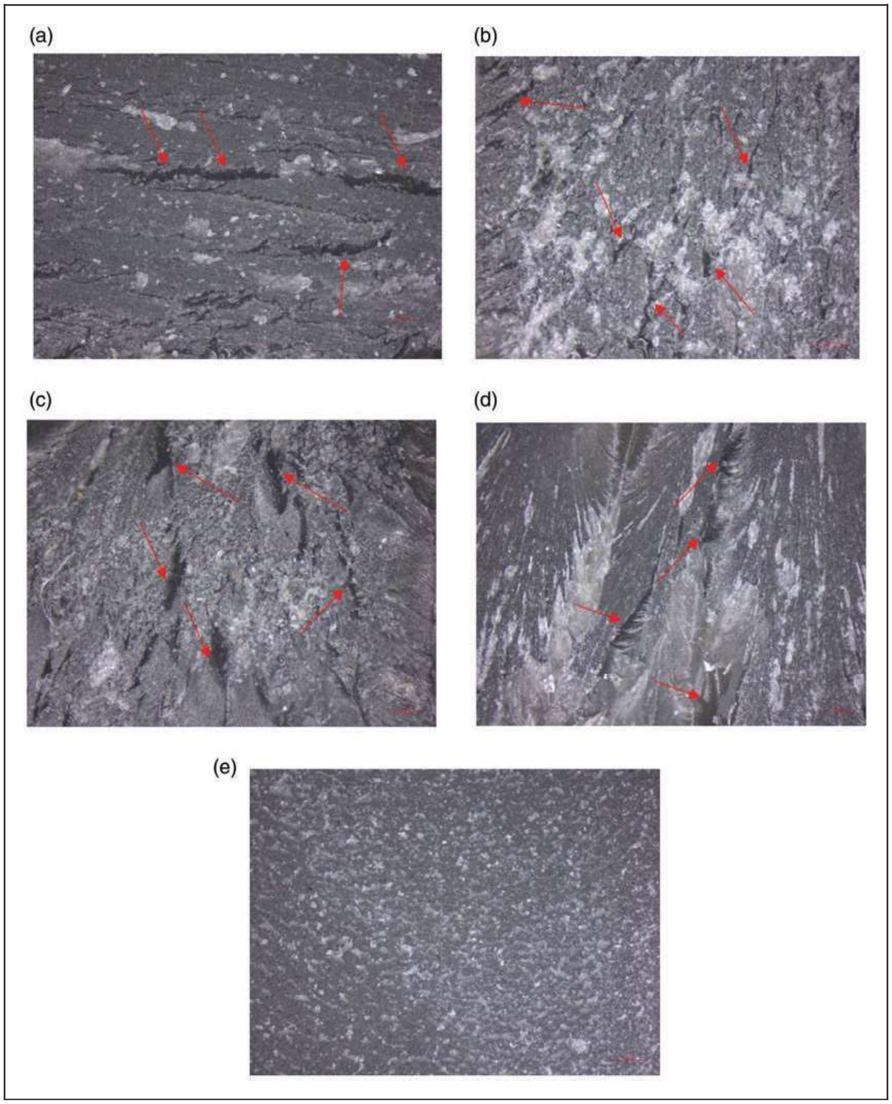

Figure 6. Images of fracture surfaces of tensile specimens for print orientations. (a) 0°. (b) 22.5°. (c) 45°. (d) 67.5°. (e) 90°.

tests. It is due to the fact that the specimens are subjected to both tensile and compressive stresses during bending.[34] Figure 13 shows the effect of print orientation on flexural strength of the specimens. It can be seen from the figure that the flexural strength increases with increase in print angle from 0° to 67.5°.

In the flexural specimens, the printing was such that the layers were parallel to the smaller length of the rectangular cross section of the specimen which was designated as vertical printing. The flexural strength of the specimens could be increased by printing the specimens such that the layers were parallel to the larger length of the rectangular cross section of the specimen with the designation as horizontal printing. The difference in these two types of printing is pictorially represented in Figure 14.

Figure 15 shows the flexural strength of the horizontally printed specimens. It can be seen from the figure that the flexural strength increases with increase in print angle from 0° to 67.5°. Comparing Figures 13 and 15, there is increase in flexural strength from 10 to 20% when the specimens are printed in horizontal direction as compared to the vertical direction. It is due to the fact that the specimen is placed such that the bending load is taken by the flat printed layer as compared to the specimen which is taken by the vertically printed layer.

Impact testing

The impact energy absorbed is a measure of the toughness of material. The Charpy impact test was conducted and the impact energy was converted into impact strength (kJ/m^2) using equation (1) for notched specimen

$$a = \frac{E_C}{h.b_N} \times 10^3 \tag{1}$$

Figure 7. Experimental setup for the compressive testing.

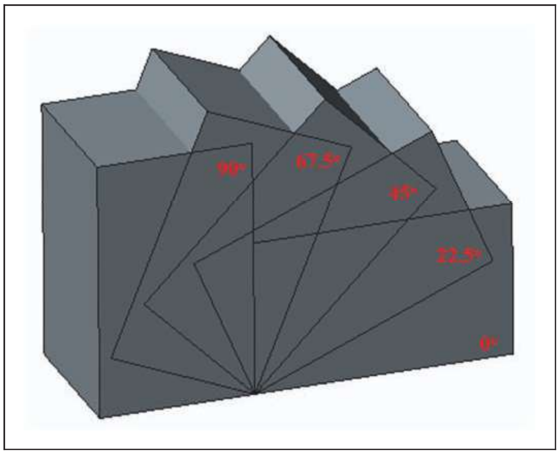

Figure 8. Different print orientations for compression specimens.

where E_c is the corrected energy (J) absorbed by breaking the test specimen, h is the thickness (mm) of the test specimen and b_N is the remaining width (mm) of the test specimen.

For each orientation tested, the average values of impact strength of 10 specimens were presented. Figure 16 shows the impact strength of the specimens with respect to the different vertical print orientations. To further analyse the impact strength, the specimens were printed such that the print layer was parallel to the larger length of the cross-section of the specimen. These two types of printings are pictorially represented in Figure 17.

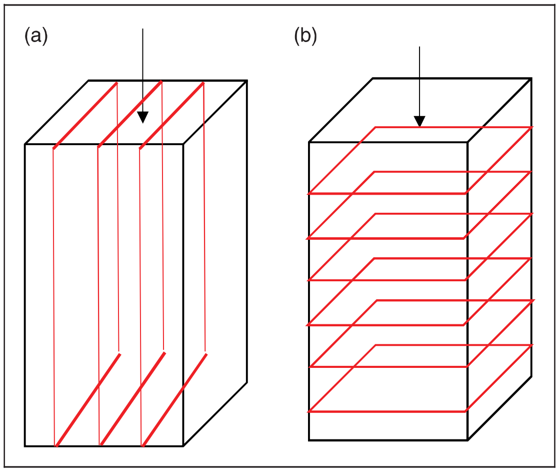

Figure 9. Direction of loading with respect to print orientation in compressive testing. (a) 0°. (b) 90°.

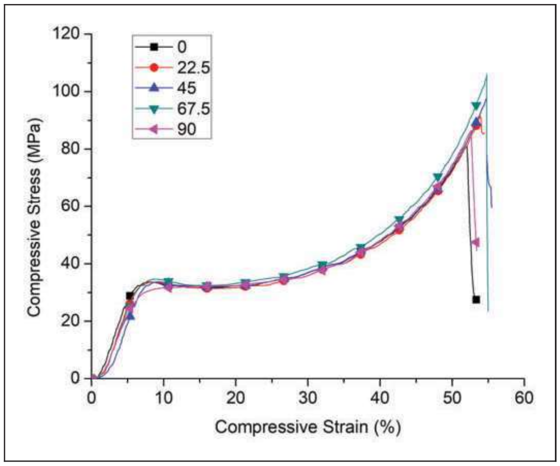

Figure 10. Stress-strain curves during compression testing for all the print orientations.

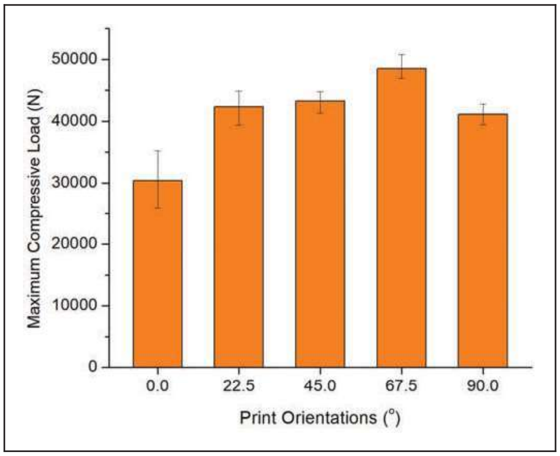

Figure 11. Maximum compressive load with respect to print orientation.

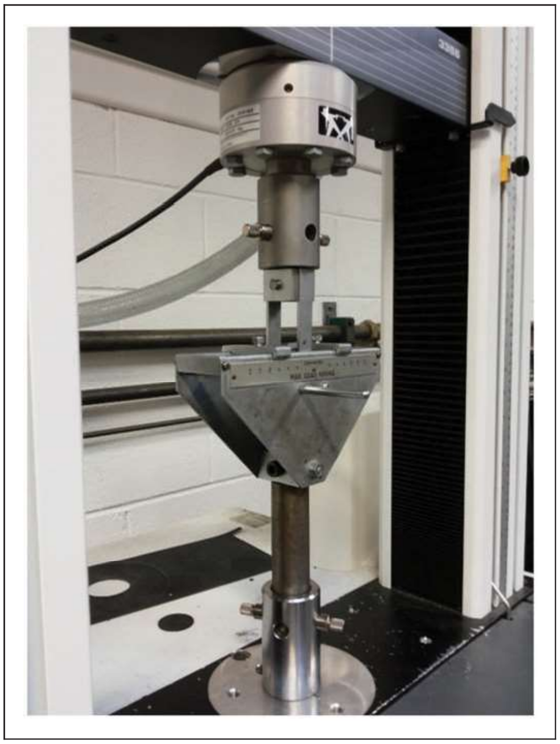

Figure 12. Experimental setup for the flexural testing.

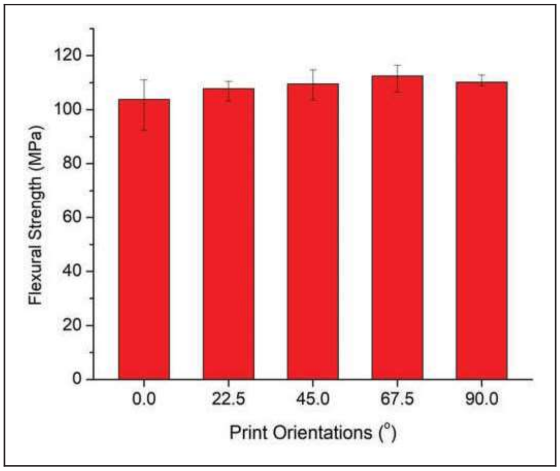

Figure 13. Effect of vertical print orientation on flexural strength.

Figure 18 shows the impact strength of the specimens with the horizontal printed layers. It can be seen from Figures 16 and 18 that the impact strength of the specimens is maximum with 0° print orientation as compared to other orientations. It is due to the fact that the print layer in 0° orientation is in perpendicular direction to the direction of impact which gives maximum resistance to the impact given to the specimen. The impact strength decreases as the print angle increases from 0° to 45°. This is due to the fact that

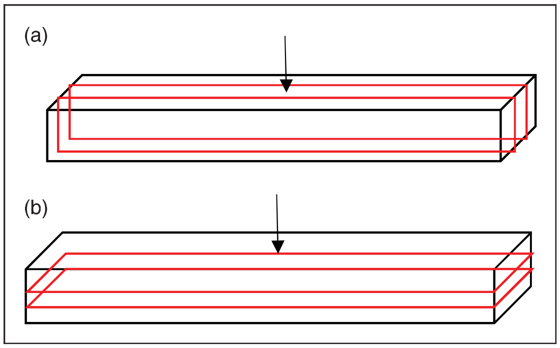

Figure 14. Orientation of print layers with respect to loading. (a) Vertical (0°). (b) Horizontal (0°).

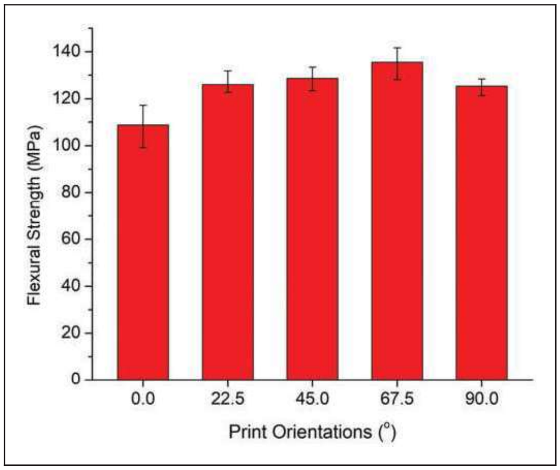

Figure 15. Effect of horizontal print orientation on flexural strength.

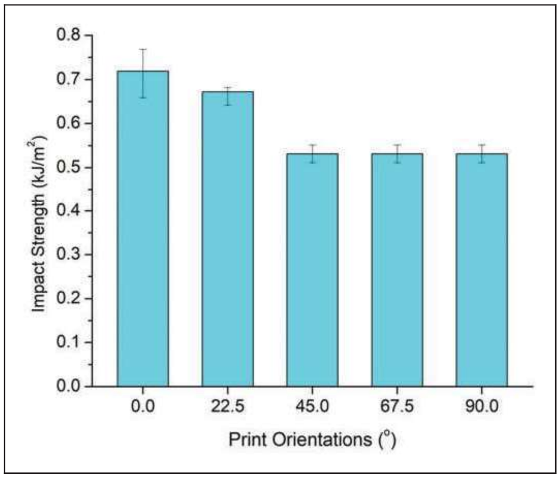

Figure 16. Effect of vertical print orientation on impact strength.

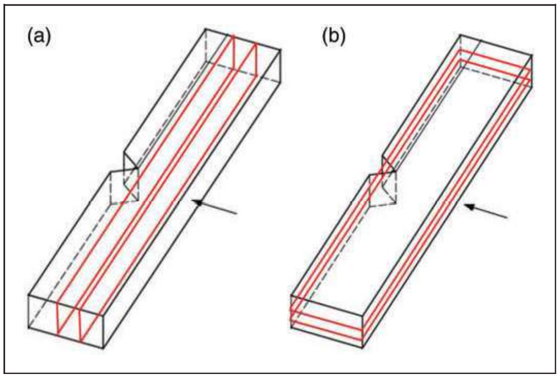

Figure 17. Orientation of print layers with respect to notch and hammer blow. (a) Vertical (0°). (b) Horizontal (0°).

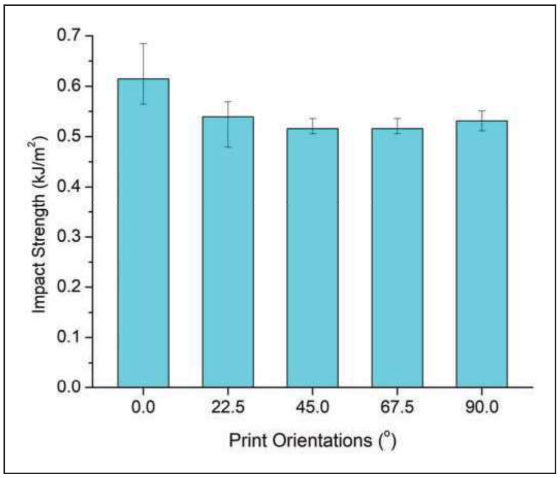

Figure 18. Effect of horizontal print orientation on impact strength.

the print layer is inclined which facilitates the movement of crack from the notch through the layer. There is a minor increase in the impact strength as the print angle changes to 67.5° and 90°. It may be the resistance given by the print layer to the propagation of the crack.

It was found that all the print orientations failed with a neat straight line failure along the cross-section through the notch. The stress concentration at the tip of the notch initiated the crack which propagated through its cross-section. Figure 19 shows the failure modes for some of the print orientations.

Figure 20 shows the optical images taken for the impact test specimens. The images were taken with the help of Zeiss AX10 optical microscope using the extended depth of focus (EDF) option available in the microscope. The images were taken at three different location of the tested specimens as shown in Figure 20(a). It can be seen that the location 1 is the lowest point of the notch with the maximum stress concentration. The specimens start breaking from this location as the hammer hits its opposite face. The specimens start breaking with the development of the crack which normally propagates through the angle of printed layer. This can be seen from images at location 1 for different orientations. As the crack propagates, the two halves of the specimens separate out with the smooth surface at location 2. The images at location 2 show a very smooth parting off of the specimens. The location 3 shows the final separation of two parts of each specimen. It can be seen from images at different locations that specimens part-off at the angle of printed layer.

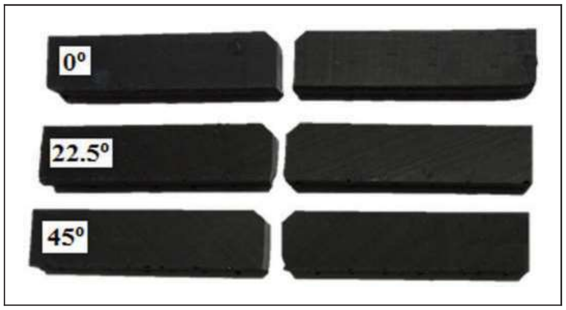

Figure 19. Failure mode for impact specimens.

Fatigue testing

A number of applications have repeated loading on the component resulting in material failures at much lower value compared to its ultimate strength. Fatigue test results of the 3D printed materials are therefore an important consideration when choosing materials. The fatigue testing of the specimens was done on the Instron 8801 machine, shown in Figure 21, in the load-controlled mode. The load was applied as a sinusoidal waveform.

For each orientation tested, the average of three readings was presented for fatigue testing. Figure 22 shows the number of cycles withstood by the specimens prepared with different print orientations. It can be found from Figure 22 that the specimen printed at 0° orientation failed after withstanding maximum number of cycles. This is due to the fact that the specimen with 0° orientation had the layers printed in the direction parallel to the applied cyclic fatigue loading. All the layers equally share the cyclic load giving the maximum resistance to the fatigue failure. This helped the specimens to withstand the larger amount of load under fatigue loading.

Figure 23 shows the type of failure modes in the specimens printed at different orientations. It can be seen from the figure that the specimen with 0° print orientation fails with the two sections breaking along the straight line giving a very clean break as the layers are in the direction parallel to the applied load. The shape of the failure is very much similar in the specimens with 90° print orientations. It is due to the fact that the layer is perpendicular to the direction of the

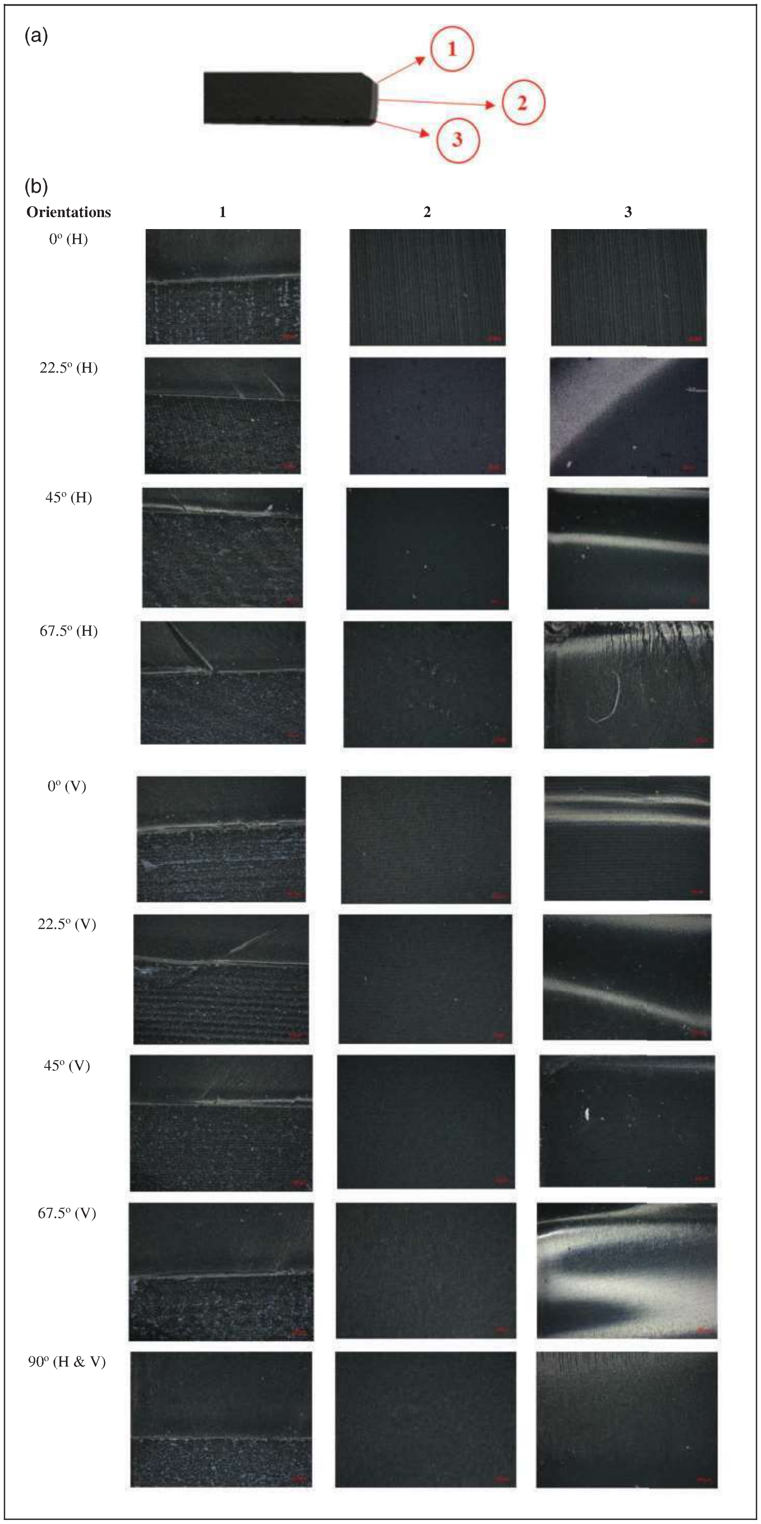

Figure 20. Optical images of impact tested specimens. (a) Location at which images taken. (b) Optical images for different orientations.

applied load which completely removes one layer from another layer. Figure 23 also shows the failure mode of the specimen with 45° print orientation. It can be seen that the specimen fails with the crack propagating in the inclined direction. The failure is much similar in case of specimens with print orientations at 22.5° and 67.5° in which again the crack propagates in the inclined direction.

Figure 24 shows the images of fracture surfaces of fatigue specimens for print orientations of 45° and 90°. The crack propagations were similar to the specimens which failed in tensile loading. The angle of print orientation affected the direction of crack propagation. The major difference was in the specimen printed at 90° orientation. As can be seen from Figure 24(b), there were smaller visible cracks within the specimens as compared to the specimen which failed under tensile loading. It is due to the fact that there is cyclic loading in fatigue testing which weakens the specimens by cyclic elongation and compression of the layers. This helps to develop the internal cracks within the layers of the specimens which were clearly visible in the specimen with 90° print orientations.

Figure 21. Experimental setup for fatigue testing.

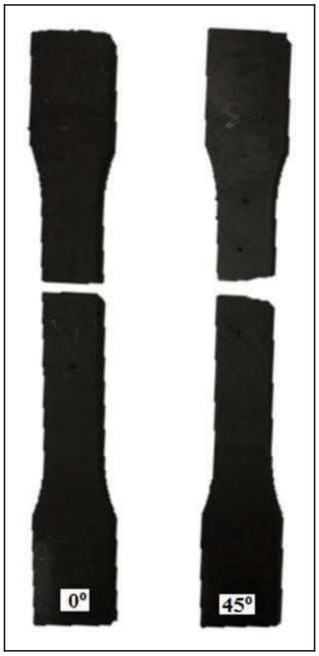

Figure 23. Failure mode in specimens with 0° and 45° print orientations.

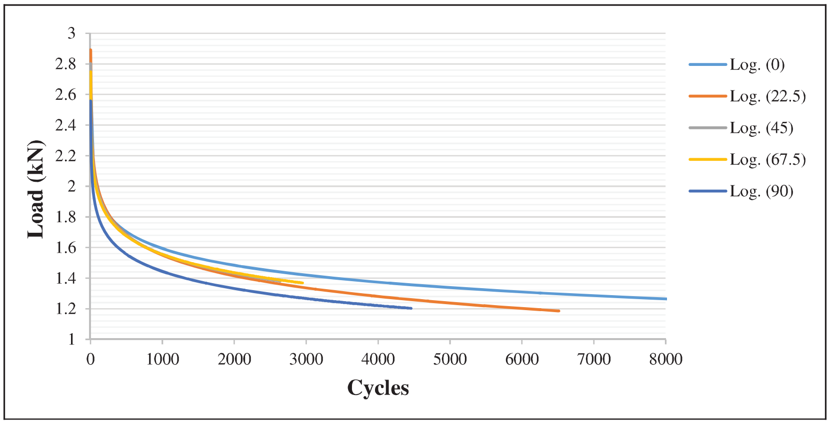

Figure 22. Fatigue loading of specimens printed at different orientations.

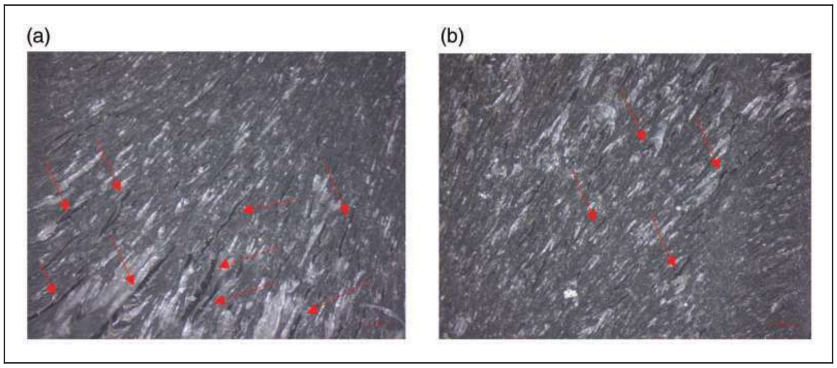

Figure 24. Images of fracture surfaces of fatigue specimens for orientations. (a) 45°. (b) 90°.

Dynamic testing

Figure 25 shows a cantilever beam specimen mounted in the SmartShaker. In order to identify the natural frequencies, the frequency response function (FRF) was calculated between the input excitation, as measured by a PCB accelerometer mounted on the clamp, and the beam response measured by the Polytec laser vibrometer. Measurements were made for 240 s at a sample rate of 32,768 Hz and the FRF was calculated with a block length of 131,072 points, 50% overlap with a Hanning window applied for 117 averages. This gave a frequency resolution of the FRF of 0.25 Hz. According to the Euler–Bernoulli beam equation, the natural frequency is given by equation (2)

$$\omega_n = (\beta_n l)^2 \sqrt{\frac{EI}{\rho l^4}} \tag{2}$$

where ω_n is the natural frequency in radians per second, E is the modulus of elasticity, I is the area moment of inertia of the cross section, l is the length, ρ is the mass per unit length and $(\beta_n l)^2$ is a constant equal to 3.54 for the fundamental natural frequency and 22.0 for the second natural frequency. For the specimens in question, the fundamental natural frequency was in the region of 35 Hz and the second natural frequency was in the region of 230 Hz.

The repeatability of the measurement was insured by dismounting and remounting specimens for repeat tests. In order to assess the repeatability of the specimens themselves, two vertically orientated samples were produced for each of the five print orientations. A single set of horizontally orientated samples was produced with the exclusion of 0° due to repeat print failures at this orientation.

Figure 26 reports the calculated modulus of elasticity from the fundamental and second natural frequencies of the cantilever beams. The results of the flexural testing showed that the horizontal print orientations had a higher flexural strength than the vertical orientations. While the specimens with the highest modulus of elasticity was 45° horizontal print orientation, the general spread in the data is greater than what was observed for the flexural testing. There are considerable differences between the modulus of elasticity results for the vertical print orientations at all angles apart from 67.5°. Since the test results for an individual specimen were highly repeatable, this variation between specimens is due to inconsistencies between separate prints. Differences exist between the dynamic material properties extracted from flexural resonance testing and equivalent static testing.[35] As shown in the results here, there is a frequency dependence in the material properties and the modulus of elasticity is higher across all samples and angles when based on the second resonance mode.

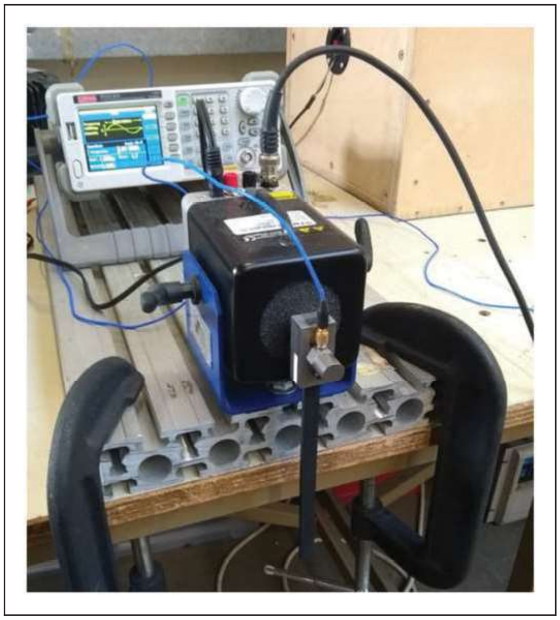

Figure 25. Cantilever beam sample mounted in the SmartShaker test rig.

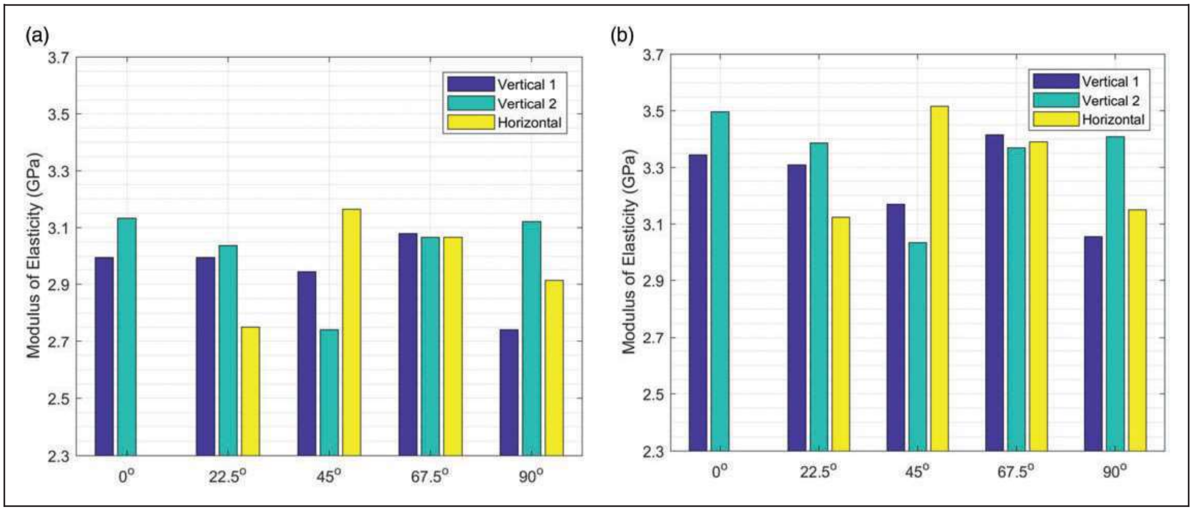

Figure 26. Effect of print orientation on modulus of elasticity. (a) Fundamental natural frequency. (b) Second natural frequency.

When compared to the manufacturer's stated value of the flexural modulus of 1.25 GPa, the dynamic values are approximately two to three times higher which are comparable to the differences found in equivalent tests.[36]

Conclusions

The present work analysed the effect of different print orientations on the mechanical properties of the polymer material. The following conclusions can be drawn based on the different results.

(i) In the tensile, compression and flexural tests, the specimens with the layers printed at an angle bear higher failure loads. It is due to the fact that the print layers are at an angle to the applied load which withstand higher load before its ultimate failure. The maximum tensile and compressive load are being taken by the specimens printed at an angle of 22.5° and 67.5°, respectively. The specimen printed at 67.5° orientation again have higher flexural strength. In tensile test, the failure of specimens with 0° and 90° print orientations is as a clear straight line separation of the two ends, whereas in the specimens with inclined orientations, the failure is with the crack propagating along the line of inclination.

(ii) The maximum impact strength is for the specimen with 0° print orientation. It is due to the fact that the print layer is perpendicular to the direction of hammer blow which gives the maximum resistance to the impact given by the hammer blow.

(iii) For the cyclic loading in fatigue testing, the specimen with 0° print orientation withstands maximum number of cycles before its failure. It is due to the fact that the printed layers are parallel to the direction of cyclic loading which helps all the layers to bear the same amount of load giving the maximum resistance to the cyclic loads. In the fatigue test, the failure of the specimens is in the same pattern as were in tensile testing. The specimens with 0° and 90° print orientations had a straight line breaking but the specimens with inclined orientations had the failure with the cracks propagating at the inclined direction. The images of the failure surfaces show that the failure was similar to the failure in the tensile tests. The only difference was in the specimens with 90° print orientation in which there were initiation of cracks within the printed layers due to the cyclic loading of the specimens.

(iv) The dynamic testing revealed greater inconsistencies between samples of the same print orientation with differences of up to 0.2 GPa observed in the modulus of elasticity for identical print orientations. The dynamic testing does not take the sample to the point of failure and the influence of minor geometric variations between samples may be exaggerated under these conditions. This may also explain why the results of the 67.5° orientation showed greater consistency as there are optimal angles for orientating prints within the build volume of the machine and for the design of supports. This may lead to greater geometric accuracy for some print orientations and although parts were precisely weighed and measured, as required for the correct application of the Euler–Bernoulli beam equation, these differences may not be fully accounted for in the calculations.

Declaration of Conflicting Interests

The author(s) declared no potential conflicts of interest with respect to the research, authorship, and/or publication of this article.

Funding

The author(s) disclosed receipt of the following financial support for the research, authorship, and/or publication of this article: The material and 3D printing machine used for the work received funding through the AERIALIST project no: 723367 European Union H2020-EU.3.4. SOCIETAL CHALLENGES – Smart, Green and Integrated Transport. Dr. J. S. Saini was financially supported through Post-Doctoral fellowship given by Thapar Institute of Engineering and Technology, Patiala, Punjab, India for research work at Trinity College, Dublin, Ireland.

ORCID iD

JS Saini https://orcid.org/0000-0002-6770-5967

References

1. Wang X, Jiang M, Zhou Z, et al. 3D printing of polymer matrix composites: a review and prospective. *Compos Part B* 2017; 110: 442–458.
2. Stansbury JW and Idacavage MJ. 3D printing with polymers: challenges among expanding options and opportunities. *Dental Mater* 2016; 32: 54–64.
3. Tymrak BM, Kreiger M and Pearce JM. Mechanical properties of components fabricated with open-source 3D printers under realistic environmental conditions. *Mater Des* 2014; 58: 242–246.
4. Wittbrodt B and Pearce JM. The effects of PLA color on material properties of 3D printed components. *Add Manuf* 2015; 8: 110–116.
5. Tanikella NG, Wittbrodt B and Pearce JM. Tensile strength of commercial polymer materials for fused filament fabrication 3D printing. *Add Manuf* 2017; 15: 40–47.
6. Wendel B, Rietzel D, Kuhnlein F, et al. Additive processing of polymers. *Macromol Mater Eng* 2008; 293: 799–809.
7. Masood SH. Intelligent rapid prototyping with fused deposition modelling. *Rapid Prototyp J* 1996; 2: 24–33.
8. Cooke MN, Fisher JP, Dean D, et al. Use of stereolithography to manufacture critical-sized 3D biodegradable scaffolds for bone ingrowth. *J Biomed Mater Res Part B* 2003; 64B: 65–69.
9. Agarwala M, Bourell D, Beaman J, et al. Direct selective laser sintering of metals. *Rapid Prototyp J* 1995; 1: 26–36.
10. Tumbleston JR, Shirvanyants D, Ermoshkin N, et al. Continuous liquid interface production of 3D objects. *Science* 2015; 347: 1349–1352.
11. Cooperstein I, Layani M and Magdassi S. 3D printing of porous structures by UV-curable O/W emulsion for fabrication of conductive objects. *J Mater Chem* 2015; C3: 2040–2044.
12. Dizon JRC, Espera AH, Chena Q, et al. Mechanical characterization of 3D-printed polymers. *Add Manuf* 2018; 20: 44–67.
13. Xu F, Loh HT and Wong YS. Considerations and selection of optimal orientation for different rapid prototyping systems. *Rapid Prototyping J* 1999; 5: 54–60.
14. Thrimurthulu K, Pandey PM and Reddy NV. Optimum part deposition orientation in fused deposition modeling. *Int J Mach Tools Manuf* 2004; 44: 585–594.
15. Lee CS, Kim SG, Kim HJ, et al. Measurement of anisotropic compressive strength of rapid prototyping parts. *J Mater Process Technol* 2007; 187–188: 627–630.
16. Vega V, Clements J, Lam T, et al. The effect of layer orientation on the mechanical properties and microstructure of a polymer. *J Mater Eng Perform* 2011; 20: 978–988.
17. Sood AK, Ohdar RK and Mahapatra SS. Parametric appraisal of mechanical property of fused deposition modeling processed parts. *Mater Des* 2010; 31: 287–295.
18. Sood AK, Ohdar RK and Mahapatra SS. Experimental investigation and empirical modeling of FDM process for compressive strength improvement. *J Adv Res* 2012; 32: 81–90.
19. Durgun I and Ertan R. Experimental investigation of FDM process for improvement of mechanical properties and production cost. *Rapid Prototyp J* 2014; 20: 228–235.
20. Mueller J, Shea K and Daraio C. Mechanical properties of parts fabricated with inkjet 3D printing through efficient experimental design. *Mater Des* 2015; 86: 902–912.
21. Torrado AR and Roberson DA. Failure analysis and anisotropy evaluation of 3D-printed tensile test specimens of different geometries and print raster patterns. *J Fail Anal Prevent* 2016; 16: 154–164.
22. Rankouhi B, Javadpour S, Delfanian F, et al. Failure analysis and mechanical characterization of 3D printed ABS with respect to layer thickness and orientation. *J Fail Anal Prevent* 2016; 16: 467–481.
23. Cantrell JT, Rohde S, Damiani D, et al. Experimental characterization of the mechanical properties of 3D-printed ABS and polycarbonate parts. *Rapid Prototyping J* 2017; 23: 811–824.
24. Wang L, Gramlich WM and Gardner DJ. Improving the impact strength of Poly(lactic acid) (PLA) in fused layer modeling (FLM). *Polymer* 2017; 114: 242–248.
25. Zaldivar RJ, Witkin DB, McLouth T, et al. Influence of processing and orientation print effects on the mechanical and thermal behavior of 3D-Printed ULTEM 9085 material. *Add Manuf* 2017; 13: 71–80.
26. Song Y, Li Y, Song W, et al. Measurements of the mechanical response of unidirectional 3D-printed PLA. *Mater Des* 2017; 123: 154–164.
27. Turk DA, Brenni F, Zogg M, et al. Mechanical characterization of 3D printed polymers for fiber reinforced polymers processing. *Mater Des* 2017; 118: 256–265.
28. Caracciolo R, Gasparetto A and Giovagnoni M. Measurement of the isotropic dynamic young's modulus in a seismically excited cantilever beam using a laser sensor. *J Sound Vib* 2000; 231: 1339–1353.
29. Kang X, Tay CJ, Quan C, et al. Evaluation of young's modulus of a vibrating beam by optical method. *Opt Eng* 2003; 42: 3053–3058.
30. Thomson W. *Theory of vibration with applications*. 4th ed. New Jersey, NJ: Prentice Hall, 1993.
31. Inman D. *Engineering vibration*. 4th ed. New Jersey, NJ: Prentice Hall, 1994.
32. Rao SS. *Mechanical vibrations*. 3rd ed. Boston, MA: Addison-Wesley Publishing Company, 1995.

33. Han SM, Benaroya H and Wei T. Dynamics of transversely vibrating beams using four engineering theories. *J Sound Vib* 1999; 225: 935–988.
34. Riley W, Sturges L and Morris D. *Mechanics of materials*. 6th ed. New Jersey, NJ: John Wiley & Sons, 2006.
35. Haines DW, Leban JM and Herb C. Determination of young's modulus for spruce, fir and isotropic materials by the resonance flexure method with comparisons to static flexure and other dynamic methods. *Wood Sci Technol* 1996; 30: 253–263.
36. Yoshihara H, Kubojima Y, Nagaoka K, et al. Measurement of the shear modulus of wood by static bending tests. *J Wood Sci* 1998; 44: 15–20.